# Single Rare-Earth Ions in Solid-State Hosts: A Platform for Quantum Networks

Thesis by
Andrei Ruskuc

In Partial Fulfillment of the Requirements for the
Degree of
Doctor of Philosophy


CALIFORNIA INSTITUTE OF TECHNOLOGY
Pasadena, California

2024
Defended September 21, 2023

Andrei Ruskuc
ORCID: 0000-0001-7684-7409

# ACKNOWLEDGEMENTS

First, thank you Andrei for welcoming me into the Faraon Lab. The past 6 years have been a formative and enjoyable period of my life. This is, in large part, due to the collaborative, supportive environment that you have fostered in our lab. Thank you for giving me the freedom to pursue my ideas, the discussions, advice and opportunities.

Next I would like to thank and acknowledge Chun-Ju's contribution: we have worked together on nearly all aspects of the nuclear spin and entanglement projects. We started working together three years ago and I honestly couldn't have asked for a better lab partner and friend. I've always been impressed by your unwavering enthusiasm and hard work. I am glad to be leaving the project in such capable hands.

Joonhee, thank you for being a wonderful collaborator. Ever since we started working together, I have always looked forward to our discussions. I have learned a lot from you over the years. Thank you for sharing your enthusiasm, for brainstorming ideas, and for giving me career advice!

Jon and John, thank you for being amazing mentors and role models during the first two years of graduate school. Jon: for the opportunity to work together on the first single Yb paper and for the continued discussions and advice throughout my PhD. John: for your generosity, ideas, and enthusiasm for rare-earths.

Thank you, also, to the new generation of single-ion team members: Sophie, Emanuel, and Erin, for bringing fresh eyes to the project and for your support in the final stages of my PhD.

Thank you to Ioana for your advice and insightful questions; Jake for guidance on all things fab-related; Mi, Tian, and Riku for all the helpful discussions.

And to all the other Faraon Lab members, past and present, for creating a friendly and productive environment.

Thank you to Prof. Endres, Prof. Painter, Prof. Hutzler, and Prof. Vahala for your time and advice on my candidacy and defense committees and for the excellent classes at the beginning of my PhD.

Thank you to Christy for all the encouragement and enthusiasm, to Cecilia and Jennifer for the countless things you do to support our progress throughout the PhD.

Thank you to all my friends for helping me escape the lab. Greg: for all the hiking, skiing, running, and office shenanigans; Terry for the late-night discussions and good food; Celia for the conversations and moral support; Prakriti for the crosswords and hiking trips; Newton for being an amazing room-mate and inspiring friend; Mi Ding and Yuchen for the skiing trips, and Fernando for the early morning runs. And thank you to Jacob, Fred, Joachim, and Michael for visiting from across the pond and staying in touch. Our friendships have been a highlight of the last 6 years and hopefully for many more to come, thank you!

Finally (and by no means least), I would like to thank my family: Mum, Dad and Emma, for your love, support, and encouragement through all these years. I couldn't have done it without you.

# ABSTRACT

Solid-state defects have emerged as leading candidates for quantum network nodes due to their compatibility with scalable device engineering and local nuclear spins for quantum processing. Rare-earth ions in crystalline hosts are particularly attractive due to their long optical and spin coherence times at cryogenic temperatures. However, until recently, detection and utilization of single rare-earth ions in quantum technologies has been hindered by their inherently weak optical transitions. In this thesis I present progress towards realizing a novel quantum network node architecture using single $^{171}Yb^{3+}$ ions in $YVO_4$, coupled to a nanophotonic cavity.

First, we demonstrate coherent operation of single $^{171}Yb^{3+}$ ions as optically addressed qubits. To do this, we leverage first order insensitivity of optical and spin transitions to electric and magnetic fields, thereby protecting the qubits from environmental noise. We demonstrate initialization, high fidelity control and readout of a hyperfine spin qubit with long quantum storage times. We also characterize the optical transitions and find a lifetime-limited echo coherence, thereby enabling a coherent spin-photon interface.

Next, we focus on realizing an auxiliary quantum register. The high-fidelity spin control of our $^{171}Yb^{3+}$ qubit is leveraged to access local nuclear spins. These spins comprise a dense ensemble which serves as a deterministic quantum resource. We utilize Hamiltonian engineering to generate tailored interactions, enabling polarization, coherent control and preparation of many-body nuclear spin states. Finally, we implement a spin-wave based memory protocol and demonstrate storage and retrieval of quantum states.

Moving beyond a single quantum node, in the final section of this thesis we will realize a small-scale quantum network using this platform. As a first step we demonstrate time-resolved quantum interference between photons emitted by ions in two separate devices. Then, we demonstrate a novel heralded entanglement protocol which incorporates optical dynamical decoupling and frequency erasure via precise photon detection. This protocol counteracts both static and dynamic inhomogeneity in the ions' optical transition frequencies, thereby enabling entanglement generation between any pair of qubits in a scalable fashion.

These results showcase single rare-earth ions as a promising platform for the future quantum internet.

# PUBLISHED CONTENT AND CONTRIBUTIONS

[1] A. Ruskuc, C.-J. Wu, E. Green, S. L. N. Hermans, E. Paul, J. Choi, and A. Faraon. "Tripartite remote entanglement of distinguishable optically addressable spins." In preparation.
A.R. built the experimental setup, performed the measurements, processed the data, and wrote the manuscript.

[2] A. Ruskuc, C.-J. Wu, J. Rochman, J. Choi, and A. Faraon. "Nuclear spin-wave quantum register for a solid-state qubit." In: *Nature* 602 (2022), pp. 408–413. DOI: 10.1038/s41586-021-04293-6.
A.R. built the experimental setup, performed the measurements, processed the data, and wrote the manuscript.

[3] J. M. Kindem, A. Ruskuc, J. G. Bartholomew, J. Rochman, Y. Q. Huan, and A. Faraon. "Control and single-shot readout of an ion embedded in a nanophotonic cavity." In: *Nature* 580 (2020), pp. 201–204. DOI: 10.1038/s41586-020-2160-9.
A.R. participated in building the setup, performing the measurements, processing the data, and writing the manuscript.

# TABLE OF CONTENTS

*Chapter 1*

# INTRODUCTION

Over the past 100 years, the development and impact of quantum physics on society has been accelerating at an unprecedented rate.

The first quantum revolution, led by pioneers like Heisenberg and Schrodinger[1] caused a paradigm shift in our understanding of the physical world, enabling a comprehensive description of matter and light at the most fundamental level. This propelled the development of technologies like the laser, transistor, magnetic resonance imaging (MRI) and atomic clocks.

We are currently in the midst of a second quantum revolution [1] where technologies that exploit the full power of quantum mechanics will be leveraged to perform useful tasks. Its distinguishing characteristic is the utilization of quantum entanglement in many-body quantum systems which can be engineered and controlled at an unprecedented level (the entanglement frontier [2]). The most promising applications include computation, simulation, communication, sensing and metrology.

For example, the discovery of quantum algorithms which leverage entanglement and superposition to achieve exponential speedup over their classical counterparts [3] have spurred the development of quantum computers [4]. A number of promising platforms have emerged based on trapped ions, atoms and superconducting qubits. A major goal is to achieve the fault-tolerance threshold where error correcting codes applied to many physical qubits can implement a logical qubit with reduced error rate [5, 6].

Another application leverages the no cloning theorem[2] to share a random key between two parties in a provably secure manner [7, 8]: quantum key distribution [9]. Sending keys over global length scales will require robust, macroscopic entanglement distribution.

Finally, in the context of metrology, entanglement enables the estimation of physical parameters with improved sensitivity [10]. This approach has been applied to gravitational wave detection [11], atomic clocks [12, 13] and magnetometry [14] (to

[1] Max Planck, Albert Einstein, Niels Bohr, Louis de Broglie, Max Born, Paul Dirac, Wolfgang Pauli, and Richard Feynman.

[2] It is impossible to make an identical copy of an unknown quantum state.

name but a few examples). Ultimately, the Heisenberg limit dictates that estimation error scales inversely with the number of entangled quantum probes.

A common feature in all three of these fields is the requirement to scale both the number of qubits and physical extent of quantum systems in order to realize useful technologies. The concept of a quantum internet was proposed to overcome these challenges [15]. In this thesis I will present progress towards a novel quantum network implementation consisting of single rare earth ions in a solid state host, coupled to nanophotonic cavities; this will be used as a test-bed for the future quantum internet.

## 1.1 Outline of This Thesis

The remainder of this chapter will provide an introduction to the field of quantum networking and an overview of the current state of the art with a particular focus on solid state systems and single rare-earth ions.

In Chapter 2, I will provide an introduction to the $^{171}Yb^{3+}$ platform utilized in this thesis, including the energy level structure, nuclear spin environment and coupling to nanophotonic cavities.

In Chapter 3, I present results demonstrating single $^{171}Yb^{3+}$ ions as good optically-addressed qubits with stable optical transitions, coherent optical and spin control and a long-lived quantum memory.

In Chapters 4 and 5, I will lay the groundwork for utilizing the nuclear spin environment around the $^{171}Yb^{3+}$ as a quantum resource. This will involve first developing a comprehensive understanding of ytterbium-vanadium interactions followed by the development of a novel quantum storage scheme which utilizes dynamic Hamiltonian engineering to implement coherent quantum information transfer.

Chapter 6 presents experimental results of this quantum storage protocol, demonstrating that vanadium nuclear spins can be utilized as a deterministic quantum memory.

In Chapter 7, I will change focus and start working towards remote quantum networking protocols. In this chapter I demonstrate indistinguishable emission from two $^{171}Yb^{3+}$ ions in separate devices via Hong-Ou-Mandel interferometry.

In Chapters 8, 9, and 10, I present a novel scheme for heralding remote entanglement between optically-addressed qubits. I provide a detailed description of a new

setup that I built for these experiments. Finally, I also present experimental results demonstrating entanglement between two remote $^{171}Yb^{3+}$ ions.

The final chapter will conclude with a discussion of new experiment directions, some of which we are actively pursuing, and future opportunities/challenges for this platform.

## 1.2 Applications and Progress in Quantum Networking

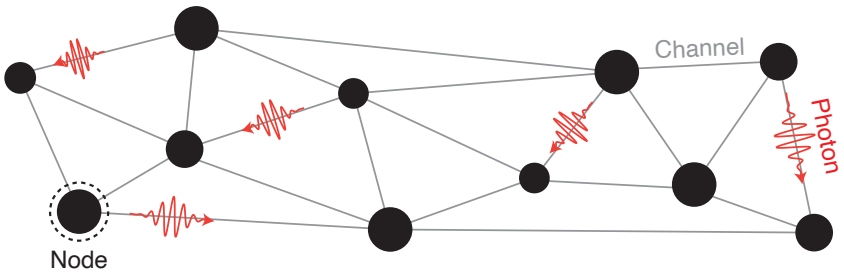


Figure 1.1: Quantum networks consist of nodes which can store and process quantum information and quantum channels (usually implemented via itinerant photons) which interconnect the nodes.

The quantum internet [15] was proposed as a method to overcome the scaling challenges associated with local quantum systems. Quantum networks consist of nodes which can store and process quantum information and quantum channels which interconnect the nodes in a manner that preserves quantum coherence (Figure 1.1). This enables generation of non-local entanglement without the need for direct (local) interaction. Whereas the Hilbert space size of classically connected quantum nodes would scale as $\sim A2^N$ (where there are $A$ nodes, each with $N$ qubits), it would scale as $\sim 2^{AN}$ for a fully connected quantum network. In this sense, a quantum network can be considered as a non-local quantum many body system with tailorable topology defined by the quantum interconnects.

Since this proposal, many implementations, platforms and applications of quantum networking have been studied. A recent review paper [16] categorized different approaches to quantum networking in terms of technological functionality, breaking development into four stages:

1. Prepare and measure networks;
2. Entanglement distribution networks;
3. Quantum memory networks;
4. Fault tolerant networks.

The first stage consists of nodes which can exchange qubits; however, both transmission and measurement are not deterministic. Such networks are useful for quantum key distribution (QKD) [7] and have been implemented commercially. The second stage involves deterministic or heralded entanglement distribution where an entangled state is known to exist without needing to collapse its wave-function (applications include device-independent QKD [17]). The third stage adds quantum memory functionality to each node combined with a universal local gate-set on the node qubit(s). This stage will enable advanced applications such as extending the baseline of telescopes [18] and enhancing the stability of a distributed set of atomic clocks [19]. In the final stage, each node consists of a local quantum computer which can process and store information fault-tolerantly. This is the holy-grail of quantum networking and will enable the implementation of fully distributed quantum processing and simulation [20, 21].

State of the art quantum memory networks have been experimentally implemented and used to realize non-local quantum gates [22, 23], entanglement distillation[3] [24, 25], deterministic teleportation [26–28], verifiable blind quantum processing [29] and preparation of tripartite GHZ states [30] useful for quantum secret sharing [31].

However, the quality of qubit control, storage and entanglement generation needs to be addressed in order to access the advanced applications associated with these networks (and ultimately build fault tolerant networks). This motivates the search and development of novel quantum networking platforms.

[3] Entanglement distillation is the process by which a higher fidelity entangled state can be generated from two lower fidelity entangled pairs. It relies on local operations at each node combined with classical communication (LOCC).

### 1.3 Large Scale Quantum Networking: The Quantum Repeater

While there have been demonstrations of advanced quantum networking protocols over small distances, expanding these to global length scales is an outstanding challenge and even the most basic (prepare and measure) quantum networks have not been realized over such large scales.

The fundamental issue is an exponential decrease in entanglement rate with increasing channel length ($L$):

$$R \propto \frac{1}{L} e^{-L/2L_0} \tag{1.1}$$

where $L_0$ is the attenuation length of the fiber and $R$ is the entanglement rate [32] (Figure 1.2a).

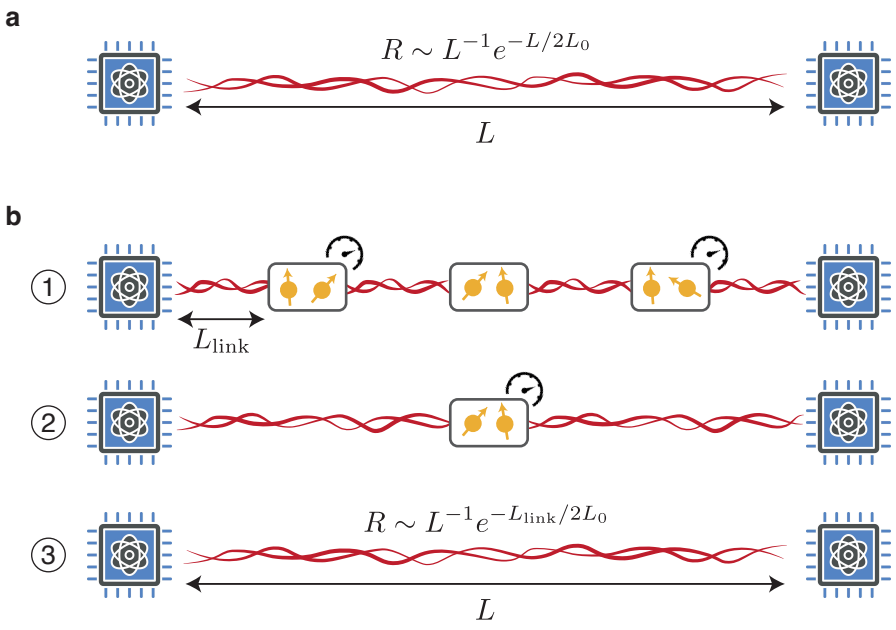


Figure 1.2: Quantum repeater schematic. a) Using direct entanglement generation schemes the entanglement rate exponentially decreases with channel length. b) A schematic of an $n = 2$ quantum repeater. Entanglement is generated simultaneously between adjacent segment of length $L_{\text{link}}$, a series of nested entanglement swapping operations (1–3) lead to entanglement of end nodes with rate inversely proportional to channel length.

To overcome this challenge, the quantum repeater protocol has been proposed [33]. The protocol operates as follows:

1. A single quantum channel is divided into $2^n$ elementary segments of length $L_{\text{link}}$ with $2^n - 1$ intermediate quantum repeater nodes.
2. Each repeater node consists of two qubits which are entangled with adjacent nodes, thereby establishing a set of $2^n$ entanglement links.
3. The entanglement links are purified to achieve the required link fidelity.
4. Pairs of adjacent entanglement links are combined via entanglement swapping at every second node, leading to links of distance $2L_{\text{link}}$. The entanglement swapping operation involves a Bell-state measurement (BSM) of the two qubits within a repeater node.
5. The process of entanglement purification and subsequent entanglement swapping is repeated in a nested-fashion with exponentially increasing entanglement lengths achieved after each round.
6. In total, $n$ nested purification and entanglement swapping steps are performed culminating in a link with length $L$.

By entangling the individual elementary links simultaneously, the quantum repeater protocol can beat the exponential scaling of the direct approach, leading to an entanglement time of:

$$R \propto \frac{1}{L} e^{-L_{\text{link}}/2L_0} \tag{1.2}$$

where $L$ is the total channel length and $L_{\text{link}}$ is the length of an elementary repeater link. We can see that this scales polynomially with $L$. See Figure 1.2b for a schematic of this protocol with $n = 2$.

We also note that there are some more advanced one-way quantum repeater proposals that rely on photonic cluster state transmission between adjacent nodes [34].

The functionality and requirements for implementing a quantum repeater are slightly less strict than for the end nodes discussed in the previous section. It turns out that these requirements can be satisfied using atomic ensembles [35] and their application for the quantum repeater protocol is motivated by an enhanced atomic cooperativity with light fields.

However, one important distinction between ensemble and single-qubit based repeater nodes needs to be highlighted. Specifically, it is impossible to perform a deterministic bell state measurement (BSM) using linear optics with these ensembles [36]. The time required to transfer classical messages, signalling BSM success for ensemble-based quantum repeaters will scale as $L/c$. Hence, given the finite coherence time of matter qubits, the entangled state fidelity will scale as $\mathcal{F} \propto e^{-L/cT_2}$. In order to mitigate this detrimental exponential scaling with channel length, it is preferred to encode the repeater node qubits using single atoms/ions.

### 1.4 Requirements for Quantum Network Nodes

From the previous two sections we can see that building application-oriented quantum network nodes and establishing long-range entanglement are somewhat different (if complementary) goals. Hybrid approaches to quantum networking use two different physical systems for the end nodes and repeater nodes, combined with a transduction protocol to convert quantum information between these systems [37–39]. However, there are inherent advantages in system complexity and efficiency associated with developing a single platform that is useful for both applications.

The subsequent list and Figure 1.3 summarize the requirements for a quantum memory network node which is also compatible with the requirements of a long-range quantum repeater:

- A qubit which can be initialized, controlled and read-out with high fidelity.
- A quantum memory (usually the qubit itself) which can robustly store quantum information during entanglement generation and subsequent processing.
- A coherent photonic interface which couples the qubit to optical photons for remote entanglement[4].
- Auxiliary qubits + Bell-state measurement functionality with the primary qubit. These enable multi-node entanglement and entanglement swapping[5].

The goal of my PhD has been to demonstrate all of these key areas of functionality in a novel quantum networking platform.

[4] Ideally these photons should be in the low-loss telecom band to minimize transmission losses.

[5] If the auxiliary qubits have an optical interface, then a BSM is sufficient to implement the quantum repeater protocol. However, if they do not, we additionally need a SWAP gate between the primary and auxiliary qubits.

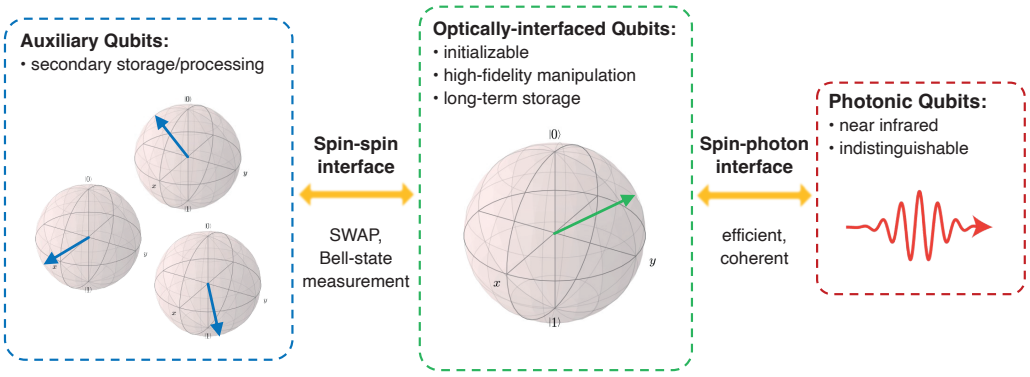


Figure 1.3: Quantum repeater nodes require a qubit with quantum memory and a coherent optical interface, they also require at least one auxiliary qubit with Bell state measurement functionality (a SWAP gate is also necessary if the auxiliary qubit doesn't have an optical interface).

## 1.5 Cavity QED in Quantum Networking

Optical photons are ideal carriers of quantum information between remote quantum network nodes due to their inherently weak interaction with the environment. Unfortunately, this also impedes our ability to coherently interface them with matter qubits.

One solution is working with atomic ensembles with a collectively enhanced light-matter interaction strength [35]; however, there are considerable challenges associated with realizing multi-qubit registers with universal quantum control.

Cavity quantum electrodynamics (CQED) is an alternative approach which generates an enhanced light-matter interaction by confining optical fields in resonators with high quality factor and small mode volumes. The study of CQED and its application to novel matter systems has been instrumental in the development of experimental implementations of quantum networking.

The nature of light-matter interaction is characterized by four key parameters:

- $g$, the interaction strength between the atom and cavity mode,
- $\kappa$, the energy loss rate from the cavity,
- $\Gamma$, the atomic decay rate,
- $\gamma$, the transition line-width.

See Figure 1.4 for a schematic.

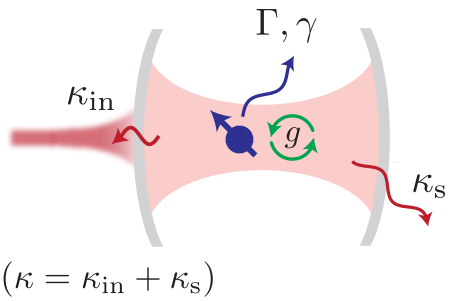


Figure 1.4: Cavity QED parameters. Atom has free-space decay rate $\Gamma$ and linewidth $\gamma$ and is coupled to the cavity mode with interaction strength $g$. The cavity mode decays with over-all rate $\kappa$ which can be divided into emission into a detected 1D waveguide mode $\kappa_{\text{in}}$ and loss to other channels $\kappa_s$.

The strong coupling regime is characterized by $g$ dominating all other rates, i.e., $g > \{\kappa, \Gamma, \gamma\}$. Strong coupling in the optical frequency domain has been achieved with trapped atoms [40], ions [41], and quantum dots[6] [43, 44]. In this regime reversible transfer of excitations between the atom and cavity can be achieved (vacuum Rabi oscillations).

Many solid-state quantum networking platforms operate in the so-called 'bad cavity regime,'[7] characterized by a dominant cavity decay rate $\kappa \gg g > \Gamma$ [45]. In this context any photon occupation of the cavity mode will quickly dissipate, and the coupling of the atom to the cavity effectively adds another decay pathway to the atom with rate $4g^2/\kappa$. The Purcell factor is defined as the ratio of this enhanced rate to the intrinsic atomic decay rate: $F_p = 4g^2/\kappa\Gamma$. Cavities are often engineered such that their dominant energy decay pathway is into a specific 1D waveguide mode. Hence atomic emission is funneled into a quantum channel: precisely the functionality required for quantum networking. An added benefit of this regime is the reduced ion lifetime, which is particularly important for the detection of single rare-earth ions. This regime has been demonstrated in many quantum networking platforms [46–54].

Another crucial parameter in the context of CQED is the cooperativity: $C = 4g^2/\kappa\gamma$ which quantifies the ratio between coherent atom-cavity interaction and other dephasing mechanisms. For radiatively broadened[8] systems $\Gamma/\gamma = 1$; however, in the

[6] Despite not operating in the optical regime, it would be remiss not to mention the pioneering experiments by Haroche in a discussion of cavity QED [42].

[7] Quantum dots are a notable exception.

[8] This condition is often referred to as fourier, transform or lifetime limited.

context of solid state emitters, dephasing mechanisms often dominate and $\Gamma < \gamma$. In this case, the bad-cavity regime can be subdivided into two further categories: $C < 1$ and $C > 1$. The benefits of the bad cavity regime mentioned in the previous paragraph are universal (regardless of $C$). When $C > 1$, coherent atom-cavity interactions enables additional quantum network node functionality, including the ability to mediate spin-spin interactions via the photonic mode [55], the perfect absorption of optical photons [56, 57] and the ability to generate deterministic interactions with and between itinerant photons [58, 59].

As we will see later in the thesis, the generation of remote entanglement relies on the coherent emission of photons, entangled with the internal state of an emitter. One might assume that this precludes the use of the $C < 1$ bad cavity regime when generating remote entanglement; however, this is not the case. It turns out, that if photonic emission occurs within a short window ($\delta t < 1/\gamma$) after optical excitation, the post-selected photons will be coherent. However since this is a non-deterministic process, the ratio $\Gamma/\gamma$ will limit the entanglement heralding rate [60]. Operating in the $C > 1$ regime would enable an increased entanglement efficiency (and potentially even deterministic entanglement generation if system losses are minimized).

### 1.6 Solid State Systems for Quantum Networking

In this section I will review platforms that have been proposed and, in many cases, have demonstrated the necessary quantum node functionality described in Section 1.4. While there has been considerable interest and progress in the development of single trapped ion [61–63] and atom [64–66] quantum networks, in this thesis we are going to focus on solid state systems for the following reasons:

- Solid state systems can be integrated with devices including nanophotonic cavities and microwave circuits. Fabrication of these devices is often readily scalable using established nanofabrication techniques.
- Qubits' microscopic environment is resource-rich containing nuclear spins, electronic spins, and phonons which can be leveraged as quantum resources.
- Defects can be doped or implanted into these materials, often with deterministic positioning, without the need for complex trapping infrastructure.

Initial efforts in solid-state quantum networking focused on quantum dots and nitrogen vacancy centers in diamond. Both of these platforms were used to demonstrate

two-node entanglement at a fairly early stage [67, 68]; however, progress has been hindered for different reasons. Quantum dots have very strong optical coupling leading to high entanglement rates [69], though, their noisy nuclear spin environment has limited the implementation of a quantum memory with coherence time longer than a few microseconds [70]. Nitrogen vacancy centers, on the other hand, have an excellent intrinsic quantum memory ($\sim$ 1 s coherence time [71]) and access to a large resource of $^{13}$C nuclear spins (these can implement large registers with $>$ 10 qubits [72] and coherence times $>$ 1 minute [73]). However, their optical transitions are considerably weaker; furthermore, transition enhancement using the CQED protocols discussed previously has been hindered by a first order DC Stark sensitivity leading to reduced optical coherence properties when incorporated into nanostructures [74]. Despite this limitation, NV centers have recently been used to implement state of the art three node quantum networks [30, 75].

Motivated by the early success of these solid state platforms, in recent years, there has been an explosion in the study of novel optically addressed solid-state qubits, with the goal of finding a platform that can simultaneously be incorporated into nanophotonic cavities and satisfies the requirements for a quantum network node. I will attempt to summarize these platforms:

Group IV defects in diamond such as SiV (both negatively [76] and neutrally [77] charged), $SnV^-$ [78, 79], $GeV^-$ [80] and $PbV^-$ [81] centers lead to an interstitial defect with centrosymmetric site symmetry and no 1st order DC stark shift. The $SiV^-$ is the most developed of these platforms, but requires cooling to millikelvin temperatures (in dilution fridges) to prevent phonon transitions between two orbital branches separated by $\sim$ 50GHz [82]. There has been recent progress using strained sites with increased orbital splitting [83] to relax the operating temperature requirements. Using heavier interstitial elements like the $SnV^-$ center leads to a larger spin-orbit interaction and higher operating temperature (1.7K); however, this also requires increased strain to enable efficient spin driving [79].

Interest in SiC as a host material has been motivated by its compatibility with advanced CMOS fabrication techniques [48, 84, 85]. A range of defects and vacancies have been explored in this material with the neutral divacancy [86] and silicon vacancy [87] being the most actively studied. These have both demonstrated millisecond-level spin coherence times and stable optical transitions. Emerging defects like the nitrogen vacancy [88], $Cr^{4+}$ ion [89] and $V^{4+}$ ion [90] have also been studied, with the latter exhibiting transitions in the telecom O band.

Recently, there has been significant interest in so-called 'radiation damage centers' in silicon which boast telecom O-band transitions. Of all solid state host materials, silicon is the easiest to nano-fabricate, so identification of a good quantum emitter would lead to rapid scalability. There have been several studies of G centers as single photon sources [50, 91]; however, they lack a ground state spin. T centers are emerging as a promising candidate [92] as they have a ground state spin; however, their optical transitions are relatively weak compared to other diamond-based defects[9] (lifetimes are typically $\sim 1\ \mu$s). There have been DFT-based studies to idenitfy novel defects in silicon which simultaneously satisfy the requirements of a ground state spin and fast telecom transition with no DC stark sensitivity [93].

Molecular qubits have demonstrated a bottoms-up approach with the potential for microscopic configurability [94, 95]. This field started three decades ago with the detection of single dye molecules in organic host matrices [96] which have been explored as single photon sources and coupled to cavities with high cooperativity [97]. However, their application to quantum networking has been hindered by the lack of an optically addressed spin. Two platforms recently emerged that could overcome this challenge: chromium bonded to organic ligands demonstrated 10 $\mu$s coherence times, albeit with poor optical properties [98]. Europium molecular crystals demonstrate exceptionally narrow optical line-widths (5-30kHz) but lack an electronic spin, necessitating storage in nuclear spin states that couple weakly to microwave control fields [99].

Motivated by their extensive utilization in condensed matter physics, 2D materials have been explored as single photon sources [100]. In particular, hexagonal boron nitride (hBN) has a wide bandgap and hosts optically addressable spin qubits like the $V_B^-$ defect [101]. This defect has demonstrated radiatively-limited optical transitions [102] and can be coupled to nanophotonic devices [103]; however, spin coherence times are fairly low ($\sim 4\ \mu$s) due to the noisy boron nuclear spin bath [104, 105]. Of particular interest are techniques to deterministically place defects in 2D materials [106].

Rare earth ions will be discussed in detail in the next section of this thesis and are just mentioned here for completeness.

I would also point the interested reader to the following review articles for a more comprehensive overview of these solid state platforms [107–109].

[9] Still faster than rare-earths though!

## 1.7 Overview of Rare Earth Ions

This thesis will explore the use of single rare-earth ions as quantum network nodes. In this section I will introduce the reader to some basic properties and aspects of rare-earth ion physics. A more detailed discussion of our specific platform is provided in Chapter 2, the reader is also directed to these textbooks [110, 111] and review papers [112, 113] for a more comprehensive overview.

### Electronic Configuration and Energy Levels

Rare-earth elements comprise the Lanthanide series in the periodic table, they are usually found in solids in the trivalent state with electron configuration given by $[Xe]4f^N$ consisting of a Xenon core and partially filled 4f shell (Figure 1.5). The 4f orbitals are closer to the nucleus compared to the filled 5s and 5p orbitals and hence do not contribute significantly to bond formation. As a result, the 4f electrons are shielded from the crystalline environment and the properties of inter-4f-transitions are largely independent of the host material (at least compared to other solid state defects). This has motivated the exploration and use of a wide variety of different solid-state hosts.

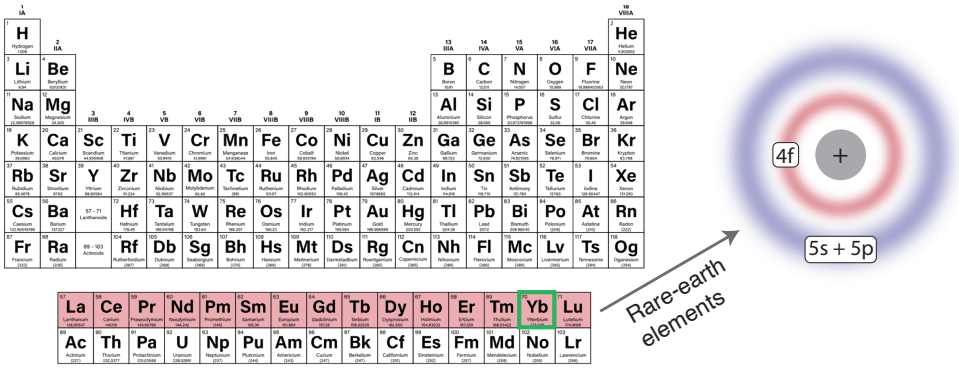


Figure 1.5: Rare-earth elements comprise the Lanthanide series of the periodic table. They are commonly found in solids in the 3+ charge state where unfilled 4f electronic orbitals are shielded by filled 5s and 5p orbitals.

The energy level structure of the 4f electrons can be understood by a hierarchy of different interactions (listed in order of decreasing strength) [111]:

- Free ion Hamiltonian,
- Crystal field interaction,
- Hyperfine interaction,
- Superhyperfine interaction.

The free ion Hamiltonian consists of energy terms independent of the crystalline host (i.e., kinetic energy, coulomb attraction to the nucleus, spin-orbit interaction and coulomb repulsion of the electrons). Energy levels can be derived using Hartree-Fock and yield levels that are labelled $^{2S+1}L_J$ (where $S$, $L$ and $J$ are the spin, orbital and total angular momenta). These levels have $(2J + 1)$ degeneracy and are spread by frequencies $\sim$ 300 THz (i.e., optical frequencies).

The crystal field interaction breaks the degeneracy of these multiplets leading to so-called crystal field levels (with $\sim$ 10 THz splittings). For rare-earth ions with odd numbers of electrons, Kramers' theorem states that the resulting energy levels will have a minimum twofold degeneracy (in the absence of magnetic fields). Site symmetry determines the number of crystal field levels and corresponding transition selection rules. We prefer to work with Kramers ions since they have electronic-like spin transitions. These can be driven more easily and quickly with microwave fields[10], compared to nuclear spin transitions in non-Kramers ions, and thus can lead to more reliable qubits.

For rare-earth ions with a nuclear spin, the hyperfine interaction with the electronic spin will break the degeneracy imposed by Kramers' theorem leading to $2(2I + 1)$ hyperfine levels (some of which may be degenerate). This splitting is usually on the scale of $\sim$ 1 GHz.[11]

Finally, for nuclear-spin-rich hosts, the hyperfine interaction with lattice nuclear spins can yield spectrally resolvable transitions dependent on the surrounding nuclear spin states. This is termed superhyperfine structure and is usually in the range of 10 kHz–1 MHz.

This rich energy level structure consisting of optical transitions for photonic interfaces, electronic transitions that can be driven strongly and nuclear spin states for long-term storage make rare-earth ions a versatile platform for quantum information applications.

[10] ns–$\mu$s timescales

[11] For rare-earth ions with nuclear spin greater than 1/2 the nuclear quadrupole interaction will also add an energy term ($\sim$ 10 MHz).

### Spin Properties

For large temperatures, the spin relaxation rate in Kramers rare-earth ions scales as $T^9$ and is limited by two-phonon Raman processes [114]. In order to mitigate this effect, experiments are performed at cryogenic temperatures $\leq 4$ K[12]. At sufficiently low temperatures, the spin relaxation rate becomes limited by spin exchange with other rare-earth ions, this can be mitigated by using more dilute ensembles or optically polarizing the spin bath [115].

Under these conditions, the coherence properties of spin transitions are usually limited either by interactions with nuclear spins or paramagnetic defects in the host lattice. The most common host materials ($YVO_4$, YAG, $Y_2SiO_5$) have dense nuclear spin baths, additionally, they contain Yttrium which is difficult to purify and often contains non-negligible quantities of paramagnetic rare-earth impurities (see Appendix A). As a result, there has been considerable recent effort to identify and work with magnetically quiet hosts [116]. Paramagnetic defects can also be frozen-out (their spin bath dynamics can be suppressed) by operating at large magnetic fields and low temperatures [117].

The longest coherence times measured in any optically-addressed solid state platform were achieved with Europium nuclear spins in $Y_2SiO_5$ with $T_2 = 6$ hours [118].

### Optical Properties

4f-4f optical transitions of rare-earth ions are quite weak, with lifetimes in the range of $\sim$ 100 $\mu$s to $\sim$ 10 ms. In free-space these transitions would be parity-forbidden, but, in the presence of a crystal field they become perturbatively allowed[13]. Furthermore, due to the isolated nature of 4f electrons, these optical transitions are highly radiative with coherence properties often limited by the spin coherence[14].

The final key advantage of rare-earth ions is that they often have considerably narrower optical ensemble inhomogeneities compared to other solid state systems (frequency distributions as narrow as $\sim$ 10 MHz were observed in Nd:$YLiF_4$ [120]). In the context of remote entanglement heralding between single ions, we will see that this narrow inhomogeneity enables the preparation of entangled states between any pair of ions using measurement-based frequency erasure.

[12] For $^{171}$Yb studied in this work, experiments were performed at 0.5 K, coherence and lifetimes were robust up to 1 K.

[13] Interestingly, in some rare-earth ions the strength of weakly allowed electronic dipole transitions is comparable to magnetic dipole transitions [119].

[14] As we will see, the optical linewidth of the single ions in this work might be limited by electric field fluctuations; this is likely due to nearby interfaces associated with the nanophotonic cavity.

**Applications of Rare-earths in Quantum Information**

In this subsection I will summarize quantum information-related applications of rare-earth ions focusing on the utilization of ensembles. A detailed discussion of progress with single rare-earth ions is presented in the next subsection.

Rare-earth ion ensembles have found extensive application as photonic quantum memories. Under ideal operating conditions, these memories should perfectly absorb a photon, store it for some duration (which could either be pre-determined or dynamically selected) and subsequently re-emit the photon with high efficiency whilst preserving the original quantum state [121]. Some key demonstrations include multi-mode storage [122], high efficiency storage [123] (69%), long storage times up to 20 ms [124] and on-demand recall using spin-wave memories [125]. Furthermore, there have been recent demonstrations of remote entanglement between pairs of ensemble-based memories [126, 127]. A related topic is the proposed application of rare-earth ion spin ensembles as memories for superconducting qubits. Information would be stored as a delocalized spin excitation in a similar manner to the optical quantum memories [128].

Motivated by the progress in superconducting qubit-based quantum computing, microwave to optical transduction aims to convert single photons between between the microwave and optical frequency domains (with high efficiency and low added noise), thereby enabling large-scale quantum networking of superconducting qubits. For transduction mediated by rare-earth ion ensembles, the basic idea is to use a Raman scattering protocol in a three-level system, combined with ensemble strong coupling to both optical and microwave resonators [129]. There have been a number of experimental demonstrations using this approach [39, 130–132]. More recently, there have been efforts to utilize stoichiometric crystals (where the rare earth ion is fully concentrated in the crystal lattice). In this context, microwave photons would couple to a collective ferromagnetic (or antiferromagnetic) resonance of the electronic spin ensemble [133, 134].

**Progress with Single Rare-earth Ions**

The first detection of single rare earth ions in a crystal was performed with $Pr^{3+}$ ions in yttrium aluminium garnet (YAG) [135], this was achieved using an upconverted readout scheme, whereby population in an excited $4f^2$ level was transferred to a 4f5d state, from where fast, parity-allowed emission at ultraviolet wavelengths enabled efficient detection. However, the incoherent nature of this photon emission process meant that it could only be used for readout and precluded a coherent spin-photon interface. Nevertheless, this enabled a range of optical and spin coherence properties of these ions to be studied [136], and a demonstration of nanometer-precision implantation [137]. We note that a similar approach was also used to detect single $Pr^{3+}$ ions in $LaF_3$ [138] and to detect and measure coherence properties of single $Ce^{3+}$ ions in YAG [139–142], including demonstration of coupling to individual nuclear spins [143].

Around a similar time, a very different approach utilizing photoionization was pursued to demonstrate detection of single Erbium ions in silicon. After optical excitation on a coherent 4f–4f transition, the ion can undergo non-radiative relaxation causing a nearby charge trap to ionise, this process was detected using a single electron transistor [144]. This approach has been leveraged to perform spectroscopy [145, 146] and characterize the relaxation and optical coherence properties of single Er ions [147–149]. It has also been used to detect interacting Erbium ion pairs [150] and to perform atomic-scale mapping of electric and strain fields [151]. However, demonstrating a spin memory and correlating the electrical detection with fluorescence detection remain outstanding challenges.

The first demonstration of single ion detection using photoluminescence on the coherent inter-4f optical transitions was performed with $Pr^{3+}$ ions in $Y_2SiO_5$ [152] using an anomalously fast transition with 2 $\mu$s lifetime (detection using a slower transition with $\sim$ 100 $\mu$s lifetime was also demonstrated [153]), these measurements were performed using bulk samples.

The first demonstrations of Purcell-enhanced detection of single rare-earth ions coupled to nanophotonic cavities (using the coherent 4f–4f transitions) were demonstrated by our lab using single $Nd^{3+}$ ions in $YVO_4$ [154] and the Thompson Lab at Princeton using single $Er^{3+}$ ions in $Y_2SiO_5$ [46]. In order to demonstrate a coherent qubit, our lab switched to studying $^{171}$Yb in $YVO_4$, which has ground state and optical clock transitions[15], using this platform we demonstrated coherent

[15] Which are robust against the noisy magnetic environment in the $YVO_4$ crystal.

optical transitions, spin memory and single-shot readout of the spin state [155]. Concurrently, the Thompson lab demonstrated similar spin functionality using the $Er^{3+}$:YSO platform [156] and parallelized measurement of six $Er^{3+}$ ions in a single device combined with independent spin control [157]. Both labs also used these platforms to study interactions with environmental nuclear spins, we realized a quantum register using four local Vanadium ions [158] while the Thompson lab demonstrated quantum control of an impurity hydrogen nuclear spin (a proton) [159].

There is a specific focus in the community on single Erbium ions due to their intrinsic telecom transitions. However, a major limitation of the $Er^{3+}$:YSO platform is the presence of a 1st order DC stark shift, which has lead to poor optical coherence in nano-fabricated platforms (in fact, this sensitivity has been used recently to demonstrate Stark tuning of individual emitters [160]). This has motivated systematic studies of new host materials for Er ions with low magnetic noise and no DC stark sensitivity [116], single Er ions have also been detected in MgO [119], Si [53, 161], $LiNbO_3$[162, 163] (which has also been demonstrated as a host for single Yb ions [164]) and $CaWO_4$ [165]. The latter result is particularly notable as it demonstrated coherent optical and spin transitions (measured via time-delayed two-photon interference and spin dynamical decoupling, respectively.)

It is worth noting that there are three different approaches currently pursued by the community for fabricating optical cavities and Purcell-enhancing single rare-earth ions, these each have their respective advantages/disadvantages:

1. Monolithic nanophotonic cavities fabricated directly from the host crystal using focused ion beam milling [166] (the approach utilized in this thesis). The modal field maximum is removed from nanophotonic interfaces maximizing optical coherence; however the fabrication process needs to be re-optimized for different host materials.

2. Hybrid approaches where the cavity is fabricated from silicon [46, 167] or GaAs [168] and transferred onto a pristine crystal surface, enhancement occurs via an evanescently decaying field. This approach is easily translated to different host materials; however, since it preferentially enhances ions close to the crystal surface it might cause a limitation to coherence properties.

3. Macroscopic Fabry-Perot cavities [169]. As with approach (1) this enables enhancement of ions that are removed from interfaces. However, ensuring narrow cavity line-widths requires vibration isolation in cryostats which is quite challenging [170].

Of all these platforms, the two which are most promising as quantum network nodes (i.e. have demonstrated the most comprehensive range of functionality) are $^{171}$Yb:$YVO_4$ and Er:$CaWO_4$. The next step in the development of these platforms is to demonstrate basic quantum networking protocols involving remote entanglement generation. This will be discussed further (and demonstrated) in the second half of this thesis.

Finally, I would also like to note a novel (and recently developed) approach to detect single Er ion spins in $CaWO_4$ [171]. In this work a 7GHz spin transition was Purcell-enhanced, the microwave fluorescence was detected using a microwave single photon detector and $g^{(2)}$ autocorrelation and spin coherence measurements were performed.

*Chapter 2*

# OVERVIEW OF EXPERIMENTAL PLATFORM

## 2.1 Introduction

The specific rare-earth ion platform investigated in this thesis is the $^{171}Yb^{3+}$ ion doped into $YVO_4$ (see Figure 2.1). It is a Kramers rare-earth ion (odd number of electrons), having an electronic spin 1/2 ground state. This enables fast control of spin qubits using magnetic dipole like transitions.

Furthermore, $^{171}Yb^{3+}$ is the only Kramers rare-earth ion with a nuclear spin of $1/2$ [110]. This leads to the simplest possible hyperfine energy level structure consisting of four states associated with each crystal field level (see the following section for more detail). The mixing of nuclear and electronic degrees of freedom via the hyperfine interaction, leads to clock transitions with reduced sensitivity to magnetic field noise (we note that there are several other solid state systems that also use clock transitions to reduce noise sensitivity [95, 118, 172, 173]).

These properties make $^{171}Yb^{3+}$ a promising rare-earth ion to study and utilize in quantum technologies, over the past few years it has been studied in a range of host materials [173–177] with several demonstrations of single-ion addressability [155, 164].

Our choice of host material (yttrium orthovanadate, $YVO_4$) is motivated by two considerations. First, the local Y site symmetry (which the Yb substitutes) is non-polar ($D_{2d}$) which precludes a first order DC Stark shift and reduces the sensitivity of optical transitions to electric field noise. Second, $Yb^{3+}$ has a relatively large optical dipole moment in this host (compared to other rare-earth ions/host materials) with $f = 5.4 \times 10^{-6}$ ($|\mu| = 1.06 \times 10^{-31}$ C·m) for the main transition used in this thesis. The radiative lifetime of this transition is 267 $\mu$s [175]. While this is still prohibitively long to address single ions directly, it relaxes the requirements on device fabrication (i.e., requires lower Purcell factor devices to achieve a specific lifetime compared to other hosts).

We also note that there are established methods for fabricating nanophotonic devices in this material [166], demonstrated previously in our research group.

The wavelength of the optical transitions used in this work is 984.5 nm. This near-

infra-red portion of the spectrum incurs fiber transmission losses of approximately 2 dB/km. While this is better than diamond-based defects (e.g., 637 nm for NV centers), for minimal losses over long distances we would want to operate in the telecom band (1260–1675 nm). Luckily frequency conversion between these wavelengths is fairly straightforward [178–183], we note that this is not demonstrated in this work and is left for future projects.

There are two potential downsides to this host material choice. First, its large concentration of (Vanadium) nuclear spins which generate magnetic field noise with 2 G standard deviation [158]. It is for this reason that the clock transitions mentioned previously are crucial for coherent operation of this qubit. In fact, as we will see in Chapters 4 and 5, there are benefits to operating with this dense nuclear spin environment as it provides a deterministic quantum resource.

The second downside is that Yttrium is hard to purify and often contains substantial concentrations of Lanthanide elements. The $YVO_4$ material used in this thesis has a 140ppb concentration of $Yb^{3+}$ of which 20ppb is $^{171}Yb^{3+}$ (a full characterization of impurities in these crystals can be found in Appendix A). While this concentration was suitable for the work considered here, being able to operate with lower concentrations would be beneficial for improving spin lifetimes.

In this section we will provide a detailed description of the energy levels and transitions associated with $^{171}Yb^{3+}$:$YVO_4$, the nuclear spin environment and an overview of the nanophotonic cavities/device platform used to address single rare-earth ions.

## 2.2 $^{171}$Yb:$YVO_4$ Energy Level Structure

The energy level structure of $^{171}$Yb:$YVO_4$ at zero magnetic field is shown in Figure 2.2.

The free ion energy levels under consideration are shown in Figure 2.2a and consist of two sets of degenerate multiplets: the ground state has $J = 7/2$ with 8 levels and the excited state has $J = 5/2$ with 6 levels. When embedded in a crystal, the degeneracy of these levels is lifted into so-called crystal field levels (Figure 2.2b) leading to four doubly-degenerate levels in the ground state and three doubly-degenerate levels in the excited state.

In this work we focus on the lowest ground state and lowest excited state crystal field levels ($^2F_{5/2}(0)$ and $^2F_{7/2}(0)$) which are separated by an optical transition at 984.5 nm [184]. Operating with the lowest ground state level prevents decay via

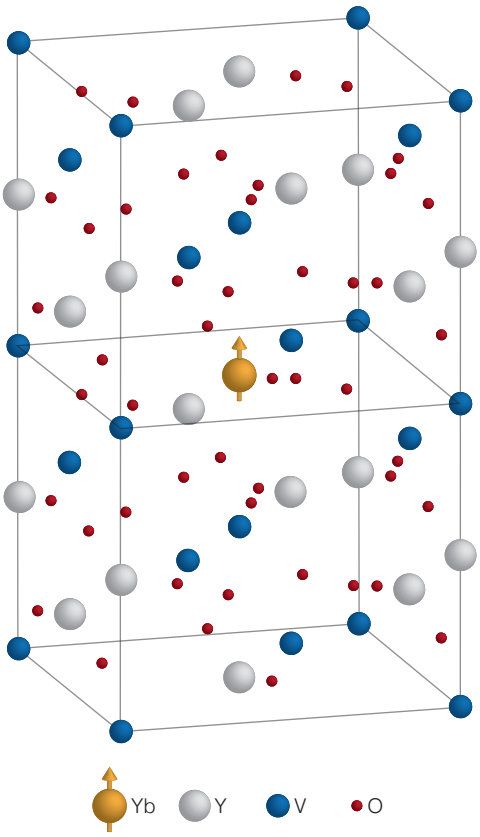


Figure 2.1: The crystal structure of $YVO_4$, Yb substitutes for Y in a single site with non-polar ($D_{2d}$) symmetry.

thermal processes/spontaneous emission. Thermal excitation is inhibited by working at cryogenic temperatures. This also prevents the excited state level, $^2F_{5/2}(0)$, from thermalizing with any other excited state levels; however, decay from this state can occur to all four ground state levels. In fact, the branching ratio to $^2F_{7/2}(0)$ is only $\beta = 0.45$. The optical cyclicity of this transition is improved via Purcell enhancement: since the cavity is only resonant with the $^2F_{5/2}(0) \leftrightarrow^2 F_{7/2}(0)$ and not with any other crystal field transitions.

Focusing on these two crystal field levels, Figure 2.2c shows the hyperfine structure resulting from the interaction between the Yb electronic and nuclear spins. The effective spin-1/2 Hamiltonian for the $^2\mathrm{F}_{7/2}(0)$ $^{171}\mathrm{Yb}^{3+}$ ground state is given by [175]:

$$\hat{H}_{\mathrm{eff}} = \mu_B \mathbf{B} \cdot \mathbf{g} \cdot \hat{\mathbf{S}} + \hat{\mathbf{I}}_{\mathrm{Yb}} \cdot \mathbf{A} \cdot \hat{\mathbf{S}} \tag{2.1}$$

where $\mathbf{B}$ is the magnetic field, $\hat{\mathbf{S}}$ and $\hat{\mathbf{I}}_{\mathrm{Yb}}$ are vectors of $^{171}$Yb electron and nuclear spin-1/2 operators, respectively, and we neglect the nuclear Zeeman term. The

ground state **g** tensor is given by [185]:

$$\mathbf{g} = \begin{pmatrix} g_x & 0 & 0 \\ 0 & g_x & 0 \\ 0 & 0 & g_z \end{pmatrix} = \begin{pmatrix} 0.85 & 0 & 0 \\ 0 & 0.85 & 0 \\ 0 & 0 & -6.08 \end{pmatrix}, \tag{2.2}$$

which is a uniaxial tensor with the extraordinary axis parallel to the $c$-axis of the crystal and the two ordinary axes aligned with the crystal $a$-axes. The ground state **A** tensor is given by [175]:

$$\mathbf{A} = 2\pi \times \begin{pmatrix} 0.675 & 0 & 0 \\ 0 & 0.675 & 0 \\ 0 & 0 & -4.82 \end{pmatrix} \text{GHz} \tag{2.3}$$

with the same principal axes. The excited state spin Hamiltonian has the same form but with different uniaxial tensors [175]:

$$\mathbf{g} = \begin{pmatrix} 1.7 & 0 & 0 \\ 0 & 1.7 & 0 \\ 0 & 0 & 2.51 \end{pmatrix}, \ \mathbf{A} = 2\pi \times \begin{pmatrix} 3.37 & 0 & 0 \\ 0 & 3.37 & 0 \\ 0 & 0 & 4.86 \end{pmatrix} \text{GHz}. \tag{2.4}$$

The principal axes of the excited state tensors are the same as the ground state tensors. (Note here that we have taken the convention $\hbar = 1$ and neglected the nuclear Zeeman interaction).

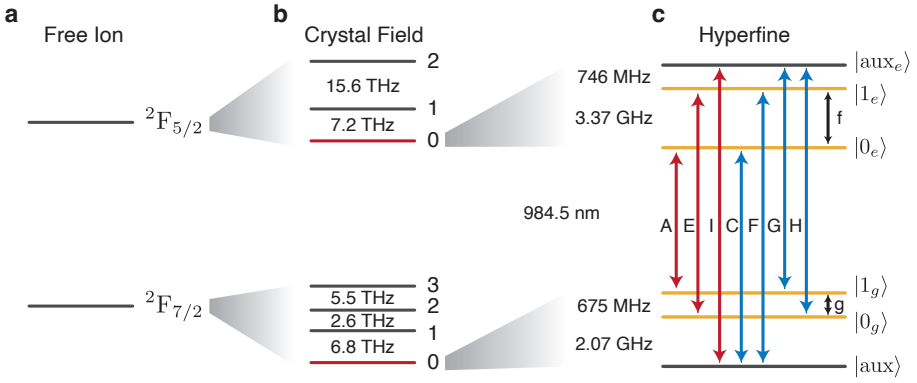


Figure 2.2: Energy level structure of $^{171}Yb^{3+}$:$YVO_4$. a) Free ion energy levels with degenerate $J = 5/2$ and $J = 7/2$ multiplets. b) Crystal field splitting into doublets. We utilize the lowest excited and ground state levels separated by 984.5 nm. c) Hyperfine level structure of these two doublets. Yellow levels have no 1$^{st}$ order sensitivity to magnetic fields, red (blue) transitions are polarized parallel (perpendicular) to the crystal $c$ axis. Microwave transitions with magnetic field polarization along the $c$ axis are labelled in black.

Denoting the ground state electron spin as $|\downarrow_g\rangle$ and the ground state nuclear spin as $|\Downarrow_g\rangle$, the ground state energy levels have the following form:

$$\begin{aligned} |1_g\rangle &= \frac{1}{\sqrt{2}}\left(|\uparrow_g\Downarrow_g\rangle + |\downarrow_g\Uparrow_g\rangle\right) \\ |0_g\rangle &= \frac{1}{\sqrt{2}}\left(|\uparrow_g\Downarrow_g\rangle - |\downarrow_g\Uparrow_g\rangle\right) \\ |\text{aux}\rangle &= |\uparrow_g\Uparrow_g\rangle\,, |\downarrow_g\Downarrow_g\rangle \end{aligned} \tag{2.5}$$

where the $|\text{aux}\rangle$ state is doubly degenerate. Note that $|0_g\rangle$ and $|1_g\rangle$ have no 1st order sensitivity to magnetic fields, i.e., $\langle 0_g|\,\hat{S}_{x/y/z}\,|0_g\rangle = \langle 1_g|\,\hat{S}_{x/y/z}\,|1_g\rangle = 0$. This means that the $|0_g\rangle \leftrightarrow |1_g\rangle$ transition at 675 MHz is a clock transition; indeed, this is why we use it as our qubit. The transition can be driven with an oscillating z-directed magnetic field[1] since $\langle 0_g|\,\hat{S}_z\,|1_g\rangle \neq 0$.

To predict the sensitivity of our qubit transition to magnetic fields, we consider second-order effects which generally scale as $\sim g^2/\Delta E$, where $\Delta E$ is the energy separation between a pair of unperturbed eigenstates. By taking into account the fact that $g_z$ is roughly 7 times larger than $g_x$, $g_y$ and $\hat{S}_z$ terms in $\hat{H}_{\text{eff}}$ mix $|0_g\rangle$ and $|1_g\rangle$ with small $\Delta E$ whereas $\hat{S}_x$ and $\hat{S}_y$ mix the $^{171}$Yb qubit states and $|\text{aux}\rangle$ with large $\Delta E$, we identify that perturbations along the $z$ axis (crystalline $c$ axis) dominate. Hence we can approximate this second order detuning with magnetic field as:

$$\Delta = \frac{g_z^2\mu_B^2 B_z^2}{2\omega_{01}\hbar^2} \tag{2.6}$$

where $\omega_{01}$ is the frequency of the $|0_g\rangle \leftrightarrow |1_g\rangle$ transition. This is why, experimentally, we primarily care about cancelling residual fields along the $z$ direction to optimize qubit coherence.

The expressions for the excited state energy levels (in terms of nuclear and electronic spins) can be found in [175]. For the purposes of this discussion it is sufficient to note that $|0_e\rangle$ and $|1_e\rangle$ also have no 1st order sensitivity to magnetic fields.

This also means that any optical transitions connecting $|0_g\rangle$, $|1_g\rangle$ to $|0_e\rangle$, $|1_e\rangle$ will also be insensitive to magnetic field noise (i.e., the $A$ and $E$ transitions).

Considering the optical transitions in Figure 2.2c, the three transitions highlighted in red (A, E, I) are polarized parallel to the $c$ axis of the crystal. The blue transitions (C, F, G, H) are polarized perpendicular to the $c$ axis.

[1] Throughout this thesis we adopt a convention that $z$ is parallel to the crystalline $c$ axis.

Note that experimentally we observe a small splitting of both the doubly-degenerate $|\text{aux}\rangle$ and $|\text{aux}_e\rangle$ energy levels, typically around 0–40 MHz. We attribute this to local strain in the crystal which reduces the site symmetry. As a result the $F$ transition (which we use during our initialization protocol) is split into two distinct frequencies which we label $F_1$ and $F_2$.

### 2.3 Nuclear Spin Environment

The $^{171}Yb^{3+}$ ion substitutes for yttrium in a single site of the $YVO_4$ crystal. The local crystalline environment consists of $^{89}Y$, $^{51}V$ and $^{16}O$ ions. Naturally abundant V and Y contain 99.8% $^{51}V$ and 100% $^{89}Y$ isotopes with nuclear spins of 7/2 and 1/2, respectively. Hence each $^{171}Yb$ ion experiences a near-identical nuclear spin environment[2].

Note that there is a stark difference between this nuclear spin environment compared to most other solid state platforms. The most commonly studied regime consists of a localized electronic spin coupled to a sparse, non-interacting nuclear spin bath (Figure 2.3a). In this case, individual spins are spectrally resolvable via their different hyperfine interaction strengths with the central electronic spin and can be used as independent qubits, this regime occurs with $^{13}C$ nuclear spins in diamond coupled to NV [186–192] and SiV centers [193], hydrogen nuclei coupled to Er ions in $Y_2SiO_5$ [159] and $^{29}Si$ nuclear spins coupled to vacancies in SiC [194], Ce ions in $Y_2SiO_5$ [143], donors in silicon [195] and gate-defined quantum dots [196]. An alternative regime is encountered with InGaAs strain-defined quantum dots where a highly delocalized electronic spin (spanning $\sim$ 10 nm) is homogeneously coupled to a large number (typically $\sim 10^5$) of dense, interacting, indistinguishable nuclear spins [197–201] (Figure 2.3c). High fidelity initialization and quantum control of such a large many-body system is difficult and utilizing nuclear spins as a quantum resource in this regime is an outstanding challenge.

Our system realizes an intermediate regime where a highly localized electronic spin is coupled to a dense, confined, nuclear spin ensemble consisting of $\sim$ 10 nuclear spins (Figure 2.3b). This yields a deterministic quantum resource with nuclear spin positions and interactions prescribed by the lattice. Furthermore, due to the small number of spins this is a highly controllable quantum many-body system (as we will see later in this thesis)[3].

[2] Naturally abundant oxygen contains a negligible fraction of nuclear spinful isotopes.

[3] Note that this regime has been partly explored in the context of rare-earth ion ensembles coupling to local nuclear spins.[54, 202].

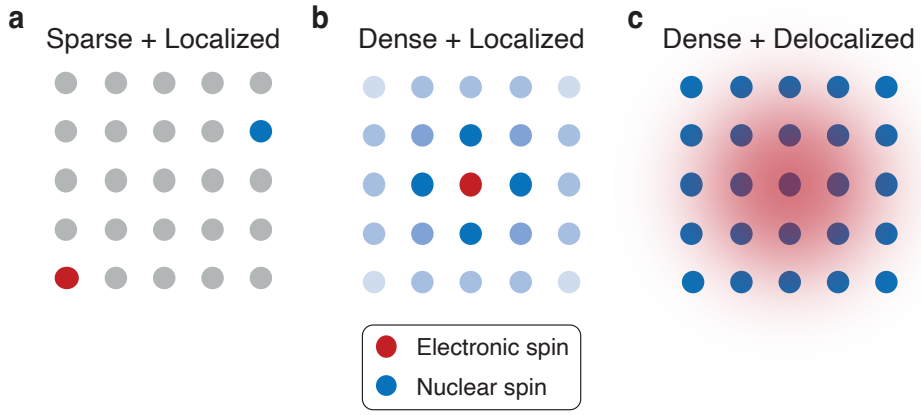


Figure 2.3: Different nuclear spin bath regimes encountered in solid state platforms. a) A sparse nuclear spin bath is coupled to a localized electronic spin. Nuclear spins can be spectrally resolved and used as independent qubits. b) A dense nuclear spin bath is coupled to a localized electronic spin (our regime). Leading to a confined, deterministic many-body system. c) A dense nuclear spin bath coupled to a delocalized electronic spin yields a complex, large many body system.

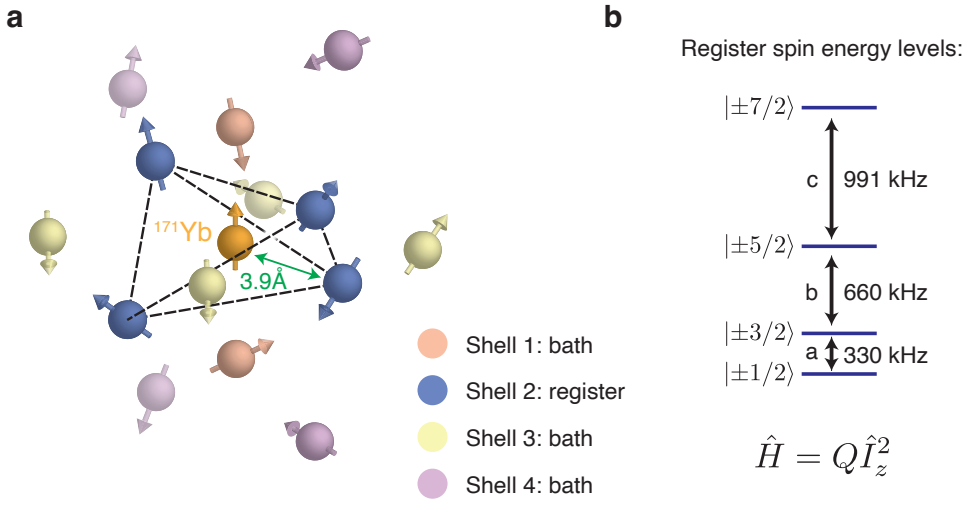


Figure 2.4: Vanadium nuclear spin environment. a) V spins around the Yb are arranged in equidistant shells. The second shell contains 4 spins and is termed the register. All other spins belong to the bath. b) Zero field nuclear quadrupole structure of I=7/2 Vanadium register spins consisting of four quadratically spaced doublets.

$^{51}$V with nuclear spin 7/2 has the largest magnetic dipole moment and zero-field structure due to a quadrupole interaction with the lattice electric field [203], we will therefore focus our subsequent discussion exclusively on this ion/isotope.

The resulting zero-field energy level structure of the $^{51}$V spins is given by:

$$\hat{H}_{\mathrm{V}} = Q\hat{I}_z^2 \tag{2.7}$$

where $Q/2\pi$ = 171 kHz measured using nuclear magnetic resonance (NMR) on bulk $YVO_4$ crystals [203] and $\hat{I}_z$ is the $^{51}$V nuclear spin-7/2 spin operator along the $c \equiv z$ axis. This leads to four quadratically-spaced, doubly degenerate energy levels, $\{|\pm m_I\rangle\}$ ={$|\pm 1/2\rangle$, $|\pm 3/2\rangle$, $|\pm 5/2\rangle$, $|\pm 7/2\rangle$}, and three magnetic-dipole allowed transitions $a$, $b$, $c$ (Figure 2.4b).

The local $^{51}$V ions surrounding the $^{171}$Yb qubit experience a frozen-core detuning, likely due to a modification of the electric field environment. They are arranged in shells of equidistant nuclear spins. Due to symmetry, all nuclear spins within a given shell have equal frequency detuning and are indistinguishable from the perspective of interaction with the Yb (see Section 4.2 for more discussion).

The positions of the six nearest $^{51}$V ions are tabulated in Table 2.1, where $\mathbf{r} = [x\ y\ z]$ is the $^{171}$Yb–$^{51}$V position vector with magnitude $r$ and direction cosines $\{l, m, n\}$. Their positions are also depicted in Figure 2.4a.

| $^{51}$V ion # | Shell | $r$ (Å) | $x$ (Å) | $y$ (Å) | $z$ (Å) | $l$ | $m$ | $n$ |
|---|---|---|---|---|---|---|---|---|
| 1 | 1$^{st}$ | 3.1 | 0 | 0 | -3.1 | 0 | 0 | -1 |
| 2 | 1$^{st}$ | 3.1 | 0 | 0 | 3.1 | 0 | 0 | 1 |
| 3 | 2$^{nd}$ | 3.9 | 0 | -3.6 | 1.6 | 0 | -0.91 | 0.40 |
| 4 | 2$^{nd}$ | 3.9 | 0 | 3.6 | 1.6 | 0 | 0.91 | 0.40 |
| 5 | 2$^{nd}$ | 3.9 | -3.6 | 0 | -1.6 | -0.91 | 0 | -0.40 |
| 6 | 2$^{nd}$ | 3.9 | 3.6 | 0 | -1.6 | 0.91 | 0 | -0.40 |

Table 2.1: Positions and direction cosines of local Vanadium nuclear spins.

We divide these spins into two distinct classes, register spins and bath spins. Specifically, the register spins comprise the second shell. They are distinguished by two factors: first their frozen core detuning spectrally resolves them from other bath spins ($Q/2\pi$ = 165 kHz, Figure 2.4b). They are also distinguished by the nature of their interaction mechanism with Yb, this will be discussed in more detail in Chapter 4. We will see in Chapter 5 how we can use these spins as a many-body quantum register.

We also note that the $^{51}$V ions have a uniaxial g-tensor with form [204]:

$$\mathbf{g}_{\mathrm{V}} = \begin{pmatrix} g_{vx} & 0 & 0 \\ 0 & g_{vx} & 0 \\ 0 & 0 & g_{vz} \end{pmatrix} \tag{2.8}$$

with $g_{vx} = 0.6$ and $g_{vz} = 1.6$ [158].

## 2.4 Purcell Enhancement and Devices

As discussed previously, the weak dipole moments and long lifetimes of the 4f-4f transitions make it difficult to address single rare-earth ions (REIs). For comparison, other solid state platforms such as nitrogen vacancy centers and InGaAs quantum dots have lifetimes of $\sim$ 10 ns and $\sim$ 0.5 ns whereas REIs typically have lifetimes between $0.1 - 10$ ms.

The accepted approach to resolve this issue (which has been adopted by many labs studying single rare-earth ions) is to couple them to an optical cavity [46, 53, 154, 162, 164, 169]. By engineering the photonic environment around the emitter, we can preferentially enhance its coupling to a specific optical mode, thereby enabling a faster channel for extracting photons from the emitter compared to 'natural' decay into free-space radiation modes.

Understanding the coupling of a single atom to a cavity is described by cavity quantum electrodynamics. Many textbooks/course notes cover this topic (for example [205] and [206]) while here I will provide quick overview; a more detailed discussion is presented in section 8.5.

The three key processes needed to understand an atom coupling to a cavity are as follows:

1. Unitary dynamics associated with a two level system coupling to an optical mode via an electric-dipole-like transition.

2. Dissipative dynamics associated with the two level system radiating into free-space optical modes.

3. Dissipative dynamics associated with radiation leakage out of the cavity.

The first item is described via the Jaynes Cummings Hamiltonian:

$$\hat{H} = \hbar g(\hat{a}\hat{\sigma}^{+} + \hat{a}^{\dagger}\hat{\sigma}^{-}) \tag{2.9}$$

where $\hat{a}$, $\hat{a}^{\dagger}$ are bosonic annihilation/creation operators for the cavity mode, $\hat{\sigma}^{+}$, $\hat{\sigma}^{-}$ are raising/lowering operators for the two level system and $g = \sqrt{\frac{\mu^2\omega}{2\epsilon\epsilon_0\hbar V}}$ with $\mu$ the transition dipole moment, $\epsilon\epsilon_0$ the permittivity of the medium surrounding the emitter, $\omega$ the transition frequency and $V$ the optical mode volume. We have assumed that the ion is resonant with the cavity and moved into a rotating frame for both the emitter and cavity mode.

The second item can be described by Lindbladian dynamics, i.e., a master equation with the following form:

$$\dot{\rho} = \Gamma\left(\hat{\sigma}^{-}\rho\hat{\sigma}^{+} - \frac{1}{2}\left\{\hat{\sigma}^{+}\hat{\sigma}_{-}, \rho\right\}\right) \tag{2.10}$$

where $\Gamma$ is the optical decay rate, $\Gamma = \frac{\omega^3 n\mu^2}{3\pi\hbar c^3\epsilon_0}$.

The third item can be described by a second master equation:

$$\dot{\rho} = \kappa\left(\hat{a}\rho\hat{a}^{\dagger} - \frac{1}{2}\left\{\hat{a}^{+}\hat{a}^{\dagger}, \rho\right\}\right) \tag{2.11}$$

where $\kappa$ is energy decay rate of the cavity (i.e., $Q = \omega/\kappa$).

See Figure 2.5b for an illustration of these different rates where we have separated cavity dissipation into two separate channels, $\kappa_s$ is associated with light scattered into unobserved optical modes, $\kappa_{in}$ corresponds to light coupled to a 1D waveguide (optical fiber), these are connected to the overall cavity decay rate via: $\kappa = \kappa_s + \kappa_{in}$.[4]

The relative magnitudes of $\kappa$, $g$ and $\Gamma$ determine which regime of cavity QED we are operating in. All examples in this thesis will be in the 'bad cavity regime' where $\kappa$ dominates over all other rates: $\kappa \gg g > \Gamma$. In this regime, any photon occupation of the cavity mode will quickly dissipate, hence the coupling of the atom to the cavity effectively adds another decay pathway.

If we solve the dynamics associated with these processes we find that the atomic decay rate is modified from $\Gamma$ to $\Gamma + \frac{4g^2}{\kappa}$. The ratio of these two rates is $1 + F_p$ where

[4]Note that, in principle, coupling to the waveguide is a coherent (non-dissipative) process. This is why photonic emission into the waveguide can be used as a channel for mediating long-range spin entanglement. In section 8.5 we will use an alternative formalism where the decay into the waveguide is separated from the scattered light and treated using unitary dynamics.

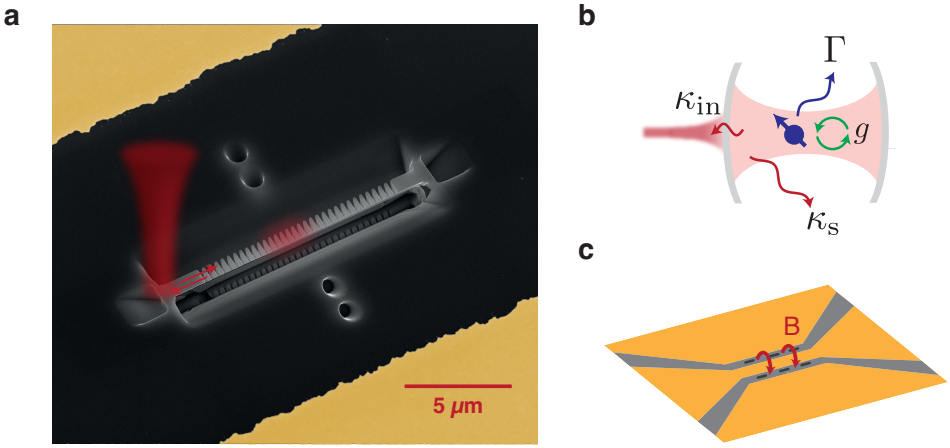


Figure 2.5: Device and cavity QED a) SEM image of the nanophotonic cavity milled from the $YVO_4$ host crystal (grey) with a surrounding gold coplanar waveguide (yellow). Light impinges vertically onto the chip, the angled coupler reflects it into the waveguide mode. The cavity mode is highlighted in red in the center of the nanobeam. b) Schematic of rates relevant for ion-cavity coupling. c) Schematic of coplanar waveguide on chip. The magnetic field direction is indicated with a red arrow, the devices sit in the gaps between the ground plane and center strip.

$F_p = \frac{4g^2}{\kappa\Gamma}$ is termed the Purcell factor [45]. By substituting expressions for $\kappa$, $g$, $\Gamma$ we can derive $F_p = \frac{3}{4\pi^2}Q\frac{(\lambda/n)^3}{V}$. As we can see, reducing the lifetime of our emitter boils down to fabricating cavities with a small mode volume and large quality factor.

Note, for multi-level systems there is a subtlety in the definition of the Purcell factor. In this case, $\beta\frac{3}{4\pi^2}Q\frac{(\lambda/n)^3}{V} = \frac{4g^2}{\kappa\Gamma}$ where $\beta$ is the branching ratio. Both $\frac{4g^2}{\kappa\Gamma}$ and $\frac{3}{4\pi^2}Q\frac{(\lambda/n)^3}{V}$ can be termed the Purcell factor.

The optical cavities used in this thesis are nanophotonic cavities directly fabricated from the $YVO_4$ host crystal using focused ion beam milling (see Figure 2.5a). This process is detailed in [166]; briefly, it involves first milling a suspended triangular nanobeam via a series of angled cuts. Subsequently, a photonic crystal is fabricated via a series of periodic cuts orthogonal to the beam. The period of the cuts is quadratically tapered towards the center of the beam to define a TM cavity mode with electric field along the $c$ axis of the crystal. There are more mirror periods on one side of the tapered region compared to the other, this leads to preferential emission of cavity light into one side of the suspended waveguide. A 45 degree angled cut at the end of the waveguide couples light into free space (via total internal reflection) in a direction travelling orthogonally to the chip surface. These cavities

have a quality factor of $\sim 10,000$ and a mode volume of approximately $(\lambda/n)^3$.

The first cavity used in this work was fabricated by Jake Rochman; it has survived for 5 years and has been used for three separate projects with negligible degradation, a testament to the robustness of these devices. We fabricated a second cavity more recently for the entanglement project using the same recipe.

The cavity QED parameters for the best coupled ions in the first device are: $g = 2\pi \times 23.5$ MHz, $\kappa = 2\pi \times 31$ GHz, $\Gamma = 3.7$ kHz leading to a lifetime reduction of 122. The ratio $\kappa_{\text{in}}/\kappa \approx 0.12$, meaning that approximately 12% of light in the cavity couples into the waveguide mode.

In addition to reducing the lifetime of the emitter there are two additional benefits to the Purcell enhancement. First, it leads to preferential emission of photons into the cavity mode: $\beta F_p/(1+\beta F_p) \approx 0.99$ of emitted light goes into the cavity. Second, it enhances the cyclicity of cavity coupled transitions, the branching ratio of the $|0_e\rangle$ state decay via the A transition is $\beta_A \approx 0.35$, in the cavity this is boosted to $(1+F_p)\beta_A/(1+\beta_A F_p) \approx 0.999$.

We note that since the cavity mode is polarized along the $c$ axis of the crystal, $A, E$ and $I$ transitions are Purcell enhanced whereas $C, F, G$, and $H$ are not. These transitions can then be used for different applications. Cyclic transitions are good for qubit readout as we can repeatedly excite the ion and detect photons without deteriorating the qubit populations. Un-enhanced transitions (in combination with an enhanced transition, forming a $\Lambda$ system) are useful for qubit initialization as discussed in Section 3.3.

In addition to the optical cavities, we fabricate a coplanar waveguide (CPW) on the surface of the chip (gold-colored regions in Figures 2.5a and c). The nanophotonic cavities are fabricated in the slots between the ground planes and center strip of the waveguide. This exposes them to an RF magnetic field perpendicular to the chip's surface (parallel to $c$), this is the correct polarization for driving the ground state qubit transition between $|0_g\rangle \leftrightarrow |1_g\rangle$ (transition $g$) and also the excited state transition between $|0_e\rangle \leftrightarrow |1_e\rangle$ (transition $f$).

More detail regarding the experimental setup for single ion measurements presented in this thesis can be found in [155]. The experimental setup for two device measurements is described in Chapter 9.

*Chapter 3*

# SINGLE $^{171}$YB:$YVO_4$ QUANTUM NODES

## 3.1 Detection and Verification of Single Ions

To detect single ions we first perform resonant photoluminescence (PL) spectroscopy. We apply a long (10 $\mu$s) laser pulse which drives any ions' optical transitions to saturation. We subsequently detect emitted photons which are temporally resolved from the laser excitation. We sweep the laser frequency in an 800 MHz range around the optical $A$ transition and plot the integrated (and normalized) PL counts at each frequency (Figure 3.1a). The spectrum shows a set of clustered peaks, the isolated peak labelled 'Ion 1' is a single $^{171}$Yb ions which is studied further in this section.

Figure 3.1b shows a histogram of photon emission times after the optical excitation. We see a mono-exponential decay with lifetime of $2.18 \pm 0.04$ $\mu$s. This corresponds to a lifetime reduction of $\beta F_P = 122$ and a Purcell factor of 350. The single photon coupling rate is $g = 2\pi \times 23.5$ MHz. Based on these results, the probability that the ion emits into the cavity mode is 99.2%.

Finally, to verify that this is indeed a single ion, we perform a pulsed $g^{(2)}$ autocorrelation measurement [207]. This yields a value of $g^{(2)}(0) = 0.015 \pm 0.002$. The slight bunching feature observed around 0 time delay indicates that there is some degree of correlation between photon emission events after near-consecutive excitations. This could be due to imperfect hyperfine initialization combined with spin pumping dynamics. Essentially, the combination of laser excitation and spin thermalization lead to an effective hyperfine relaxation rate. A photon detection indicates that the ion is currently in the $|1_g\rangle$ state, and there will be an elevated probability of detection within the relaxation timescale.

## 3.2 Optical Control and Coherence

Next, we demonstrate the ability to coherently control the optical $A$ transition. We apply an optical pulse of varying duration and plot the integrated photon emission in Figure 3.2a. We see a Rabi oscillation with Rabi frequency equal to $\Omega = 2\pi \times 3.9$ MHz. The solid curve corresponds to a simulation which includes optical decay, quasi-static frequency fluctuations and pure dephasing, parameters for the simulation were independently measured using the subsequently described experiments. The model fits remarkably well to the data with no free parameters.

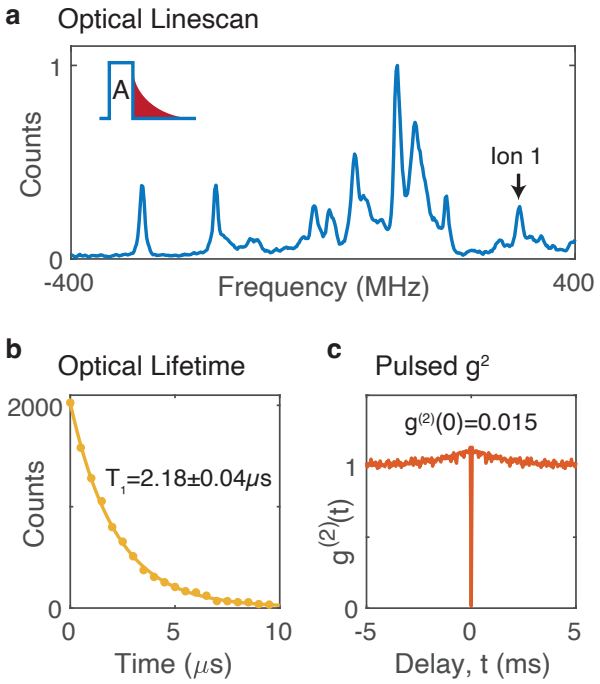


Figure 3.1: Verification of single $^{171}$Yb:$YVO_4$. a) A pulsed luminescence measurement centered on the A transition. The isolated peak labelled Ion 1 is a single ion investigated in this chapter. b) Optical lifetime of a single ion obtained by time-resolving the photoluminescence. Fit is to a mono-exponential decay with lifetime $T_1 = 2.18 \pm 0.04$ $\mu$s. c) Pulsed $g^{(2)}$ autocorrelation measurement with $g^{(2)}(0) = 0.015 \pm 0.002$ verifies that this is a single ion.

Next, we use the optical Rabi experiment to calibrate an optical $\pi/2$ pulse and perform a Ramsey coherence measurement (Figure 3.2b). This data is integrated for approximately one hour and yields a Gaussian decay with timescale $T_2^* = 320 \pm 10$ ns corresponding to a FWHM linewidth of 1.7 MHz. We note that this is considerably broader than the transform limited linewidth of 99 kHz, equivalently, the Ramsey coherence is much shorter than the lifetime limit: $T_2^* \ll 2T_1 = 4.36\mu s$.

The Gaussian decay envelope in the Ramsey measurement indicates that frequency fluctuations may be quasi-static. Therefore, in Figure 3.2c we add a single optical $\pi$ pulse to rephase contribution from quasi-static frequency variation (i.e., perform an optical echo). The resulting coherence time of $3.4 \pm 0.1$ $\mu$s is much closer to the lifetime limit, we predict an excess pure dephasing rate of $69 \pm 9$ kHz. The ability to extend the optical coherence in this manner will be leveraged in Section 10.2 to obtain a considerably increased two-ion entanglement rate.

Finally, we explore the temporal correlations in ion emission frequency. To do this, we first perform an optical Ramsey measurement as described previously, then we apply a weak frequency-selective probe pulse and count any photons emitted after the probe, this experiment is repeated many times. Each Ramsey measurement will only be accepted if the number of probe photons in a 3.5 ms window centered at some fixed separation $\tau_{\text{sep}}$ exceeds a certain threshold (in this case $N > 2$). When $\tau_{\text{sep}} = 0$ we observe an extended Ramsey decay timescale of $T_2^* = 0.77 \pm 0.05\ \mu$s (Figure 3.2d). This verifies the presence of temporal frequency correlations, note that in this case the Ramsey measurement was performed with a 1 MHz detuning. We plot the Ramsey decay timescale as a function of the offset ($\tau_{\text{sep}}$) between the measurement and probe acceptance window. Assuming that the optical detuning $\Delta(t)$ is a Gaussian stochastic process we expect the frequency correlation to decay according to $C_{\Delta\Delta}(t) = \langle\Delta(t)\Delta(0)\rangle \propto e^{-t/\tau_c}$. Figure 3.2d shows an extracted correlation timescale of $9 \pm 1$ ms.

Based on our modelling of the nuclear spin environment (see Chapter 4) the contribution to optical linewidth due to interactions with local nuclear spins is $\sim 40$ kHz. Furthermore, due to the low doping concentration of $^{171}$Yb, spin-spin interaction strength is $\sim 50$Hz. We therefore postulate that the optical linewidth is limited by electric field fluctuations combined with a DC stark shift. This could either be a quadratic shift as predicted by the ideal site symmetry, or a small residual linear shift caused by reduced site symmetry from local strain. Further experiments are required to ascertain the DC stark susceptibility and source of optical linewidth broadening.

### 3.3 Spin Initialization and Readout

Since experiments are performed at 0.5K, the equilibrium population is distributed between $|1_g\rangle$, $|0_g\rangle$ and $|\text{aux}\rangle$ levels in the ratio 1:1.1:2.6. Initialization starts by pumping population out of the $|\text{aux}\rangle$ state into the qubit manifold. This is achieved by applying alternating 2.5 $\mu$s pulses to the $F_1$ and $F_2$ transitions, followed by a 2.5 $\mu$s wait for optical decay. This process is repeated 200 times. We measure the initialization fidelity by comparing the photon count rate from the $|1_g\rangle$ and $|0_g\rangle$ states right after initialization with the count rates achieved after the ions have thermalized (see discussion of spin $T_1$ times in Section 3.5). We extract an initialization fidelity into the qubit manifold of $95 \pm 5\%$.

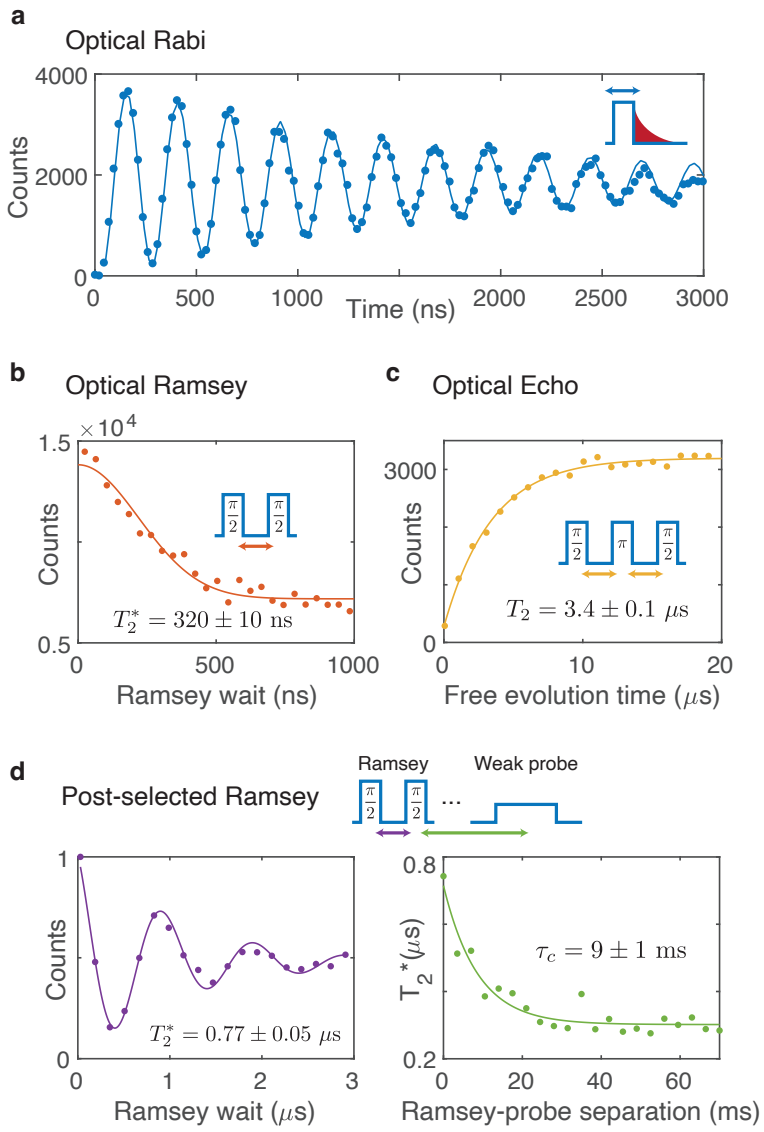


Figure 3.2: Optical control and coherence of single $^{171}$Yb:YVO$_4$. a) Optical Rabi oscillation on the $A$ transition with Rabi frequency $\Omega = 2\pi \times 3.9$ MHz. b) Optical Ramsey coherence measurement yields $T_2^* = 320 \pm 10$ ns and a 1.7 MHz line-width. c) Echo coherence time of $T_2 = 3.4 \pm 0.1$ $\mu$s is nearly lifetime limited with an excess pure dephasing rate of $69 \pm 9$ kHz. d) Post-selected Ramsey measurements: Ramsey photon counts are accepted conditional on emission after a weak, frequency-selective probe. The separation between the probe and Ramsey measurement is varied yielding a frequency correlation timescale of $9 \pm 1$ ms.

Next, we pump population out of the $|1_g\rangle$ state into $|0_g\rangle$. Note that since there are no two-photon $\Lambda$ transitions connecting these levels at B=0, we employ a three-photon scheme. More precisely, we optically excite $|1_g\rangle$ population into $|0_e\rangle$ via a $\pi$ pulse on the $A$ transition. Then we apply a microwave $\pi$ pulse on the excited state spin transition thereby transferring $|0_e\rangle$ to $|1_e\rangle$. Population from the $|1_e\rangle$ state decays to $|0_g\rangle$ via the cavity enhanced $E$ transition. This process is repeated 15 times.

To estimate the fidelity, we read out the $|1_g\rangle$ population by applying a single optical $\pi$ pulse and collecting photons. We subtract dark counts and contributions from other ions by temporally resolving the photon count distribution and only considering the portion that decays at the pre-determined ion optical lifetime. We compare this to the $|0_g\rangle$ population by applying a qubit $\pi$ pulse followed by the same single optical $\pi$ pulse photon measurement. With these results we estimate a qubit initialization fidelity of $0.9976 \pm 0.0003$. We also estimate a single photon detection efficiency of $(9.81 \pm 0.07) \times 10^{-3}$ and a dark count rate of $16.3 \pm 0.5$ Hz. We measure the dark count rate with all laser pulses far-detuned from any Yb optical transitions, this lets us further distinguish two separate dark count contributions: an off resonant rate of $8.0 \pm 0.2$ Hz coming from laser leakage or ambient light, and a resonant contribution of $8.3 \pm 0.5$ Hz likely coming from off-resonant excitation of long-lived ions.

The cyclicity of the optical $A$ transition is measured to be 0.9978, during typical experiments, we can leverage this to read out the qubit with a higher efficiency. First we read out the $|1_g\rangle$ state by applying a train of 100 optical $\pi$ pulses to the $A$ transition, each followed by a 10 $\mu$s photon counting time. We then apply a qubit $\pi$ pulses and repeat the process to read out the $|0_g\rangle$ state. We assign the qubit state to $|0_g\rangle$ ($|1_g\rangle$) if we get 0 ($\geq 1$) photons during the first readout and $\geq 1$ (0) photons during the second readout. The resulting readout efficiency is 59%. However, this yields a lower readout fidelity compared to the single optical $\pi$ pulse case, primarily due to spin relaxation during the readout process. We estimate the readout infidelity by noting that it will be several orders of magnitude larger than the initialization infidelity. We prepare $|0_g\rangle$ and $|1_g\rangle$ states and measure their populations, this yields $F_{|1_g\rangle} = 0.961 \pm 0.002$ and $F_{|0_g\rangle} = 0.977 \pm 0.001$. We can use these measurements to calculate a correction matrix for the readout process:

$$\begin{pmatrix} P_{|1_g\rangle} \\ P_{|0_g\rangle} \end{pmatrix} = \begin{pmatrix} 1.048 & -0.025 \\ -0.048 & 1.025 \end{pmatrix} \begin{pmatrix} \tilde{P}_{|1_g\rangle} \\ \tilde{P}_{|0_g\rangle} \end{pmatrix} \tag{3.1}$$

where $P_{|0_g\rangle}$, $P_{|1_g\rangle}$ are the actual qubit populations for the $|0_g\rangle$ and $|1_g\rangle$ states respectively, and $\tilde{P}_{|0_g\rangle}$, $\tilde{P}_{|1_g\rangle}$ are the corresponding measured qubit populations.

### 3.4 Spin Control and Randomized Benchmarking

We demonstrate coherent spin control by initializing the qubit as described in the previous section, applying a microwave pulse of variable duration and frequency and then reading out the qubit population. Figure 3.3a shows the experimental results with a characteristic Rabi chevron. We typically operate experiments with Rabi frequencies in the range $\Omega = 2\pi \times (5 - 10)$ MHz. We use the spin Rabi oscillation to calibrate $\pi$ and $\pi/2$ pulses.

We characterize our single qubit gate fidelity using randomized benchmarking [208], which provides a value independent from state preparation or measurement (SPAM) errors. We apply randomly sampled single qubit Clifford gates constructed using $\pi$ and $\pi/2$ rotations around the $x$ and $y$ directions followed by the single-gate inverse operation. When the number of gates, $M_{\text{gate}}$, increases, the sequence error accumulates and the probability of returning to the initial $|0_g\rangle$ state reduces according to an exponential decay:

$$P = 0.5 + P_0 d^{M_{\text{gate}}}. \tag{3.2}$$

When ensemble-averaged over a sufficiently large number of random gate sets (in our case 100), $f = \frac{1}{2}(1 + d)$ becomes a reliable estimate of the average single-qubit gate fidelity. Measurement results are presented in Figure 3.3b, leading to an extracted average single qubit gate fidelity of $f = 0.99975 \pm 0.00004$.

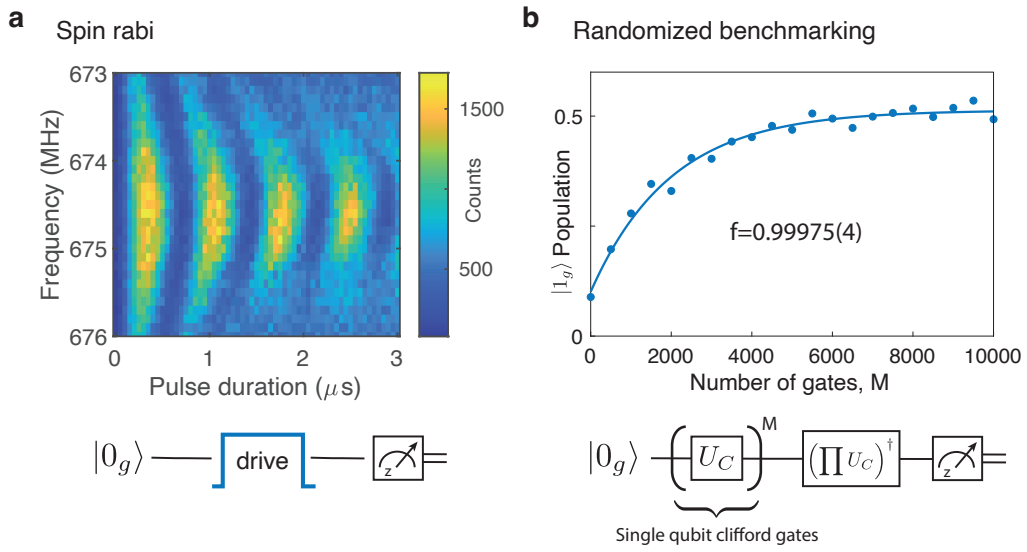


Figure 3.3: Spin control. a) Spin Rabi oscillation dependence on pulse duration and frequency b) Randomized benchmarking yields an average single qubit gate fidelity of $0.99975 \pm 0.00004$.

### 3.5 Spin Coherence and Lifetime

Figure 3.4a shows a Ramsey coherence measurement on the qubit transition with 1 MHz detuning. The solid line is the result of a Monte Carlo simulation of the local Vanadium nuclear spin environment (see Section 6.4 for more details). The decay timescale is approximately 8 $\mu$s; however, this is not a trivial Gaussian or exponential decay profile due to the discrete nature of the spin bath and also the asymmetric frequency distribution (due to the quadratic magnetic field sensitivity). Note that the model is fitted to the data with one free parameter: the nuclear spin z-directed g factor which is estimated to be $g_{vz} = 1.6$.

The nuclear spin environment that limits the Ramsey coherence is slowly fluctuating and we can therefore use dynamical decoupling to extend the spin coherence. Figure 3.4b shows the result of a Hahn-echo experiment with coherence time $43 \pm 1$ $\mu$s. More generally, we can use sequences with larger numbers of $\pi$ pulses, e.g., the Carr-Purcell-Meiboom-Gill sequence (CPMG) [209, 210]. We investigate the increase in spin coherence time with increasing number of $\pi$ pulses ($N$) in Figure 3.4c. We extract a power-law dependence of the form $T_2 \propto N^{0.70\pm0.01}$. This indicates a noise spectral density of the form $S(\omega) \propto \omega^{-2.3\pm0.1}$, which agrees well with the expected $S(\omega) \propto \omega^{-2}$ for coupling to a dipolar spin bath approximated by a classical source of Ornstein-Uhlenbeck noise [211].

To extend the coherence time even further, we operate with a fixed pulse separation and measure the coherence time by increasing the number of dynamical decoupling periods in a floquet fashion. The inter-pulse separation is chosen to be $2\tau = 5.8$ $\mu$s and satisfies two requirements: 1) It avoids accidental driving of the local nuclear spin environment as discussed in Section 4.6 and 2) it is as small as possible to filter out the $1/\omega^2$ noise identified earlier. We also switch from using a CPMG sequence to an XY8 sequence [212, 213]. This is because CPMG is only robust to pulse errors for superposition states prepared parallel to the $\pi$ pulse Rabi axis, whereas XY8 is robust to pulse errors for any prepared superposition state. Therefore, XY8 coherence times are more experimentally useful as they robustly preserve coherence for any quantum state. We measure an XY8 coherence time of $21.2 \pm 0.7$ ms, combined with the spin relaxation time measurements we can extract a pure spin dephasing rate of $38 \pm 2$ Hz.

It is currently unknown what causes excess dephasing in the dynamically-decoupled spin coherence times. One possibility is interactions between nuclear spins which would cause a time-varying nuclear Overhauser field. These interactions could

either be direct nuclear magnetic dipole-dipole interactions or interactions that are enhanced by the presence of the Yb (see Chapter 4 for more details). However, we note the presence of a frozen-core effect which prevents Vanadium ions at different distances from the Yb from exchanging spin excitations. For instance, the two Vanadium ions closest to the Yb (Shell 1 in Figure 2.4a), which are primarily responsible for the Ramsey decay, cannot interact with any other more distant V ions due to a relative frequency shift. Furthermore, due to the local symmetry, any spin exchange between these two V ions preserves the total magnetic field at the Yb location. Therefore magnetic field fluctuations due to these two ions are doubly forbidden. An alternative explanation is the presence of paramagnetic defects in the crystal, for example other rare earth ions or quadruply ionized Vanadium ($V^{4+}$) [214], identifying the limitation in these coherence measurements is a topic of current experimental investigation via DEER (double electron-electron resonance )sequences [213] and will be verified via correlated-cluster-expansion (CCE) simulations [215].

Finally, we also characterize the spin population relaxation rates. We measure the qubit lifetime by initializing, waiting for a variable time and then reading out the difference in population between the $|0_g\rangle$ and $|1_g\rangle$ states. As shown in Figure 3.4e, this yields $T_1 = 53 \pm 3$ ms. We also measure the decay rate to the $|\text{aux}\rangle$ state by measuring the time-dependence of the combined $|0_g\rangle$ and $|1_g\rangle$ population, this yields a decay time of $26 \pm 2$ s. Spin lifetime measurements were performed at cryostat temperatures up to 1.2 K. We observed less than a factor of two change in the decay rate on the $|0_g\rangle \leftrightarrow |1_g\rangle$ transition over this range, indicating that this is unlikely to be dominated by a phonon-assisted process that would be expected to scale strongly with temperature [114]. Instead, we postulate a direct spin-spin relaxation mechanism mediated by magnetic dipole-dipole interactions with other $^{171}$Yb ions in the crystal. This is expected to be a significant effect in this system due to the narrow inhomogeneous line-widths of the spin transition at zero field (<1 MHz). Furthermore, the large difference between the $|0_g\rangle \leftrightarrow |1_g\rangle$ and $|0_g\rangle, |1_g\rangle \leftrightarrow |\text{aux}\rangle$ relaxation rates is in agreement with the $g^4$ scaling for this mechanism (corresponding g-factors for these two transitions are -6.08 and 0.85, respectively). More measurements are necessary to further investigate the underlying relaxation mechanism, for example we are currently evaluating crystals from alternative vendors with lower doping concentrations which should hopefully lead to longer qubit relaxation times. Alternatively, polarization of the entire $^{171}$Yb ensemble could also be used to extend this relaxation timescale [115].

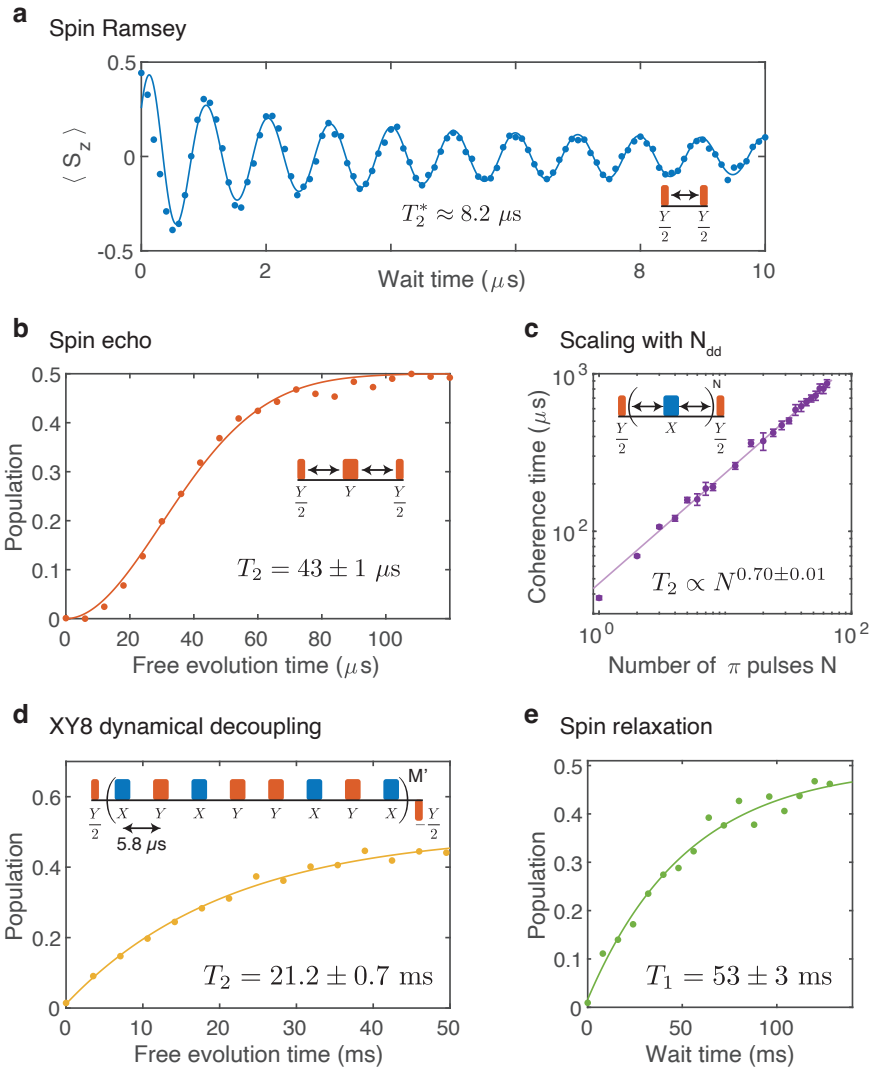


Figure 3.4: Spin coherence and lifetime. a) Spin Ramsey measurement with 1 MHz detuning. Solid line is a Monte-Carlo simulation modelling different local nuclear spin configurations. The decay timescale is approximately 8 $\mu$s. b) Spin echo yields a coherence decay with timescale 43 ± 1 $\mu$s c) CPMG measurements with increasing numbers of $\pi$ pulses (N) yield an improvement in coherence time that scales as $N^{0.70\pm0.01}$. d) XY8 coherence measurement performed with a fixed pulse spacing of 5.8$\mu s$ measured by increasing the number of dynamical decoupling periods yields $T_2$ = 21.2 ± 0.7 ms., e) Qubit transition lifetime measurement yields $T_1$ = 53 ± 3 ms.

*Chapter 4*

# NUCLEAR SPIN INTERACTIONS

## 4.1 Introduction

Solid-state nuclear spins surrounding individual, optically addressable qubits [216, 217] provide a crucial resource for quantum networks [30, 33, 73, 218–220], computation [54, 112, 191, 192, 221, 222] and simulation [223]. While hosts with sparse nuclear spin baths are typically chosen to mitigate qubit decoherence [109], developing coherent quantum systems in nuclear spin-rich hosts enables exploration of a much broader range of materials for quantum information applications.

As discussed previously, the $^{51}V^{5+}$ lattice ion nuclear spins surrounding the $^{171}$Yb ion generate a noisy magnetic field environment due to their large magnetic moment and high spin (I=7/2). Coherent $^{171}$Yb qubit operation is enabled by magnetically-insensitive transitions, leading to long coherence times (21 ms) and high gate fidelities (0.99975) (see Sections 3.4 and 3.5). Whilst decoupling from sources of magnetic noise achieves an excellent operating regime for the $^{171}$Yb qubit, the $^{51}$V nuclear spins could also provide a readily accessible resource for quantum information storage due to their inherently weak interactions with the environment.

Critically, interfacing with these nuclear spins whilst preserving high qubit coherence necessitates a comprehensive understanding of Yb-nuclear spin interactions which will be the focus of this section.

## 4.2 Intuitive Understanding and Basic Model (Theory)

In this section we provide a basic perturbation theory model for the Yb–V interactions.

At zero field, the $^{171}$Yb $|0_g\rangle$, $|1_g\rangle$ states have no intrinsic magnetic dipole moment and thus dipole-dipole interactions with $^{51}$V register spins are forbidden to first order. Therefore, one might assume a direct second-order interaction with the register spins dominates. It turns out, this is not entirely correct.

Instead, a weak $^{171}$Yb dipole moment is induced by a random magnetic field originating from the bath (the nuclear Overhauser field, with $z$ component $B_z^{\mathrm{OH}}$). This weak induced dipole moment can then mediate a $^{171}$Yb–$^{51}$V register interaction. It turns out that this mechanism dominates over direct second order interactions with the register spins. A schematic of this process is shown in Figure 4.1.

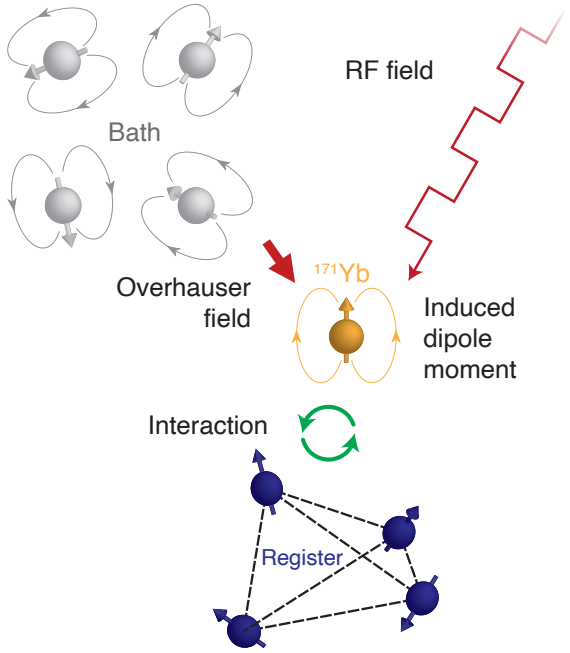


Figure 4.1: Dominant mechanism for Yb interaction with the nuclear spin register. A weak dipole moment is induced on the Yb via two magnetic field sources: a random Overhauser field generated by the bath spins and any externally applied field(s). This induced dipole moment mediates an electronic-nuclear magnetic dipole-dipole interaction between Yb and the register. Since the Overhauser field fluctuates in time its contribution to the interaction cannot be used for coherent quantum control.

### $^{171}$Yb–$^{51}$V Interactions

The magnetic dipole-dipole interaction between the $^{171}$Yb qubit and a single $^{51}$V ion can be described by the following Hamiltonian:

$$\hat{H}_{dd} = \frac{\mu_0}{4\pi}\left[\frac{\boldsymbol{\mu}_{\mathrm{Yb}}\cdot\boldsymbol{\mu}_{\mathrm{V}}}{r^3} - \frac{3(\boldsymbol{\mu}_{\mathrm{Yb}}\cdot\mathbf{r})(\boldsymbol{\mu}_{\mathrm{V}}\cdot\mathbf{r})}{r^5}\right] \tag{4.1}$$

where $\boldsymbol{\mu}_{\mathrm{Yb}} = -\mu_B\mathbf{g}\cdot\hat{\mathbf{S}}$, $\boldsymbol{\mu}_{\mathrm{V}} = \mu_N\mathbf{g}_{\mathrm{V}}\cdot\hat{\mathbf{I}}$ (note that $\mathbf{S}$ and $\mathbf{I}$ are vectors of $^{171}$Yb and $^{51}$V spin operators, respectively), $\mu_B$ is the Bohr magneton, $\mu_N$ is the nuclear magneton, $\mu_0$ is the vacuum permeability and $\mathbf{r}$ is the $^{171}$Yb–$^{51}$V displacement vector with magnitude $r$. Due to the highly off-resonant nature of the $^{171}$Yb–$^{51}$V interaction, a secular approximation would be appropriate. To first order; however, all secular terms involving the $^{171}$Yb qubit basis are zero, i.e., $\langle 0_g|\,\hat{H}_{dd}\,|0_g\rangle = 0$, $\langle 1_g|\,\hat{H}_{dd}\,|1_g\rangle = 0$.

To proceed, we consider second-order effects which generally scale as $\sim g^2/\Delta E$, where $\Delta E$ is the energy separation between a pair of unperturbed eigenstates. By taking into account the fact that $g_z$ is roughly 7 times larger than $g_x$, $g_y$ and $\hat{S}_z$ terms in $\hat{H}_{dd}$ mix $|0_g\rangle$ and $|1_g\rangle$ with small $\Delta E$ whereas $\hat{S}_x$ and $\hat{S}_y$ mix the $^{171}$Yb qubit states and $|\text{aux}_g\rangle$ with large $\Delta E$, we restrict our consideration to the $\hat{S}_z$ terms in $\hat{H}_{dd}$:

$$\hat{H}_{dd} \approx \frac{\mu_0 \mu_B \mu_N g_z}{4\pi r^3} \hat{S}_z \left[ 3lng_{vx}\hat{I}_x + 3mng_{vx}\hat{I}_y + (3n^2-1)g_{vz}\hat{I}_z \right] \tag{4.2}$$

where $\{l, m, n\}$ are direction cosines of the $^{171}$Yb–$^{51}$V displacement vector. Note that the $\hat{S}_z$ operator is the electron spin-1/2 operator defined as $\hat{S}_z = 1/2(|0_g\rangle\langle 1_g| + |1_g\rangle\langle 0_g|)$ in the basis of the hybridized eigenstates of the $^{171}$Yb qubit.

**Nuclear Overhauser Field**

As introduced in the Section 2.3, we can divide the $^{51}$V spins into two ensembles: register spins and bath spins. The bath spins comprise $^{51}$V ions which are not driven by the $^{171}$Yb qubit for the following two reasons:

1. **Ions which are not driven due to position**: certain ions (such as 1 and 2 in Table 2.1) only interact via an Ising-type $\hat{S}_z\hat{I}_z$ Hamiltonian. Hence the $^{171}$Yb qubit cannot be used to drive transitions between the $^{51}$V $z$-quantized quadrupole levels.

2. **Ions which are not driven due to detuning**: As discussed in Section 2.3 and experimentally demonstrated in Section 6.2, more distant spins are spectrally separated from the nearby ions comprizing the register.

We assume that the bath spins are in an infinite-temperature mixed state: $\rho_{\text{V}} = \mathbb{I}_{\text{V}}/Tr\{\mathbb{I}_{\text{V}}\}$, where $\mathbb{I}_v$ is the identity matrix in the Hilbert space for the bath spins. In the mean field picture, their effect on the $^{171}$Yb can be approximated as a classical fluctuating magnetic field, commonly termed the nuclear Overhauser field [224]. As mentioned previously, since $g_z^2 \gg g_{x,y}^2$, the $z$-component of the Overhauser field is dominant, given by

$$B_z^{\text{OH}} = \sum_{\text{i}\in\text{bath}} \frac{\mu_0 \mu_N g_{vz}}{4\pi (r^{(i)})^3} (3(n^{(i)})^2 - 1) m_I^{(i)}, \tag{4.3}$$

where $r^{(i)}$ and $n^{(i)}$ are the distance and $z$-direction cosine between the $^{171}$Yb and $i^{\text{th}}$ bath spin, and $m_I^{(i)} \in \{-7/2, -5/2, ..., 5/2, 7/2\}$ is the nuclear spin projection at site $i$. Note that $B_z^{\text{OH}}$ is randomly fluctuating due to the stochastic occupation of

the 8 possible $|m_I\rangle$ states; however, it is quasi-static on the timescale of our control sequences, hence we do not label the time dependence.

Crucially, the nuclear Overhauser field generates some weak mixing between $|0_g\rangle$ and $|1_g\rangle$ leading to perturbed eigenstates $|\tilde{0}_g\rangle$ and $|\tilde{1}_g\rangle$ which have a small, induced, $z$-directed dipole moment. These states have the form

$$\begin{aligned} |\tilde{0}_g\rangle &= |0_g\rangle - \frac{\gamma_z(B_z^{\mathrm{OH}} + B^{\mathrm{RF}}(t))}{2\omega_{01}} |1_g\rangle \\ |\tilde{1}_g\rangle &= |1_g\rangle + \frac{\gamma_z(B_z^{\mathrm{OH}} + B^{\mathrm{RF}}(t))}{2\omega_{01}} |0_g\rangle \end{aligned} \tag{4.4}$$

where $\gamma_z = g_z\mu_B$ is the longitudinal gyromagnetic ratio of the $^{171}$Yb qubit and $\omega_{01}/2\pi = 675$ MHz is the unperturbed $^{171}$Yb $|0_g\rangle \leftrightarrow |1_g\rangle$ transition frequency. Here we have added the effect of an externally applied, $z$-directed, RF magnetic field $B^{\mathrm{RF}}(t)$ with amplitude $B^{\mathrm{RF}}$ which will be used in the next chapter to mediate a coherent interaction with the nuclear spins. In addition, these fields induce a detuning of the $^{171}$Yb $|0_g\rangle \leftrightarrow |1_g\rangle$ transition, which can be calculated using second-order perturbation theory as $\Delta(t) = \gamma_z^2(B_z^{\mathrm{OH}} + B^{\mathrm{RF}}(t))^2/2\omega_{01}$.

**Interaction with Register Ions**

The second nearest shell of four $^{51}$V ions (ions 3–6 in Table 2.1) comprise the register. These four ions are equidistant from the $^{171}$Yb and interact via both an $\hat{S}_z\hat{I}_z$ term and $\hat{S}_z\hat{I}_x$ or $\hat{S}_z\hat{I}_y$ terms. To identify an effective interaction Hamiltonian in the perturbed basis $\{|\tilde{0}_g\rangle, |\tilde{1}_g\rangle\}$, we consider only secular matrix elements of $\hat{H}_{dd}$ (equation (4.2)):

$$\hat{\tilde{H}}_{dd} = \langle\tilde{0}_g|\,\hat{H}_{dd}\,|\tilde{0}_g\rangle\,|\tilde{0}_g\rangle\,\langle\tilde{0}_g| + \langle\tilde{1}_g|\,\hat{H}_{dd}\,|\tilde{1_g}\rangle\,|\tilde{1}_g\rangle\,\langle\tilde{1}_g| \tag{4.5}$$

where

$$\begin{aligned} \langle\tilde{0}_g|\,\hat{H}_{dd}\,|\tilde{0}_g\rangle &= -\frac{\mu_0\mu_N\gamma_z^2(B_z^{\mathrm{OH}} + B^{\mathrm{RF}}(t))}{8\pi r^3\omega_{01}}\left[3lng_{vx}\hat{I}_x + 3mng_{vx}\hat{I}_y + (3n^2-1)g_{vz}\hat{I}_z\right] \\ \langle\tilde{1}_g|\,\hat{H}_{dd}\,|\tilde{1}_g\rangle &= +\frac{\mu_0\mu_N\gamma_z^2(B_z^{\mathrm{OH}} + B^{\mathrm{RF}}(t))}{8\pi r^3\omega_{01}}\left[3lng_{vx}\hat{I}_x + 3mng_{vx}\hat{I}_y + (3n^2-1)g_{vz}\hat{I}_z\right]. \end{aligned}$$

Hence the effective interaction between the $^{171}$Yb qubit and the four register spins, $\hat{H}_{\mathrm{int}} = \sum_{i\in\mathrm{register}} \hat{\tilde{H}}_{dd}^{(\mathrm{i})}$, can be described by

$$\hat{H}_{\mathrm{int}} = \hat{\tilde{S}}_z(B_z^{\mathrm{OH}} + B^{\mathrm{RF}}(t)) \sum_{i\in\mathrm{register}} \left(J_x^{(i)}\hat{I}_x^{(i)} + J_y^{(i)}\hat{I}_y^{(i)} + J_z^{(i)}\hat{I}_z^{(i)}\right) \tag{4.6}$$

with

$$J_x^{(i)} = \frac{3\mu_0\mu_N\gamma_z^2 g_{vx} l^{(i)} n^{(i)}}{4\pi (r^{(i)})^3 \omega_{01}}$$
$$J_y^{(i)} = \frac{3\mu_0\mu_N\gamma_z^2 g_{vx} m^{(i)} n^{(i)}}{4\pi (r^{(i)})^3 \omega_{01}}$$
$$J_z^{(i)} = \frac{\mu_0\mu_N\gamma_z^2 g_{vz} (3(n^{(i)})^2 - 1)}{4\pi (r^{(i)})^3 \omega_{01}}$$

and

$$\hat{\tilde{S}}_z = \frac{1}{2}(|\tilde{1}_g\rangle\langle\tilde{1}_g| - |\tilde{0}_g\rangle\langle\tilde{0}_g|).$$

Finally, we perform local basis transformations of each $^{51}$V ion to further simplify the Hamiltonian form. Specifically, we apply the following unitary rotation:

$$\hat{H}_{\text{int}} \rightarrow U\hat{H}_{\text{int}}U^\dagger$$
$$U = \prod_{j\in\text{register}} \exp[i\theta^{(j)}\hat{I}_z^{(j)}],$$

where $\theta^{(j)} = \tan^{-1}(m^{(j)}/l^{(j)})$, which leads to

$$\hat{H}_{\text{int}} = \hat{\tilde{S}}_z(B_z^{\text{OH}} + B^{\text{RF}}(t)) \sum_{i\in\text{register}} \left[a_x\hat{I}_x^{(i)} + a_z\hat{I}_z^{(i)}\right] \tag{4.7}$$

with $a_x = \sqrt{(J_x^{(i)})^2 + (J_y^{(i)})^2}$ and $a_z = J_z^{(i)}$. Note that the coupling coefficients $a_x$ and $a_z$ are homogeneous (i.e., independent of site index $i$) since the four register spins are equidistant from the central $^{171}$Yb and have directional cosine factors with equal magnitude.

Hereafter we simplify our notation and use $|0_g\rangle$ and $|1_g\rangle$ without tildes to represent the weakly perturbed eigenstates in the presence of any small magnetic field.

**Full System Hamiltonian**

Combining the various energy and interaction terms, the full system Hamiltonian (in a $^{171}$Yb frame rotating at $\omega_{01}/2\pi = 675$ MHz) becomes:

$$\begin{aligned}\hat{H}_{\text{full}} =& \frac{\gamma_z^2\left(B_z^{\text{OH}} + B^{\text{RF}}(t)\right)^2}{2\omega_{01}}\hat{\tilde{S}}_z + \\ & \sum_{i\in\text{register}} Q\left(\hat{I}_z^{(i)}\right)^2 + \hat{\tilde{S}}_z(B_z^{\text{OH}} + B^{\text{RF}}(t)) \sum_{i\in\text{register}} \left[a_x\hat{I}_x^{(i)} + a_z\hat{I}_z^{(i)}\right].\end{aligned} \tag{4.8}$$

### 4.3 Schrieffer-Wolff Transformation (Theory)

While the preceding section provides a sufficient description for modelling interaction with the register, there are various mechanisms which it does not capture, for instance:

- direct second order interactions with the register,
- the quantum state of the spectator nuclear spins,
- Yb-mediated interactions between different nuclear spins.

In this section I will present an analysis of the Yb-V interactions using the Schrieffer-Wolff transformation [225, 226] which provides a more rigorous way to derive the results of the preceding section and also enables modelling of all these additional effects.

The Schrieffer-Wolff transformation is a method in perturbation theory which enables the adiabatic elimination of fast degrees of freedom. Essentially, it expresses the Hamiltonian $\hat{H} = \hat{H}_0 + \hat{V}$ in a dressed basis which is diagonal in the perturbation $\hat{V}$. Consider an unperturbed Hamiltonian $\hat{H}_0$ which consists of slow and fast degrees of freedom ($A$ and $B$, respectively) such that $\hat{H}_0 = \hat{H}_A + \hat{H}_B$. I.e., if $\hat{H}_A$ ($\hat{H}_B$) has eigenstates $|\alpha\rangle$ ($|\beta\rangle$) with energies $E_\alpha$ ($E_\beta$) then the energy difference between any pair of $A$ eigenstates is much lower than the energy difference between any pair of $B$ eigenstates.

Utilizing the Schrieffer Wolf transformation up to second order, we can derive a Hamiltonian that is diagonal in the fast degree of freedom with elements $|\beta\rangle \langle\beta| H^\beta_{\text{eff}}$ where:

$$H^\beta_{\text{eff}} = \langle\beta| \hat{H}_0 + \hat{V} |\beta\rangle + \sum_{\beta'} \frac{\langle\beta| \hat{V} |\beta'\rangle \langle\beta'| \hat{V} |\beta\rangle}{E_\beta - E_{\beta'}}. \tag{4.9}$$

Applying this to our system Hamiltonian we identify the fast degrees of freedom as the Yb terms, the slow degrees of freedom are the Vanadium terms and the perturbation consists of all magnetic-dipole-dipole interactions and the nuclear Zeeman interaction of external magnetic fields with the Yb.

We can then write the effective system Hamiltonian as:

$$\hat{H}_{\text{eff}} = \sum_{i \in \text{register}} Q \left(\hat{I}^{(i)}_z\right)^2 + \frac{\hat{\tilde{S}}_z}{2} \left( \frac{\gamma_z}{\sqrt{\omega_{01}}} B^{\text{RF}}(t) + \frac{\sqrt{\omega_{01}}}{\gamma_z} \sum_i \left[ a^{(i)}_x \hat{I}^{(i)}_x + a^{(i)}_z \hat{I}^{(i)}_z \right] \right)^2 \tag{4.10}$$

where we note that the index $i$ now runs over all nuclear spins (not just the register), hence the coupling coefficients $a_x^{(i)}$ and $a_z^{(i)}$ are now no longer homogeneous and depend on the nuclear spin index, $i$.

Note that if we were to take the equation for the Overhauser field (Equation (4.3)), substitute it into this result and take the dominant terms, we would arrive at equation (4.8).

## 4.4 Nuclear Spin Coherence (Theory)

It turns out that interaction between the Yb ion and V nuclear spins also acts as a source of decoherence for the nuclear spins.

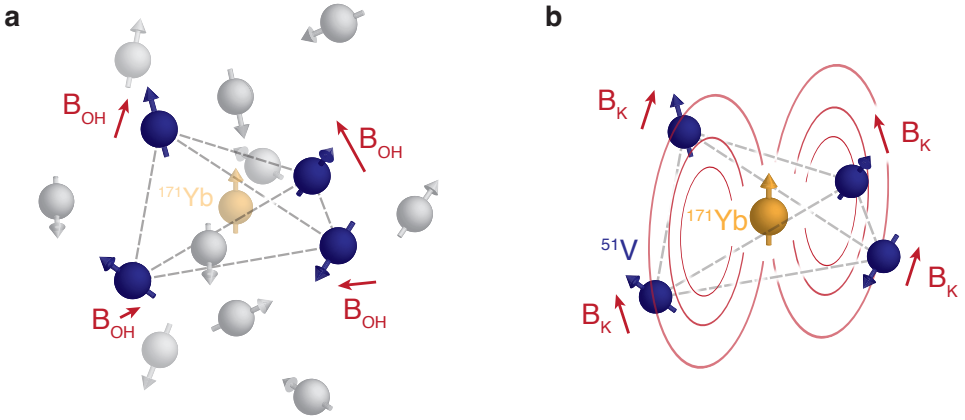


Figure 4.2: Sources of decoherence for the V register. a) The Overhauser field generated by bath spins causes frequency shifts via the nuclear Zeeman interaction. b) The Yb dipole moment (induced by the bath) also generates a magnetic field termed the Knight field. This field fluctuates with the Overhauser field and is amplified by approximately 3×, hence this source of decoherence dominates.

Specifically, the bath-induced $^{171}$Yb dipole moment generates a randomly fluctuating magnetic field (termed the Knight field [224]) at each $^{51}$V ion, with $z$ component given by:

$$B_{\mathrm{K},z} = \mp g_{vz}\mu_N B_z^{\mathrm{OH}} A_z \tag{4.11}$$

with

$$A_z = \frac{\mu_0 \gamma_z^2 (1 - 3n^2)}{8\pi r^3 \omega_{01}}.$$

Here, the $-$ and $+$ cases in equation (4.11) correspond to $^{171}$Yb in $|1_g\rangle$ and $|0_g\rangle$, respectively. We note that $A_z$ corresponds to an effective local field amplification

factor with value $A_z \approx 3.1$ for the register spins.

The second source of decoherence for the register spins is the nuclear Zeeman interaction with the Overhauser field from the bath: Since the energy levels are quantized along the $z$-axis, magnetic fluctuations along the $z$-direction dominate, which can be captured by the following Hamiltonian

$$\hat{H}_{\mathrm{nz}} = \sum_{i \in \mathrm{register}} \mu_N g_{vz} B_z^{\mathrm{OH}}(\mathbf{r}_i)\, \hat{I}_z^{(i)} \tag{4.12}$$

where $B_z^{\mathrm{OH}}(\mathbf{r}_i)$ is the $z$-component of the Overhauser field evaluated at the position of the $i^{\mathrm{th}}$ register ion, $\mathbf{r}_i$.

We note that since the local field amplification factor $A_z$ is greater than 1, the Knight field is the dominant source of decoherence. Luckily, as we will see in Section 6.5, we can effectively cancel this interaction by driving the Yb. Specifically, by applying periodic $\pi$ pulses to the $^{171}$Yb, we flip its state between $|0_g\rangle$ and $|1_g\rangle$, thereby switching the sign of the Knight field. This leads to the cancellation of $^{51}$V phase accumulation between successive free evolution periods, in a process analogous to motional narrowing, resulting in a longer coherence time.

Finally, it is also interesting to note the difference in spatial correlation of these two fields at each of the register ion positions. This is depicted in Figure 4.2. Since the register is embedded in a dense nuclear spin environment the Overhauser field is highly uncorrelated. The Knight field, on the other hand, is perfectly correlated due to the symmetry of the four register ion positions relative to the Yb.

## 4.5 Summary of System Parameters

Table 4.1 summarizes physical and experimental parameters relevant to the joint $^{171}$Yb–$^{51}$V register system, relevant for Chapters 4, 5, and 6:

| Physical parameter description | Symbol | Value |
|---|---|---|
| $^{171}$Yb qubit frequency | $\omega_{01}$ | $2\pi \times 675$ MHz |
| $^{171}$Yb electronic $g$-factors | $\{g_x,\ g_y,\ g_z\}$ | $\{0.85,\ 0.85,\ -6.08\}$ |
| $^{171}$Yb qubit drive Rabi frequency | $\Omega$ | $2\pi \times 10$ MHz |
| $^{51}$V electric quadrupole parameter | Q | $2\pi \times 165$ kHz |
| $^{51}$V register transition frequencies | $\{\omega_a,\ \omega_b,\ \omega_c\}$ | $2\pi \times \{330,\ 660,\ 991\}$ kHz |
| $^{51}$V register nuclear $g$-factors | $\{g_{vx},\ g_{vy},\ g_{vz}\}$ | $\{0.6,\ 0.6,\ 1.6\}$ |
| Overhauser field mean value | $\overline{B_z^{\mathrm{OH}}}$ | 0 G |
| Overhauser field standard deviation | std$[B_z^{\mathrm{OH}}]$ | 1.9 G |
| $^{51}$V register coupling coefficients | $\{\lvert a_x\rvert,\ \lvert a_z\rvert\}$ | $2\pi \times \{6.1\ , 22\}$ kHz/G |
| RF amplitude for swap gate | $B^{\mathrm{RF}}$ | 1.6 G |
| Spin exchange rate for swap gate | $J_{\mathrm{ex}}$ | $2\pi \times 11$ kHz |
| Knight field amplification factors | $\{\lvert A_{x,y}\rvert,\ \lvert A_z\rvert\}$ | $\{6.7,\ 3.1\}$ |
| RF amplitude for $^{51}$V direct driving | $B_z^{\mathrm{osc}}$ | 1.9 G |
| $^{51}$V direct drive Rabi frequency | $\Omega_D$ | $2\pi \times 7.7$ kHz |

Table 4.1: System parameters relevant for interaction with vanadium nuclear spin ensemble.

## 4.6 CPMG Spectroscopy (Experiment)

The first sign of interaction with nuclear spins was observed while performing time-resolved Carr-Purcell-Meiboom-Gill (CPMG) coherence measurements [209, 210]. Specifically, we apply an $8\pi$ pulse CPMG sequence and sweep the inter-pulse separation $2\tau$. The experimental results are shown in Figure 4.3a and b.

There are two features worth noting here: first an underlying stretched exponential decay with a timescale of $\sim 10\ \mu$s[1]. This is due to dynamics of a dipolar spin bath with noise spectral density of the form $S(\omega) \propto \omega^{-2.3}$ as discussed in Section 3.5. Second, there are pronounced, periodic dips in the coherence at specific pulse separations.

We perform a simulation of the CPMG sequence using the model of Yb–V interactions described in Section 4.2 (Figure 4.3c) and find a very close correspondence with the experimental data (Figure 4.3b). Based on the simulation we find that the three labelled dips correspond primarily to interaction with the $a$, $b$ and $c$ transitions of the V spins.

[1]Note: this decay timescale is in units of pulse separation, $2\tau$, not coherence time.

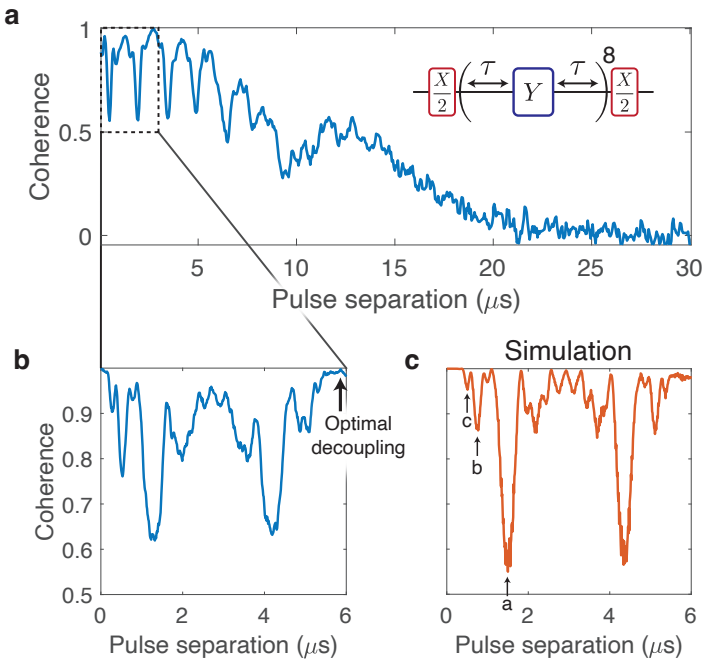


Figure 4.3: Time resolved CPMG measurements. a) and b) Experimental results showing the qubit coherence as a function of pulse separation for an $8\pi$ pulse CPMG sequence. c) Simulations of the same sequence. The labels indicate resonances with the $a$, $b$ and $c$ transitions of surrounding Vanadium nuclear spins.

An intuitive explanation of this phenomenon is as follows: the Overhauser field induces a dipole moment on the Yb. Applying periodic $\pi$ pulses repeatedly flips the Yb state, leading to the generation of a toggling magnetic field at each V ion location with period $2\tau$. This field drives a given quadrupolar transition of the V ions when the pulse spacing satisfies the condition: $\omega_{a/b/c} = M\pi/\tau$ where $M$ is an odd integer. Under these resonance conditions there exists a Fourier harmonic of the toggling field that is resonant with (and can drive) the nuclear spins. As the nuclear spins undergo Rabi oscillation they become entangled with the Yb state, thus appearing as a source of decoherence.

Note that this effect is caused by the $\hat{S}_z\hat{I}_x$ interaction between the Yb and V spins. In Chapter 5 we will consider the interplay between these dipole-dipole interactions and periodic pulsed control of the Yb in a much more formal context using average Hamiltonian theory. We also note that the CPMG results can also be treated using the filter function formalism described in detail in [227]. Since we already have simulations which adequately reproduce the data we will not go into more detail on this formalism here.

In section 3.5 we demonstrated long spin coherence times (21 ms), these measurements were performed by choosing a pulse separation which optimally decouples from any V transition resonances (arrow, Figure 4.3b) and probing the coherence by varying the number of dynamical decoupling periods.

### 4.7 Hartmann-Hahn Spectroscopy (Experiment)

We also use Hartmann-Hahn (HH) double resonance [228] to perform spectroscopy of the nuclear spin environment. This method enables spin exchange between two systems with different transition frequencies by resonantly driving a qubit with a Rabi frequency that matches the energy level splitting of the environmental nuclear spins. In our case, we resonantly drive the $^{171}$Yb at 675 MHz to generate a pair of dressed states $|\pm\rangle = \frac{1}{\sqrt{2}}\left(|0_g\rangle \pm i\,|1_g\rangle\right)$ with splitting $\Omega$ which we sweep over a range $\approx 2\pi\times$(0–2.3) MHz (Figure 4.4). The $^{171}$Yb qubit is initialized into the $|-\rangle$ dressed state by a $\pi/2$ pulse preceding the driving period. If resonant with a nuclear spin transition, the $^{171}$Yb qubit undergoes spin exchange at a rate dictated by the interaction strength. Finally we read out the $^{171}$Yb $|+\rangle$ dressed state population to determine whether spin exchange has occurred.

Figure 4.4b shows experimental results of HH spectroscopy where we vary both the HH drive Rabi frequency ($\Omega$) and also the HH pulse duration ($t$). The counts plotted on the colour-bar are proportional to the $|+\rangle$ dressed state population. We find three clear resonances at evenly spaced pulse amplitudes 0.15, 0.30 and 0.45 corresponding to the $a$, $b$ and $c$ $^{51}$V transitions; notably, unlike CPMG, the HH sequence only has one harmonic leading to a single resonant interaction per transition. Note the lack of oscillations when varying the pulse duration, $t$, on resonance with either of the three transitions: this is because the spin exchange is driven by the randomized, Overhauser field induced $^{171}$Yb dipole moment. For this reason, the HH sequence cannot be used to generate a coherent interaction with the nuclear spins. In the case of no driving ($\Omega = 0$), the signal rapidly saturates as $t$ increases as a result of Ramsey dephasing of the initial state. However, as $\Omega$ exceeds the $^{171}$Yb spin line-width ($\sim$ 50 kHz [155]), this effect diminishes due to the emergence of spin-locking effects and consequently leads to an increased saturation timescale when not resonant with the $^{51}$V transitions. The resolution of this measurement is also limited by the $^{171}$Yb spin line-width, and we therefore cannot resolve separate resonances associated with the register and bath transitions as observed in Chapter 6. The results agree well with simulations (Figure 4.4c) indicating that interactions with the $^{51}$V quadrupolar structure dominate these measurements.

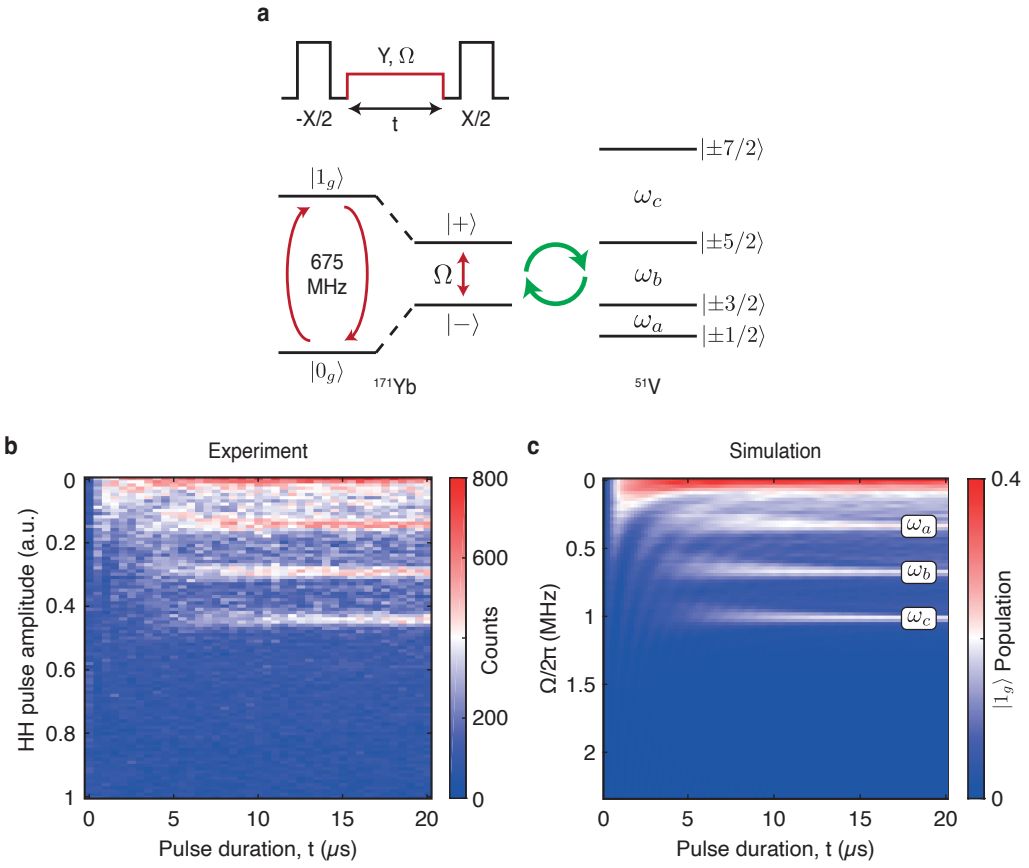


Figure 4.4: Hartmann Hahn spectroscopy. a) Hartmann Hahn (HH) sequence used to perform spectroscopy of the nuclear spin environment. During the HH pulse (red), the $^{171}$Yb $|0_g\rangle \leftrightarrow |1_g\rangle$ qubit transition is driven resonantly for duration $t$ with $y$-phase leading to a pair of dressed states, $|\pm\rangle = \frac{1}{\sqrt{2}}(|0_g\rangle \pm i\,|1_g\rangle)$, separated by energy splitting equal to the Rabi frequency, $\Omega$. An initial $-x$-phase $\pi/2$ pulse prepares the $^{171}$Yb qubit in the $|-\rangle$ dressed state. When the Rabi frequency of the HH pulse is tuned to equal one of the $^{51}$V transition frequencies, the $^{171}$Yb is transferred into the $|+\rangle$ dressed state as a result of resonant population exchange (green arrows). The $|+\rangle$ state population is mapped to $|1_g\rangle$ with a final $x$-phase $\pi/2$ pulse for readout. b) HH spectroscopy experimental results. To identify nuclear spin resonances, both the HH pulse amplitude and duration are varied. The three evenly-spaced horizontal resonance features occurring at pulse amplitudes of 0.15, 0.3, and 0.45 (in arbitrary units, a.u.) correspond to interaction with the $\omega_a$, $\omega_b$ and $\omega_c$ transitions, respectively. In the no driving ($\Omega = 0$) case, the sequence probes the decoherence dynamics of the prepared $|-\rangle$ state, i.e., it measures the Ramsey coherence time. c) HH spectroscopy simulation results. Simulation results agree well with the experiment, corroborating that $^{171}$Yb–$^{51}$V interactions are dominant in our system.

*Chapter 5*

# NUCLEAR SPIN STORAGE PROTOCOL AND PULSE SEQUENCE DESIGN

## 5.1 Introduction

As outlined in Section 1.4, auxiliary quantum storage at each node is critically important for building long-range quantum networks, this can be used to implement the quantum repeater and other advanced networking protocols. In the context of nitrogen vacancy centers in diamond, $^{13}$C nuclear spins have been utilized for high fidelity, versatile long-term storage for precisely these applications. One might assume that we could therefore utilize equivalent protocols to store quantum information on the $^{51}$V nuclear spins surrounding our Yb qubits; however, this is not the case for two key reasons.

First, at zero field, the $^{171}$Yb $|0_g\rangle$, $|1_g\rangle$ states have no intrinsic magnetic dipole moment and thus interactions with $^{51}$V register spins are forbidden to first order. Furthermore, as introduced in Section 4.2, a weak $^{171}$Yb dipole moment is induced by a random magnetic field originating from the bath (the nuclear Overhauser field, with $z$ component $B_z^{\mathrm{OH}}$), giving rise to a $^{171}$Yb–$^{51}$V register interaction of the form:

$$\hat{H}_{\mathrm{int}} = \hat{\tilde{S}}_z B_z^{\mathrm{OH}} \sum_{i \in \mathrm{register}} \left( a_x \hat{I}_x^{(i)} + a_z \hat{I}_z^{(i)} \right). \tag{5.1}$$

Note that $B_z^{\mathrm{OH}}$ varies randomly in time as the bath changes state in a stochastic fashion, rendering this second order interaction Hamiltonian unreliable for register quantum state manipulation.

Second, the four register ions are spectrally indistinguishable, meaning that we cannot interact with a single isolated nuclear spin. This prevents us from using individual nuclear spins as qubits (the regime which has been extensively studied/utilized for $^{13}$C in diamond). Thus, we need to explore methods of quantum storage using collective states of all four register spins.

It turns out that collective modes of dense nuclear spin ensembles have been proposed as a basis for quantum storage in the context of quantum dots [229]. However, experimental realizations of these protocols have thus far remained elusive, limited by the large number of nuclear spins addressed by a single quantum dot (typically

$\sim 10^5$) and the associated complex polarization dynamics. Realizing this protocol for our system would require a coherent spin-exchange interaction (as will be described in the next section), which unfortunately, is not natively present in our Yb–V interaction Hamiltonian.

The focus of this chapter will be to describe how we can, in fact, generate a deterministic $^{171}$Yb–$^{51}$V spin exchange interaction via Hamiltonian engineering which will subsequently be utilized for implementing auxiliary quantum state storage.

Unlike conventional, disordered nuclear spin based quantum memories [143, 187–190, 193–196], this approach is deterministic and reproducible, ensuring identical quantum registers for all $^{171}Yb^{3+}$ qubits. This provides a framework for utilizing the complex structure of dense nuclear spin baths, paving the way for building large-scale quantum networks using single rare-earth ion qubits [152, 154, 155, 157, 230].

### 5.2 Nuclear Spin Storage Protocol

As originally proposed for quantum dots [229], single spin excitations of a polarized nuclear spin ensemble can be used for quantum information storage. These states are often termed spin waves or nuclear magnons and can be generated by spin-preserving exchange dynamics. Specifically, preparing these collective nuclear spin states relies, first, on initializing the thermal register ensemble into a pure state, $|0_v\rangle = |\downarrow\downarrow\downarrow\downarrow\rangle$, where $\{|\uparrow\rangle, |\downarrow\rangle\} = \{|\pm 5/2\rangle, |\pm 7/2\rangle\}$ is a two-level sub-manifold of the nuclear spin-7/2 $^{51}$V ion (Figure 5.1a,b).

Next, with access to coherent exchange dynamics of the form $\hbar\alpha_{\text{ex}} \sum_i \left(\hat{\tilde{S}}_- \hat{I}_+^{(i)} + \hat{\tilde{S}}_+ \hat{I}_-^{(i)}\right)$ and $^{171}$Yb initialized in $|1_g\rangle$, the system undergoes time evolution given by:

$$|\psi(t)\rangle = |1_g\rangle\,|0_v\rangle \cos(J_{\text{ex}} t/2) - i\,|0_g\rangle\,|W_v\rangle \sin(J_{\text{ex}} t/2) \tag{5.2}$$

where the spin-exchange frequency is given by $J_{\text{ex}} = 2\sqrt{N}\alpha_{\text{ex}}$ (with $N = 4$ being the number of V spins in the register) and $|W_v\rangle$ [231] is given by

$$|W_v\rangle = \frac{|\uparrow\downarrow\downarrow\downarrow\rangle + |\downarrow\uparrow\downarrow\downarrow\rangle + |\downarrow\downarrow\uparrow\downarrow\rangle + |\downarrow\downarrow\downarrow\uparrow\rangle}{2} \tag{5.3}$$

(Figure 5.1c). Note that this state consists of a single spin excitation equally delocalized across the four register spins, this is due to coupling homogeneity as determined by the lattice geometry and naturally realizes an entangled four-body W-state.[1] Note

[1] Note that even if the spins were not homogeneously coupled, this storage protocol could be used. However, the contributions of the different single spin excitations in the W state would no longer be equally weighted, see [229] for details.

also that the spin-exchange rate is collectively enhanced by a factor of $\sqrt{N}$, leading to faster dynamics for larger numbers of participating spins. When we fix $t = \pi/J_{\mathrm{ex}}$ we can perfectly transfer a single excitation from the $^{171}$Yb to the register.

If the $^{171}$Yb qubit is initialized into $|0_g\rangle$ there are no spin excitations in the system and the $^{51}$V register remains in $|0_v\rangle$.

Crucially, these dynamics realize a quantum swap gate between a target state prepared by the $^{171}$Yb qubit, $|\psi\rangle = \alpha\,|0_g\rangle + \beta\,|1_g\rangle$, and the $|0_v\rangle$ state of the $^{51}$V register, leading to

$$\left(\alpha\,|0_g\rangle + \beta\,|1_g\rangle\right)|0_v\rangle \rightarrow |0_g\rangle\left(\alpha\,|0_v\rangle + \beta\,|W_v\rangle\right). \tag{5.4}$$

After waiting for a period of time, the stored quantum state can be retrieved by applying a second swap gate (Figure 5.1d). Note that the spin-wave like state $|W_v\rangle$ of the nuclear ensemble is being utilized as a constituent of the quantum memory basis.

We also note that in this protocol it is possible to transfer a second spin excitation to the register. More specifically, the spin-preserving exchange interaction couples the state $|1_g\rangle\,|W_v\rangle$ to $|0_g\rangle\,|2_v\rangle$, where $|2_v\rangle$ is a $^{51}$V state with two spins in $|\uparrow\rangle$. To avoid undesired excitation to states outside of the effective $\{|0_v\rangle, |W_v\rangle\}$ manifold, we always prepare the $^{171}$Yb qubit in $|0_g\rangle$ before retrieving stored states from the $^{51}$V register. Hence the swap gate realized by this interaction operates on a limited basis of states.

To realize this storage protocol we require $^{171}$Yb–$^{51}$V spin-exchange interactions that are independent from the random, bath-induced dipole moment (equation (5.1)), the next section describes how we generate such interactions.

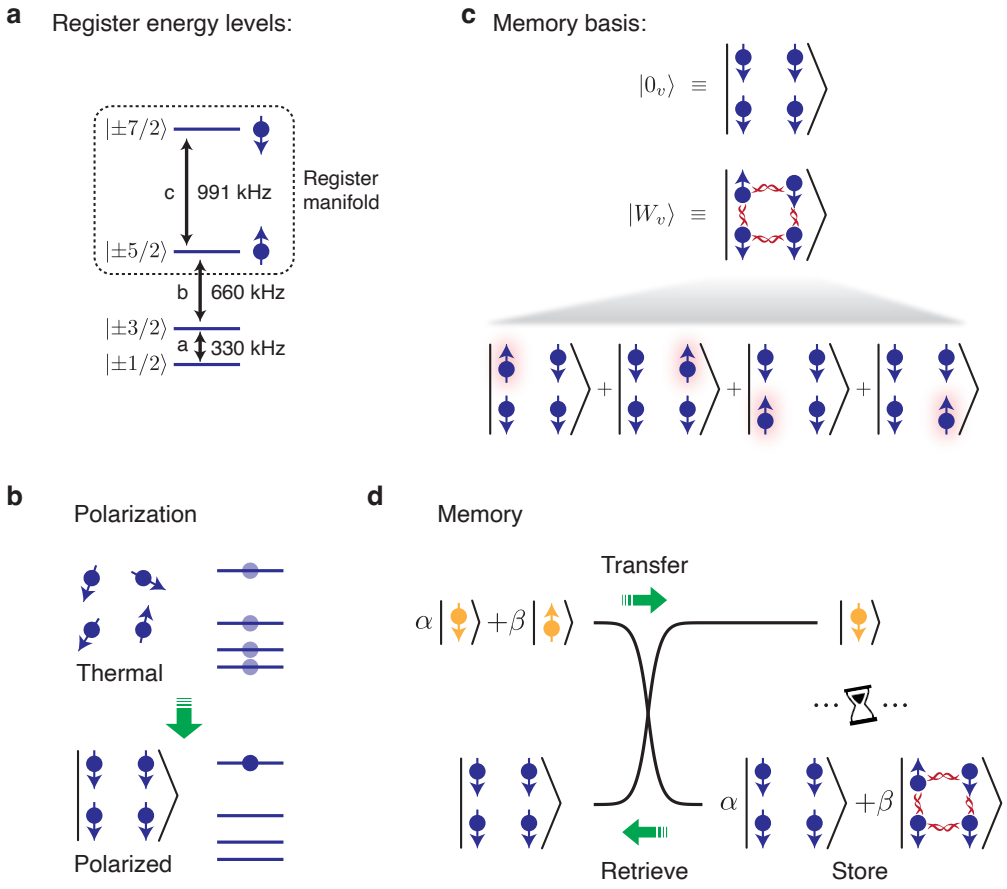


Figure 5.1: Illustration of quantum storage protocol. a) Energy levels of register nuclear spins, with effective spin-1/2 manifold highlighted. b) Nuclear spins are polarized into the uppermost quadrupole level (spin down). c) States used as quantum memory basis: the fully polarized state $|0_v\rangle$ and the W-state $|W_v\rangle$ consisting of a single spin excitation equally delocalized across all four nuclear spins. d) Quantum memory protocol demonstrating the storage (and retrieval) of a quantum state $\alpha\,|0_g\rangle + \beta\,|1_g\rangle$ on the nuclear spins as $\alpha\,|0_v\rangle + \beta\,|W_v\rangle$

### 5.3 ZenPol Pulse Sequence

We consider a system of a single $^{171}$Yb qubit coupled to four neighbouring nuclear spin-7/2 $^{51}$V ions. This hybrid spin system is described by the effective Hamiltonian (setting $\hbar = 1$):

$$\hat{H} = \Delta(t)\hat{\tilde{S}}_z + \sum_{i\in\text{register}} Q(\hat{I}_z^{(i)})^2 + \sum_{i\in\text{register}} \hat{\tilde{S}}_z \left[B_z^{\text{OH}} + B^{\text{RF}}(t)\right]\left[a_x\hat{I}_x^{(i)} + a_z\hat{I}_z^{(i)}\right] \quad (5.5)$$

where $\Delta(t) = \gamma_z^2(B_z^{\text{OH}} + B^{\text{RF}}(t))^2/2\omega_{01}$ is the effective energy shift due to both $z$-directed nuclear Overhauser ($B_z^{\text{OH}}$) and external RF ($B^{\text{RF}}(t)$) magnetic fields, $\omega_{01}/2\pi = 675$ MHz is the $^{171}$Yb qubit transition frequency, $\gamma_z/2\pi = -8.5$ MHz/G is the $^{171}$Yb ground-state longitudinal gyromagnetic ratio, $Q/2\pi = 165$ kHz is the $^{51}$V register nuclear quadrupole splitting, $\hat{\tilde{S}}_z$ is the $^{171}$Yb qubit operator along the $z$-axis, $\hat{I}_{x,z}$ are the $^{51}$V spin-7/2 operators along the $x$- and $z$-axis, and $a_{x,z}$ are the effective coupling strengths between $^{171}$Yb and $^{51}$V along the $x$- and $z$-axes. See Section 4.2 for a detailed derivation of this effective Hamiltonian.

Coherent polarization transfer between the $^{171}$Yb and $^{51}$V and can be achieved via periodic driving of the $^{171}$Yb qubit. Specifically, periodic pulsed control can dynamically engineer the original Hamiltonian (equation (5.5)) to realize effective spin-exchange interaction between $^{171}$Yb and $^{51}$V ions of the form, $\sum_i \hat{\tilde{S}}_+\hat{I}_-^{(i)} + \hat{\tilde{S}}_-\hat{I}_+^{(i)}$, in the average Hamiltonian picture [213, 232]. One example of such a protocol is the recently developed PulsePol sequence [233]; however, it relies on states with a constant, non-zero magnetic dipole moment and therefore cannot be used in our system since the $^{171}$Yb qubit has no intrinsic magnetic dipole moment. Motivated by this approach, we have developed a variant of the PulsePol sequence that accompanies a square-wave RF magnetic field synchronized with the sequence (Figure 5.2a).

The base sequence has a total of 8 free-evolution intervals with equal duration ($\tau/4$) defined by periodically spaced short pulses and is repeatedly applied to $^{171}$Yb. Following the sequence design framework presented in [232], we judiciously choose the phase and ordering of the constituent $\pi/2$ and $\pi$ pulses such that the resulting effective interaction has spin-exchange form with strength proportional to the RF magnetic field amplitude ($B^{\text{RF}}$), whilst decoupling from interactions induced by the nuclear Overhauser field ($B_z^{\text{OH}}$). We also design the sequence to cancel detuning induced by both of these fields and to retain robustness against pulse rotation errors to leading order. We term this new sequence 'ZenPol' for '**ze**ro first-order Zeeman **n**uclear-spin **pol**arization.'

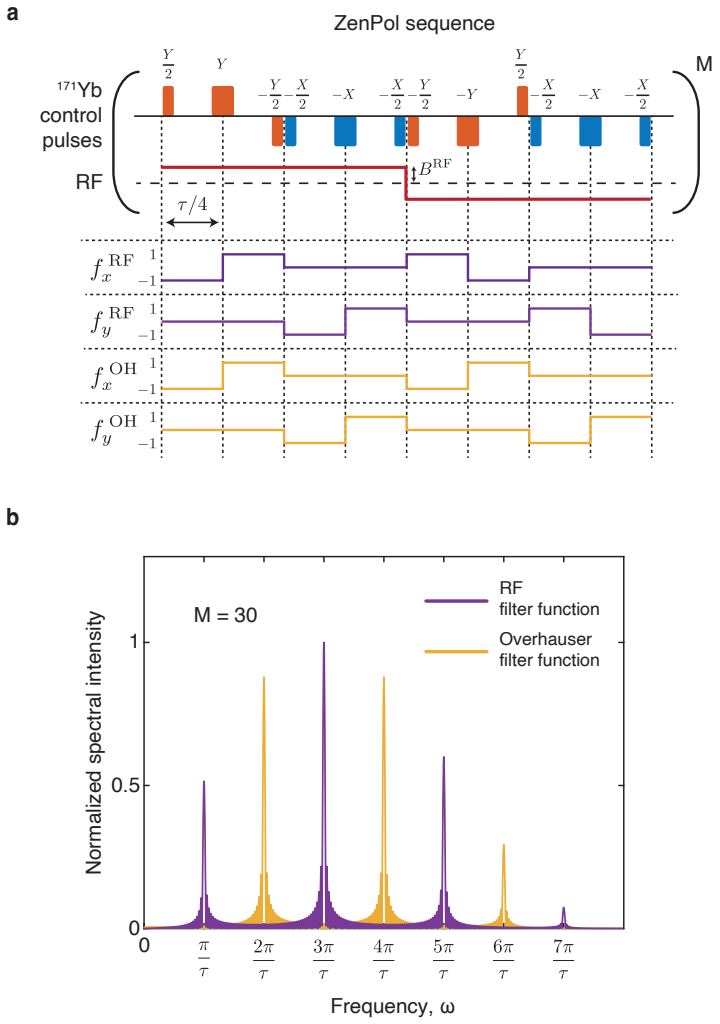


Figure 5.2: ZenPol sequence detail. a) ZenPol sequence with the toggling-frame transformation of the $\hat{\tilde{S}}_z$ operator for the $^{171}$Yb qubit. The Overhauser- and RF-induced interactions are determined by the toggling-frame transformations of $\hat{\tilde{S}}_z$ which are given by $\hat{\tilde{S}}_x f_x^{\mathrm{OH}} + \hat{\tilde{S}}_y f_y^{\mathrm{OH}}$ and $\hat{\tilde{S}}_x f_x^{\mathrm{RF}} + \hat{\tilde{S}}_y f_y^{\mathrm{RF}}$, respectively (see yellow and purple lines). b) ZenPol sequence filter functions corresponding to the Fourier transforms of $f_x^{\mathrm{OH}}$ (yellow) and $f_x^{\mathrm{RF}}$ (purple). For a sequence with fixed $\tau$, the peak positions determine the resonant frequencies at which $^{171}$Yb–$^{51}$V interactions can occur. Note that the incoherent Overhauser-induced interactions occur at even-$k$ resonances and are spectrally separated from the coherent RF-induced interactions occurring at odd-$k$ resonances.

To understand how the ZenPol sequence works, one can consider a toggling-frame transformation of the $^{171}$Yb qubit operator along the quantization axis ($\hat{\tilde{S}}_{z,\mathrm{tog}}(t)$): we keep track of how this operator is transformed after each preceding pulse. For example, the first $\pi/2$ pulse around the $y$-axis transforms $\hat{\tilde{S}}_z$ into $-\hat{\tilde{S}}_x$ and the subsequent $\pi$ pulse around the $y$-axis transforms $-\hat{\tilde{S}}_x$ into $+\hat{\tilde{S}}_x$. Over one sequence period, the toggling-frame transformation generates a time-dependent Hamiltonian $\hat{H}_{\mathrm{tog}}(t)$ that is piecewise constant for each of 8 free-evolution intervals, which can be expressed as

$$\begin{aligned}\hat{H}_{\mathrm{tog}}(t) = \Delta(t)\left[f_x^{\mathrm{OH}}(t)\hat{\tilde{S}}_x + f_y^{\mathrm{OH}}(t)\hat{\tilde{S}}_y\right] + \sum_{i\in\mathrm{register}} Q(\hat{I}_z^{(i)})^2 + \\ \sum_{i\in\mathrm{register}} B_z^{\mathrm{OH}}\left[f_x^{\mathrm{OH}}(t)\hat{\tilde{S}}_x + f_y^{\mathrm{OH}}(t)\hat{\tilde{S}}_y\right]\left[a_x\hat{I}_x^{(i)} + a_z\hat{I}_z^{(i)}\right] + \\ \sum_{i\in\mathrm{register}} B^{\mathrm{RF}}\left[f_x^{\mathrm{RF}}(t)\hat{\tilde{S}}_x + f_y^{\mathrm{RF}}(t)\hat{\tilde{S}}_y\right]\left[a_x\hat{I}_x^{(i)} + a_z\hat{I}_z^{(i)}\right].\end{aligned} \tag{5.6}$$

Here, $f_{x,y}^{\mathrm{OH}}(t)$ describes the time-dependent modulation of the $^{171}$Yb qubit operator along the $z$ axis ($\hat{\tilde{S}}_{z,\mathrm{tog}}(t) = f_x^{\mathrm{OH}}(t)\hat{\tilde{S}}_x + f_y^{\mathrm{OH}}(t)\hat{\tilde{S}}_y$) (Figure 5.2a). Note that $f_z^{\mathrm{OH}}(t) = 0$ for all intervals. Since the externally-applied square-wave RF field is constant for each half-sequence period, we can replace $B^{\mathrm{RF}}(t)$ with the amplitude $B^{\mathrm{RF}}$ and transfer the time dependence to $f_{x,y}^{\mathrm{OH}}$ by applying sign flips, thus leading to redefined modulation functions $f_{x,y}^{\mathrm{RF}}$ (Figure 5.2a).

The spin-7/2 $^{51}$V ion exhibits three distinct transitions at frequencies $\omega_{a,b,c}$ (Figure 5.1a). In the following, we consider an effective spin-1/2 system for the $^{51}$V ions using the $\omega_c$ manifold, $\{|\uparrow\rangle = |\pm 5/2\rangle, |\downarrow\rangle = |\pm 7/2\rangle\}$, with $\hat{\tilde{I}}_x = \frac{1}{2}\left(|\uparrow\rangle\langle\downarrow| + |\downarrow\rangle\langle\uparrow|\right)$, $\hat{\tilde{I}}_y = \frac{1}{2i}\left(|\uparrow\rangle\langle\downarrow| - |\downarrow\rangle\langle\uparrow|\right)$ and $\hat{\tilde{I}}_z = \frac{1}{2}\left(|\uparrow\rangle\langle\uparrow| - |\downarrow\rangle\langle\downarrow|\right)$. In a rotating frame with respect to the target frequency $\omega_c$, the nuclear spin operators become $\hat{\tilde{I}}_x \to \hat{\tilde{I}}_x\cos(\omega_c t) + \hat{\tilde{I}}_y\sin(\omega_c t)$ and $\hat{\tilde{I}}_z \to \hat{\tilde{I}}_z$. Thus, the leading-order average Hamiltonian, $\hat{H}_{\mathrm{avg}} = \frac{1}{2\tau}\int_0^{2\tau} dt\ \hat{H}_{\mathrm{tog}}(t)$, in the rotating frame is given by:

$$\begin{aligned}\hat{H}_{\mathrm{avg}} = \sum_{i\in\mathrm{register}} \frac{a_x\sqrt{7}}{2\tau}\int_0^{2\tau} dt\Big\{ \\ B_z^{\mathrm{OH}}\Big[f_x^{\mathrm{OH}}(t)\hat{\tilde{S}}_x + f_y^{\mathrm{OH}}(t)\hat{\tilde{S}}_y\Big]\Big[\hat{\tilde{I}}_x^{(i)}\cos(\omega_c t) + \hat{\tilde{I}}_y^{(i)}\sin(\omega_c t)\Big] + \\ B^{\mathrm{RF}}\Big[f_x^{\mathrm{RF}}(t)\hat{\tilde{S}}_x + f_y^{\mathrm{RF}}(t)\hat{\tilde{S}}_y\Big]\Big[\hat{\tilde{I}}_x^{(i)}\cos(\omega_c t) + \hat{\tilde{I}}_y^{(i)}\sin(\omega_c t)\Big]\Big\}.\end{aligned} \tag{5.7}$$

Here, various terms are excluded as they time average to zero (rotating-wave approximation). The $\sqrt{7}$ prefactor comes from mapping the original spin-7/2 operators

to the effective spin-1/2 ones. Additionally, the energy shift induced by $B_z^{\mathrm{OH}}$ and time-dependent $B^{\mathrm{RF}}$ is cancelled. The Fourier transforms of the modulation functions $f_{x,y}(t)$, termed the filter functions [227], directly reveal resonance frequencies at which equation (5.7) yields non-zero contributions (Figure 5.2b). Resonant interactions with strength proportional to the nuclear Overhauser field are achieved at sequence periods $2\tau$ which satisfy $\frac{1}{2\tau} = \frac{\omega_c}{2\pi\times 2}, \frac{\omega_c}{2\pi\times 4}, \frac{\omega_c}{2\pi\times 6}, \cdots$; interactions proportional to the RF field occur at sequence periods satisfying $\frac{1}{2\tau} = \frac{\omega_c}{2\pi\times 1}, \frac{\omega_c}{2\pi\times 3}, \frac{\omega_c}{2\pi\times 5}, \cdots$. Critically, these two sets of resonances occur at different values of $2\tau$, hence we can preferentially utilize the coherent, RF-induced interactions whilst decoupling from those induced by the randomized Overhauser field. We also note that the $\omega_a$ transition cannot be independently addressed by the ZenPol sequence due to the multiplicity of the three $^{51}$V transitions determined by the quadratic Hamiltonian ($\omega_a = \omega_b/2 = \omega_c/3$).

To achieve a targeted interaction with the $\omega_c$ transition, we use the RF-driven resonance identified at $\frac{1}{2\tau} = \frac{\omega_c}{2\pi\times 5}$ by setting the free-evolution interval to $\frac{\tau}{4} = \frac{5\pi}{4\omega_c}$. Under this resonance condition, the average Hamiltonian (equation (5.7)) is simplified to

$$\begin{aligned}
\hat{H}_{\mathrm{avg}} &= \sqrt{7}\left(\frac{1+\sqrt{2}}{5\pi}\right) a_x B^{\mathrm{RF}} \times \sum_{i\in\mathrm{register}} \left( (\hat{\tilde{S}}_x + \hat{\tilde{S}}_y)\hat{\tilde{I}}_x^{(i)} + (-\hat{\tilde{S}}_x + \hat{\tilde{S}}_y)\hat{\tilde{I}}_y^{(i)} \right) \\
&= \sqrt{7}\left(\frac{\sqrt{2}+2}{5\pi}\right) a_x B^{\mathrm{RF}} \sum_{i\in\mathrm{register}} \left( \hat{\tilde{S}}'_x \hat{\tilde{I}}_x^{(i)} + \hat{\tilde{S}}'_y \hat{\tilde{I}}_y^{(i)} \right) \\
&= b_{(5,\omega_c)} B^{\mathrm{RF}} \sum_{i\in\mathrm{register}} \left( \hat{\tilde{S}}'_+ \hat{\tilde{I}}_-^{(i)} + \hat{\tilde{S}}'_- \hat{\tilde{I}}_+^{(i)} \right).
\end{aligned}$$

Here, going from the first to the second line, we change the local $^{171}$Yb basis by rotating 45 degrees around the $z$-axis such that $\hat{\tilde{S}}'_x = (\hat{\tilde{S}}_x + \hat{\tilde{S}}_y)/\sqrt{2}, \hat{\tilde{S}}'_y = (-\hat{\tilde{S}}_x + \hat{\tilde{S}}_y)/\sqrt{2}$, and from the second to the third line, $\hat{\tilde{S}}'_\pm = \hat{\tilde{S}}'_x \pm i\hat{\tilde{S}}'_y$ and $\hat{\tilde{I}}_\pm = \hat{\tilde{I}}_x \pm i\hat{\tilde{I}}_y$ are used. We define the coefficient $b_{(k,\omega_j)}$ which determines the interaction strength for the $k^{\mathrm{th}}$ resonance addressing transition $\omega_j$ (for example, $b_{(5,\omega_c)} = \sqrt{7}(\sqrt{2}+2)a_x/10\pi$). Hereafter, we omit the primes on the $^{171}$Yb qubit operators for the sake of notational simplicity. The same analysis can be performed for other transitions, yielding a similar spin-exchange Hamiltonian, albeit with different interaction strength given by $b_{(k,\omega_j)}B^{RF}$.

Combining this effective Hamiltonian with the dynamics discussed in the previous section, we identify the spin-exchange rate to be $J_{\mathrm{ex}} = 2\sqrt{N}B^{\mathrm{RF}}b_{(k,\omega_j)} = 4B^{\mathrm{RF}}b_{(k,\omega_j)}$.

We note that while the nuclear spin can stochastically occupy either the $\{|+m_I\rangle\}$ or $\{|-m_I\rangle\}$ manifold of states, our protocol is insensitive to this sign. We emphasize that the ZenPol sequence operates at zero magnetic field where a long $^{171}$Yb coherence time can be maintained; it is insensitive to the presence of random noise from the bath; and is also robust against pulse rotation errors.

*Chapter 6*

# NUCLEAR SPIN REGISTER EXPERIMENTAL RESULTS

## 6.1 Introduction

In this section we will present experimental results implementing the protocols discussed in the previous chapter. This will involve first performing spectroscopy of the nuclear spin environment and identifying transitions associated with the isolated register and more distant bath ions. Next, we will polarize the register ions, thereby preparing them into the initial state $|0_v\rangle$. We will examine various aspects of the spin exchange dynamics between this polarized ensemble and the Yb qubit. We will then demonstrate quantum information storage in the register ensemble and examine different methods of extending the register coherence time. Finally, we will demonstrate preparation and measurement of joint Yb-V Bell states, which serve as vital components of the quantum repeater protocol.

## 6.2 ZenPol Spectroscopy

We use the ZenPol sequence to perform spectroscopy of the $^{171}$Yb nuclear spin environment. Figure 6.1 shows a ZenPol spectrum obtained by initializing the $^{171}$Yb into $|0_g\rangle$, applying an $M = 30$ period ZenPol sequence with variable inter-pulse spacing ($\tau/4$) followed by $^{171}$Yb population readout. We anticipate resonant interactions when the following condition is satisfied:

$$\frac{1}{2\tau} = \frac{\omega_j}{2\pi k}, \tag{6.1}$$

where $\omega_j$ with $j = a,\ b,\ c$ is the frequency of a given nuclear spin transition.

As a result of the engineered, coherent, RF-induced exchange interaction, we find that the $|0_g\rangle$ population decreases at $\tau$ values corresponding to the odd-$k$ $^{51}$V resonances (red line, Figure 6.1). Even-$k$ resonances are also observed even in the absence of the RF field, and are associated with incoherent interaction generated by the random nuclear Overhauser field (blue line, Figure 6.1). As discussed previously, since the coherent, RF-induced interactions are spectrally resolved (occur at different pulse spacing) we can mitigate the effect of incoherent interaction by only working with the odd $k$ resonances. The addressed transition and resonance orders are labelled above each resonance dip. Note the degeneracy for certain resonances resulting from $\omega_a = \omega_b/2 = \omega_c/3$ due to the quadratic Hamiltonian.

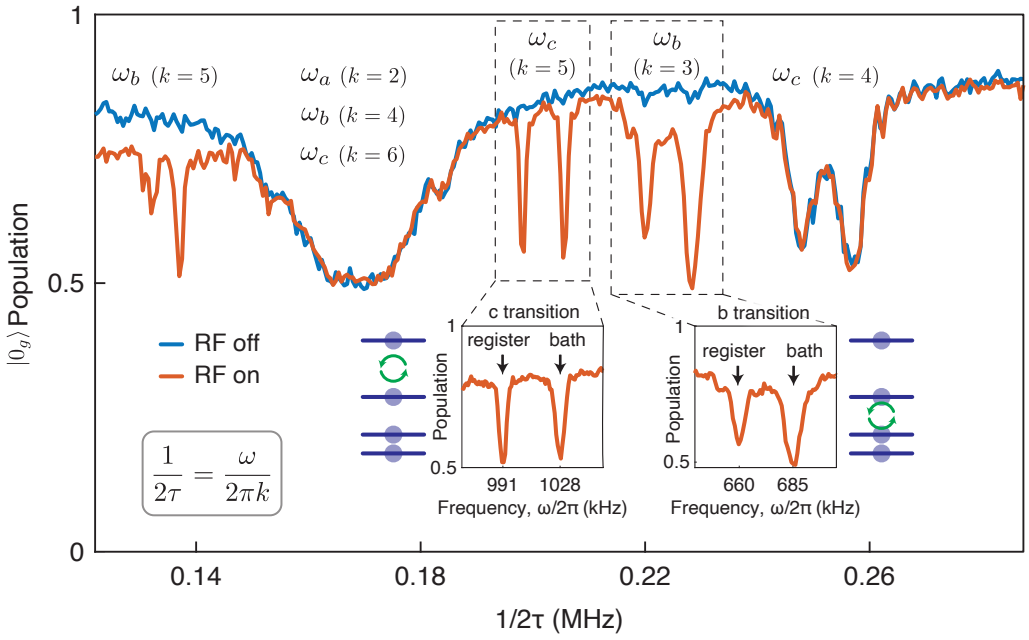


Figure 6.1: ZenPol sequence spectroscopy, using $M = 30$ and $B^{\mathrm{RF}} = 0.6$ G. $^{171}$Yb–$^{51}$V resonance is achieved for a given $^{51}$V transition, $\omega_j$, when $1/2\tau = \omega_j/2\pi k$ with integer $k$. We use the isolated, RF-induced $\omega_c$ $(k = 5)$ and $\omega_b$ $(k = 3)$ transitions to interact with the nuclear spins of neighbouring $^{51}$V ions (dashed boxes). Split-resonance features are attributed to two distinct $^{51}$V ensembles: the four $^{51}$V register spins experience a frozen-core detuning relative to the more distant bath.

In particular, we note that all odd-$k$ resonances are split near each isolated $^{51}$V transition (dotted boxes, Figure 6.1). For example, resonance frequencies of {660 kHz, 685 kHz} and {991 kHz, 1028 kHz} are identified around the $\omega_b$ $(k = 3)$ and $\omega_c$ $(k = 5)$ transitions, respectively. In both cases, the higher-frequency resonance agrees well with values extracted using NMR on $YVO_4$ crystals [203]. We therefore postulate the presence of two nuclear spin ensembles: a distant large ensemble with unperturbed frequency (constituents of the bath) and a local ensemble with a frequency shift due to the modified electric field distribution in the vicinity of the $^{171}$Yb ion (the register). The line-widths of the register resonances are limited by that of the filter function.

### 6.3 Nuclear Spin Polarization

Polarization of the nuclear spin register relies on repeated application of the ZenPol sequence, resonant with a targeted transition, interleaved with re-initialization of the $^{171}$Yb qubit leading to unidirectional transfer of $^{51}$V population.

Polarization dynamics are explored using the PROPI method (polarization readout by polarization inversion) [234]. This sequence uses the back-action of the $^{51}$V spins on the $^{171}$Yb to measure the register polarization after successive ZenPol polarization cycles. For instance, when polarizing into $|\uparrow\rangle = |\pm 5/2\rangle$ on the $\omega_c$ transition, the $^{171}$Yb is initialized into $|1_g\rangle$ and undergoes spin exchange with any $^{51}$V population in $|\downarrow\rangle = |\pm 7/2\rangle$. The $^{171}$Yb $|0_g\rangle$ population after interaction is therefore related to the residual $^{51}$V $|\downarrow\rangle$ population. As presented in Figure 6.2a, we measure the $^{171}$Yb population after each of 20 consecutive polarization cycles and observe a saturation after 10 cycles, indicating that the $^{171}$Yb polarization has been transferred to the $^{51}$V register. The high-contrast signal obtained in this measurement is enabled by alternating the $^{51}$V polarization direction, i.e., periods of polarization into $|\uparrow\rangle$ are interleaved with periods of polarization into $|\downarrow\rangle$. This mitigates the need to wait for slow register thermalization ($T_1^{(0)} = 0.54\ s$, see Section 6.6) between consecutive experiment repetitions. These measurements are repeated with ZenPol sequences on the $\omega_b$ transition, demonstrating similar levels of polarization saturation after approximately 10 cycles (Figure 6.2b).

These results inform the design of polarization sequences used in subsequent single-spin excitation experiments where 40 polarization cycles interleaved between the $\omega_b$ and $\omega_c$ transitions are sufficient to polarize the register into $|0_v\rangle = |\downarrow\downarrow\downarrow\downarrow\downarrow\rangle$. Based on simulations discussed in Section 6.4 we estimate this protocol achieves $\approx 84\%$ single spin polarization fidelity into the $|\downarrow\rangle$ state. Note that we do not use the ZenPol sequence to directly polarize the $\omega_a$ transition due to spectral overlap with $\omega_b$ and $\omega_c$, i.e., an attempt to use ZenPol on $\omega_a$ would lead to unintentional population redistribution on $\omega_b$ and $\omega_c$. We postulate that the high degree of polarization can still be achieved even in the absence of direct $\omega_a$ transition control due to two factors:

1. The thermalization timescale of the $\omega_a$ transition is significantly shorter than the interrogation time. Specifically, our experiments typically run for several minutes whereas the $\omega_a$ thermalization rate is likely similar to $T_1^{(0)} = 0.54$ s. Thus, undesired population in the $|\pm 1/2\rangle$ level can still pumped to $|\pm 7/2\rangle$ once it relaxes to $|\pm 3/2\rangle$.

2. Once successfully initialized into the $\omega_c$ manifold the probability of shelving into the $|\pm 1/2\rangle$ level is small as it necessitates two consecutive decays on the $\omega_b$ and $\omega_a$ transitions, both of which are considerably slower than our experiment/polarization repetition rate (20 ms).

We tried to improve the polarization fidelity by incorporating driving on the $\omega_a$ transition (using the method in Section 6.5) during the polarization protocol, thus leading to fast population exchange between $|\pm 1/2\rangle$ and $|\pm 3/2\rangle$. However, there was no improvement to the contrast of the resulting spin exchange oscillations thereby indicating that shelving into $|\pm 1/2\rangle$ is not a limiting factor in our experiments.

We also note that pumping into dark states (such as the other single-spin excitation states, $\{|\alpha_v\rangle\,,\ |\beta_v\rangle\,,\ |\gamma_v\rangle\}$ identified in Section 6.6) is unlikely to be a limiting factor in the polarization fidelity. This is because our density matrix coherences decay on a considerably shorter timescale ($T_2^* = 58\ \mu$s) than the wait time between ZenPol polarizing cycles (170 $\mu$s). This leads to a sufficiently long time for population to be redistributed between dark states and bright, polarizable states during the polarization sequence.

Finally, we perform pump-probe spectroscopy where, after polarizing the register ensemble, we probe the nuclear spins using a ZenPol sequence with variable $\tau$ (as in Section 6.2). As we can see in Figures 6.2c and d (which compare ZenPol spectra with/without polarization), the $\omega_b$ and $\omega_c$ register transitions nearly completely disappear. Note that the resonances at 685 kHz and 1028 kHz are unaffected, corroborating the existence of two distinct $^{51}$V ensembles.

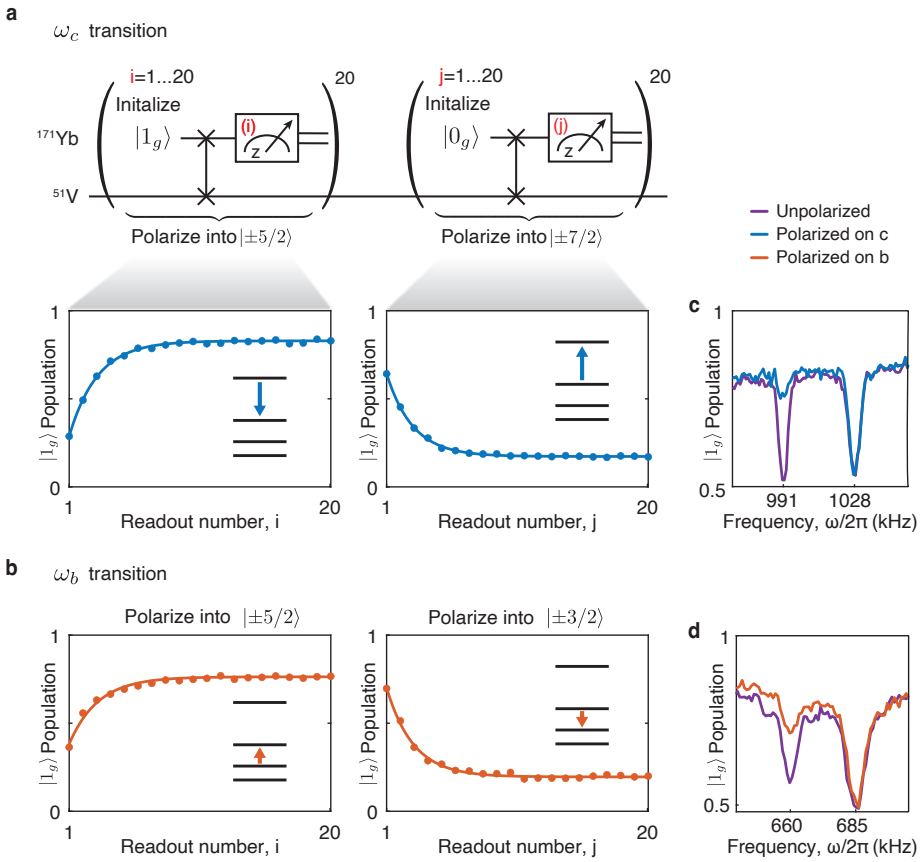


Figure 6.2: Polarization of multi-level nuclear register spins. a) Polarization readout by polarization inversion (PROPI) experiments for the $^{51}$V register $\omega_c$ transition. The PROPI sequence performs a repeated swap operation based on the ZenPol sequence, periodically interleaved with $^{171}$Yb qubit readout and re-initialization into $|1_g\rangle$. A total of 20 polarizing cycles are applied to the $\omega_c$ transition to polarize the $^{51}$V register into $|\pm5/2\rangle$. As a result of register polarization, the $^{171}$Yb population in $|1_g\rangle$ increases over time, indicating the accumulation of the $^{51}$V population in $|\pm5/2\rangle$ (left panel). We observe that the register polarization saturates after approximately 10 cycles. Subsequently, we perform repolarization cycles where $^{171}$Yb is initialized into $|0_g\rangle$ and $^{51}$V register spins are transferred to $|\pm7/2\rangle$ with similar saturation timescale (right panel). b) Equivalent measurements for the $\omega_b$ transition. The $^{51}$V register is polarized into $|\pm5/2\rangle$ ($|\pm3/2\rangle$), left panel (right panel). c) and d) After polarizing the $b$ and $c$ transitions, ZenPol spectroscopy reveals a near complete suppression of the register resonances and no change in the bath resonances. Purple lines are unpolarized spectra for reference.

## 6.4 Coherent Spin Exchange

After initializing all four register $^{51}$V spins into a polarized state $|0_v\rangle = |\downarrow\downarrow\downarrow\downarrow\rangle$, the ZenPol sequence (Figure 6.3) can also induce coherent oscillations of a single spin excitation between the $^{171}$Yb qubit and the polarized $^{51}$V ensemble.

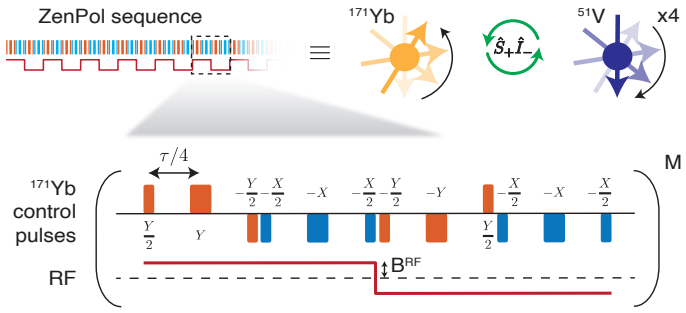


Figure 6.3: Engineered spin-exchange interactions via the ZenPol sequence. Equidistant $\pi/2$ and $\pi$ pulses combined with a square-wave RF magnetic field with amplitude $B^{\mathrm{RF}}$ are applied to the $^{171}$Yb qubit. The sequence has period $2\tau$ and is repeated $M$ times.

Figure 6.4a shows the $^{171}$Yb population as a function of sequence period, $M$, when the single-spin exchange is targeted at the $\omega_c$ transition (by fixing the ZenPol period to $2\tau = 5.048\ \mu$s). With $^{171}$Yb initialized in $|1_g\rangle$, the quantum state evolves according to:

$$|\psi(t_M)\rangle = |1_g\rangle\,|0_v\rangle\cos(J_{\mathrm{ex}}t_M/2) - i\,|0_g\rangle\,|W_v\rangle\sin(J_{\mathrm{ex}}t_M/2) \tag{6.2}$$

with spin-exchange rate $J_{\mathrm{ex}} = 4b_{(5,\omega_c)}B^{\mathrm{RF}}$ (red, Figure 6.4a) and interrogation time $t_M = 2\tau M$. Note that when $J_{\mathrm{ex}}t_M = \pi$, the sequence realizes a swap gate (black arrow), whereby a single-spin excitation is completely transferred to the register, i.e., $|1_g\rangle\,|0_v\rangle \rightarrow |0_g\rangle\,|W_v\rangle$. Furthermore, $J_{\mathrm{ex}}$ can be accurately controlled by varying $B^{\mathrm{RF}}$, allowing for swap gate fidelity optimization. By contrast, with $^{171}$Yb initialized in $|0_g\rangle$, exchange interactions are forbidden and thus oscillations are suppressed (blue, Figure 6.4a).

In the following subsections we will examine different aspects of these spin exchange dynamics and provide detail on the simulations which we use to interpret our experimental results and extract the degree of register polarization.

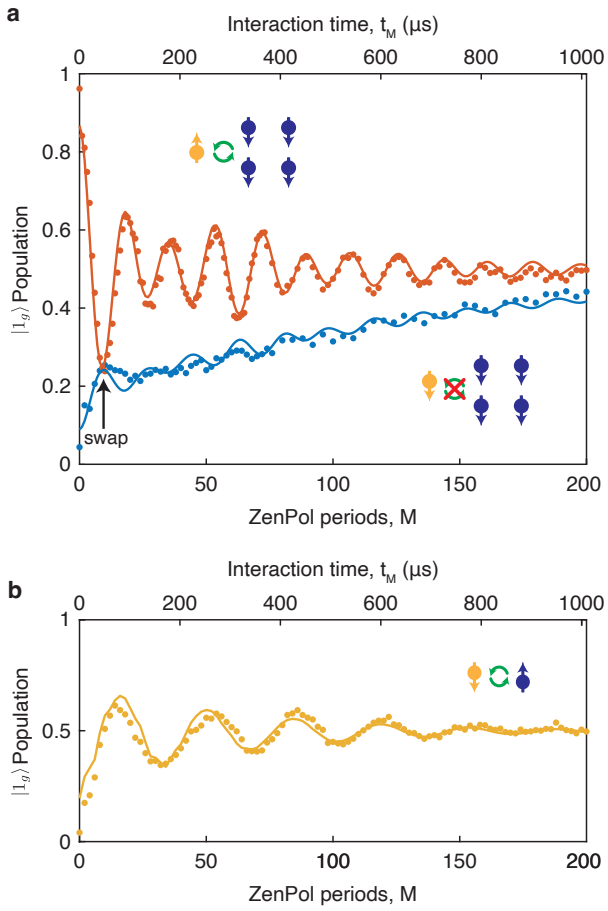


Figure 6.4: Spin exchange between $^{171}$Yb and $^{51}$V ions. a) The $^{171}$Yb qubit and $^{51}$V register spins are initialized into $|1_g\rangle$ and $|0_v\rangle$ ($\equiv |\downarrow\downarrow\downarrow\downarrow\rangle$), respectively. Our pulse sequence induces resonant spin exchange on the $\omega_c$ transition leading to oscillation between $|1_g\rangle\,|0_v\rangle \leftrightarrow |0_g\rangle\,|W_v\rangle$ where $|W_v\rangle$ is a spin-wave like W-state (red markers). Oscillation envelope beating arises from a residual $|\pm 5/2\rangle$ initial population. With $^{171}$Yb in $|0_g\rangle$ oscillations are suppressed (blue markers). A ZenPol sequence with $M = 10$ periods ($t_M = 50\ \mu$s) realizes a swap gate (black arrow). b) Spin-exchange dynamics with a single $^{51}$V nuclear spin. Three $^{51}$V spins are shelved in $|\pm 3/2\rangle$ and a single spin is prepared in $|\uparrow\rangle = |\pm 5/2\rangle$, leading to a reduced $\omega_c$ transition spin-exchange frequency. In a,b, equal values of $B^{\mathrm{RF}} = 1.6$ G are used and solid lines are from simulations with phenomenological decay constants.

**Collective Enhancement of Exchange Rate**

The spin-exchange rate is collectively enhanced by a factor of $\sqrt{N}$, where $N$ is the number of indistinguishable spins forming the register. We verify this by controlling the number of spins in the $\omega_c$ transition manifold and measuring the effect on $J_{\text{ex}}$.

Specifically, the ability to shelve population in different quadrupole levels enables the operation of the $^{51}$V register with an alternative set of many-body states: $|0'_v\rangle$ and $|1'_v\rangle$. For this experiment we polarize the $^{51}$V spins down the energy ladder on the $\omega_b$ and $\omega_c$ transitions leading to polarization primarily into the $|\pm 3/2\rangle$ level, with a small residual population in $|\pm 1/2\rangle$. For the purpose of this analysis we will assume perfect polarization into $|\pm 3/2\rangle$; however we note that $\omega_a$ transition polarization would be required for this.

We prepare the register $|1'_v\rangle$ state by injecting a single spin excitation on the $\omega_b$ transition (i.e., from $|\pm 3/2\rangle \rightarrow |\uparrow\rangle = |\pm 5/2\rangle$), this is achieved using the corresponding ZenPol resonance at $\omega_b$, $k = 3$:

$$|1'_v\rangle = \frac{1}{2}\left(\left|\uparrow, \frac{3}{2}, \frac{3}{2}, \frac{3}{2}\right\rangle + \left|\frac{3}{2}, \uparrow, \frac{3}{2}, \frac{3}{2}\right\rangle + \left|\frac{3}{2}, \frac{3}{2}, \uparrow, \frac{3}{2}\right\rangle + \left|\frac{3}{2}, \frac{3}{2}, \frac{3}{2}, \uparrow\right\rangle\right). \tag{6.3}$$

Here we omit the $\pm$ sign in the state label for simplicity. Subsequently, we prepare the $^{171}$Yb in $|0_g\rangle$ and induce a spin exchange oscillation between $|\uparrow\rangle$ and $|\downarrow\rangle = |\pm 7/2\rangle$ via a ZenPol sequence resonant with the $\omega_c$ transition. The resulting time evolution is given by:

$$|\psi(t)\rangle = |0_g\rangle\,|1'_v\rangle \cos\left(\frac{J'_{\text{ex}}t}{2}\right) - i\,|1_g\rangle\,|0'_v\rangle \sin\left(\frac{J'_{\text{ex}}t}{2}\right) \tag{6.4}$$

where

$$|0'_v\rangle = \frac{1}{2}\left(\left|\downarrow, \frac{3}{2}, \frac{3}{2}, \frac{3}{2}\right\rangle + \left|\frac{3}{2}, \downarrow, \frac{3}{2}, \frac{3}{2}\right\rangle + \left|\frac{3}{2}, \frac{3}{2}, \downarrow, \frac{3}{2}\right\rangle + \left|\frac{3}{2}, \frac{3}{2}, \frac{3}{2}, \downarrow\right\rangle\right) \tag{6.5}$$

and $J'_{\text{ex}} = 2b_{(5,\omega_c)}B^{\text{RF}}$. Notice that the spin-exchange oscillation rate, $J'_{\text{ex}}$, no longer has a $\sqrt{N}$ rate enhancement; this is because every ket in the $|1'_v\rangle$ and $|0'_v\rangle$ states contains only a single spin in the $\omega_c$-transition manifold.

Experimental results for this protocol are shown in Figure 6.4b, where we find that the resulting exchange frequency is reduced by a factor of $\approx \sqrt{4}$ compared to the standard initialization method.[1] Based on this experimental result and our understanding of the $YVO_4$ lattice structure, this verifies our hypothesis that the register consists of the second-nearest shell of four equidistant $^{51}$V ions. This assumption is also supported by close agreement between experiment and numerical simulation.

[1] Note that the measurements in Figures 6.4a and b are performed with the same value of $B^{\text{RF}}$

We note that using the $\{|0'_v\rangle, |1'_v\rangle\}$ manifold of states for information storage would have several benefits. For instance, direct microwave driving of the register $\omega_c$ transition would lead to Rabi oscillation between $|0'_v\rangle$ and $|1'_v\rangle$ and could therefore be used to realize local gates in this basis. Additionally, a second spin excitation is not allowed in this scheme, therefore the ZenPol sequence reproduces a complete two-qubit swap gate regardless of the $^{171}$Yb state. For these reasons, we believe that there may be some advantages to working with the $\{|0'_v\rangle, |1'_v\rangle\}$ manifold if the state initialization fidelity into $|\pm 3/2\rangle$ can be improved via direct $\omega_a$ transition polarization. We leave this for future work.

**Interaction Frequency**

Analogous to the Rabi oscillation of a two-level system, the oscillation frequency and contrast of these spin exchange oscillations also depend on the detuning of the ZenPol sequence relative to the $^{51}$V transition. Specifically, we expect the following relations:

$$J_{\text{ex}}(\delta) = \sqrt{J_{\text{ex}}(0)^2 + \delta^2} \tag{6.6}$$

$$C(\delta) = \frac{J_{\text{ex}}(0)^2}{J_{\text{ex}}(0)^2 + \delta^2}. \tag{6.7}$$

Here $J_{\text{ex}}$ and $C$ are the spin-exchange frequency and oscillation contrast, respectively, and $\delta$ is the detuning of the ZenPol sequence resonance relative to a target nuclear spin transition. We polarize the register into $|0_v\rangle$ and measure the frequency detuning dependence of the spin-exchange oscillations in Figure 6.5b. These results agree well with the corresponding simulations shown in Figure 6.5a.

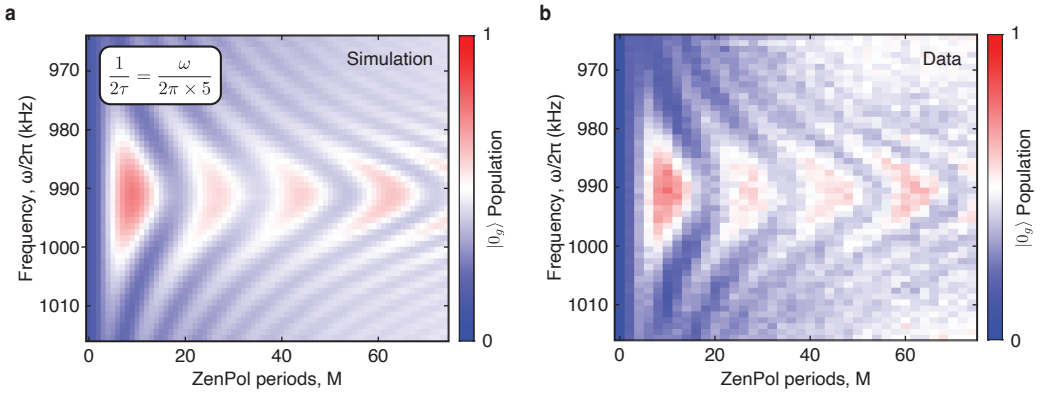


Figure 6.5: Spin-exchange dynamics near the $\omega_c$ transition at $k = 5$, probed as a function of sequence resonance frequency $\omega$ and the number of ZenPol periods, $M$. a) Simulation results. b) Measured spin-exchange dynamics showing good agreement with the numerical simulation in a.

**Polarization**

We demonstrate the effect of incomplete register polarization on the spin-exchange oscillation by varying the number of polarization cycles on the $\omega_b$ and $\omega_c$ transitions prior to each experiment (Figure 6.6a). As expected, we see that coherent spin-exchange oscillations emerge as an increasing number of polarization cycles are applied.

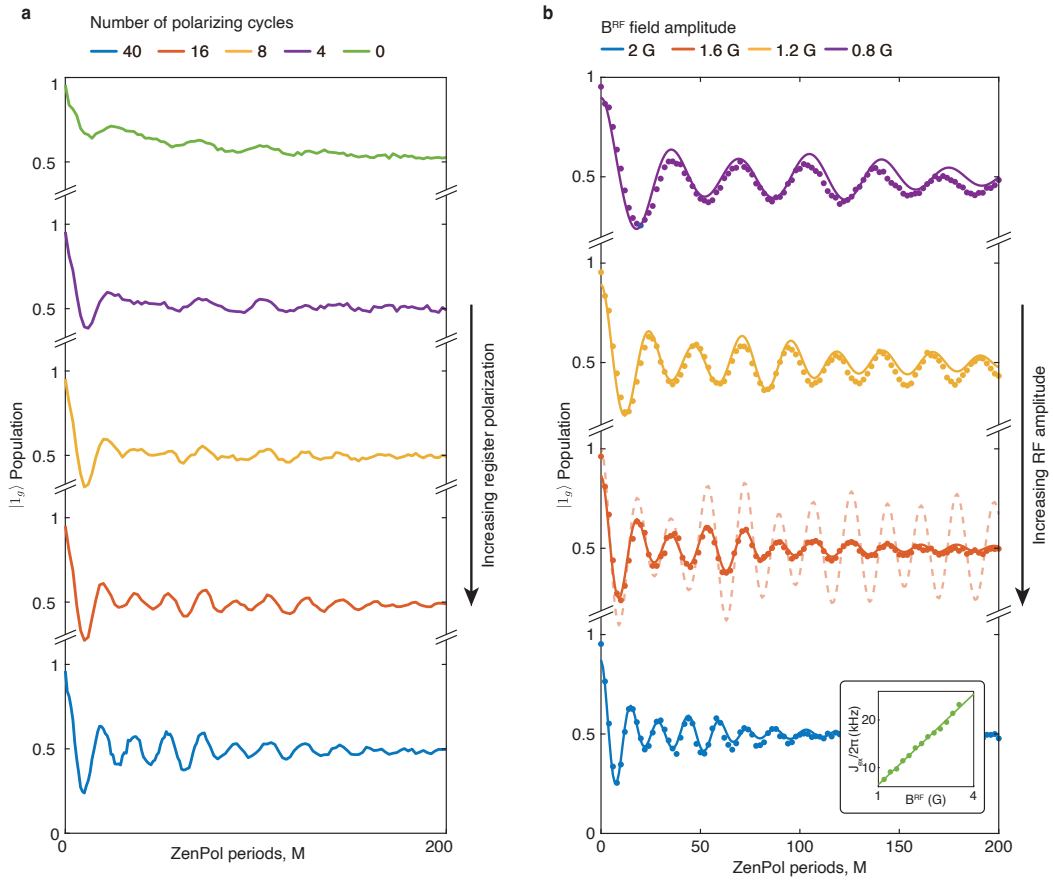


Figure 6.6: Spin exchange dynamics. a) Experimental results of ZenPol spin-exchange with varying degree of $^{51}$V register polarization. As the number of polarization cycles used to prepare $|0_v\rangle = |\pm 7/2\rangle^{\otimes 4}$ increases, the subsequent spin-exchange oscillations become more pronounced. b) Experimental demonstration of tunable spin-exchange rate by varying $B^{\mathrm{RF}}$. When increasing $B^{\mathrm{RF}}$ from 0.8 G to 2.0 G, we observe a corresponding linear increase in the spin-exchange rate. In all cases, numerical simulations (solid lines) show reasonable agreement with the experimental data (markers). A simulation result without a phenomenological exponential decay (dashed line) displays a discrepancy, which needs further investigation.

**Exchange Rate**

We also demonstrate control of the spin exchange frequency by varying the RF magnetic field amplitude ($B^{\mathrm{RF}}$). Figure 6.6b shows the spin-exchange dynamics for four different values of $B^{\mathrm{RF}}$ = 0.8 G, 1.2 G, 1.6 G and 2.0 G. The inset plots extracted spin exchange frequencies $J_{\mathrm{ex}}$ for a range of different $B^{\mathrm{RF}}$ demonstrating linear dependence as expected. This leads to accurate control of the engineered interaction strength enabling optimization of the swap gate.

**Simulating Spin Exchange**

We simulate our coupled spin system using the effective Hamiltonian derived in Section 4.2; however, we add three additional terms:

1. Nuclear Zeeman interactions of the $^{51}$V register spins with the Overhauser field from the bath: Since the energy levels are quantized along the $z$-axis, magnetic fluctuations along the $z$-direction dominate, which can be captured by the following Hamiltonian

$$\hat{H}_{\mathrm{nz}} = \sum_{i \in \mathrm{register}} \mu_N g_{vz} B_z^{\mathrm{OH}}(\mathbf{r}_i)\, \hat{I}_z^{(i)} \tag{6.8}$$

   where $B_z^{\mathrm{OH}}(\mathbf{r}_i)$ is the $z$-component of the Overhauser field evaluated at the position of the $i^{\mathrm{th}}$ register ion, $\mathbf{r}_i$.

2. Nuclear magnetic dipole-dipole interactions of the register spins:

$$\hat{H}_{\mathrm{ndd}} = \sum_{\substack{i,j \in \mathrm{register} \\ i<j}} \frac{\mu_0}{4\pi} \left[ \frac{\boldsymbol{\mu}_V^{(i)} \cdot \boldsymbol{\mu}_V^{(j)}}{r_{ij}^3} - \frac{3(\boldsymbol{\mu}_V^{(i)} \cdot \mathbf{r}_{ij})(\boldsymbol{\mu}_V^{(j)} \cdot \mathbf{r}_{ij})}{r_{ij}^5} \right] \tag{6.9}$$

   with $\mathbf{r}_{ij}$ the displacement vector between $^{51}$V register spins at sites $i$ and $j$.

3. $^{171}$Yb-enhanced register spin-spin interactions: These terms are derived by considering second-order perturbations using the Schrieffer-Wolff transformation (see Section 4.3). For example, the dominant Ising-type terms take the form

$$\hat{H}_{\mathrm{edd}} = \sum_{i,j \in \mathrm{register}} \frac{1}{2\omega_{01}} \left[ \left(3n^2 - 1\right) \frac{\mu_0 \mu_N \gamma_z g_{vz}}{4\pi r^3} \right]^2 \hat{\tilde{S}}_z \hat{I}_z^{(i)} \hat{I}_z^{(j)}, \tag{6.10}$$

   where $r$ and $n$ are the magnitude and $z$-direction cosine of the $^{171}$Yb–$^{51}$V register ion displacement vector. However, we note that the ZenPol sequence cancels these interactions to first order.

By simulating $^{171}$Yb Ramsey coherence times we extract $g_{vz} \approx 1.6$. We note that estimation of the bare $^{51}$V coherence time indicates a potential discrepancy in this value by up to 25%, discussed further in Section 6.5; however, this has a negligible impact on the ZenPol sequence simulations. We obtain an estimate for $g_{vx} \approx 0.6$ by calibrating the RF field amplitude and comparing with the experimental results of direct $^{51}$V spin driving in Figure 6.9.

We compute the nuclear Overhauser field $B_z^{\mathrm{OH}}$ according to equation (4.3) by randomly sampling the bath states for each Monte-Carlo simulation repetition. We include a simple model of the bath dynamics by incorporating stochastic jumps of the bath spins on magnetic-dipole allowed transitions.

We simulate the register spin dynamics in a reduced Hilbert space by considering only the $\omega_c$ manifold. This enables fast simulation of all four register spins plus the $^{171}$Yb qubit transition (Hilbert space with dimension 32). Imperfect polarization of the $^{51}$V register into $|\downarrow\rangle = |\pm 7/2\rangle$ is categorized into two distinct types:

1. Imperfect polarization within the $\omega_c$ transition, i.e., a small residual population $\epsilon_1$ in $|\uparrow\rangle = |\pm 5/2\rangle$.

2. Imperfect polarization outside the $\omega_c$ manifold, i.e., a small residual population $\epsilon_2$ in $|\pm 1/2\rangle$ and $|\pm 3/2\rangle$.

This leads to a $|\downarrow\rangle$ population of $1 - \epsilon_1 - \epsilon_2$. We incorporate incomplete polarization by sampling different register initial states for each Monte-Carlo repetition. For case 1, this involves occasionally initializing a given $^{51}$V ion into $|\uparrow\rangle$, while for case 2 this involves reducing the Hilbert space dimension by removing the $^{51}$V ion from the simulation. We note that our assumption of a mixed $^{51}$V register initial state is justified by the relatively short density matrix coherence decay time ($T_2^* = 58\ \mu$s). In experimental sequences we wait for 1.7 ms after $^{51}$V register polarization which ensures this condition is met. We also take into account finite pulse duration effects by modeling the ZenPol sequence using 25 ns $\pi/2$ and 50 ns $\pi$ pulses.

As shown in Figure 6.6b, the spin-exchange oscillations from numerical simulation (red dashed line) exhibit slower decay than the measured experimental results (red markers). We add a phenomenological exponential decay envelope, $ce^{-M/\tau_M}$, to the simulation results where $c$ and $\tau_M$ are free parameters, and $M$ is the ZenPol sequence period. The additional decay could be caused by heating due to the RF field, excess $^{171}$Yb dephasing or additional register spin interactions which we have not

considered here. We fit this model by optimizing multiple parameters: $\epsilon_1$, $\epsilon_2$, $B^{\mathrm{RF}}$, $c$ and $\tau_M$. The resulting values of $\epsilon_1$ and $\epsilon_2$ are 0.12 and 0.04, respectively, indicating $\approx 84\%$ polarization into $|\downarrow\rangle$; the RF magnetic field amplitude is $B^{\mathrm{RF}} \approx 1.6$ G and the phenomenological exponential decay parameters are $c = 0.8$ and $\tau_M = 90$ leading to a close fit with the experimental results (red solid line, Figure 6.4a and Figure 6.6b). Additional simulation results following this methodology with varying $\tau$ are presented in Figure 6.5.

Finally, we model the results with a single-spin excitation in the $\omega_c$-manifold by including the $|\pm 3/2\rangle$ level in the simulation (Figure 6.4b). The initial state used in this simulation is partially polarized between the $|\pm 3/2\rangle$ level with population $1-\epsilon$ and the $|\pm 1/2\rangle$ level with population $\epsilon$. We use the same value of $B^{\mathrm{RF}} = 1.6$ G as in Figure 6.4a, and optimize the polarization level leading to $1-\epsilon = 0.8$. The close correspondence between the measured and simulated oscillation profiles suggests that the register does indeed consist of the second shell of four homogeneously coupled $^{51}$V ions.

## 6.5 Quantum Information Storage

To evaluate the performance of the $^{51}$V register as a quantum memory, we characterize its information storage times under various conditions. Specifically, we first transfer a superposition state from the $^{171}$Yb qubit, $\frac{1}{\sqrt{2}}\left(|0_g\rangle + i\,|1_g\rangle\right)$, to the $^{51}$V register via the ZenPol-based swap gate. Subsequently, the transferred state $\frac{1}{\sqrt{2}}\left(|0_v\rangle + |W_v\rangle\right)$ is stored for a variable wait time, $t$. Finally, we swap the state back to the $^{171}$Yb and measured along the $x$-axis, thereby probing the coherence of the retrieved state. The full pulse sequence for this experiment (including Yb initialization and register polarization) is depicted in Figure 6.7.

### Ramsey Coherence Time

First consider the case where we leave the system unperturbed during the wait time $t$, which is equivalent to a Ramsey coherence measurement. Figure 6.8a shows the experimental result where the coherence undergoes Gaussian decay with a $1/e$ time of $T_2^* = 58 \pm 4$ $\mu$s, predominantly limited by local magnetic field noise from two sources: a fluctuating $^{171}$Yb dipole moment ($^{171}$Yb Knight field) and the nuclear Overhauser field (as described in Section 4.4).

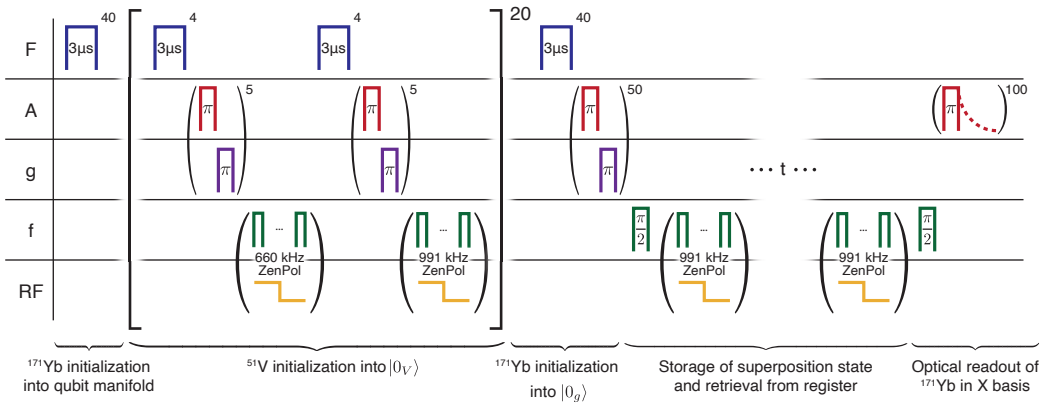


Figure 6.7: Pulse sequence detail for quantum information storage and retrieval experiments. After initializing the Yb into the qubit manifold, the nuclear spin register is polarized via repeated unidirectional spin exchange on the $b$ and $c$ transitions, interleaved with Yb qubit initialization. Subsequently, the Yb qubit is prepared in a superposition state which is swapped onto the register, stored for duration $t$ and then swapped back. Finally, the Yb coherence is read out.

### Decoupling from Knight Field

In Figure 6.8b, we decouple the V register from the Knight field by applying periodic $\pi$ pulses to the $^{171}$Yb. This flips its state between $|0_g\rangle$ and $|1_g\rangle$, thereby switching the sign of the Knight field and leading to the cancellation of $^{51}$V phase accumulation between successive free evolution periods, in a process analogous to motional narrowing [235]. This leads to an increased $1/e$ coherence time of $T_2^* = 225 \pm 9$ $\mu$s.

### Decoupling from Overhauser Field

In Figure 6.8c, we further extend the coherence time by performing dynamical decoupling on the $^{51}$V register to mitigate the decoherence effect of the nuclear Overhauser field. Specifically, during the wait time, $t$, we apply two $\pi$ pulses to the nuclear spins' $c$ transition (in addition to the Yb $\pi$ pulses used to decouple the Knight field). This leads to a significantly extended $1/e$ coherence time of $T_2 = 760 \pm 14$ $\mu$s. A detailed explanation of how we drive the nuclear spin $c$ transition for this dynamical decoupling sequence is provided later in this section. Note that even numbers of $^{51}$V $\pi$ pulses are necessary to return the register to the $\{|0_v\rangle, |W_v\rangle\}$ manifold prior to state retrieval.

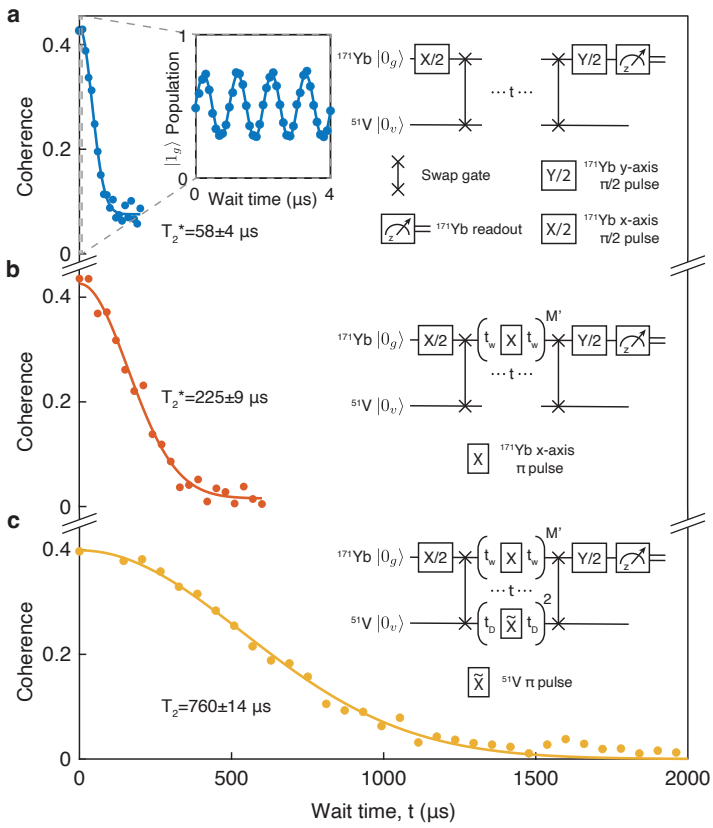


Figure 6.8: Quantum information storage in the nuclear spin-wave register. a) Ramsey coherence measurement with no decoupling during the wait time, $t$. Fast oscillations are observed at the $^{51}$V $\omega_c/2\pi = 991$ kHz frequency (inset) and the coherence is derived from the oscillation contrast. The coherence is normalized to have maximum value 1 when in a perfect superposition state and at $t = 0$ is limited by the swap gate fidelity. The resulting $1/e$ coherence decay time is measured to be $58 \pm 4$ $\mu$s. Note that the wait time excludes the swap gate duration. b) Coherence time extension via motional narrowing of the $^{171}$Yb Knight field. By applying $x$-axis $\pi$ pulses spaced by $2t_w = 6$ $\mu$s to the $^{171}$Yb qubit, the coherence time of the $^{51}$V register is extended to $225 \pm 9$ $\mu$s. c) Further coherence enhancement via dynamical decoupling of the $^{51}$V register. In addition to the $\pi$ pulses acting on $^{171}$Yb, two $\pi$ pulses are applied to the $^{51}$V register with a variable inter-pulse delay time, $2t_D$. This rephases contributions to the detuning from the nuclear Overhauser field and leads to an extended memory time of $760 \pm 14$ $\mu$s.

**Coherence Simulation**

We numerically simulate the register coherence times using the method outlined in Section 6.4. When limited by the $^{171}$Yb Knight field, simulation yields a Gaussian decay with a $1/e$ coherence time of 33 $\mu$s (equivalent to experimental results in Figure 6.8a). We also predict an upper bound for the coherence time when decoupled from the $^{171}$Yb Knight field by turning off Hamiltonian terms associated with equation (4.11), yielding an extended Gaussian decay of 417 $\mu$s (equivalent to experimental results in 6.8b). These simulated values are consistent with the corresponding experimental results (58 ± 4 $\mu$s and 225 ± 9 $\mu$s, respectively) to within a factor of two. We note that this could indicate an error in our estimation of $g_{vz}$ by up to 25%, potentially caused by a small discrepancy in the position of the two $^{51}$V bath spins closest to $^{171}$Yb. Further analysis of these parameters is left for future work.

**Nuclear Spin Driving**

Performing dynamical decoupling on the register requires selective driving of the froze-core $^{51}$V nuclear spins without perturbing the bath and is achieved through a two-fold mechanism. First, with the $^{171}$Yb qubit in $|0_g\rangle$ we apply a sinusoidal $z$-directed RF magnetic field at $\omega_c/2\pi = 991$ kHz through the coplanar waveguide to induce an oscillating $^{171}$Yb magnetic dipole moment (Figure 6.9a). This generates an $x$ or $y$-directed field component at each $^{51}$V spin, where the driving Hamiltonian is given by $\hat{H}_{\text{drive}} = \mu_N g_{vx} A_{x,y} B_z^{\text{osc}} \sin(\omega_c t) \hat{I}_{x,y}$ with $A_x = -3ln\mu_0\gamma_z^2/8\pi r^3\omega_{01}$ and $A_y = -3mn\mu_0\gamma_z^2/8\pi r^3\omega_{01}$. The lattice symmetry of the host leads to equidistant spacing of the four proximal $^{51}$V spins from the central $^{171}$Yb qubit allowing homogeneous coherent driving of all register spins.

In this direct driving scheme, we note that the effect of $B_z^{\text{osc}}$ is amplified by a factor of $|A_{x,y}| \approx 6.7$ for the frozen-core register spins at a distance of r = 3.9 Å. Crucially, the amplification factor scales as $A_{x,y} \propto 1/r^3$ with distance $r$ from the $^{171}$Yb qubit, leading to a reduced driving strength for distant $^{51}$V bath spins. Moreover, the transition frequency of the bath, $\omega_c^{\text{bath}}/2\pi = 1028$ kHz, is detuned by 37 kHz from that of the register, $\omega_c/2\pi = 991$ kHz, further weakening the bath interaction due to off-resonant driving provided that the Rabi frequency is less than the detuning.

In a rotating frame at frequency $\omega_c$, the driving Hamiltonian $\hat{H}_{\text{drive}}$ gives rise to Rabi oscillation dynamics of the register spins within the $\omega_c$ manifold, $\{|\uparrow\rangle = |\pm 5/2\rangle, |\downarrow\rangle = |\pm 7/2\rangle\}$. To calibrate $^{51}$V $\pi$ pulse times, we initialize the register into

$|0_v\rangle = |\downarrow\downarrow\downarrow\downarrow\rangle$, drive the register for variable time, and read out the $|0_v\rangle$ population by preparing the $^{171}$Yb qubit in $|1_g\rangle$ and applying a swap gate to the $\omega_c$ transition. If the final $^{51}$V spin state is in $|\downarrow\rangle$ ($|\uparrow\rangle$) the swap will be successful (unsuccessful) and the $^{171}$Yb qubit will end up in $|0_g\rangle$ ($|1_g\rangle$). Using this method, we induce resonant Rabi oscillations of the register at a Rabi frequency of $\Omega_D = 2\pi \times (7.65 \pm 0.05)$ kHz (blue markers, Figure 6.9c) which exhibit exponential decay on a $280 \pm 30$ $\mu$s timescale, limited by dephasing caused by the fluctuating $^{171}$Yb Knight field. This can be decoupled using motional narrowing techniques whereby we periodically apply $\pi$ pulses to the $^{171}$Yb every 6 $\mu s$ during the drive period. In order to drive the $^{51}$V spins in a phase-continuous manner, we compensate for the inversion of the $^{171}$Yb magnetic dipole moment after each $\pi$ pulse by applying a $\pi$ phase shift to the sinusoidal driving field (Figure 6.9b). This leads to an extended $1/e$ Gaussian decay time of $1040 \pm 70$ $\mu$s (red markers, Figure 6.9c).

The arrow in Figure 6.9c indicates the 69 $\mu$s $^{51}$V $\pi$ pulse time used for dynamical decoupling. In contrast to the spin-preserving exchange interaction, this direct drive protocol provides independent, local control of the four $^{171}$V spins with no constraints on the number of excitations, thereby coupling the $^{51}$V register to states outside the two-level manifold spanned by $|0_v\rangle$ and $|W_v\rangle$. For example, at odd multiple $\pi$ times, we find

$$|0_v\rangle \rightarrow |\uparrow\uparrow\uparrow\uparrow\rangle$$
$$|W_v\rangle \rightarrow \frac{(|\downarrow\uparrow\uparrow\uparrow\rangle + |\uparrow\downarrow\uparrow\uparrow\rangle + |\uparrow\uparrow\downarrow\uparrow\rangle + |\uparrow\uparrow\uparrow\downarrow\rangle)}{2},$$

both of which contain more than a single excitation. For this reason, we use an even number of $^{51}$V $\pi$ pulses in our decoupling sequences to always return the $^{51}$V register to the memory manifold prior to state retrieval.

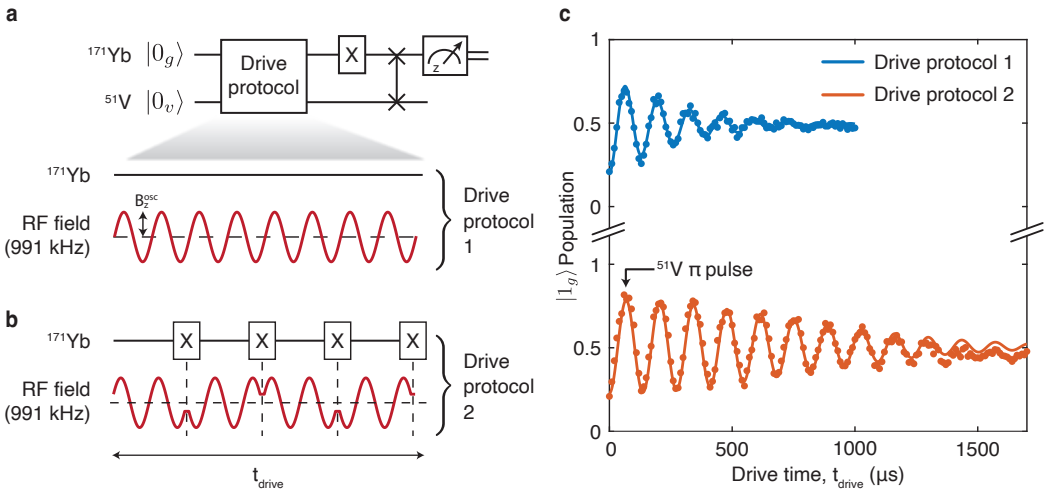


Figure 6.9: Direct $^{51}V$ nuclear spin driving. a) To directly drive the $^{51}$V nuclear spin $\omega_c$ transition, a sinusoidal $z$-directed RF magnetic field, $B_z^{\text{osc}} \sin(\omega_c t)$, is applied to the system at a frequency of $\omega_c/2\pi = 991$ kHz (Drive Protocol 1). This induces an oscillating magnetic dipole moment on the $^{171}$Yb qubit which in turn generates an amplified transverse driving field at each $^{51}$V. Consequently, the four $^{51}$V register spins undergo independent Rabi oscillation. b) To improve the nuclear spin control fidelity, a train of equidistant $\pi$ pulses are applied to the $^{171}$Yb during the driving period, thereby cancelling dephasing due to the $^{171}$Yb Knight field (Drive Protocol 2). Each $\pi$ pulse is accompanied by a $\pi$ phase shift of the sinusoidal field to ensure phase continuity of the nuclear Rabi driving. c) Measured $^{51}$V register Rabi oscillations using the aforementioned schemes. The black arrow at $t \approx 69$ $\mu$s indicates the $^{51}$V $\pi$ pulse time.

## 6.6 $T_1$ Relaxation

We measure the population decay of both the $|0_v\rangle$ and $|W_v\rangle$ states (timescales $T_1^{(0)}$ and $T_1^{(W)}$, respectively) by preparing the $^{51}$V register in the appropriate state and waiting for a variable time, $t$, before swapping to the $^{171}$Yb for readout.

The $|0_v\rangle$ state exhibits slow exponential decay with $1/e$ time constant $T_1^{(0)} = 0.54 \pm 0.08$ s (Figure 6.10b). There are two contributions which could be limiting this decay:

1. Resonant population exchange between the register spins and unpolarized frozen-core 'dark spins.' For instance, the two nearest $^{51}$V ions (ions 1 and 2 in Table 2.1) may interact resonantly with the neighbouring register spins. However, we cannot detect or polarize these dark spins since they only interact with the $^{171}$Yb via Ising-like $\hat{S}_z\hat{I}_z$ terms.

2. Off-resonant population exchange between the register and detuned unpolarized bath spins.

As for the $|W_v\rangle$ state, it exhibits a Gaussian decay with a much faster $1/e$ time constant of $T_1^{(W)} = 39.5 \pm 1.3$ $\mu$s (Figure 6.10a). This can be explained by considering the effect of dephasing on the register spins. Specifically, the $|W_v\rangle$ state which our $^{171}$Yb qubit interacts with is given by

$$|W_v\rangle = \frac{1}{2}\left(|\uparrow\downarrow\downarrow\downarrow\rangle + |\downarrow\uparrow\downarrow\downarrow\rangle + |\downarrow\downarrow\uparrow\downarrow\rangle + |\downarrow\downarrow\downarrow\uparrow\rangle\right).$$

Crucially, there are three additional orthogonal states required to span the $^{51}$V register single excitation subspace:

$$|\alpha_v\rangle = \frac{1}{2}\left(|\uparrow\downarrow\downarrow\downarrow\rangle + |\downarrow\uparrow\downarrow\downarrow\rangle - |\downarrow\downarrow\uparrow\downarrow\rangle - |\downarrow\downarrow\downarrow\uparrow\rangle\right)$$
$$|\beta_v\rangle = \frac{1}{2}\left(|\uparrow\downarrow\downarrow\downarrow\rangle - |\downarrow\uparrow\downarrow\downarrow\rangle + |\downarrow\downarrow\uparrow\downarrow\rangle - |\downarrow\downarrow\downarrow\uparrow\rangle\right)$$
$$|\gamma_v\rangle = \frac{1}{2}\left(|\uparrow\downarrow\downarrow\downarrow\rangle - |\downarrow\uparrow\downarrow\downarrow\rangle - |\downarrow\downarrow\uparrow\downarrow\rangle + |\downarrow\downarrow\downarrow\uparrow\rangle\right).$$

We assume uncorrelated noise at each of the four $^{51}$V spins and apply a pure-dephasing master equation model. In the single excitation subspace, this becomes:

$$\dot{\rho} = 2\Gamma\left[\mathcal{D}\left(|\uparrow\downarrow\downarrow\downarrow\rangle\langle\uparrow\downarrow\downarrow\downarrow|\right) + \mathcal{D}\left(|\downarrow\uparrow\downarrow\downarrow\rangle\langle\downarrow\uparrow\downarrow\downarrow|\right)\right. \tag{6.11}$$
$$\left.+\mathcal{D}\left(|\downarrow\downarrow\uparrow\downarrow\rangle\langle\downarrow\downarrow\uparrow\downarrow|\right) + \mathcal{D}\left(|\downarrow\downarrow\downarrow\uparrow\rangle\langle\downarrow\downarrow\downarrow\uparrow|\right)\right]\rho \tag{6.12}$$

where the dephasing channel (Lindbladian) is given by

$$\mathcal{D}\left(\hat{a}\right)\rho = \hat{a}\rho\hat{a}^{\dagger} - \frac{1}{2}\{\hat{a}^{\dagger}\hat{a}, \rho\} \tag{6.13}$$

and $\Gamma$ is the dephasing rate on the $\omega_c$ transition of a single $^{51}$V spin. We solve this equation for different initial states $\rho(0)$. When $\rho(0) = |0_v\rangle\langle 0_v|$, dephasing does not contribute to $T_1^{(0)}$, i.e., $\rho(t) = \rho(0)$. However, when $\rho(0) = |W_v\rangle\langle W_v|$ the state evolves according to

$$\rho(t) = |W_v\rangle\langle W_v| e^{-2\Gamma t} + \frac{1}{4}\left(1 - e^{-2\Gamma t}\right)\mathbb{I}^{(\mathrm{SEM})} \tag{6.14}$$

where $\mathbb{I}^{(\mathrm{SEM})}$ is the single excitation manifold identity operator:

$$\mathbb{I}^{(\mathrm{SEM})} = |W_v\rangle\langle W_v| + |\alpha_v\rangle\langle\alpha_v| + |\beta_v\rangle\langle\beta_v| + |\gamma_v\rangle\langle\gamma_v|,$$

i.e., dephasing leads to decay of $|W_v\rangle$ into $\mathbb{I}^{(\mathrm{SEM})}$ at rate $2\Gamma$. For completeness we also consider the decay of the off-diagonal coherence term $\rho_{01} = \langle 0_v|\rho|W_v\rangle$ and find that

$$\rho_{01}(t) = \rho_{01}(0)e^{-\Gamma t}. \tag{6.15}$$

Essentially, the pure dephasing model predicts $T_2^* = 2T_1^{(W)}$ for our system.

We verify that dephasing is the main source of $|W_v\rangle$ population decay by demonstrating lifetime extension using the same motional narrowing approach employed to improve the coherence time. Specifically, during the wait time, we apply a series of $\pi$ pulses to the $^{171}$Yb separated by 6 $\mu$s leading to an extended lifetime of $T_1^{(W)} = 127 \pm 8$ $\mu$s (Figure 6.10a). We note that both the bare and motionally-narrowed $T_1^{(W)}$ and $T_2^*$ times are close to the $T_2^* = 2T_1^{(W)}$ limit identified above. We further extend the $T_1^{(W)}$ lifetime to $640 \pm 20$ $\mu$s using two $^{51}$V $\pi$ pulses applied during the wait time, thereby achieving dynamical decoupling from the nuclear Overhauser field.

Finally we note that if $T_1^{(W)}$ is limited by the $^{171}$Yb Knight field as a common noise source, there may be some discrepancy in the predictions of this model due to a high degree of noise correlation between the four $^{51}$V register spins arising from lattice symmetry. However, when performing motional narrowing we decouple the $^{171}$Yb Knight field and are likely limited by the, considerably less correlated, local Overhauser field. Further exploration of these correlated/uncorrelated fields is left for future work.

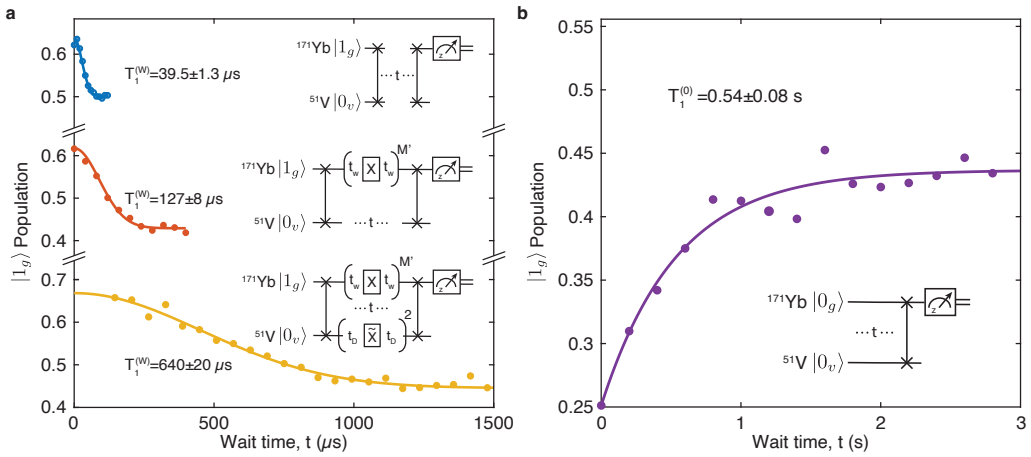


Figure 6.10: $^{51}$V spin register population relaxation. a) Measured relaxation timescales, $T_1^{(W)}$, of the entangled register state, $|W_v\rangle$, under various conditions. Top: with no dynamical decoupling we obtain $T_1^{(W)} = 39.5 \pm 1.3$ $\mu$s (blue trace), limited by dephasing of the entangled $|W_v\rangle$ state. Middle: the $T_1^{(W)}$ lifetime can be extended by motionally narrowing the $^{171}$Yb Knight field leading to an extended $1/e$ lifetime of $T_1^{(W)} = 127 \pm 8$ $\mu$s (red trace). Bottom: further extension of the $T_1^{(W)}$ lifetime via dynamical decoupling leads to $T_1^{(W)} = 640 \pm 20$ $\mu$s (yellow trace). b) The polarized register state $|0_v\rangle$ relaxation timescale is measured to be $T_1^{(0)} = 0.54 \pm 0.08$ s, likely limited by incoherent population transfer to the bath.

## 6.7 Population Basis Measurements

We develop a sequential tomography protocol [25] to read out the populations of the joint $^{171}$Yb–$^{51}$V density matrix $\rho$ in the effective four-state basis, $\{|0_g 0_v\rangle, |0_g W_v\rangle, |1_g 0_v\rangle, |1_g W_v\rangle\}$. This is achieved using two separate sequences: Readout sequence 1 and Readout sequence 2, applied alternately, which measure the $\{|0_g 0_v\rangle, |0_g W_v\rangle\}$ and $\{|1_g 0_v\rangle, |1_g W_v\rangle\}$ populations, respectively. As shown in Figure 6.11a, these sequences are distinguished by the presence (absence) of a single $\pi$ pulse applied to the $^{171}$Yb qubit at the start of the sequence. This is followed by a single optical readout cycle on the A transition; results are post-selected on detection of a single optical photon during this period. Hence the presence (absence) of the first $\pi$ pulse results in $|0_g\rangle$ ($|1_g\rangle$) state readout after post selection. Furthermore, in all post-selected cases the $^{171}$Yb qubit is initialized to $|1_g\rangle$ by taking into account this conditional measurement outcome. Subsequently, an unconditional $\pi$ pulse is applied to the $^{171}$Yb, preparing it in $|0_g\rangle$ and a swap gate is applied, thereby transferring the $^{51}$V state to the $^{171}$Yb. Finally, we perform single-shot readout of the $^{171}$Yb state according to the protocol developed in [155]. Specifically, we apply two sets of 100 readout cycles to the A transition separated by a single $\pi$ pulse which inverts the $^{171}$Yb qubit population. The $^{51}$V state is ascribed to $|W_v\rangle$ ($|0_v\rangle$) if $\geq 1$ (0) photons are detected in the second readout period and 0 ($\geq 1$) photons are detected in the third. We summarize the possible photon detection events and state attributions in Figure 6.11b.

We demonstrate this protocol by characterizing the state preparation fidelities of the four basis states. The measured histograms are presented in Figure 6.11c alongside the respective gate sequences used for state preparation. The resulting uncorrected (corrected) preparation fidelities for these four basis states are:

$$\begin{aligned}
\mathcal{F}_{|0_g 0_v\rangle} &= 0.79 \pm 0.01 \ (0.82 \pm 0.02), \\
\mathcal{F}_{|0_g W_v\rangle} &= 0.50 \pm 0.02 \ (0.64 \pm 0.02), \\
\mathcal{F}_{|1_g 0_v\rangle} &= 0.79 \pm 0.01 \ (0.82 \pm 0.02), \\
\mathcal{F}_{|1_g W_v\rangle} &= 0.50 \pm 0.02 \ (0.64 \pm 0.02).
\end{aligned}$$

We note that the reduced fidelity of $|0_g W_v\rangle$ and $|1_g W_v\rangle$ relative to $|0_g 0_v\rangle$ and $|1_g 0_v\rangle$ arises from the swap gate used for the $|W_v\rangle$ state preparation. The procedure for correcting readout infidelity is described in Appendix B.

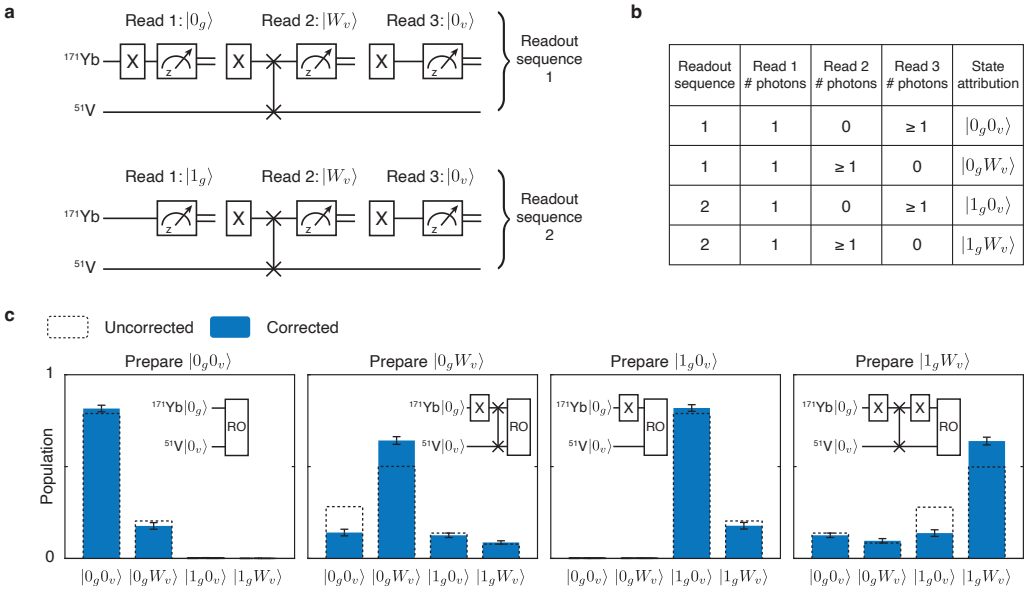


| Readout sequence | Read 1 # photons | Read 2 # photons | Read 3 # photons | State attribution |
|---|---|---|---|---|
| 1 | 1 | 0 | ≥ 1 | $\|0_g0_v\rangle$ |
| 1 | 1 | ≥ 1 | 0 | $\|0_gW_v\rangle$ |
| 2 | 1 | 0 | ≥ 1 | $\|1_g0_v\rangle$ |
| 2 | 1 | ≥ 1 | 0 | $\|1_gW_v\rangle$ |

Figure 6.11: Population measurement histograms for register fidelity characterization. a) Sequential tomography protocol for characterizing $^{171}$Yb–$^{51}$V populations in the basis spanned by $\{|0_g0_v\rangle, |0_gW_v\rangle, |1_g0_v\rangle, |1_gW_v\rangle\}$. b) Table summarizing the post-processing criteria for state attribution. c) Reconstructed population distributions for estimating state preparation fidelity. The four basis states, $\{|0_g0_v\rangle, |0_gW_v\rangle, |1_g0_v\rangle, |1_gW_v\rangle\}$, are independently prepared (see the insets of each subplot). Subsequently, the sequential tomography protocol for state readout (RO) is applied iteratively, alternating between Readout 1 and 2 sequences to fully reconstruct the population probability distributions.

## 6.8 Bell State Preparation and Measurement

We benchmark our multi-spin register by characterizing fidelities of $^{171}$Yb–$^{51}$V Bell state generation and detection, serving as a vital component of the quantum repeater protocol [33]. In particular, the maximally entangled Bell state $|\Psi^+\rangle = \frac{1}{\sqrt{2}}\left(|1_g\rangle|0_v\rangle - i|0_g\rangle|W_v\rangle\right)$ can be prepared by initializing the system in $|1_g\rangle|0_v\rangle$ and applying a $\sqrt{\text{swap}}$ gate based on the ZenPol sequence satisfying $J_{\text{ex}}t_M = \pi/2$ (equation (6.2)). The Bell state coherence is evaluated by waiting for a free evolution time $t$, during which a parity oscillation occurs between $|\Psi^+\rangle$ and its conjugate, $|\Psi^-\rangle = \frac{1}{\sqrt{2}}\left(|1_g\rangle|0_v\rangle + i|0_g\rangle|W_v\rangle\right)$ at the $\omega_c$ transition frequency [236] (Appendix C). Finally the coherence is measured via a second $\sqrt{\text{swap}}$ gate which maps the parity to $^{171}$Yb population. Figure 6.12a shows the measured parity oscillations decaying with a $1/e$ time of $T^*_{2,\text{Bell}} = 8.5 \pm 0.5$ $\mu$s, limited by the $T_2^*$ dephasing time of the $^{171}$Yb qubit [155]. To improve the coherence, we apply an XY-8 decoupling sequence [212] to the $^{171}$Yb which simultaneously extends the Yb coherence time and motionally narrows the Knight field. This leads to an enhanced value of $T^*_{2,\text{Bell}} = 239 \pm 6$ $\mu$s (Figure 6.12b); now limited by the Overhauser field interacting with the $^{51}$V register.

In order to estimate the Bell state preparation fidelity, defined as $\mathcal{F} = \langle\Psi^+|\rho|\Psi^+\rangle$, we perform a sequential tomography protocol [25] to reconstruct the density matrix $\rho$ in the effective manifold spanned by four states $\{|0_g0_v\rangle, |0_gW_v\rangle, |1_g0_v\rangle, |1_gW_v\rangle\}$ (Figure 6.11 and Appendix C). Taking into account errors in state readout, we obtain a corrected Bell state fidelity of 0.76±0.01, as summarized in Figure 6.12c (the uncorrected fidelity is measured to be 0.61±0.01). We speculate that this is limited by incomplete register initialization, imperfect Hamiltonian engineering and dephasing during Bell state generation (see Appendix C for a detailed explanation of fidelity estimation).

## 6.9 Register Reproducibility

We stress that utilizing the dense, lattice nuclear spins ensures near identical registers for all $^{171}$Yb ions. Figure 6.13 shows ZenPol spectra near the $\omega_c$ transition, collectively enhanced spin-exchange oscillations and motionally-narrowed $T_2^*$ times for three $^{51}$V registers coupled to three different $^{171}$Yb ions. The $^{171}$Yb optical and microwave frequencies were re-calibrated for each ion; however, all aspects of the experimental sequences related to register control and readout were identical. This demonstrates that the 4-spin V register is a deterministic quantum resource.

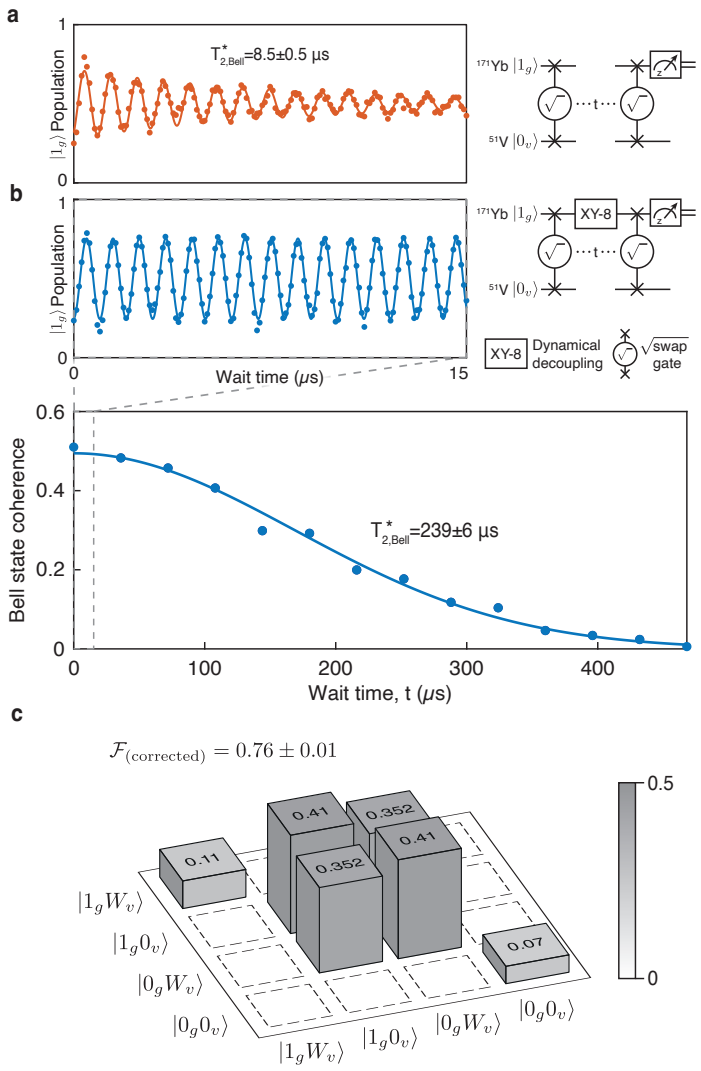


Figure 6.12: Characterization of maximally entangled $^{171}$Yb–$^{51}$V register Bell state. a) Parity oscillations between $|\Psi^+\rangle$ and $|\Psi^-\rangle$ revealing the Bell state coherence time with a $1/e$ decay timescale of $T^*_{2,\mathrm{Bell}} = 8.5 \pm 0.5$ $\mu$s. b) During the parity oscillation, we apply an XY-8 decoupling sequence to the $^{171}$Yb qubit. This leads to a significantly extended Bell state coherence time of $T^*_{2,\mathrm{Bell}} = 239 \pm 6$ $\mu$s. c) Reconstructed Bell state density matrix. Diagonal entries representing populations are extracted through a sequential tomography protocol. Off-diagonal matrix elements representing coherences are obtained from the parity oscillation contrast. Note that all density matrix values have been corrected to account for readout error, yielding a fidelity of $0.76 \pm 0.01$.

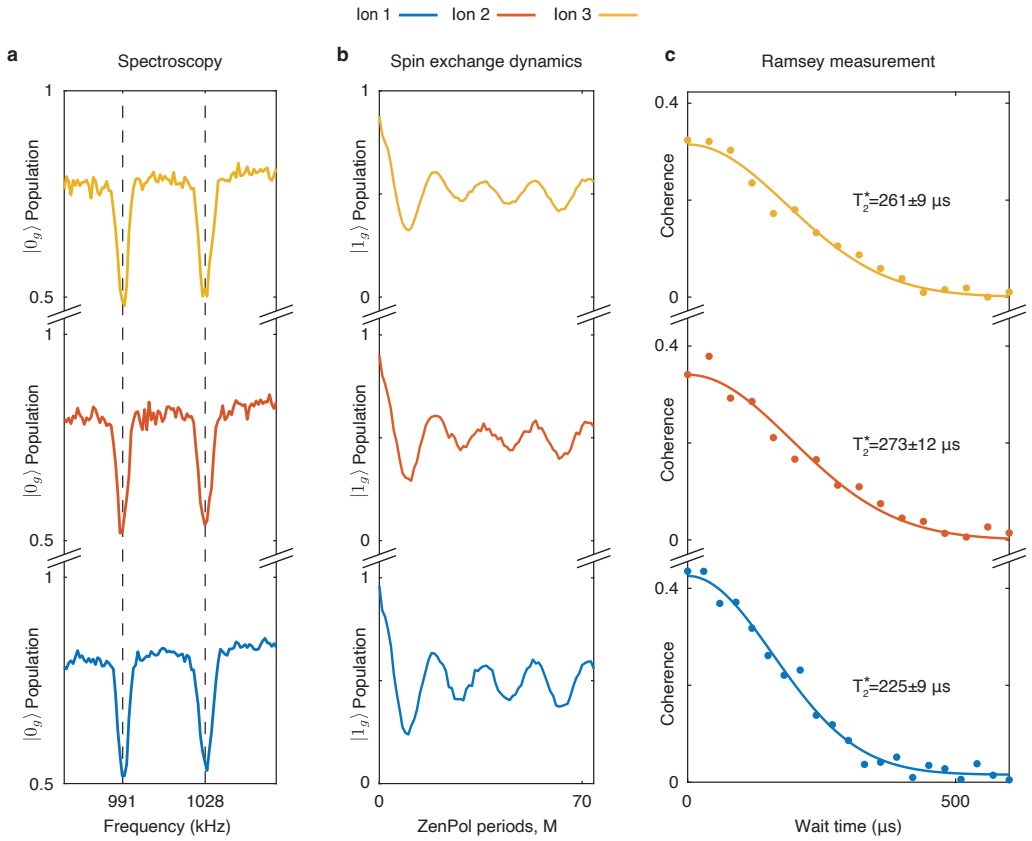


Figure 6.13: Experimental demonstration of deterministic nuclear spin register. To demonstrate the deterministic nature of the nuclear spin register, we perform the same measurements on two additional $^{171}$Yb ion qubits present in the device: Ion 2 (red) and Ion 3 (yellow). Results for Ion 1 (blue) are reproduced from the previous figures for ease of comparison. a) ZenPol spectra near the $\omega_c$ ($k = 5$) resonance of the $^{51}$V register spins. Notice that for all three ions, the bath and register transitions are identified at the same resonance frequencies of $\omega_c^{\text{bath}}/2\pi = 1028$ kHz and $\omega_c/2\pi = 991$ kHz, respectively. b) Dynamically engineered spin-exchange dynamics between the $^{171}$Yb qubit and $^{51}$V register. Using constant ZenPol square-wave RF amplitude we obtain equal spin-exchange rates for all three ions. c) Characterization of $^{51}$V register coherence times with decoupling from the $^{171}$Yb Knight field. The $1/e$ coherence times are measured to be $225 \pm 9$ $\mu$s, $273 \pm 12$ $\mu$s and $261 \pm 9$ $\mu$s for Ions 1, 2 and 3, respectively.

*Chapter 7*

# HONG-OU-MANDEL INDISTINGUISHABILITY MEASUREMENTS

## 7.1 Introduction

In the second half of this thesis we will work towards preparation of remote entangled states of two ions in two separate devices. This process relies on coherent emission of single photons, entangled with the internal state of the ion [237]. These photons need to be interfered and measured in a basis which projects the two ions into an entangled state (entanglement swapping [238]). Coherently measuring two photons in this manner is commonly referred to as 'which-path-erasure' [239] and requires the two photons to be mutually indistinguishable.

In this section we examine two-photon indistinguishably using a Hong-Ou-Mandel (HOM) interference experiment [240]. When two perfectly indistinguishable photons impinge on two ports of a beamsplitter, interference of their quantum wavefunctions leads to their emergence from the same output port. By monitoring the two output ports we therefore expect to measure bunching in the auto-correlation of detection times from any single detector and anti-bunching in the cross-correlation between the two detectors. The number of two-photon coincidences measured between the two output ports is therefore used as a measure of the photon distinguishability. This effect was first demonstrated in photons generated via spontaneous parametric down-conversion (SPDC) [240], but has since been observed in emission from trapped atoms [241], ions [242], quantum dots [243–245], molecules [246] and solid state emitters [247–250].

The degree of indistinguishability is limited by various factors [251]:

1. static frequency difference between the two photons ($\Delta\omega_0$),
2. a variable frequency difference between the two photons, linked to emitter dephasing ($\delta\omega$),
3. the wavepacket shape of the two photons,
4. the polarization of the photons.

Regarding (1), a static frequency difference will cause temporal oscillation in the HOM interference (commonly referred to as 'quantum beating' [252, 253]). Specif-

ically, an oscillation between bunching and antibunching with detection time difference. Since this is a coherent phenomenon, this form of distinguishability is not detrimental and can be accommodated in entanglement protocols, we therefore use the contrast of this oscillation as a revised definition of indistinguishability.

Regarding (2), variation in the photon emission frequency across multiple experimental repetitions leads to a Gaussian decay in the indistinguishability with relative measurement time. Generally, the Gaussian decay time constant is inversely proportional to the root-mean-square frequency fluctuation.

Regarding (3), photons generated via spontaneous emission will have an exponentially decaying spatio-temporal wavepacket shape, indistinguishability is caused by different decay time constants. Interestingly, even with dramatically different decays, two photons will still appear indistinguishable for sufficiently short detection time differences. Usually, variation in emission frequency dominates over this effect.

Regarding (4), photons are always emitted in a definite polarization state, unitary transformations (implemented with waveplates) can be used to match the photon polarizations at the beamsplitter.[1]

The results presented in this section are the first demonstration of HOM interference from two separate rare-earth ions, and serve as a crucial demonstration of mutual photonic coherence, a pre-requisite for the subsequent entanglement experiments.

## 7.2 Experimental Setup

The setup used for this experiment is explained in detail in Chapter 9. Specific aspects relevant to the following discussion are as follows:

We utilize two separate devices located in the same cryostat. We study one ion in each device, their optical frequency difference is 32.9 MHz (Figure 9.1). Light from the two devices exits the cryostat in two separate optical fibers which are combined on a polarizing beamsplitter (PBS), such that they exit in the same spatial mode, but with orthogonal polarizations.[2] Subsequently the light passes through a half wave plate which rotates the polarization by 45° before passing through a second PBS, the two output ports of this PBS are fiber coupled and sent to two separate single photon detectors (Figure 7.1).

[1] The specific experimental setup used (elaborated in section 7.2) uses polarizing beamsplitters and ensures that photons incident on the same detector always have the same polarization.

[2] The polarization of light in each of the two fibers prior to the PBS is adjusted to optimize the transfer of light from each device into the same spatial mode afterwards.

## 7.3 Theory

This section presents theoretical detail for the HOM measurement depicted in Figure 7.1[3]. The photons we consider travel in a 1D waveguide (optical fiber). Electromagnetic fields in this waveguide can be described via a set of continuum operators. For example, single-frequency operators $\{\hat{a}_\omega\}$ that satisfy $[\hat{a}_\omega, \hat{a}^\dagger_{\omega'}] = \delta(\omega - \omega')$ [255]. Note, however, that emitters will generate photons in a specific spatio-temporal mode with wavepacket given by:

$$\zeta_0(z,t) = \frac{1}{\sqrt{T_1}}\mathcal{H}(t)e^{-\frac{t}{2T_1}-i(\omega t - kz+\phi)} \tag{7.1}$$

where $\mathcal{H}(t)$ is the Heaviside step function and the photon is emitted at $t = 0$ [256]. We can simplify our analysis considerably by describing our 1D electromagnetic fields with a mode set that includes this specific mode. This process is termed 'discretizing the continuum' and involves defining a new set of operators $\hat{A}_k$ (with associated spatio-temporal modes $\zeta_k(z,t)$) that satisfy $[\hat{A}_k, \hat{A_{k'}}^\dagger] = \delta_{k,k'}$, whereby $\hat{A}_0$ is our emission mode of interest.

Crucially, the field operator in this new basis is defined according to:

$$\hat{E}^+(z,t) = \sum_k \zeta_k(z,t)\hat{A}_k \tag{7.2}$$

which provides a simple approach to extract photodetection probabilities [257].

Now consider the polarizing beamsplitter in Figure 7.1. We define two electric field operators for the orthogonally polarized input channels, $\hat{E}^+_A(z,t)$ (horizontal) and $\hat{E}^+_B(z,t)$ (vertical), where modes $\hat{A}_0$ and $\hat{B}_0$ are populated by Ion 1 and Ion 2, respectively. The electric field operators for the two photodetection channels are $\hat{E}^+_C(z,t)$ and $\hat{E}^+_D(z,t)$ for transmission and reflection, respectively. The half wave plate and PBS transform the input channels into the output channels according to:

$$\begin{aligned}\hat{E}^+_C(z,t) &= \cos(2\theta)\hat{E}^+_A(z,t) + \sin(2\theta)\hat{E}^+_B(z,t)\\ \hat{E}^+_D(z,t) &= -\cos(2\theta)\hat{E}^+_B(z,t) + \sin(2\theta)\hat{E}^+_A(z,t)\end{aligned} \tag{7.3}$$

where $\theta$ is the rotation angle of the half wave plate. Note, when $\theta = \pi/8$, the input mode contributions to the output mode are balanced, this is the condition for optimum HOM visibility.

[3] For more detail, there are many textbooks/papers that comprehensively cover this topic [251, 254].

The joint photon detection probability (probability of detecting a photon at time $t$ in detector $C$ and $t'$ in detector $D$) is given by:

$$\begin{aligned} P(t,t') &= \langle 0|\, \hat{A}_0\hat{B}_0\hat{E}_C^-(t)\hat{E}_D^-(t')\hat{E}_C^+(t)\hat{E}_D^+(t')\hat{A}_0^\dagger\hat{B}_0^\dagger\,|0\rangle \\ &= \frac{1}{4}\left[|\zeta_0^{(1)}(t)\zeta_0^{(2)}(t')|^2 + |\zeta_0^{(1)}(t')\zeta_0^{(2)}(t)|^2 - 2\mathfrak{Re}\{\zeta_0^{(1)}(t)\zeta_0^{(1)}(t')\zeta_0^{(2)}(t)\zeta_0^{(2)}(t')\}\right] \\ &\propto e^{-t/T_1^{(1)}}e^{-t'/T_1^{(2)}} + e^{-t'/T_1^{(1)}}e^{-t/T_1^{(2)}} - 2e^{-\frac{t+t'}{\tau}}\cos((\omega_1-\omega_2)(t-t')) \end{aligned} \tag{7.4}$$

where, for simplicity, we have dropped the positional coordinate and $\zeta_0^{(i)}$, $\omega_i$ and $T_1^{(i)}$ are the wavepacket, frequency and lifetime of ion $i$, respectively. $\tau$ is defined according to $1/\tau = 1/T_1^{(1)} + 1/T_1^{(2)}$.

Finally, we define the photon arrival time difference $\Delta t = t' - t$ and marginalize over the remaining temporal degree of freedom to arrive at the coincidence probability:

$$\begin{aligned} P(\Delta t) =& \eta^{BC}\eta^{AD}e^{-\Delta t/T_1^{(2)}} + \eta^{AC}\eta^{BD}e^{-\Delta t/T_1^{(1)}} \\ &- 2\sqrt{\eta^{BC}\eta^{AD}\eta^{AC}\eta^{BD}}e^{-\Delta t/2\tau}e^{-\Delta t^2\sigma^2}\cos(\Delta\omega_0\Delta t). \end{aligned} \tag{7.5}$$

Note here that we have introduced efficiencies $\eta^{AC}$ and $\eta^{AD}$ which are the probabilities for photons originating from Ion 1 to reach detectors $C$ and $D$, respectively. Similarly, $\eta^{BC}$ and $\eta^{BD}$ are the probabilities for photons originating from Ion 2 to reach detectors $C$ and $D$, respectively. We have also assumed that the measurement window size is much larger than either of the two ions' lifetimes. Furthermore, we have taken an ensemble average over frequency differences between the two ions, $\sigma$ is given by: $\sigma = \sqrt{1/(T_2^{*(1)})^2 + 1/(T_2^{*(2)})^2}$, where $T_2^{*(i)}$ is the optical Ramsey coherence time for ion $i$. $\Delta\omega_0$ is the static frequency difference between the two ions.

Note that the condition for perfect HOM interference is given by:

$$\frac{\eta^{AC}}{\eta^{AD}} = \frac{\eta^{BC}}{\eta^{BD}} \tag{7.6}$$

experimentally, this condition is obtained by choosing an appropriate half wave plate angle. If we assume some imperfection in this condition we can account for this with a parameter $\alpha$ according to $\eta^{AC}\eta^{BD} = \alpha\eta^{AD}\eta^{BC}$. The visibility of the two-photon correlation measurement is then given by:

$$V(\Delta t) = \frac{2\sqrt{\alpha}e^{-\Delta t/2\tau}e^{-\Delta t^2\sigma^2}}{e^{-\Delta t/T_1^{(2)}} + \alpha e^{-\Delta t/T_1^{(1)}}}. \tag{7.7}$$

This is also termed the photon indistinguishability. Note that if $\alpha = 1$ we have perfect indistinguishability at $\Delta t = 0$.

Note, when modelling the two-photon coincidences we also consider the effect of dark counts on either of the two detectors. We assume that dark count rates are sufficiently small that the probability of coincidences due to a double dark count are negligible. Instead, the dominant contribution occurs when a dark count is measured at one detector and an ion count is measured at the other detector. We also take into account the effect of a finite window size. These expressions are not written out here for conciseness.

### 7.4 Experimental Results

This section presents experimental results summarized in Figure 7.1. The setup is described in Section 7.2 whereby the half-waveplate angle is optimized to ensure the ratio of probabilities matches equation (7.6). We measure the resulting balance ratio $\alpha = 0.993$. The two ions' optical frequency difference is 32.9 MHz.

Figure 7.1a shows a normalized histogram of coincidences between the two detectors with a bin size of 160 ns. Since this is much larger than the inverse of the optical frequency difference, we obtain an average count rate and the photons appear distinguishable. In other words, by measuring imprecisely we do not erase frequency information.

Figure 7.1b shows the same measurement with a 3 ns window size where the window positions are chosen to coincide with the trough of each oscillation. In this case, a conventional Hong-Ou-Mandel result is obtained. Figure 7.1c shows the central region with $|\Delta t| < 200$ ns, we can clearly observe an oscillation between bunching and antibunching at 32.9 MHz.

In Figure 7.1d we consider the HOM visibility when averaged over a window which extends from $-W/2 < \Delta t < W/2$. We plot the average visibility against the window size, $W$. For the smallest window size ($W = 6$ ns) we obtain a visibility of $96 \pm 4\%$. Given the measured imbalance ($\alpha = 0.993$), the bin size (3 ns) and the optical frequency 32.9 MHz, we expect the maximum possible measured visibility to be 97.95%. This agrees well, given the measurement error.

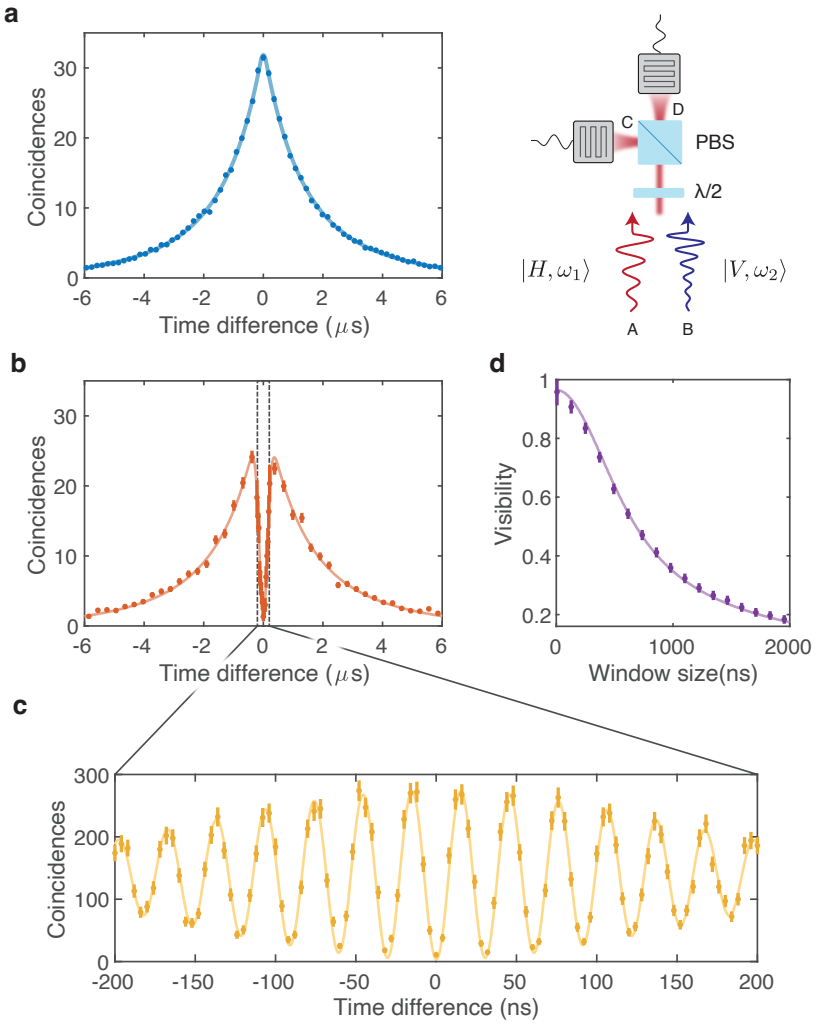


Figure 7.1: Hong-Ou-Mandel two photon interference. Photons from two ions in two separate devices interfere via a polarizing beamsplitter (PBS). Two single photon detectors on the PBS output ports are used to study time-resolved coincidences. a) Coincidences are binned with 160 ns window size, thereby rendering the photons distinguishable. b), c) Coincidences are binned with a 3 ns window size leading to frequency erasure. In (c) we see the emergence of quantum beats at the optical frequency difference. In (b) we plot the counts at the trough of each oscillation, thereby obtaining a 'conventional' Hong-Ou-Mandel anti-bunching feature. d) The average interference visibility plotted vs acceptance window size. For the smallest window size of 6 ns, a 96% visibility is achieved.

*Chapter 8*

# TWO ION ENTANGLEMENT OVERVIEW AND THEORY

## 8.1 Introduction

As discussed in Section 1.2, distributing entanglement between remote qubits is a critical component of future long-range quantum networks [16].

To date, several quantum networking platforms have achieved this milestone: trapped atoms [64, 258], trapped ions [61, 62], quantum dots [68, 69] and nitrogen vacancy centers in diamond [67, 218, 259]. While initial demonstrations were limited to two node entanglement, recent results using NV centers have demonstrated entanglement of three remote nodes [30, 75]. Note that there have also been demonstrations of heralded entanglement between a pair of silicon vacancy centers in diamond; however, these were within the same cavity [260].

In the next three chapters of this thesis we develop protocols and experimentally demonstrate remote entanglement between two single rare-earth ion qubits. To do this, we will leverage a variety of properties that were previously demonstrated, including long spin coherence times (Section 3.5), coherent optical transitions (Section 3.2) and two-photon interference (Section 7.4).

There are three main challenges that need to be addressed in order to demonstrate entanglement using our platform:

1. low photon detection efficiencies (typically around 1%),
2. non-transform-limited optical linewidths ($\approx 10\times$ broader),
3. static disorder (inhomogeneity) in the optical transition frequencies (200 MHz).

To overcome these challenges we develop a single-photon entanglement heralding protocol which will be elaborated in this chapter. This protocol incorporates a novel type of dynamical decoupling (which we term dynamic rephasing). It is designed to mitigate the effect of stochastic phase accumulation associated with random photon emission during entanglement heralding, it also enables lifetime limited

entanglement rates and fidelities even in the presence of non-transform limited line-widths. Relaxing the photonic coherence requirements for entanglement heralding will enable the re-evaluation of a broad range of solid state emitter platforms which were previously discarded due to excessive spectral diffusion.

Furthermore, the narrow optical inhomogeneous line-widths of rare-earth ions provides us with a unique advantage in addressing static disorder. This is because, generally, frequency information can be erased if photons are detected with a timing resolution much smaller than the inverse of the optical frequency difference. Compared to other solid state platforms, rare-earth ions are the only system compatible with the timing resolution of commercially available single photon detectors. Our platform can uniquely leverage frequency erasure for scalable entanglement distribution between any pair of emitters.

In Chapter 9 we will present details of the experimental setup used for these measurements, in Chapter 10 we present the experimental results.

## 8.2 Single Photon Entanglement Protocols

Nearly all remote entanglement protocols consist of two key ingredients:

- the ability to entangle the internal spin state of an atom/ion with an itinerant photon;
- entanglement swapping, where a measurement of the photon(s) projects the ions/atoms into an entangled state.

There are many different proposed protocols [32]; however, for the purposes of this discussion I will focus on just two: the Barrett-Kok [261] and single photon [262, 263] schemes, these are the most commonly encountered. They involve entanglement of each atom with a photonic qubit in the $\{|0\rangle, |1\rangle\}$ Fock basis. Subsequently, photons emitted from each device travel to a central location where the two optical paths are combined on a beamsplitter and measured in a manner that erases 'which-path' information (i.e., a Bell state measurement).[1]

The Barrett Kok scheme starts with both ions prepared in the $|+X\rangle$ state:

$$|\psi\rangle = \frac{1}{2}\left[|0_g 0_g\rangle + |1_g 0_g\rangle + |0_g 1_g\rangle + |1_g 1_g\rangle\right] \tag{8.1}$$

[1] There are several different optical measurement setups used in these experiments, they are elaborated in Section 9.5.

both ions are optically excited, detection of a single photon would herald[2] $\frac{1}{\sqrt{2}}(|0_g 1_g\rangle + |1_g 0_g\rangle)$. However, since most commercial detectors are not photon number resolving (and the photon detection process is usually quite inefficient) there is still a possibility of being in $|1_g 1_g\rangle$. To remove this component, a spin $\pi$ pulse is applied to both ions and the optical excitation + photon heralding steps are repeated. However, this scheme is usually quite inefficient as the entanglement rate scales with the detection efficiency squared ($\eta^2$).

The single photon protocol provides a more efficient scheme for entanglement generation and will be the approach pursued in this thesis. The protocol looks like the first half of the Barrett-Kok scheme; however, we start with a direct-product state of a slightly different form [264]:

$$\begin{aligned} |\psi\rangle &= \left(\sqrt{1-\alpha}\,|0_g\rangle + \sqrt{\alpha}\,|1_g\rangle\right)\left(\sqrt{1-\alpha}\,|0_g\rangle + \sqrt{\alpha}\,|1_g\rangle\right) \\ &= (1-\alpha)\,|0_g 0_g\rangle + \sqrt{\alpha(1-\alpha)}\left[|1_g 0_g\rangle + |0_g 1_g\rangle\right] + \alpha\,|1_g 1_g\rangle \end{aligned} \tag{8.2}$$

where $\alpha$ can be chosen freely between 0 and 1, it quantifies the strength of superposition for each of the single-ion states. As before, excitation and detection of a single photon carves out the optically dark component (removes $|0_g 0_g\rangle$). The $|1_g 1_g\rangle$ component is treated as an infidelity in the entangled state, note that it is suppressed by a probability factor $\alpha$ relative to the Bell state and leads to a maximum entangled state fidelity of $\mathcal{F} = 1 - \alpha$. Hence, by choosing sufficiently small $\alpha$ we can make this component negligible. The entanglement heralding rate is given by $\mathcal{R} = 2\eta\alpha$, since $\eta$ is typically quite small, this can be a considerable improvement over the Barrett-Kok scheme. Crucially, this determination relies on the choice of $\alpha$ which should be minimized so that it does not dominate over other sources of error in the system. Specifically, if the maximum permitted infidelity is greater than the photon detection efficiency then it makes sense to use this approach.[3]

The single photon protocol has been applied to a wide variety of platforms [68, 126, 259, 265].

[2] Note, that if measuring with two detectors, one would expect the Bell state phase to depend on which detector clicked. The heralded Bell states for different detection scenarios are discussed in Section 9.5.

[3] For our devices $\eta \sim 0.01$ and typical fidelities are $\mathcal{F} \sim 0.75$.

## 8.3 Coherence in Entanglement Heralding

In this section we provide more detail on the basic single photon protocol which was introduced in the previous section, discuss the impact of phase and optical decoherence on the entangled state and propose two alternative sequences which overcome limitations associated with this decoherence.

### Ramsey Protocol

The most basic entanglement sequence is presented in Figure 8.1a. Each ion is initialized into the $|0_g\rangle$ state, a microwave pulse prepares a weak superposition with a small probability, $\alpha$, of being in the optically bright $|1_g\rangle$ state. The resulting two ion state is:

$$|\psi\rangle = (1-\alpha)\,|0_g 0_g\rangle + \sqrt{\alpha(1-\alpha)}\left[|1_g 0_g\rangle + |0_g 1_g\rangle\right] + \alpha\,|1_g 1_g\rangle\,. \tag{8.3}$$

Subsequently, each ion is resonantly optically excited and the entangled state is heralded on the detection of a single photon with a detection time $t_0$. The resulting heralded density matrix is given by [264]:

$$\rho = (1-\alpha)\,|\psi(t_0)\rangle\,\langle\psi(t_0)| + \alpha\,|1_g 1_g\rangle\,\langle 1_g 1_g| \tag{8.4}$$

where:

$$|\tilde{\psi}(t_0)\rangle = \left[\frac{e^{-t_0/2T_1^{(1)}}}{\sqrt{T_1^{(1)}}}e^{-i(\omega_1 t_0+\phi)}\,|1_g 0_g\rangle + \frac{e^{-t_0/2T_1^{(2)}}}{\sqrt{T_1^{(2)}}}e^{-i(\omega_2 t_0)}\,|0_g 1_g\rangle\right] \tag{8.5}$$

with $|\psi(t_0)\rangle = |\tilde{\psi}(t_0)\rangle / \sqrt{\langle\tilde{\psi}(t_0)|\tilde{\psi}(t_0)\rangle}$. $\omega_1$, $\omega_2$ and $T_1^{(1)}$, $T_1^{(2)}$ are the optical frequencies and lifetimes of the two ions, respectively. We define $\phi = \phi_1 - \phi_2$, where $\phi_i$ corresponds to the phase of the excitation laser at ion $i$ combined with the phase of the subsequently emitted photon as it travels to the detector. This will be discussed more in Section 9.6.

Assuming that the two ions have the same optical lifetime ($T_1^{(1)} = T_1^{(2)} = T_1$), that the optical phase is zero ($\phi = 0$) and that $\alpha$ is sufficiently small such that the infidelity due to $|1_g 1_g\rangle\,\langle 1_g 1_g|$ can be ignored, this protocol heralds the preparation of a pure state:

$$|\psi(t_0)\rangle = \frac{1}{\sqrt{2}}\left[|1_g 0_g\rangle + |0_g 1_g\rangle\, e^{-i\Delta\omega t_0}\right] \tag{8.6}$$

where $\Delta\omega = \omega_2 - \omega_1$ [4].

[4] A note on rotating frames: throughout this and the next section, we will assume that we are working in a rotating frame for the ground state spin transition (i.e., $|0_g\rangle$ and $|1_g\rangle$ have 0 energy) and that we are operating in the lab frame for the excited state level (i.e., $|0_e\rangle$ has energy $\hbar\omega$). We will ignore spin dephasing for simplicity. We will assume that the laser excitation phase is 0 at the start of the heralding window for each ion.

Now we note two things. First, the Bell State phase will depend on the optical frequency difference and the photon detection time. This is addressed in Section 8.4.

Second, variations in the optical frequency difference will cause uncertainty in the heralded phase. Typically, the optical frequency distribution will be Gaussian in nature: $\Delta\omega = \Delta\omega_0 + \delta\omega$, where $\Delta\omega_0$ is a static frequency splitting and $\delta\omega$ is a stochastic, Gaussian-distributed frequency with $\text{std}(\delta\omega) = \sigma_\omega$ and $\langle\delta\omega\rangle = 0$. Much like a Ramsey experiment, this variation leads to a Gaussian decay of the entangled state coherence with photon detection time:

$$C(t_0) = 2\Re\left\{\langle 0_g 1_g| \rho |1_g 0_g\rangle\right\} = \cos(\Delta\omega_0 t_0) e^{-t_0^2\sigma_\omega^2/2}. \tag{8.7}$$

Assuming that the spectral diffusion of the two ions' optical transitions are uncorrelated, we can derive the relation: $\sigma_\omega = \sqrt{2/(T_2^{*(1)})^2 + 2/(T_2^{*(2)})^2}$ where $T_2^{*(i)}$ is the optical Ramsey coherence time for the $i^{\text{th}}$ ion. This yields an unfortunate trade-off in systems which do not have lifetime limited coherence (i.e., where $T_2^* < 2T_1$). Either one can accept photon counts for the entire optical emission period, this maximizes the entanglement heralding rate, but limits the heralded fidelity to $(\mathcal{F} - 0.5) \sim T_2^*/2T_1$. Alternatively, one can accept photons only within the optical coherence time, but this limits the entanglement rate to $\mathcal{R} \sim T_2^*/2T_1$. Usually, one opts for the latter case.

**Precompensated Phase Accumulation**

Next, we apply the concept of dynamical decoupling to the entanglement heralding pulse sequence, as we will see, if the optical frequency difference is quasi-static on the timescale of an experiment sequence the trade-off described in the previous section is not necessarily fundamental.

This sequence is depicted in Figure 8.1b and starts as before with the preparation of a superposition state followed by optical excitation; however, this time $\alpha$ is chosen such that $(1 - \alpha) \ll 1$. Under this condition we can ignore the $|0_g 0_g\rangle$ component. After optical excitation, the un-normalized quantum state is given by[5]:

$$|\psi\rangle = \sqrt{\alpha(1-\alpha)}\left[|0_e 0_g\rangle + |0_g 0_e\rangle\right] + \alpha\,|0_e 0_e\rangle\,. \tag{8.8}$$

[5]Another note on rotating frames: in this section it seems like I have chosen the laser to have 0 phase at the start of both the rephasing period and heralding periods. In reality, this is not a requirement, as any laser phase imparted to the state after the first optical $\pi$ pulse is subsequently removed by the second optical $\pi$ pulse (within the composite pulse). Hence the only laser phase that impacts the final entangled state is the final optical $\pi$ pulse. Without loss of generality, we can set the laser phases to be zero at this singular point as in the previous section.

Next, the quantum state evolves for a pre-determined duration, $\tau_0$, during which optical phase is accumulated at a rate given by $\Delta\omega = \Delta\omega_0 + \delta\omega$.

$$|\psi\rangle = \sqrt{\alpha(1-\alpha)}\left[|0_e 0_g\rangle + |0_g 0_e\rangle\, e^{(-i(\Delta\omega_0+\delta\omega)\tau_0)}\right] + \alpha\,|0_e 0_e\rangle\, e^{-i\omega_2\tau_0} \tag{8.9}$$

Next, we apply a $\pi$ pulse which exchanges the states $|0_e\rangle$ and $|0_g\rangle$. This leads to the following state:

$$|\psi\rangle = \sqrt{\alpha(1-\alpha)}\left[|0_g 0_e\rangle + |0_e 0_g\rangle\, e^{-i\delta\omega\tau_0}\right] + \alpha\,|0_g 0_g\rangle\, e^{-i\delta\omega_2\tau_0} \tag{8.10}$$

where $\delta\omega_2$ is the detuning of the $2^{\text{nd}}$ ion from its respective driving laser and we have assumed that the frequency difference between the two driving lasers is set to $\Delta\omega_0$. Note that the $|0_g\rangle \leftrightarrow |0_e\rangle$ transition (marked in green in Figure 8.1) is forbidden for our system at B=0. We therefore utilize a composite pulse consisting of an optical $\pi$ pulse on the $A$ transition, followed by a spin dynamical decoupling sequence with an odd number of periods[6] and finally a second optical $\pi$ pulse on the $A$ transition. Finally, we herald the preparation of an entangled state by detecting a single photon at time $t_0$:

$$|\psi(t_0)\rangle = \frac{1}{\sqrt{2}}\left[|0_g 1_g\rangle + |1_g 0_g\rangle\, e^{-i[\delta\omega(\tau_0-t_0)-\Delta\omega_0 t_0]}\right]. \tag{8.11}$$

The coherence of the resulting entangled state is now maximized when the photon emission satisfies $t_0 = \tau_0$, i.e., $C(t_0) = \cos(\Delta\omega_0 t_0) e^{-(t_0-\tau_0)^2\sigma_\omega^2/2}$. While the coherence still decays with rate $\sigma_\omega/\sqrt{2}$, by shifting the point of maximum coherence to $t_0 > 0$ we can now herald with a two-sided acceptance window (i.e., both before and after this point). This enables us to boost the entanglement rate by a factor of two compared to the previous protocol whilst still maintaining the same fidelity. Note that any optical decay during the first evolution of duration $\tau_0$ will lead to infidelity in the entangled state; however, this can be mitigated by choosing $\tau_0$ to be much less than the optical lifetime.

**Dynamic Rephasing**

The critical issue with the previous sequence is that optical dephasing is pre-compensated with an evolution period of fixed duration $\tau_0$, whereas dephasing occurs for a subsequent random duration $t_0$. It is therefore impossible to perfectly rephase the entangled state for all photon emission times.

[6] During the dynamical decoupling sequence $\pi$ pulses are applied simultaneously to the ground and excited state spin transitions. In principle, the dynamical decoupling sequence could be replaced with a single ground state $\pi$ pulse; however, with a relatively high optical $\pi$ pulse infidelity, this sequence acts to reduce gate error in the population basis.

The final pulse sequence we consider (depicted in Fig 8.1c), overcomes this issue by reversing the order of the phase compensation and entanglement heralding steps. It then uses the photon emission time (measured during the preceding heralding period) to dynamically adjust the duration of the rephasing period.

More precisely, the sequence heralds an entangled state using the standard Ramsey method described at the beginning of this section. The total optical heralding window has duration $\tau_R$, therefore, at the end of the window the quantum state has accumulated phase for duration $t_0$ in the excited state and duration $t_s = \tau_R - t_0$ in the ground state:

$$|\psi(t_0)\rangle = \frac{1}{\sqrt{2}}\left[|1_g 0_g\rangle + |0_g 1_g\rangle\, e^{-i(\Delta\omega_0+\delta\omega)t_0}\right]. \tag{8.12}$$

Note, for simplicity we are going to ignore any ground state (spin) dephasing when writing the quantum states. Next, a dynamical decoupling sequence consisting of three ground state spin $\pi$ pulses is applied and the ions are subsequently optically excited. The ions are left in the excited state for a duration $t_0$ before being transferred to the ground state with a second optical $\pi$ pulse leading to:

$$|\psi(t_0)\rangle = \frac{1}{\sqrt{2}}\left[|0_g 1_g\rangle + |1_g 0_g\rangle\, e^{-i\Delta\omega_0 t_0}\right]. \tag{8.13}$$

Note, for this protocol to work, the experiment control electronics must process the photon detection, ascertain the arrival time $t_0$ and select a matching wait time between the two optical $\pi$ pulses.[7] Finally, there is also a wait period of duration $t_s$ to rephase the spin coherence. The entangled state coherence is now $C(t_0) = \cos(\Delta\omega_0 t_0)$, where $\Delta\omega_0$ is frequency difference between the two excitation lasers (which is also equal to the unperturbed ion frequency difference). Crucially, this is no longer limited by the optical Ramsey coherence time.

There are two main factors limiting the coherence of the resulting entangled state: optical decay during only the rephasing period and any pure (Markovian) dephasing during both the heralding and rephasing periods. Including these factors, the coherence is given by: $C(t_0) = \cos(\Delta\omega_0 t_0)e^{-t_0(2\gamma_d+1/T_1)}$. Where $\gamma_d$ is the pure dephasing rate (in this case assumed equal for the two ions).

In principle, the limitation imposed by optical decay is not fundamental. If our optical cavity were narrow enough, we could operate in a regime where the $A$

[7] While, in principle, a single spin $\pi$ pulse between the heralding and optical rephasing periods would be sufficient for this protocol to work, the dynamical decoupling sequence provides time for the necessary real-time processing with minimal loss of coherence.

transition is cavity enhanced with short lifetime, whereas the $E$ transition is not enhanced and has long lifetime. Heralding would occur on the $A$ transition and rephasing could then be performed on the $E$ transition. Note that this would require an improvement in cavity quality factor by approximately 10 times and is therefore outside the scope of this work.

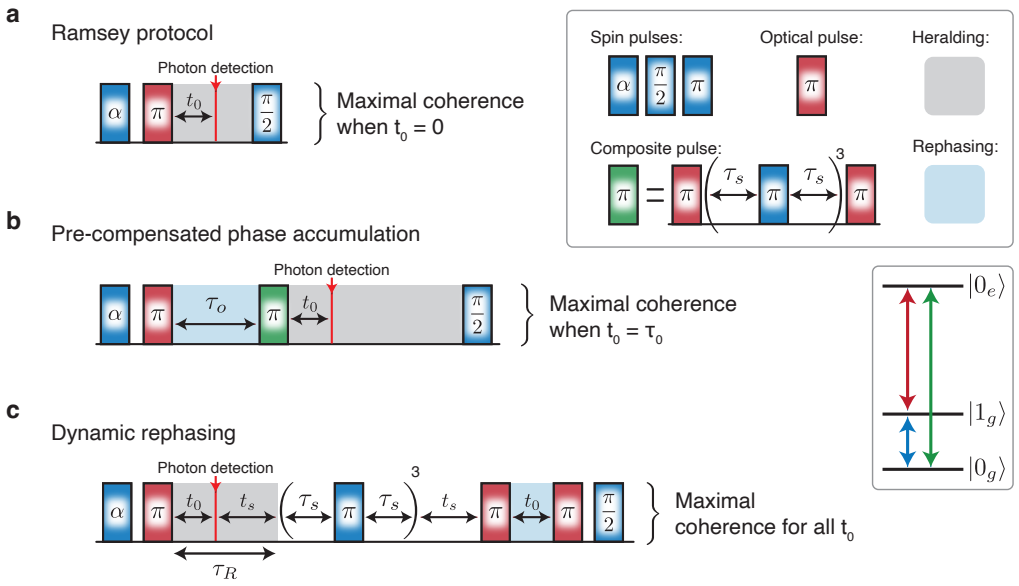


Figure 8.1: Entanglement protocols explored in this thesis. a) A basic single-photon Ramsey protocol. After preparation of a weak spin superposition of each ion (probability $\alpha$ in $|1_g\rangle$), each ion is optically excited and entanglement is heralded on a single photon detection. The $|0_g 0_g\rangle$ component is carved out and the $|1_g 1_g\rangle$ component is treated as an infidelity b) A dynamical decoupling protocol with a period of duration $\tau_0$ that pre-accumulates optical phase before the entanglement heralding window. Maximal entangled state coherence is achieved when $t_0 = \tau_0$ but the portion of photonic emission that can be used to herald entanglement is still limited by $T_2^*$ c) The dynamic rephasing protocol where rephasing occurs after heralding of the entangled state. In this sequence the rephasing period has duration exactly matching the photon emission time $t_0$ for each experiment. The entangled state coherence is maximized regardless of emission time.

## 8.4 Frequency Erasure

As introduced in section 7.1, remote entanglement protocols generally require the measurement of indistinguishable photons in order to project qubits into an entangled state.

However, since the photons emitted by our two ions have different frequencies, this is not the case. In all of the experimental protocols discussed in the previous section, the entangled state phase will depend on the photon measurement time $t_0$ and an optical frequency difference.[8] Without a method to counteract this stochastic phase, the entangled state coherences will average to 0 over multiple experiment repetitions and the state will appear classical.

There are several different methods proposed/implemented by the community to overcome such limitations:

1. The photon acceptance window could be reduced to less than $1/\Delta\omega_0$. This is an acceptable method for small frequency differences[9].

2. Defects with a first order DC Stark sensitivity can be tuned into resonance with each other via electric fields [266].

3. Photons at different frequencies can be spectrally overlapped using an electro-optic-modulator (EOM) which acts like a frequency beamsplitter [260].

4. In cases where PPLN waveguides are used to convert photon frequencies into the telecom band, inhomogeneity of optical frequencies can be compensated during the conversion process using different pump tones for each emitter [183, 267, 268].

5. If the photon is measured with a precision much greater than the inverse of the optical frequency difference, ($\delta t \ll 1/\Delta\omega_0$), then we can infer the Bell state phase from the photon arrival time. This phase can be corrected on an experiment-by-experiment basis via a differential $z$ rotation by angle $-\Delta t\omega_0$ (i.e., by applying a unitary gate $\hat{U} = \mathbb{I} \otimes e^{i\Delta t\omega_0\sigma_z/2}$). This approach was first proposed for trapped ions [269] and has been used to prepare entangled states of SPDC-generated photons [270].

[8] For the first two protocols, this is $\Delta\omega$, the difference between the two ions' frequencies, for the final protocol it is the optical drive frequency difference ($\Delta\omega_0$).

[9] In our case this would cause a dramatic reduction in entanglement rate.

In this thesis we utilize the final approach, for which our solid state system is uniquely suited. We have an optical inhomogeneous line-width of 200 MHz, which is considerably narrower than many solid state platforms (e.g., $\sim$ 1 GHz for bulk NV centers and $\sim$ 15 GHz for implanted SiV centers). Hence, even in the most extreme case where our emitters are separated by 500 MHz (see Section 10.7), the photon detection timing resolution requirement is $\Delta t \ll 2$ ns which is within the specification of commercial single photon detectors (SNSPD jitter is usually $< 100$ ps). Hence, for our platform we can deterministically entangle any pair of ions with maximal efficiency without needing to operate in narrow regions of the inhomogeneous spectrum, or utilize inefficient EOMs for frequency shifting.

## 8.5 Comprehensive Modelling Framework

To model the entanglement measurements we will utilize a Schrodinger picture master equation formalism. This will enable us to include various sources of decoherence and relaxation on both the optical and spin transitions through appropriately chosen Lindbladian superoperators.

Within this formalism, the process of photon detection to herald entangled states can be encoded via quantum jumps in a stochastic time evolution. Deriving the appropriate form of these quantum jump operators is nontrivial, and will be the focus of this section.

Initially, let us consider a single ion (labelled $i$) coupled to a cavity. The ion has optical transition frequency $\omega_i$, the cavity has frequency $\omega_c$ and bosonic creation operator $\hat{a}^\dagger$. Additionally, the cavity is coupled to a waveguide which supports an infinite set of 1D continuum mode operators $\hat{b}_i^\dagger(\omega)$ which satisfy the commutation relation $[\hat{b}_i(\omega), \hat{b}_i^\dagger(\omega')] = \delta(\omega - \omega')$ [255]. We will treat this as a closed system with Hamiltonian:

$$\begin{aligned} H =& \frac{\hbar\omega_i}{2}\hat{\sigma}_z^{(i)} + \hbar\omega_c\hat{a}^\dagger\hat{a} + \int d\omega \left[\hbar\omega\hat{b}_i^\dagger(\omega)\hat{b}_i(\omega)\right] \\ &+ \hbar\sqrt{\frac{\kappa}{2\pi}}\int d\omega \left[\hat{a}^\dagger\hat{b}_i(\omega) + \hat{a}\hat{b}_i^\dagger(\omega)\right] + \hbar g\left[\hat{a}^\dagger\hat{\sigma}_i^- + \hat{a}\hat{\sigma}_i^+\right]. \end{aligned} \tag{8.14}$$

First, we adiabatically eliminate the cavity mode $\hat{a}$, and move into a rotating frame at $\omega_i$ for the atom and at $\omega$ for each of the continuum modes. This enables us to re-write the system Hamiltonian as [271]:

$$H = \int d\omega \frac{-\hbar g\sqrt{\kappa/2\pi}}{\frac{i\kappa}{2} + (\omega - \omega_c)}\hat{\sigma}_i^-\hat{b}_i^\dagger(\omega)e^{i(\omega-\omega_i)t} + \text{H.C.} \tag{8.15}$$

Next, assume the ion is resonant with the cavity ($\omega_i = \omega_c$) and that its emission line-width is much less than $\kappa$. We Fourier transform the continuum operators to obtain $\hat{b}_i(t) = \frac{1}{\sqrt{2\pi}} \int d\omega \hat{b}_i(\omega) e^{-i(\omega-\omega_i)t}$ that annihilate single photons in temporal modes at time $t$. The resulting Hamiltonian is:

$$H = i\hbar\sqrt{\frac{4g^2}{\kappa}}\hat{\sigma}_i^- \hat{b}_i^\dagger(t) + \text{H.C.} \tag{8.16}$$

An infinitesimal time evolution for duration $\delta t$ under this Hamiltonian is given by:

$$\hat{U}(t+\delta t, t) = e^{\sqrt{\frac{4g^2}{\kappa}}\left[\hat{\sigma}_i^- \hat{b}_i^\dagger(t) - \hat{\sigma}_i^+ \hat{b}_i(t)\right]\delta t}. \tag{8.17}$$

Assuming an infinitely cold bath (all continuum modes in the ground state), this can be expanded to first order in $\delta t$ to give [272]:

$$\hat{U}(t+\delta t, t) = \hat{\mathbb{I}} + \sqrt{\frac{4g^2}{\kappa}}\hat{\sigma}_i^- \hat{b}_i^\dagger(t)\delta t - \frac{2g^2}{\kappa}\hat{\sigma}_i^+\hat{\sigma}_i^-\delta t. \tag{8.18}$$

Now, considering two ions each with its own cavity and respective set of 1D waveguide modes. We can derive a two-ion evolution operator (expanded up to $O(\delta t)$) given by:

$$\begin{aligned}\hat{U}(t+\delta t, t) =& \hat{\mathbb{I}} + \sqrt{\frac{4g^2}{\kappa}}\hat{\sigma}_1^- \hat{b}_1^\dagger(t)\delta t + \sqrt{\frac{4g^2}{\kappa}}\hat{\sigma}_2^- \hat{b}_2^\dagger(t)\delta t + \frac{4g^2}{\kappa}\hat{\sigma}_1^-\hat{\sigma}_2^-\hat{b}_1^\dagger\hat{b}_2^\dagger(t)\delta t^2 \\ &- \frac{2g^2}{\kappa}\hat{\sigma}_1^+\hat{\sigma}_1^-\delta t - \frac{2g^2}{\kappa}\hat{\sigma}_2^+\hat{\sigma}_2^-\delta t\end{aligned} \tag{8.19}$$

where, for simplicity, we have assumed $g$ and $\kappa$ are the same for both devices.

Note, in this formalism we have assumed that the entire cavity emission is concentrated in the waveguide mode. In reality, the cavity can have multiple loss paths: $\kappa = \kappa_{\text{wg}} + \kappa_{\text{s}}$ where $\kappa_{\text{wg}}$ is the energy loss rate into the waveguide and $\kappa_{\text{s}}$ is the rate of energy scatter into other modes. Furthermore, due to detection inefficiency only a fraction ($\eta$) of light in the waveguide will be detected. The total probability to detect a photon emitted by the atom is given by $p_{\text{det}} = \kappa_{\text{wg}}\eta/\kappa$. All scattered and undetected light can be treated using a Lindbladian master equation which traces over (ignores) the radiation modes. Only the detected fraction needs to be treated using unitary time evolution according to Equation (8.19).

We time-evolve the density matrix according to:

$$\begin{aligned}\frac{\rho(t+\delta t)-\rho(t)}{\delta t} = &-\frac{i}{\hbar}\left[\hat{H},\rho\right] + \sum_i \left(\hat{\mathcal{L}}_i \rho \hat{\mathcal{L}}_i^\dagger - \frac{1}{2}\left\{\hat{\mathcal{L}}_i^\dagger \hat{\mathcal{L}}_i, \rho\right\}\right) \\ &- \frac{2g^2 p_{\text{det}}}{\kappa}\left\{\hat{\sigma}_1^+\hat{\sigma}_1^-,\rho\right\} - \frac{2g^2 p_{\text{det}}}{\kappa}\left\{\hat{\sigma}_2^+\hat{\sigma}_2^-,\rho\right\} \\ &+ \frac{4g^2 p_{\text{det}}\delta t}{\kappa}\left[\hat{\sigma}_1^-\hat{b}_1^\dagger(t) + \hat{\sigma}_2^-\hat{b}_2^\dagger(t)\right]\rho\left[\hat{b}_1(t)\hat{\sigma}_1^+ + \hat{b}_2(t)\hat{\sigma}_2^+\right] \quad (8.20)\end{aligned}$$

where $\hat{H}$ describes internal atomic unitary dynamics (driving, etc.). We have simplified this equation by noting that the quantum state will eventually be projected onto a single photon subspace.

In a quantum jump picture, we can interpret this time evolution as consisting of anti-hermitian evolution ($\hat{\sigma}_i^+\hat{\sigma}_i^-$) where the atom has not emitted a photon into the waveguide and quantum jumps ($\hat{\sigma}_i^-\hat{b}_i^\dagger(t)$) which populate temporal photonic modes at time $t$.

We also define the following set of Lindbladian operators:

Undetected optical emission on the $A$ transition is described by:

$$\mathcal{L}_1 = \sqrt{\frac{4g^2(1-p_{\text{det}})}{\kappa} + \Gamma}\,|1_g\rangle\langle 0_e| \quad (8.21)$$

where $\Gamma$ is the un-enhanced optical decay rate. Optical emission on the $E$ transition is described by:

$$\mathcal{L}_2 = \sqrt{\frac{4g^2}{\kappa} + \Gamma}\,|0_g\rangle\langle 1_e|\,. \quad (8.22)$$

Ground state spin relaxation is defined by these two super-operators:

$$\begin{aligned}\mathcal{L}_3 &= \sqrt{\frac{\Gamma_s}{2}}\,|0_g\rangle\langle 1_g|\,, \\ \mathcal{L}_4 &= \sqrt{\frac{\Gamma_s}{2}}\,|1_g\rangle\langle 0_g|\end{aligned} \quad (8.23)$$

where $\Gamma_s$ is the spin relaxation rate, note that we operate in the high temperature limit where the thermalized occupation of the two qubit states is equal.

Pure dephasing on the optical transition is defined according to:

$$\mathcal{L}_5 = \sqrt{\frac{\gamma_d}{2}}\left(|0_e\rangle\langle 0_e| + |1_e\rangle\langle 1_e| - |0_g\rangle\langle 0_g| - |1_g\rangle\langle 1_g|\right) \quad (8.24)$$

where $\gamma_d$ is the optical dephasing rate. Note that this operator is constructed to ensure that the ground state spin levels and excited state spin levels, respectively, experience common-mode noise cancellation due to any optical frequency variation.

Similarly, pure dephasing on the spin transition is defined according to:

$$\mathcal{L}_6 = \sqrt{\frac{\gamma_s}{2}} \left( |0_g\rangle \langle 0_g| + |0_e\rangle \langle 0_e| - |1_g\rangle \langle 1_g| - |1_e\rangle \langle 1_e| \right) \tag{8.25}$$

where $\gamma_s$ is the spin dephasing rate. These Lindblad terms are duplicated for the two ions.

Next we consider the projective measurement of a photon on a detector at time $t_0$. Our detector can measure in two orthogonally polarized modes ($\hat{c}_H$, $\hat{c}_V$) with equal efficiency. A single photon detection leads to a classical superposition of these two measurement cases, the density matrix after a collapse at time $t_0$ is given by:

$$\rho = \frac{1}{2} \left[ \hat{c}_H(t_0)\rho(t_0)\hat{c}_H^\dagger(t_0) + \hat{c}_V(t_0)\rho(t_0)\hat{c}_V^\dagger(t_0) \right]. \tag{8.26}$$

We can use standard quantum optics techniques to propagate the temporal detection modes through our measurement setup to the respective cavities. Considering the case of a time-delayed Mach-Zehnder interferometer with delay time $\Delta t = (L_V - L_H)/c$, as shown in Figure 9.5c and discussed in Section 9.5, we can write the two detection operators as:

$$\begin{aligned} \hat{c}_V(t_0) &= \hat{b}_2(t_0 - \frac{L_V}{c}) e^{-i\omega_2(t_0 - \frac{L_V}{c})} - \hat{b}_1(t_0 - \frac{L_V}{c}) e^{-i\omega_1(t_0 - \frac{L_V}{c})}, \\ \hat{c}_H(t_0) &= \hat{b}_2(t_0 - \frac{L_H}{c}) e^{-i\omega_2(t_0 - \frac{L_H}{c})} + \hat{b}_1(t_0 - \frac{L_H}{c}) e^{-i\omega_1(t_0 - \frac{L_H}{c})} \end{aligned} \tag{8.27}$$

where $\hat{b}_1$ and $\hat{b}_2$ are temporal photon mode operators in the waveguide just outside cavity 1 and cavity 2, respectively (as defined previously). Note that we have also transformed these operators into a frame rotating at each ion's emission frequency ($\omega_1$ and $\omega_2$, respectively). $L_V$ and $L_H$ correspond to the distance travelled by photons in the two arms of the interferometer.

Combining these measurement operators with Equation (8.20) we see that photon detection at time $t_0$ can be expressed as a quantum jump on the atomic state using the following two jump operators:

$$\hat{S}_V = 2g\sqrt{\frac{p_{\text{det}}\delta t}{\kappa}}\left(\hat{\sigma}_1^- + \hat{\sigma}_2^- e^{i[\phi+(\omega_2-\omega_1)(\Delta t-t_0)]}\right),$$
$$\hat{S}_H = 2g\sqrt{\frac{p_{\text{det}}\delta t}{\kappa}}\left(\hat{\sigma}_1^- - \hat{\sigma}_2^- e^{i[\phi-(\omega_2-\omega_1)t_0]}\right) \tag{8.28}$$

where $\hat{S}_V$ collapses the atomic state at time $t_0 - \frac{L_V}{c}$ and $\hat{S}_H$ collapses the atomic state at $t_0 - \frac{L_H}{c}$. Note that we have implicitly assumed that photons emitted from the two ions travel the same distance prior to arriving at the interferometer, to account for variations in optical phase associated with this path difference we add the phase factor $e^{i\phi}$.

Finally, we also consider the possibility of dark counts. Any experiments where $> 1$ photons are detected will be rejected and furthermore we assume that the detector dead-time is sufficiently short relative to average photon measurement rates that we can ignore its effect. We model a non-uniform dark count rate as $R(t)$. The density matrix at time t, conditioned on a single photon detection within a window $\delta t$ centered at time time $t_0$ is then given by:

$$\rho(t|t_0) = R(t_0)\delta t e^{\mathcal{L}t}[\rho(0)] + e^{\mathcal{L}(t-\tilde{t}_0)}[\hat{S}_H e^{\mathcal{L}\tilde{t}_0}[\rho(0)]\hat{S}_H^\dagger] + e^{\mathcal{L}(t-\tilde{t}_0+\Delta t)}[\hat{S}_V e^{\mathcal{L}(\tilde{t}_0-\Delta t)}[\rho(0)]\hat{S}_V^\dagger] \tag{8.29}$$

where $\mathcal{L}[\rho]$ is the no-jump component of time evolution defined in equation (8.20) applied to both ions, i.e.:

$$\mathcal{L}[\rho] = -\frac{i}{\hbar}\left[\hat{H},\rho\right] + \sum_i\left(\hat{\mathcal{L}}_i\rho\hat{\mathcal{L}}_i^\dagger - \frac{1}{2}\left\{\hat{\mathcal{L}}_i^\dagger\hat{\mathcal{L}}_i,\rho\right\}\right)$$
$$-\frac{2g^2 p_{\text{det}}}{\kappa}\left\{\hat{\sigma}_1^+\hat{\sigma}_1^-,\rho\right\} - \frac{2g^2 p_{\text{det}}}{\kappa}\left\{\hat{\sigma}_2^+\hat{\sigma}_2^-,\rho\right\}. \tag{8.30}$$

*Chapter 9*

# TWO ION ENTANGLEMENT EXPERIMENTAL SETUP

In this chapter we provide a detailed overview of the experimental setup used for two device measurements. A basic schematic is presented in Figure 9.2. Two nanophotonic devices are installed in the same He-3 cryostat. Device 1 is the same device studied in Chapter 3. Most entanglement experiments presented in this thesis concern Ion 1 in Device 1 and Ion 2 in Device 2, separated by ~ 30 MHz (Figure 9.1). In section 10.7 we demonstrate entanglement of Ions 1 and 3 in the same device, separated by ~ 470 MHz.

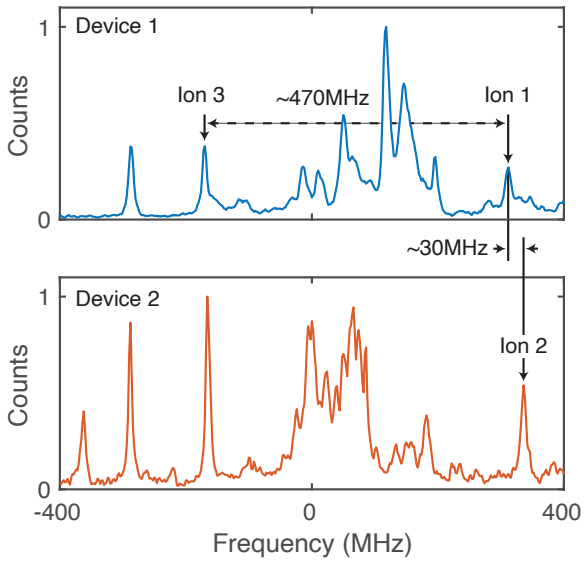


Figure 9.1: PL scans of ions in two devices used for Hong-Ou-Mandel and entanglement experiments. Ions 1 and 2 are in separate devices and are detuned by 30 MHz. Ions 1 and 3 are in the same device and detuned by 470 MHz.

This setup enables the following functionality which will be discussed further in the subsequent sections:

1. Laser setups for driving the ions' optical transitions. This is for initialization, entanglement and readout.

2. Microwave setups for driving the ions' spin transitions. An excited state transition is used during the initialization process, the ground state transition drives our qubit.

3. A detection setup which combines light from the two devices and routes it to single photon detectors for entanglement heralding and readout.

4. A phase stabilization setup which ensures that the relative optical path traversed by light from each of the two devices ($\phi$) does not vary.

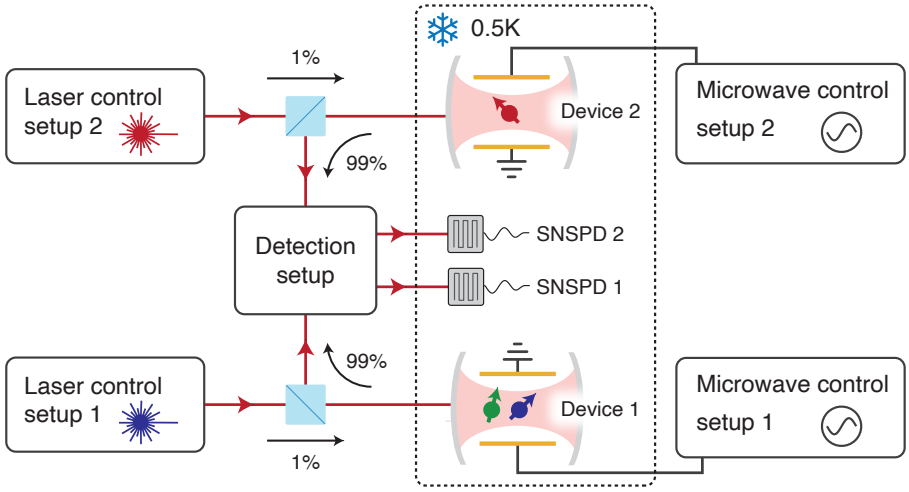


Figure 9.2: Experimental setup for the two ion measurements. Two devices are installed in a 0.5 K He-3 cryostat. Each device has a corresponding microwave setup for spin driving and an optical setup for initialization/readout. Single photons from ions inside the devices are routed to a detection setup which combines the optical paths before sending the photons to superconducting nanowire single photon detectors (SNSPDs). The SNSPDs are also installed in the 0.5K cryostat.

### 9.1 Cryogenics and Devices

The devices used in this experiment are discussed in Section 2.4. The detection efficiency for photons emitted in Device 1 is 0.98%, whereas photons emitted in Device 2 are detected with 0.48% efficiency. The discrepancy in detection efficiency is attributed to a lower free-space coupling efficiency for Device 2. All experiments were performed in a He-3 cryostat (Bluefors LD) at 500mK. The cryogenic setup is mostly explained in [155]; however, it was duplicated for this experiment in order to accommodate the second device within the same cryostat. The basic elements of the setup are as follows:

- Optical signals are fed in/out of the fridge via 1060XP fiber; once inside the cryostat an aspheric lens doublet focuses light onto the device surface. XYZ nanopositioners (Attocube) move the lens doublet relative to the device surface. This enables us to locate the individual nanophotonic resonators and optimize coupling.

- Nitrogen gas condensation is used to tune the cavity resonance to coincide with the ions' optical transitions. Nitrogen gas is frozen into a copper pipe inside the cryostat. The pipe is directed towards a device chip. A heater clamped to the pipe is used to sublimate the nitrogen which re-freezes onto the cavity thereby red-shifting the resonance. By controlling the amount of heating the cavity resonance can be precisely tuned. There is no discernible cross-talk between the two setups during this process.

- Superconducting coils are used to apply magnetic fields along the crystal's $c$ quantization axis. These are used to cancel earth's magnetic field and any residual fields present in our setup. Operating at the zero-field condition is required to maximize spin coherence.

- Coax lines with 0dB attenuators on each plate (for thermalizing the central conductor) are used to feed microwave signals to the still plate. The device is wire-bonded to a PCB launch board which connects to these coax lines.

- Superconducting nanowire single photon detectors (SNSPDs) are mounted on the same plate as the devices. An L-R shunt on the 4K plate enables automatic un-latching of the detectors. The detectors are biased through 10k$\Omega$ resistors with isolated voltage sources (SRS SIM 960). A bias tee (Minicircuits ZFBT-4R2GW+) is used to separate the low frequency biasing path from the high frequency detection path, photon signals are amplified with two low noise amplifiers (Minicircuits ZFL-1000LN+) in series.

## 9.2 Optical Control

The optical control setup is shown in Figure 9.3. All lasers are ultimately referenced to a Fabry-Perot cavity (Stable Laser Systems). The main experiment laser (Ti:Sapph, M2 Solstis titanium sapphire laser) and phase stabilization laser (ECDL 1, Moglabs Cateye external cavity diode laser) are both referenced to the cavity via Pound-Drever-Hall (PDH) locking [273] using two different modulation frequencies. The two initialization lasers (ECDL 2 and ECDL 3, Toptica DL Pro) are referenced to the Ti:Sapph laser via an offset frequency lock.

Prior to PDH locking, the Ti:Sapph is modulated with a 10 GHz phase EOM. The negative $1^{st}$ order sideband is locked to the cavity. The laser frequency can then be tuned within the bandwidth of the EOM by adjusting the sideband frequency. Note that light used in the locking setup is picked-off prior to this EOM, hence these (and the PDH) sidebands are not present in the experiment. The Ti:Sapph laser is used to address the A transition of all three ions studied in this experiment. It is first split into two paths (via BS1), one for each of the two devices. Each path then goes through an acousto optic modulator (AOM) setup (A3 and A4), these each contain two AOMs (Gooch and Housego, AOMO 3200-1113) in double-pass configuration which are used to generate laser pulses with short rise/fall times (20ns) and high extinction ratio (120dB). Furthermore, each setup can tune the laser frequency in a $\sim 400$ MHz bandwidth. This is used to shift the central laser tone in order to address Ion 1 in Device 1 and Ion 2 in Device 2.

The laser path going to Device 1 contains an additional 2-tone modulation setup (A5) which is used to entangle Ion 1 and Ion 3 in the same device. Specifically, it contains a single AOM in double-pass configuration (see Figure 9.3c) where both the $0^{th}$ and $-1^{st}$ order sidebands are accepted. It is aligned to balance the power in these two sidebands. Light entering this setup is resonant with Ion 1, the setup is driven at $(\omega_1 - \omega_3)/2$. This leads to the $0^{th}$ sideband addressing Ion 1 and the $-1^{st}$ sideband addressing Ion 3. Crucially, because these tones are generated by a single modulator, they are (passively) phase stable, this is crucial for the entanglement experiments discussed in Section 10.7. When we want to drive/read-out Ion 1 in isolation we simply do not drive setup A5. When we want to drive/read-out Ion 3 in isolation we reduce the drive frequency of A4 such that the output light is 40MHz closer to Ion 3, setup A5 is then driven at a lower frequency ($(\omega_1 - \omega_3 - 40)/2$ MHz) such that $-1^{st}$ sideband is still resonant with Ion 3; however, the $0^{th}$ sideband is no longer resonant with Ion 1. In fact, we choose the 40MHz frequency shift such that

the $0^{th}$ sideband avoids exciting any ions in the device.

While the two tones generated by A5 are passively phase stable, for entanglement experiments involving two separate devices, we also need the two optical paths originating from the Ti:Sapph and going to Device 1 and Device 2 to be phase-stable relative to each other. The phase stabilization process is described in detail in Section 9.6. It relies on a measurement of the relative optical path phase difference using a separate laser (ECDL 1), which is also split into the two device excitation paths at BS1. In order to control whether we generate pulses of light at the experiment wavelength (984.5 nm) or at the phase stabilization wavelength (987.9 nm), we introduce two additional single-pass AOM shutters (A1 and A2) which select whether we send light from the Ti:Sapph or ECDL 1.

We also use two additional lasers (ECDL 2 and ECDL 3) to address the F transitions of ions in Device 1 and Device 2, respectively. Setups A6 and A7 are used to generate pulses and tune each laser on resonance with the required transition. Specifically, ECDL 3 needs to address the $F_1$ and $F_2$ transition of Ion 2, which are separated by 8 MHz. ECDL 2 needs to address the $F_1$ and $F_2$ transitions of Ions 1 and 3 which are separated by $\sim$ 500 MHz. In order to achieve this large spread of frequencies we use three AOMs in double-pass configuration (depicted in Figure 9.3b) which enables a 600 MHz tuning range. The two ECDL initialization paths are combined with their respective Ti:Sapph laser paths via BS2 and BS3 before being sent to the two devices.

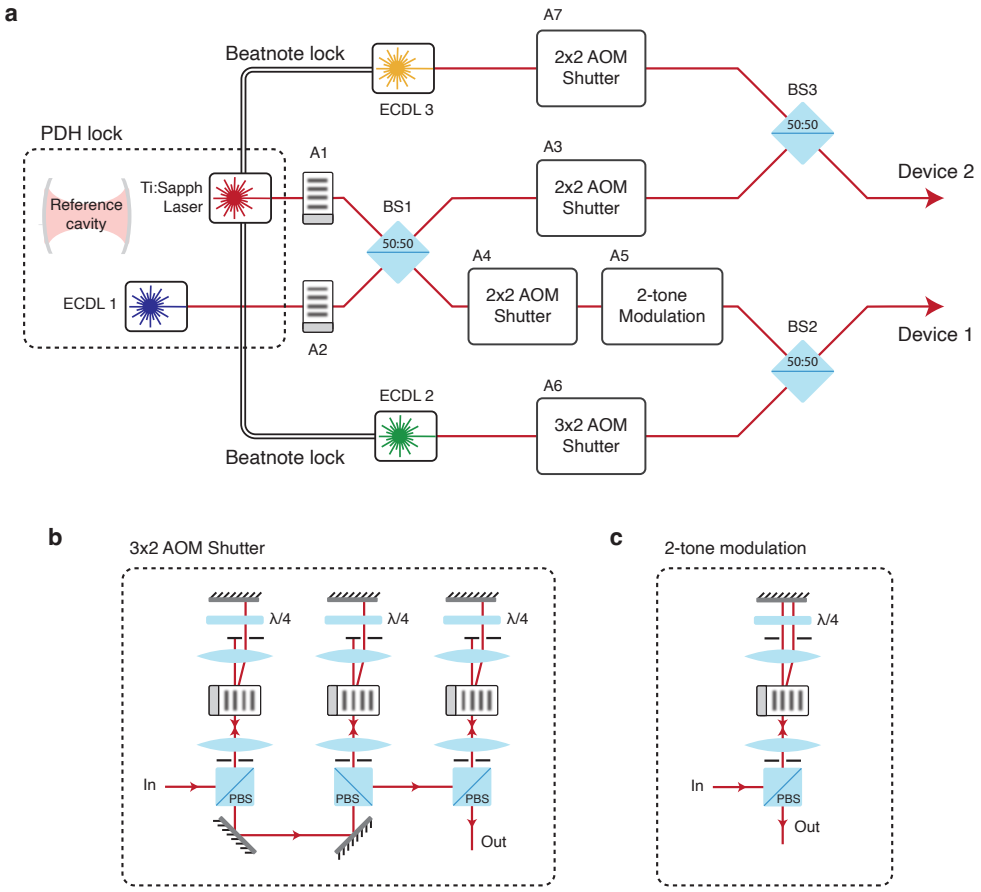


Figure 9.3: Laser setup for the two ion measurements. a) A Titanium Sapphire laser (used to address the ions' A transitions at 984.5 nm) and an external cavity diode laser (ECDL 1, used for phase stabilization at 987.9 nm) are both locked to a stable reference cavity using Pound-Drever-Hall (PDH) locking. These lasers are each gated with a single AOM shutter before being combined and split into two paths on a 50:50 beamsplitter. These paths ultimately reach device 1 and device 2, respectively. Each path has a 2x double-pass AOM shutter setup (labelled as 2x2 AOM shutter) for frequency tuning and fast, high-extinction pulse generation, one path has an additional 2-tone modulation setup for generating phase-locked laser tones. Two additional lasers (ECDL 2 and ECDL 3) are offset-frequency locked to the Ti:Sapph and modulated with AOM shutters, they are used for intialization of device 1 and 2, respectively. The use of a 3x2 shutter after ECDL 2 enables greater frequency tuneability. b) 3x double pass aom setup provides a high extinction ratio and large frequency tuneability (600 MHz). c) 2-tone modulation setup generates two phase-locked laser tones separated by 468 MHz.

### 9.3 Microwave Control

See Figure 9.4 for a schematic of the setup described in this section. Microwave tones at 3.37 GHz, used to drive the excited state spin transition, are generated with an RF signal generator (SRS SG380), gated with a microwave switch (Minicircuits ZASWA-2-50DRA+) and amplified (Minicircuits ZHL-16W-43-S+). Control pulses at the 675 MHz ground state qubit transition frequency are generated via heterodyne mixing: an IF tone at 275 MHz generated by the experiment control electronics (see Section 9.4) is mixed with a local oscillator at 950 MHz (Holzworth HS 9002A). The image is filtered out using a combination of bandpass and low pass filters. The ground state pulses are amplified (Amplifier Research 10U1000 for Device 1 and Minicircuits ZHL-20W-13SW+ for Device 2) and combined with the excited state pulses using a diplexer (Marki DPXN2) before being sent to the device.

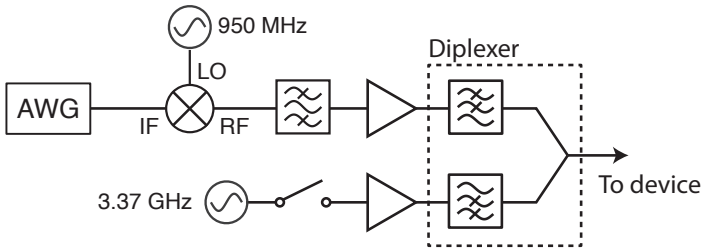


Figure 9.4: Microwave setup for spin driving. Qubit pulses at 675 MHz are generated with a heterodyne mixing scheme where a 275 MHz IF tone from an AWG is mixed with a 950 MHz local oscillator. A bandpass filter is used for image rejection. A second source at 3.37 GHz is used to drive an excited state spin transition during initialization, this is gated with a microwave switch. Both signals are independently amplified and subsequently combined on a diplexer before being sent to the device.

## 9.4 Real-time Signal Processing

There are several types of real-time experiment flow control and feedforward required for these measurements. These are listed below:

1. The ion state should only be read out when a photon is successfully detected. Without this, each entanglement attempt + associated readout would take several milliseconds which would make the experiments prohibitively long.

2. The wait time during the optical rephasing period needs to equal the previously measured photon emission time.

3. A relative phase shift of $-t_0\Delta\omega_0$ is applied between the two devices' microwave driving quadratures between entanglement heralding and readout (see Section 8.4).

4. The phase of optical drive used to excite the ions needs to counteract any phase drift between the two optical paths associated with the two devices.

In early stages of this experiment the real-time flow control (Item 1) and the feedforward required to correct stochastic phase (Item 3) were implemented via a field programmable gate array (FPGA, Red Pitaya STEMlab). At the time, we were entangling two ions in the same device separated by $\approx 470$ MHz (see Section 10.7), the 60MHz analog to digital converter (ADC) bandwidth was insufficient given the optical frequency difference. Instead, SNSPD detection signals were sent to a time to amplitude converter (Ortec 566) which converts the arrival time difference between two pulses into the amplitude of a fixed duration output pulse. The 14 bit resolution of the Red Pitaya's ADC was then sufficient to achieve $\approx 150$ ps timing resolution. The FPGA was then used to select and play a specific waveform on an arbitrary waveform generator (Tektronix 5204 AWG) via the pattern jump input.

Ultimately, this solution was quite cumbersome and required frequent calibration of the analogue time to amplitude converter's response. Hence, we switched to using a Quantum Machines Operator X system (subsequently referred to as OPX). This system has 10 analogue output channels with 350MHz bandwidth and 14 bit resolution, 10 TTL output channels and 2 analogue input channels with 350 MHz bandwidth (14 bit resolution).

The two SNSPDs used in these experiments are connected to the two analogue inputs of the OPX. One directly, the other via the high-frequency port of a 10 MHz diplexer. The low frequency port is connected to an avalanche photodiode (APD, see Section

9.6). This lets us use one analogue input for both phase stabilization and photon detection (since these operations are never performed simultaneously). Despite the 350 MHz input bandwidth, the OPX has a high resolution timetagging capability with resolution <50 ps (this is achieved by using the vertical 14 bit resolution and fitting the photon pulse waveforms) which is sufficient for these experiments.

The OPX requires approximately 400ns between photon detection and performing some real-time experiment control based on the measured time. Critically, this is shorter than our spin coherence time (we can apply dynamical decoupling during the wait). It is also shorter than our optical transition frequency correlation timescale which is necessary for the dynamic rephasing.

### 9.5 Detection and Time-delayed Interferometer

This section describes the detection setup. Its role is to combine the optical modes from the two devices and measure incident photons in a manner which projects the two ions onto an entangled state.

Figure 9.5a shows a schematic of the setup. Light from the two devices impinges on a polarizing beamsplitter (PBS1). Two electronic polarization controllers (OZ Optics EPC) are used to ensure that the incident light from Device 1 (Device 2) transmits through (reflects from) the PBS with maximal efficiency. Light from the two devices are now in the same spatial mode, albeit with orthogonal polarizations.

Light passes through an AOM (A8) which routes the light between a high sensitivity avalanche photodiode (APD) or a mode combiner/SNSPD setup. The APD is used to measure the relative optical phase as described in Section 9.6. There are three possibilities for the mode combiner + SNSPD setup which are described next.

Case 1 is depicted in Figure 9.5b. It consists of a single SNSPD, note that the SNSPD we use is polarization insensitive, therefore it measures light from either device with equal efficiency. This setup is used for the single device entanglement measurements presented in 10.7. Since photons emitted from Ions 1 and 3 in Device 1 will have the same polarization, measuring them in this fashion will project an entangled state. Note, however, that this setup cannot be used to prepare entangled states between the two devices since the SNSPD measurement is equivalent to classically combining two orthogonal measurements, i.e.:

$$\rho \rightarrow \langle H, t_0 | \rho | H, t_0 \rangle + \langle V, t_0 | \rho | V, t_0 \rangle \tag{9.1}$$

where $|H, t_0\rangle$ is a photon with horizontal polarization at time $t_0$ in the temporal continuum basis.

Case 2, depicted in Figure 9.5c, provides a method of entangling ions in two separate devices using only one detector. This setup was used to obtain the results in Chapter 10 before we installed a second SNSPD in the experimental setup. The input state to the interferometer is:

$$|\psi\rangle = \frac{1}{\sqrt{2}}(|0_g 1_g\rangle\,|V\rangle + |1_g 0_g\rangle\,|H\rangle\,e^{i\Delta\omega_0 t_0}) \tag{9.2}$$

where the photons are labelled according to their polarization state. A half wave plate is used to rotate the photon polarizations by 45 degrees such that the two output modes of PBS 2 contain a combination of photons from each of the two devices. After passing through PBS 2 the quantum state can be written as:

$$|\psi\rangle = \frac{1}{2}(|0_g 1_g\rangle + |1_g 0_g\rangle\,e^{i\Delta\omega_0 t_0})\,|V\rangle + \frac{1}{2}(|0_g 1_g\rangle - |1_g 0_g\rangle\,e^{i\Delta\omega_0 t_0})\,|H\rangle \tag{9.3}$$

where the vertically polarized photon $|V\rangle$ populates the lower arm of the Mach-Zehnder (MZ) interferometer and the $|H\rangle$ photon populates the upper arm of the interferometer. Photons propagating in the lower arm are coupled into optical fiber and delayed by a time $\Delta t = (L_V - L_H)/c$ which is chosen to satisfy $\Delta t = \pi/\Delta\omega_0$. After recombining on PBS 3 the quantum state is given by:

$$\begin{aligned}|\psi\rangle &= \frac{1}{2}(|0_g 1_g\rangle + |1_g 0_g\rangle\,e^{i\Delta\omega_0 t_0})\,|V\rangle + \frac{1}{2}(|0_g 1_g\rangle - |1_g 0_g\rangle\,e^{i\Delta\omega_0 (t_0+\Delta t)})\,|H\rangle \\ &= \frac{1}{2}(|0_g 1_g\rangle + |1_g 0_g\rangle\,e^{i\Delta\omega_0 t_0})(|H\rangle + |V\rangle)\end{aligned} \tag{9.4}$$

where $|H\rangle$ and $|V\rangle$ are now the same spatial mode but orthogonally polarized. The photons are now coupled to the same SNSPD and detected. Note that according to the transformation in Equation (9.1) the resulting state will now be:

$$|\psi\rangle = \frac{1}{\sqrt{2}}(|0_g 1_g\rangle + |1_g 0_g\rangle\,e^{i\Delta\omega_0 t_0}) \tag{9.5}$$

as required.

The final detection setup considered (case 3, Figure 9.5d) uses two SNSPDs. A half waveplate rotates the photon polarizations by 45 degrees (as before), this time the output ports of PBS 2 are coupled to the two detectors. This setup was used for the Hong-Ou-Mandel measurements discussed in Chapter 7. While the experimental results presented in this thesis were obtained using the MZ interferometer, we are currently running entanglement experiments in this configuration. In this case one detector heralds the $|\psi^+\rangle$ type entangled state: $1/\sqrt{2}(|0_g 1_g\rangle + |1_g 0_g\rangle\,e^{i\Delta\omega_0 t_0})$, the other detector heralds the $|\psi^-\rangle$ type entangled state: $1/\sqrt{2}(|0_g 1_g\rangle - |1_g 0_g\rangle\,e^{i\Delta\omega_0 t_0})$.

Since the two detectors send electrical signals to different OPX inputs, the different entangled state phases can be identified and compensated in the subsequent microwave control (via a conditional $\pi$ differential $z$ rotation).

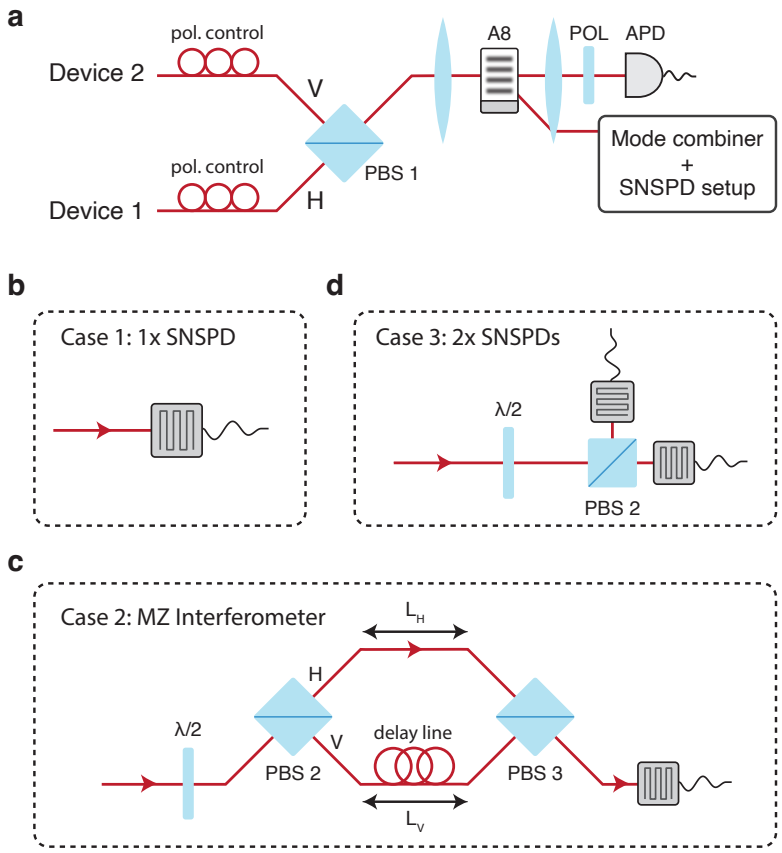


Figure 9.5: Detection setup detail. a) Light from two separate devices is combined on a polarizing beamsplitter (PBS). The polarization in each path is optimized to ensure maximum transmission/reflection into the same spatial mode, albeit with orthogonal polarization states. The light passes through an acousto-optic modulator which routes the $0^{th}$ order to a polarizer (POL) and avalanche photodiode (APD), used for heterodyne phase measurements; the $1^{st}$ order is routed to one of three different measurement setups depicted in the subsequent subfigures. b) For entanglement measurements with two ions in the same device, a single SNSPD is sufficient. c) For entangling two ions in two separate devices a single detector can still be used, but requires a time-delayed Mach-Zehnder interferometer prior to the detector. d) For the Hong-Ou-Mandel indistinguishability measurements, two separate detectors are required. The half wave plate is used to balance the likelihood of photons from each device reaching either of the two detectors.

## 9.6 Optical Phase Stabilization

The single photon entanglement heralding protocol prepares a Bell state with phase that depends on the relative optical paths between the excitation laser and detector for each of the two devices ($\phi$), see [263] and Equation (8.5). To ensure preparation of a deterministic Bell state, this phase must be actively stabilized.

A simplified version of the experimental setup relevant to this section is presented in Figure 9.6a. The experiment laser ($\lambda_1$) is gated by a single acousto-optic modulator shutter (A1) and split by a beamsplitter (BS1) into two paths. Each path travels through a high-extinction AOM shutter setup (A3 and A4, respectively), which additionally impart a relative optical frequency shift ($\Delta\nu$) and phase ($\Delta\Phi$), these can be controlled via the frequency and phase of the microwave tones driving the acousto-optic modulators. A polarizing beamsplitter (PBS1) recombines the two paths and a final AOM shutter (A8) routes the light towards a single photon detector (SNSPD) or avalanche photodiode (APD). The optical devices have not been included in this diagram for simplicity.

To ensure a fixed Bell State phase, the relative optical phase $\phi = 2\pi \times (L_2 - L_1)/\lambda_1$ must be static (where $L_1$ and $L_2$ are the optical path lengths travelled by laser pulses and photons associated with device 1 and device 2, respectively). This is achieved by, first, measuring the relative optical phase, then during the subsequent optical excitation of the two ions, the relative driving phase of A3 and A4 ($\Delta\Phi$) is adjusted to compensate.

The optical phase is measured using a secondary laser ($\lambda_2$) which is detuned from the optical cavity resonance by 3.4 nm, this minimizes device heating during the phase measurement and obviates the need for additional qubit initialization between phase measurement and entanglement heralding. Not only does this reduce the time per entanglement attempt (thereby increasing the entanglement rate), but it also ensures minimal wait time between the phase measurement and subsequent optical excitation, thereby minimizing the impact of optical phase drift.

The phase is measured using heterodyne beat-note detection. A 10 $\mu$s long pulse of light at wavelength $\lambda_2$ is generated by A2. A3 and A4 are used to impart a 5 MHz relative frequency shift between light travelling in the two paths. A8 routes light to the APD which is connected to an analog input of the OPX. The OPX measures this beatnote and demodulates it with a 5 MHz carrier tone to extract an instantaneous optical phase ($\phi$). This measurement is performed with 1.7 nW of light incident on the APD, a Fourier spectrum of the beatnote yields a signal to noise ratio of 18.

Since the two path lengths associated with the two devices are quite imbalanced ($L_2 - L_1 \approx 3$ m), even if the optical phase at the locking wavelength ($\lambda_2$) is stabilized, any variation in optical frequency difference between the locking and measurement lasers will cause a variation in the optical phase at the measurement wavelength. Specifically, this residual phase variation is given by:

$$\phi_{\lambda_2} - \phi_{\lambda_1} = \left(\frac{2\pi}{\lambda_2} - \frac{2\pi}{\lambda_1}\right)(L_2 - L_1) \tag{9.6}$$

To ensure that the phase stability at the locking wavelength is transferred to the measurement wavelength, both lasers are independently referenced and stabilized to a fabry-perot cavity via pound-drever-hall (PDH) locking [273].

To verify the optical phase stability at the experiment wavelength ($\lambda_1$), we perform a secondary heterodyne beatnote measurement (probe). However, this time, we use A1 to generate a pulse at $\lambda_1$ and we use A3 and A4 to impart a 26 MHz frequency shift which matches the frequency difference of the optical transitions of the two ions in our experiment.[1] We apply this measurement pulse with a time delay of 30 $\mu$s relative to the phase stabilization pulse, this approximately matches the time delay between stabilization and entanglement heralding in the main experiment. The whole experiment is repeated every 68.5 $\mu$s. We use the APD to measure the instantaneous optical phase at the measurement wavelength. See Figure 9.6a (inset) for the pulse sequence. This experiment is repeated multiple times, and the Fourier transform of the resulting time-dependent optical phase provides the phase noise frequency spectrum.

We now consider three distinct cases. In the first panel of figure 9.6b we see the noise spectrum when the phase correction is turned off (i.e., no phase stabilization). In the second panel, optical phase correction during the $i^{\text{th}}$ probe ($\Delta\Phi_i$) is chosen to counteract the phase measured during the previous stabilization pulse ($\phi_i$), i.e., $\Delta\Phi_i = -\phi_i$. In the final case (bottom panel), we also consider a linear extrapolation of the phase trajectory, we calculate the phase difference between consecutive stabilization pulses, and apply this as an additional correction: $\Delta\Phi_i = -\phi_i - \alpha(\phi_i - \phi_{(i-1)})$, note the scaling factor $\alpha < 1$ accounts for the time-separation between stabilization and probe pulses being less than the separation between consecutive probe pulses. Note the reduction in integrated phase noise between each of these three cases.

[1] Note that over long periods of time (weeks) the ion frequency difference changes, the optical frequency here matched the ion frequency difference at time of measurement.

To quantify the phase stability at the measurement wavelength, Figure 9.6c shows a histogram of optical phases accumulated over 20 minutes of integration time, using the linearly extrapolated correction. The resulting standard deviation ($\sigma = 0.037 \times 2\pi$ rad) corresponds to a limitation in the entangled state fidelity of $\mathcal{F} < 0.987$.

Finally, we also verify the phase stability when measuring with the SNSPD. We attenuate the probe pulses to the single-photon level and use A8 to route them to the SNSPD. We integrate the beatnote over 1 minute and histogram the resulting single photon arrival times in Figure 9.6d, the resulting contrast is 0.944, thereby verifying that timing jitter in the SNSPD measurement is not a significant limitation in these experiments.

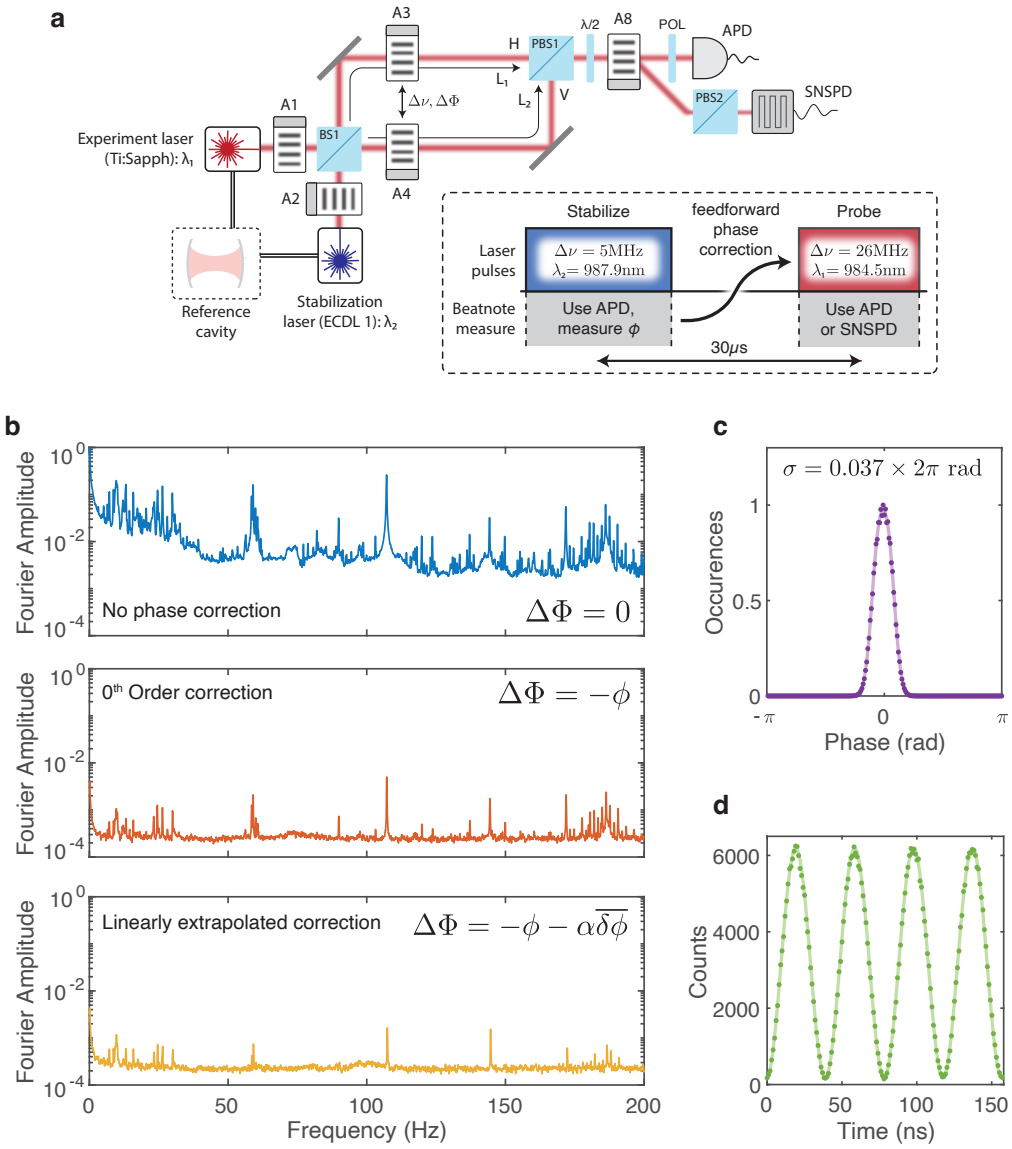


Figure 9.6: Optical phase stabilization for two-ion entanglement. a) Phase stabilization setup. Light from the stabilization laser passes through two arms of the interferometer. Each arm involves an AOM setup that shifts the light frequency by a different amount. After subsequent recombination, an APD measures the beatnote and extracts a relative phase. During a subsequent ion excitation pulse with the experiment laser, the AOM phase is adjusted to compensate for the previously measured phase, thereby counteracting any phase drift. b) Fourier spectra of the optical phase noise without phase correction, with a $0^{\text{th}}$ order correction and with a linearly extrapolated correction. c) Histogram of optical phases measured with the experiment laser over 20 minutes. The RMS phase fluctuation is $0.037 \times 2\pi$ rad d) Experiment laser beatnote with a frequency matching the ion optical frequency difference, integrated over 1 minute and detected with the SNSPD.

*Chapter 10*

# TWO ION ENTANGLEMENT EXPERIMENTAL RESULTS

## 10.1 Detailed Experimental Protocol

In this section we provide a detailed description of the protocol used to implement the dynamic rephasing entanglement experiments described in Section 8.3. An overview of the sequence is presented in Figure 10.1, it is split into 4 segments:

1. $|\text{aux}\rangle$ initialization prepares the ion into the qubit manifold.
2. The entanglement sequence initializes the qubit measures the optical phase, $\phi$, and performs a single entanglement attempt.
3. Dynamic rephasing is performed only if a photon is detected.
4. Readout is also only performed if an entanglement attempt is successful.

If 50 consecutive entanglement attempts fail, the $|\text{aux}\rangle$ initialization step is repeated. The total time spent per entanglement attempt is 81 $\mu$s.

Note, throughout this section reference should be made to the energy level diagram and transition labels in Figure 2.2.

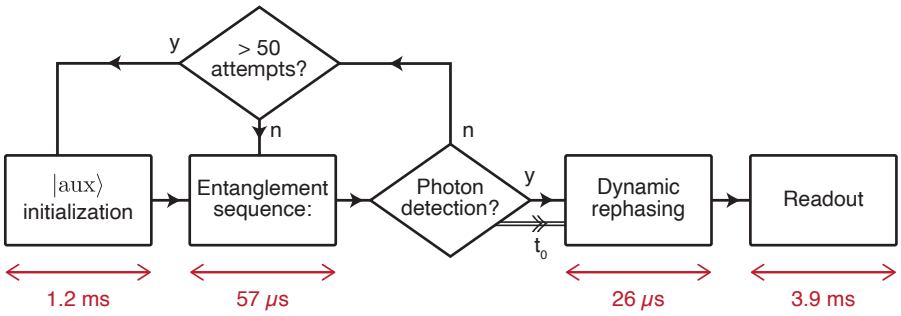


Figure 10.1: Experiment sequence. Dynamic rephasing and readout are only performed when the entanglement is successfully heralded. If there are 50 failed entanglement heralding attempts, the ion is initialized back into the qubit manifold. The duration for each step has been noted.

### |aux⟩ Initialization

Figure 10.2 depicts this part of the sequence. 2.5 $\mu$s long pulses are alternately applied to the $F_1$ and $F_2$ transitions of each ion. These are repeated 200 times. Subsequently we wait for 240 $\mu$s to allow any long-lived photo-luminescence to decay (associated with other ions overlapping with the $F$ transitions). Ultimately, all population is transferred from the |aux⟩ state into the qubit manifold.

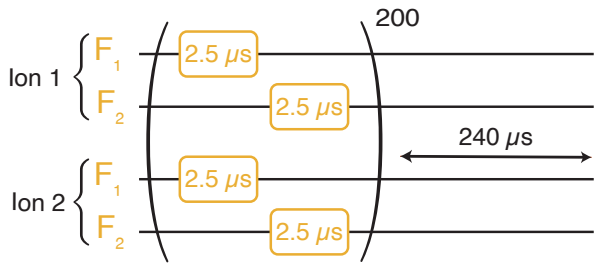


Figure 10.2: |aux⟩ initialization. Optical pulses applied to the $F$ transitions of both ions initialize them into the qubit manifold.

### Entanglement Sequence

This part of the sequence is depicted in Figure 10.3. The sequence starts by initializing the qubit into the $|0_g\rangle$ state[1]. This is achieved by applying consecutive $\pi$ pulses to the optical $A$ transition and excited state microwave $f$ transition. Any population in $|1_g\rangle$ is transferred to $|1_e\rangle$ from where it decays to $|0_g\rangle$. this process is repeated 12 times simultaneously to both ions to maximize the initialization fidelity.

Subsequently, the optical phase between the two device paths ($\phi$) is measured using the heterodyne beatnote method that was described in Section 9.6, all subsequent optical pulses applied to Ion 1 have been phase-shifted to compensate for this drift ($\Delta\Phi$ $z$ rotation applied to Ion 1 $A$ transition drive). Next, a weak superposition of $|0_g\rangle$ and $|1_g\rangle$ states is prepared by applying a $0.18\pi$ pulse to the qubit transition, $g$ (to both ions). Note that the rotation angle is selected to balance the infidelity associated with $|1_g 1_g\rangle$ at large angles and the infidelity associated with dark counts that dominates at small angles, see Section 10.6 for more detail. Subsequently, both ions are optically excited and entanglement is heralded if a single photon is detected in a window of duration $\tau_R = 3$ $\mu$s. Finally, two spin $\pi$ pulses are applied, separated

[1]Note that this is required after every failed entanglement attempt, this is because undetected photon emissions scramble the ground state qubit phase, hence, after a failed attempt, unitary operations cannot be used to return the qubit to $|0_g\rangle$.

by 5.8 $\mu$s. This dynamical decoupling sequence provides sufficient time for the OPX to determine whether entanglement was successfully heralded[2].

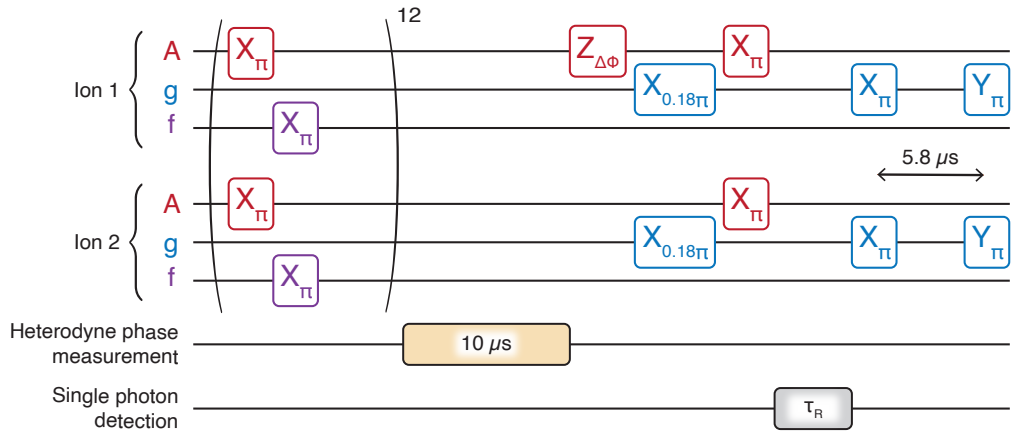


Figure 10.3: Entanglement sequence. The qubits are initialized and the relative optical phase is measured and corrected. Subsequently, a weak superposition of $|0_g\rangle$ and $|1_g\rangle$ is prepared and the qubits are optically excited. Photon detections within a window of duration $\tau_R$ are used to herald entanglement. A spin dynamical decoupling sequence provides sufficient time for the OPX to determine whether to proceed to the dynamic rephasing step.

### Dynamic Rephasing

Conditioned on a photon detection during the heralding window, the sequence proceeds to the dynamic rephasing step depicted in Figure 10.4. One more dynamical decoupling period is applied, then the spin is rephased for a duration $\tau_R - t_0$ (where $t_0$ is the photon detection time), this duration corresponds to the time spent in the ground state manifold during the preceding entanglement heralding window. Next, the optical coherence is rephased by optically exciting the ions, waiting for $t_0$ and then applying a second optical $\pi$ pulse to return the ion to the ground state[3]. Then, the phase of Ion 1's qubit drive is shifted by $\Delta\omega_0 t_0$ as described in Section 8.4. Finally, three more dynamical decoupling periods are applied, where $\pi$ pulses are simultaneously applied to the ground and excited states.

The role of this dynamical decoupling sequence is to mitigate error introduced by imperfect optical $\pi$ pulses during the preceding optical rephasing step. Specifically,

[2]Note that using an even number of $\pi$ pulses ensures that, if unsuccessful, the subsequent qubit initialization step will start with most population already in the $|0_g\rangle$ state.

[3]Note that the two optical pulses are applied about the $+X$ and $-X$ axes, the flipped Rabi vector acts to cancel any pulse area errors.

any population left in $|0_e\rangle$ will decay to $|1_g\rangle$ if we wait for a duration longer than the optical lifetime. While this will not improve the entangled state coherence[4], it will improve the fidelity of the $z$ basis measurement. Note, however, that we cannot wait sufficiently long ($\sim 10\ \mu$s) without the spin decohering, qubit dynamical decoupling fixes this. Applying excited state $\pi$ pulses ensures that the residual excited state population will decay to the correct state even when a ground state $\pi$ pulse has exchanged the $|0_g\rangle$ and $|1_g\rangle$ populations[5].

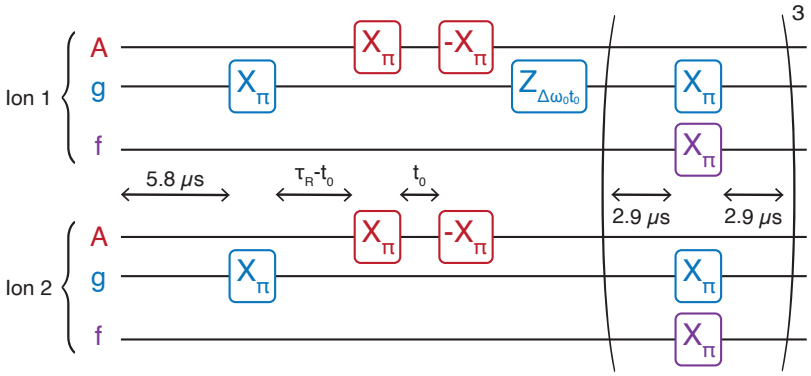


Figure 10.4: Dynamic rephasing sequence. The spin is rephased for a duration of $\tau_R - t_0$ where $\tau_R$ is the heralding window size and $t_0$ is the photon detection time. The optical coherence is rephased for a duration $t_0$. A $z$ rotation applied to Ion 1's ground state drive corrects the stochastic photon-emission induced phase.

### Readout

Finally, the two qubits are read out using the sequence depicted in Figure 10.5. 100 optical $\pi$ pulses are applied to Ion 2, each followed by a 6 $\mu$s photon detection window. the process is repeated for Ion 1 with a 10 $\mu$s detection window. Ground state $\pi$ pulses applied to both ions exchange the $|0_g\rangle$ and $|1_g\rangle$ populations and then the readout pulses are repeated.

Table 10.1 summarizes the photon counts required for the four different population assignments. All other cases are discarded. The two-qubit readout efficiency is approximately 18%. Note that we use the convention $|\text{Ion 2, Ion 1}\rangle$ when representing population assignments throughout this chapter.

[4]The emission would cause a stochastic phase on the entangled state.

[5]This is because $|0_e\rangle$ only decays to $|1_g\rangle$ and $|1_e\rangle$ only decays to $|0_g\rangle$.

| Assignment | Read Period 1 | Read Period 2 | Read Period 3 | Read Period 4 |
|---|---|---|---|---|
| $\|0_g 0_g\rangle$ | 0 | 0 | $\geq 1$ | $\geq 1$ |
| $\|0_g 1_g\rangle$ | 0 | $\geq 1$ | $\geq 1$ | 0 |
| $\|1_g 0_g\rangle$ | $\geq 1$ | 0 | 0 | $\geq 1$ |
| $\|1_g 1_g\rangle$ | $\geq 1$ | $\geq 1$ | 0 | 0 |

Table 10.1: Population assignments based on different photon detection possibilities (how many photons were detected in each read period). Read periods are depicted in Figure 10.5.

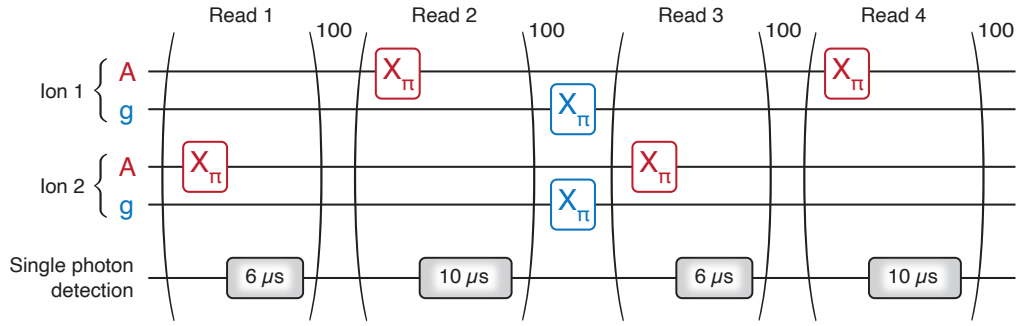


Figure 10.5: Readout pulse sequence. Each Ion is optically excited 100 times, photons are counted after each excitation period. The $|0_g\rangle$ and $|1_g\rangle$ populations are then exchanged and the readout process is repeated.

## 10.2 Dynamical Decoupling and Photonic Coherence

This section presents experimental results for the three entanglement protocols discussed in Section 8.3.

Figure 10.6a shows the entangled state coherence as a function of photon measurement time for the Ramsey entanglement protocol. The plotted result has been corrected for readout infidelity according to the procedure described in Section 3.3, but applied to the two qubit measurement. The measurement is fitted to a decaying oscillation with a Gaussian envelope with form:

$$C(t_0) = A\cos(\Delta\omega t_0 + \phi)e^{-t_0^2/\tau^2}, \tag{10.1}$$

The oscillation frequency of $\Delta\omega = 30.8 \pm 0.2$ MHz matches the two ions' optical frequency difference and the Gaussian decay timescale of $\tau = 160 \pm 40$ ns matches well with the predicted value of $180 \pm 9$ ns for two ions experiencing uncorrelated optical spectral diffusion. The oscillation contrast is $A = 0.35 \pm 0.03$, which limits the entangled state fidelity to $\mathcal{F} < 0.83$. A detailed discussion of limitations to this coherence is given in section 10.6.

The second protocol we consider involves pre-compensated phase accumulation for a duration $\tau_0$ prior to entanglement heralding. Figure 10.6b shows the resulting entangled state coherence for three different values of $\tau_0 = 150,\ 450,\ 750$ ns. The fraction of optical emission which yields a coherent entangled state is still limited by the optical frequency stability (i.e., the optical Ramsey coherene time); however, the photon emission time corresponding to maximal coherence can now be controlled and matches $\tau_0$. This enables us to herald with a window size that is twice as large compared to Figure 10.6a, and also avoid regions of the photon emission which overlap with laser reflections.

The final protocol involves rephasing the optical coherence for a duration $t_0$ after heralding an entangled state. Experimental results are shown in Figure 10.6c. The fraction of photonic emission which heralds a coherent entangled state is considerably increased. The experimental results are fitted to:

$$C(t_0) = A\cos(\Delta\omega_0 t_0 + \phi)e^{-t_0/\tau} \tag{10.2}$$

where $\Delta\omega_0$ is now fixed to the laser frequency difference, $A = 0.62 \pm 0.02$ and $\tau = 1070 \pm 50$ ns are extracted from the fit. For two ions with optical lifetimes $T_1^{(1)}$ and $T_1^{(2)}$ and pure optical dephasing rates of $\gamma_d^{(1)}$ and $\gamma_d^{(2)}$ we would expect the exponential decay timescale to satisfy $1/\tau = \gamma_d^{(1)} + \gamma_d^{(2)} + 1/(2T_1^{(1)}) + 1/(2T_1^{(2)})$ which is estimated to be $970 \pm 30$ ns (parameter values can be found in table 10.2). This simple model matches reasonably well with the experimental result; for a more comprehensive analysis see section 10.6 where the experimental results are compared to an ab-initio model.

Crucially, we can see that the coherence decay of the entangled state is now limited by the ions' optical lifetimes, even though the transitions are not Fourier limited. To our knowledge, this has not been demonstrated in any other entanglement experiments.

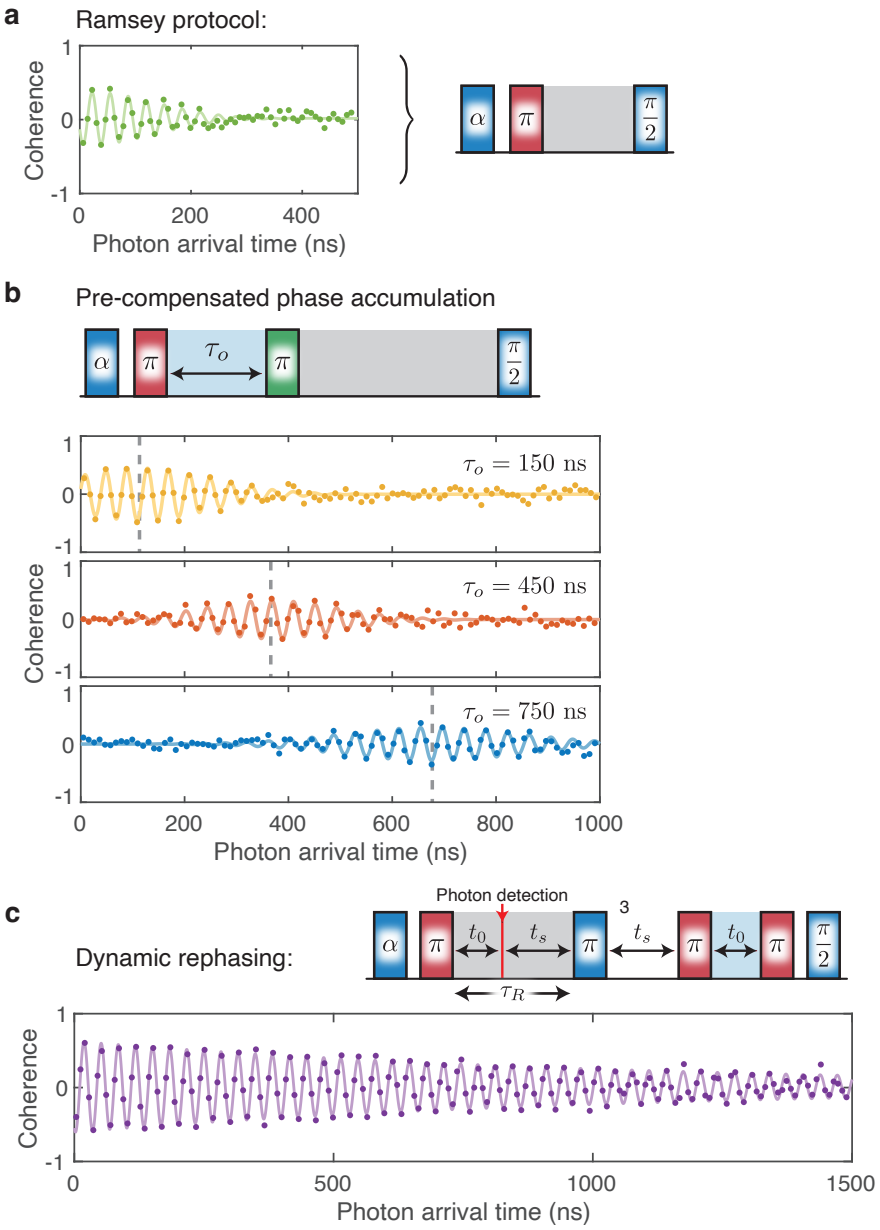


Figure 10.6: Photon detection time resolved coherence of different entanglement protocols. Detailed pulse sequences for all protocols can be found in Figure 8.1. a) Basic Ramsey protocol, note one-sided decay with $T_2^*$-dependent timescale. b) Precompensated rephasing protocol with three different phase compensation time periods: $\tau_0$ = 150, 450, 750 ns. Note the corresponding shift in rephasing time. Coherence decay is now two-sided but still limited by $T_2^*$. c) Dynamic rephasing protocol: the coherence decay now depends on the ion lifetime.

### 10.3 Feedforward for Frequency Erasure

In order to ensure deterministic preparation of a specific Bell state, we need to correct the stochastic phase associated with the random photon emission time ($t_0$) in each experiment (see Section 8.4 and [269]). This phase is given by $\Delta\omega_0 t_0$ for the dynamic rephasing protocol where $\Delta\omega_0$ is the laser drive frequency difference. Without this correction, if averaged over multiple experiment repetitions, the density matrix will be identity in the single excitation subspace $\rho = 1/2(|0_g 1_g\rangle \langle 0_g 1_g| + |1_g 0_g\rangle \langle 1_g 0_g|)$, this is a classically correlated state, not a quantum entangled state. This is depicted in the upper panel of Figure 10.7 where we see the coherence oscillating at 30.3 MHz, if one ignored the photon arrival time the resulting average coherence would be 0. Correcting this stochastic phase for ions in two separate devices is quite a simple task. One simply needs to change the phase of the X and Y spin driving quadratures for one of the two devices. This performs a differential z-rotation thereby applying a phase shift to the resulting Bell state measurements. The z-rotation angle is chosen to precisely counteract the stochastic phase, i.e., $-\Delta\omega_0 t_0$. When we repeat the experiment with this phase correction (Figure 10.7, lower panel), we see that the fast oscillation has indeed been counteracted and the coherence will average to a non-zero value. The gradual decay in coherence is due to the combination of optical dephasing and $T_1$ decay that was discussed previously.

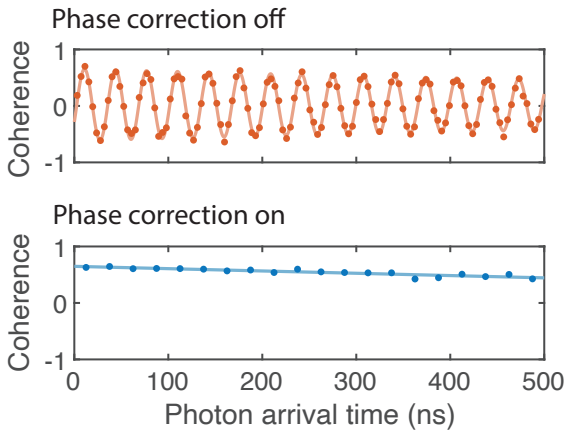


Figure 10.7: Upper panel shows the coherence of the entangled state vs photon arrival time. Note that the Bell State oscillates between $|\psi^+\rangle$ and $|\psi^-\rangle$ at the static optical drive frequency difference. In the lower panel, the photon measurement time is fed-forward and used apply a differential z-rotation before readout. The entangled state is now deterministically $|\psi^+\rangle$.

## 10.4 Quantum State Tomography

The goal of this section is to measure the density matrix for our two-qubit entangled state, thereby enabling us to verify entanglement and extract useful parameters such as the fidelity of the entangled state. Most generally, an N-qubit state is described by a Hermitian, positive semi-definite density matrix with unit trace. This leads to $4^N - 1$ real degrees of freedom required to fully describe the quantum system.

The most straightforward approach toward measuring the density matrix is to perform a linear tomographic reconstruction. This relies on the expansion of an N-qubit density matrix in the Pauli basis:

$$\rho = \frac{1}{2^N} \sum_{i,j,k,... \in \{\mathbb{I},x,y,z\}} r_{i,j,k,...} \hat{\sigma}_i \otimes \hat{\sigma}_j \otimes \hat{\sigma}_k \otimes ... \tag{10.3}$$

where $\hat{\sigma}_i,\ i \in \{\mathbb{I}, x, y, z\}$ are the identity and x,y,z Pauli operators. $r_{i,j,k,...}$ are real numbers with $r_{0,0,0...} = 1$. The values of $r_{i,j,k...}$ can be obtained by performing corresponding N-qubit Pauli measurements, i.e., $r_{i,j,k...} = \langle \hat{\sigma}_i \otimes \hat{\sigma}_j \otimes \hat{\sigma}_k ... \rangle$. The issue with this measurement method is that experimental noise/error will lead to unphysical density matrices that are not positive semi-definite [274].

To resolve this issue, we adopt an alternative approach for estimating the density matrix of our system: maximum likelihood tomography [275]. To do this, we first create a parameterization $\{t_i\}$ for physical density matrices. Then we define a likelihood function $\mathcal{L}$ which encodes the likelihood of a specific set of observations, given an assumed model (i.e., density matrix that depends on $\{t_i\}$). We then use standard optimization techniques to find the set of $\{t_i\}$ which maximize the likelihood function given our experimental observations.

More specifically, we read out our entangled state in 9 two-qubit Pauli bases: $\{\sigma_i \otimes \sigma_j\}$ where $i, j \in \{x, y, z\}$. Each measurement basis yields four photon count numbers $N_{00}^{(ij)}$, $N_{01}^{(ij)}$, $N_{10}^{(ij)}$, $N_{11}^{(ij)}$ where 00, 01, 10, 11 correspond to readout of the four 2-qubit measurement basis eigenstates (0 indicates $|0_g\rangle$, 1 indicates $|1_g\rangle$). Figure 10.8a shows the resulting populations for the $xx$, $yy$ and $zz$ measurement bases, the other 6 bases ($xy$, $yx$, $zy$, $yz$, $zx$, $xz$) are not shown but are included in the maximum likelihood reconstruction that follows.

We assume that the results of each measurement basis are multinomially distributed, i.e., have a likelihood function given by [248]:

$$\mathcal{L}^{(ij)} = \frac{N^{(ij)}!}{N_{00}^{(ij)}! N_{01}^{(ij)}! N_{10}^{(ij)}! N_{11}^{(ij)}!} \left[n_{00}^{(ij)}\right]^{N_{00}^{(ij)}} \left[n_{01}^{(ij)}\right]^{N_{01}^{(ij)}} \left[n_{10}^{(ij)}\right]^{N_{10}^{(ij)}} \left[n_{11}^{(ij)}\right]^{N_{11}^{(ij)}} \tag{10.4}$$

where $N^{(ij)} = \sum_{a\in\{00,01,10,11\}} N_a^{(ij)}$, and $\{n_a^{(ij)}\}$ are the predicted populations of each measurement basis eigenstate according to the model density matrix $\rho$. For example, if we were to measure the 00 eigenstate in the $xx$ basis, the value of $n_{00}^{(xx)} = \mathrm{Tr}\{|00\rangle\langle 00| U_{xx}^\dagger \rho U_{xx}\}$ where $U_{xx}$ rotates both qubits into the $x$ basis.

In order to account for readout infidelity, we need to define predicted population measurements $\{p_a^{(ij)}\}$ which are going to be some linear transformation of the ideal populations $\{n_a^{(ij)}\}$ with $a \in \{00, 01, 10, 11\}$. This is encoded with a readout transformation matrix:

$$\begin{pmatrix} p_{11}^{(ij)} \\ p_{10}^{(ij)} \\ p_{01}^{(ij)} \\ p_{00}^{(ij)} \end{pmatrix} = R \begin{pmatrix} n_{11}^{(ij)} \\ n_{10}^{(ij)} \\ n_{01}^{(ij)} \\ n_{00}^{(ij)} \end{pmatrix} \tag{10.5}$$

where $R_{l,m}$ is the probability of measuring state $l$, given that the two qubits were perfectly prepared in state $m$, and $l, m \in \{00, 01, 10, 11\}$.

$R$ can be derived from the single qubit readout fidelities $F_{|0\rangle}^{(i)}$ ($F_{|1\rangle}^{(i)}$), these are given in Table 10.2 and correspond to the probability of measuring Ion $i$ in $|0_g\rangle$ ($|1_g\rangle$) when it is perfectly prepared in $|0_g\rangle$ ($|1_g\rangle$). The expression for $R$ is then:

$$R = \begin{pmatrix} F_{|1\rangle}^{(2)} F_{|1\rangle}^{(1)} & F_{|1\rangle}^{(2)} \left(1 - F_{|0\rangle}^{(1)}\right) & \left(1 - F_{|0\rangle}^{(2)}\right) F_{|1\rangle}^{(1)} & \left(1 - F_{|0\rangle}^{(2)}\right)\left(1 - F_{|0\rangle}^{(1)}\right) \\ F_{|1\rangle}^{(2)} \left(1 - F_{|1\rangle}^{(1)}\right) & F_{|1\rangle}^{(2)} F_{|0\rangle}^{(1)} & \left(1 - F_{|0\rangle}^{(2)}\right)\left(1 - F_{|1\rangle}^{(1)}\right) & \left(1 - F_{|0\rangle}^{(2)}\right) F_{|0\rangle}^{(1)} \\ \left(1 - F_{|1\rangle}^{(2)}\right) F_{|1\rangle}^{(1)} & \left(1 - F_{|1\rangle}^{(2)}\right)\left(1 - F_{|0\rangle}^{(1)}\right) & F_{|0\rangle}^{(2)} F_{|1\rangle}^{(1)} & F_{|0\rangle}^{(2)} \left(1 - F_{|0\rangle}^{(1)}\right) \\ \left(1 - F_{|1\rangle}^{(2)}\right)\left(1 - F_{|1\rangle}^{(1)}\right) & \left(1 - F_{|1\rangle}^{(2)}\right) F_{|0\rangle}^{(1)} & F_{|0\rangle}^{(2)} \left(1 - F_{|1\rangle}^{(1)}\right) & F_{|0\rangle}^{(2)} F_{|0\rangle}^{(1)} \end{pmatrix}$$

With this readout correction, the predicted 00 measured population in the $xx$ basis becomes:

$$\begin{aligned} p_{00}^{(xx)} =& Tr\{|00\rangle\langle 00| U_{xx}^\dagger \rho U_{xx}\} R_{00,00} + Tr\{|01\rangle\langle 01| U_{xx}^\dagger \rho U_{xx}\} R_{00,01} + \\ & Tr\{|10\rangle\langle 10| U_{xx}^\dagger \rho U_{xx}\} R_{00,10} + Tr\{|11\rangle\langle 11| U_{xx}^\dagger \rho U_{xx}\} R_{00,11} \end{aligned} \tag{10.6}$$

similar expressions are used for the other populations and other readout bases, but are not listed here for brevity. We use a redefined likelihood function:

$$\mathcal{L}^{(ij)} = \frac{N^{(ij)}!}{N_{00}^{(ij)}! N_{01}^{(ij)}! N_{10}^{(ij)}! N_{11}^{(ij)}!} \left[p_{00}^{(ij)}\right]^{N_{00}^{(ij)}} \left[p_{01}^{(ij)}\right]^{N_{01}^{(ij)}} \left[p_{10}^{(ij)}\right]^{N_{10}^{(ij)}} \left[p_{11}^{(ij)}\right]^{N_{11}^{(ij)}}. \tag{10.7}$$

We assume that $N$ is sufficiently large that we can approximate this as a normal distribution:

$$\mathcal{L}^{(ij)} \propto \prod_{a\in\{00,01,10,11\}} e^{\frac{\left[\tilde{n}_a^{(ij)} - p_a^{(ij)}\right]^2}{2\tilde{n}_a^{(ij)}\left(1-\tilde{n}_a^{(ij)}\right)N^{(ij)}}} \tag{10.8}$$

where $\tilde{n}_a^{(ij)}$ are normalized measured populations, i.e., $\tilde{n}_a^{(ij)} = N_a^{(ij)}/N^{(ij)}$.

The likelihood function for all 9 measurement bases is simply the product of these individual basis likelihood functions:

$$\mathcal{L} = \prod_{i\in\{x,y,z\}} \prod_{j\in\{x,y,z\}} \mathcal{L}^{(ij)}. \tag{10.9}$$

Finally, we take the log-likelihood, leading to:

$$\mathcal{L} = -\sum_{i\in\{x,y,z\}} \sum_{j\in\{x,y,z\}} \sum_{a\in\{00,01,10,11\}} \left[ \frac{\left[\tilde{n}_a^{(ij)} - p_a^{(ij)}\right]^2}{2\tilde{n}_a^{(ij)}\left(1-\tilde{n}_a^{(ij)}\right)N^{(ij)}} \right]. \tag{10.10}$$

In order to extract a density matrix for this system we use the convex optimization package CVX in Matlab [276] to maximize the log-likelihood. The result of this optimization is presented in Figure 10.8b. The resulting density matrix fidelity is extracted by computing $Tr\{\rho\,|\psi^+\rangle\,\langle\psi^+|\}$ and yields $\mathcal{F} = 0.723 \pm 0.007$. This result is obtained with a 500 ns acceptance window size leading to an entanglement rate of 3.1 Hz. The dependence of fidelity and rate on window size is depicted in Figures 10.8c and d.

The error estimate in this fidelity is extracted using a bootstrapping protocol, whereby we use our predicted density matrix to generate 1000 simulated sets of experimental results. Each set involves the 9 measurement bases and the 4 populations associated with each measurement basis are randomly sampled according to the multinomial distribution. For each of these simulated experiments we perform the maximum likelihood analysis to compute a new density matrix and associated fidelity. The error estimate is the standard deviation of these 1000 simulated fidelities.

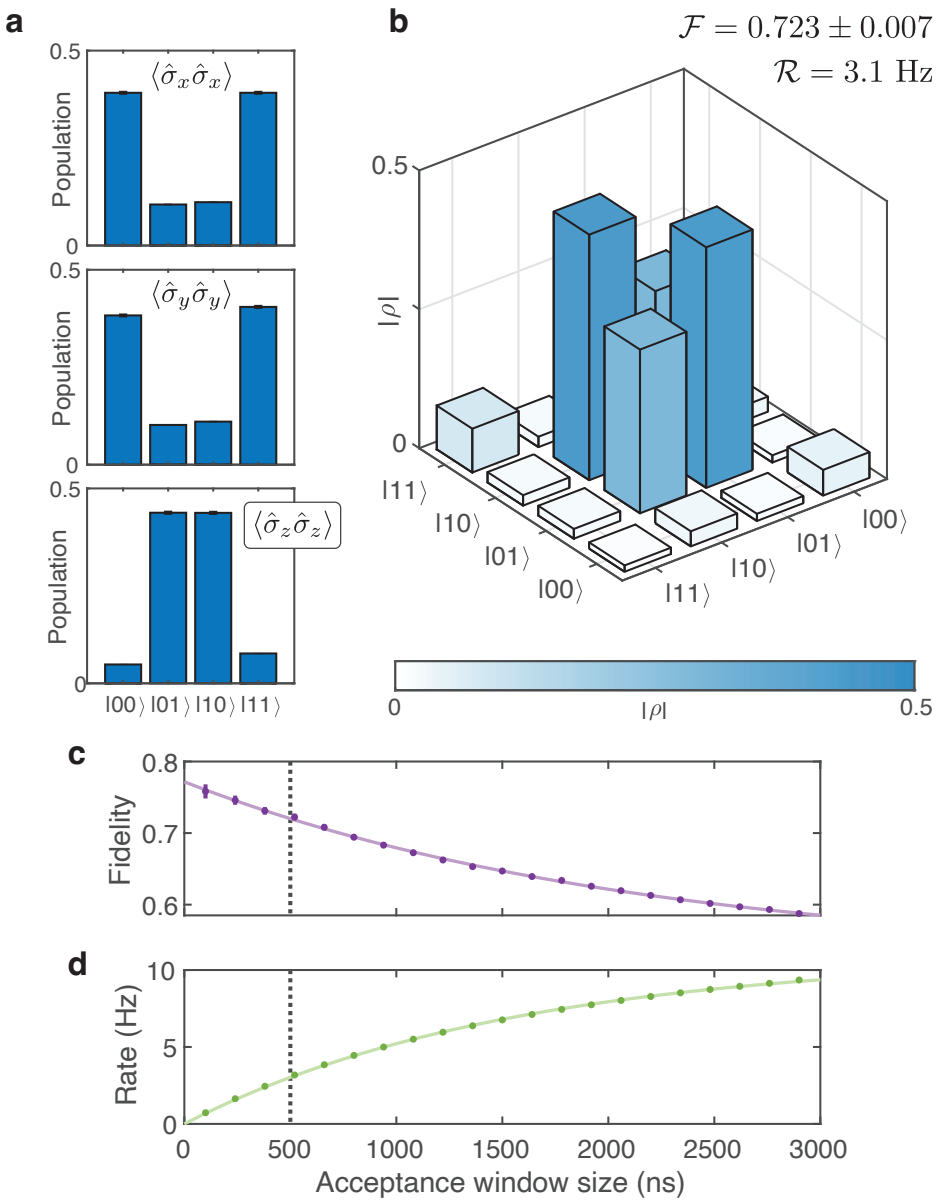


Figure 10.8: Maximum likelihood quantum state tomography of the two-ion entangled state. a) Population histogram results for the two-qubit XX, YY and ZZ basis measurements. b) Combining the results in (a) with population measurements in XY, YX, ZY, YZ, ZX and XZ bases we perform maximum likelihood quantum state tomography to extract this density matrix. The photon acceptance window was set to 500 ns leading to an entanglement rate of 3.1 Hz and fidelity of $0.723 \pm 0.007$. c) Fidelity vs photon acceptance window size, ranging from 0.758 to 0.588 for window sizes from 100 ns to 2900 ns. d) Entanglement rate vs photon acceptance window size ranging from 0.73 Hz to 9.4 Hz for window sizes from 100 ns to 2900 ns.

## 10.5 Entangled State Storage Time

Next, we verify the coherence time of the resulting entangled state. To do this, we insert an XY-8 dynamical decoupling sequence [212, 213] after entanglement heralding and before the state measurement.

We apply this dynamical decoupling sequence to both devices simultaneously as described in Section 3.5 with a 5.8 $\mu$s wait time between the consecutive $\pi$ pulses.

We measure the entangled state coherence decay as we increase the number of dynamical decoupling periods. The experimental result is presented in Figure 10.9 and yields an exponential decay with coherence time of 9.1 ± 0.4 ms.

The coherence times of each ion, when measured independently, are 21.2 ± 0.7 ms and 16.9 ± 0.7 ms. Assuming the noise sources are uncorrelated we would expect the relationship $1/T_2^{(\text{Bell})} = 1/T_2^{(1)} + 1/T_2^{(2)} = 9.4 \pm 0.3$ ms. This matches well with the experimental result.

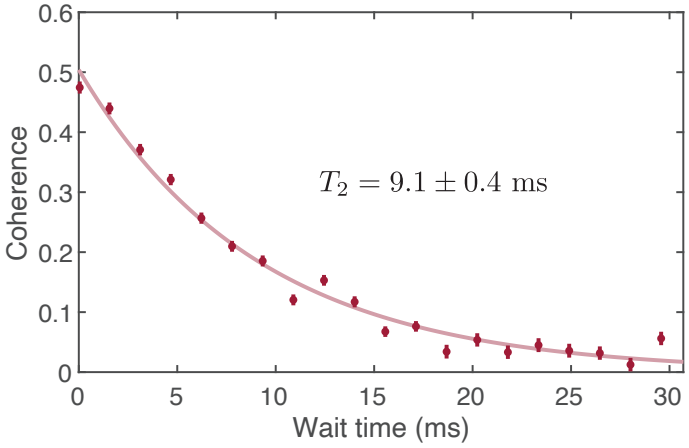


Figure 10.9: Coherence time of the two ion entangled state. After heralding the preparation of an entangled state, coherence is extended by simultaneously applying an XY-8 decoupling sequence to both qubits. The resulting coherence time is 9.1 ± 0.4 ms.

## 10.6 Simulation and Fidelity Limitations

All previously presented results in this section involved free-parameter fits to the experimental data (e.g., in Figure 10.6c, the oscillation envelope was fitted to a decaying exponential with amplitude and decay time constant being free parameters). In this section we implement an ab-initio model of the entanglement protocol (described in Section 8.5), verify that the model reproduces the experimental results and then use the model to infer dominant limitations on the entangled state fidelity.

First, we perform independent measurements of various ion parameters, summarized in Table 10.2. We also measure various properties of our experimental setup relevant to the model, summarized in Table 10.3.

| | Ion 1 | Ion 2 |
|---|---|---|
| Optical lifetime | $2.18 \pm 0.04$ $\mu$s | $0.945 \pm 0.007$ $\mu$s |
| Single photon efficiency | $(9.81 \pm 0.07) \times 10^{-3}$ | $(4.76 \pm 0.05) \times 10^{-3}$ |
| Qubit initialization fidelity | $0.9976 \pm 0.0003$ | $0.9954 \pm 0.0008$ |
| Resonant uniform dark count rate | $8.3 \pm 0.5$ Hz | $7.5 \pm 0.5$ Hz |
| Optical Ramsey coherence | $310 \pm 20$ ns | $220 \pm 10$ ns |
| Optical line-width (FWHM) | $1.7 \pm 0.1$ MHz | $2.4 \pm 0.1$ MHz |
| Optical echo coherence | $3.4 \pm 0.1$ $\mu$s | $1.75 \pm 0.04$ $\mu$s |
| Optical pure dephasing rate | $69 \pm 9$ kHz | $66 \pm 12$ kHz |
| Qubit lifetime | $53 \pm 3$ ms | $23 \pm 1$ ms |
| Qubit XY8 coherence | $21.2 \pm 0.7$ ms | $16.9 \pm 0.7$ ms |
| Spin pure dephasing rate | $38 \pm 2$ Hz | $37 \pm 3$ Hz |
| $\|0\rangle$ readout fidelity | $0.977 \pm 0.001$ | $0.967 \pm 0.001$ |
| $\|1\rangle$ readout fidelity | $0.961 \pm 0.002$ | $0.929 \pm 0.002$ |

Table 10.2: Summary of ion properties relevant for modelling two-ion entanglement. Note that when the optical $T_2$ for Ion 2 was measured, the lifetime was $0.988 \pm 0.004$ $\mu$s.

| Parameter | Value |
|---|---|
| Off-resonant uniform dark count rate | $8.0 \pm 0.2$ Hz |
| Optical phase stability ($\sigma$) | $0.037 \times 2\pi$ rad |
| Mach Zehnder (MZ) delay | 19.6 ns |
| MZ intensity imbalance (delayed/undelayed) | 0.79 |

Table 10.3: Summary of two ion entanglement setup properties.

Note that we consider two qualitatively different sources of dark counts:

1. Off resonant dark counts are not associated with fluorescence from our sample, these could be caused by laser leakage through our AOM shutter setups or ambient light.

2. Resonant dark counts are associated with undesired fluorescence from our samples. These are typically caused by excitation of weakly coupled ions in the cavity. These ions have longer optical lifetime and can also be treated as an approximately uniform contribution.

Note that the Mach-Zehnder (MZ) fiber delay line (introduced in Section 9.5) was re-spliced with a different length of fiber whenever the ion frequency difference changed significantly. The delay listed here was used while the optical frequency difference was $\sim$ 26 MHz which may not have been the case for all data presented in this thesis. The MZ imbalance quantifies the ratio in transmission efficiency for light travelling in the un-delayed/delayed arms of the MZ interferometer. This difference is due to the additional fiber-coupling losses for light that passes through the delayed portion of the interferometer. This imbalance does not directly impact the fidelity of the entangled state.

We now use these parameters to implement the model described in Section 8.5. In order to model the optical Ramsey dephasing we perform multiple Monte-Carlo repetitions of our simulation, with different optical frequencies sampled from a Gaussian distribution with FWHM given in Table 10.2. The spin Ramsey dephasing is modelled by sampling different nuclear spin bath eigenstates and calculating the resulting Overhauser field at the Yb location (see Section 4.2). The results of this model are presented in Figure 10.10.

The grey line in 10.10a plots the modelled entangled state coherence as a function of photon detection time. The shaded grey region indicates a 67% confidence interval for the model. The confidence interval is derived by repeatedly running the simulation with input parameters that are sampled from their respective error distribution (see Tables 10.2 and 10.3). The blue markers are experimental results, equivalent to those presented in Figure 10.7 (lower panel), but over a larger integration range. We attribute the discrepancy between data and simulation to systematic drifts in system properties between calibration and running the experiment. Given the relatively long data taking time ($\sim$ 24hrs), such drifts are inevitable. Figure 10.10b plots the

simulated histograms when measuring the entangled state in the $XX$, $YY$ and $ZZ$ bases, these can be compared to the experimental results in Figure 10.8a.

In Section 8.2 we introduced the concept of the single photon protocol and identified the parameter $\alpha$ which characterizes the strength of superposition prepared between the $|0_g\rangle$ and $|1_g\rangle$ states at the start of the sequence. An intuitive understanding of this parameter's effect on the entangled state is as follows. For small $\alpha$ the probability of getting a photon from the ions is suppressed. As $\alpha \rightarrow 0$ the likelihood of heralding based on a dark count increases, this leads to an ion state that is mostly $|0_g 0_g\rangle$ which, in turn, reduces the fidelity. Note that imperfect qubit initialization can also dominate as $\alpha \rightarrow 0$, in this case photon detection would herald a classically correlated state $\rho = 1/2(|0_g 1_g\rangle \langle 0_g 1_g| + |1_g 0_g\rangle \langle 1_g 0_g|)$. For large $\alpha$, the infidelity associated with the $|1_g 1_g\rangle$ component of the entangled state increases. Due to these sources of infidelity, there exists an intermediate value at which the fidelity is optimized. This is depicted in Figure 10.10c which plots the simulated entangled state fidelity for different $\pi$ pulse fractions ($f$) used to prepare the weak superposition. These are related to $\alpha$ according to $\alpha = \sin(f\pi/2)^2$. We use $f = 0.18$ in the experiment which leads to a simulated entangled state fidelity of $\mathcal{F} = 0.703 \pm 0.008$.

Next we investigate the limitations to the entangled state fidelity using this model, these results are summarized in Table 10.4 which lists various sources of infidelity, the impact of each item is quantified in two different ways, first the resulting improvement in fidelity if only that source were removed and, second, the fidelity if all other sources were neglected and that source were exclusively present.[6]

| Source of Error | $\mathcal{F}$ if Removed | $\mathcal{F}$ if Exclusively Present |
|---|---|---|
| Dark Counts | 0.763 | 0.910 |
| Initialization | 0.727 | 0.917 |
| Emission during rephasing | 0.751 | 0.917 |
| Optical dephasing | 0.717 | 0.965 |
| Spin dephasing + relaxation | 0.715 | 0.993 |
| Qubit gates | 0.718 | 0.982 |
| Optical gates | 0.759 | 0.916 |
| Optical phase stability | 0.715 | 0.985 |
| Lifetime + efficiency imbalance | 0.709 | 0.998 |

Table 10.4: Summary of limitations to entangled state fidelity. With all sources of error included, the simulation fidelity is $\mathcal{F} = 0.703 \pm 0.008$.

[6]All fidelities are quoted at a value of $\alpha$ which maximizes the resulting fidelity. This varies depending on the sources of error that are/are not included.

The largest sources of infidelity in our current experiments come from dark counts, undetected emission during the rephasing period and optical control infidelities. Dark counts can be improved by moving to purer crystals with a lower background concentration of Yb ions; in fact, some of my colleagues have already started exploring crystals grown by a different vendor with approximately 10× lower concentration. Undetected emission during rephasing can be mitigated by rephasing the optical coherence on a transition that is not Purcell enhanced, which will require an improvement in cavity Q factor by roughly 10×. Optical control infidelities can be improved by using a larger optical Rabi frequency, this will mitigate the impact of emission and detuning during the optical $\pi$ pulses; however, it might also lead to stronger excitation of background ions, hence, this should be considered in combination with purer crystals. Qubit initialization is also a significant, if slightly smaller, source of infidelity, with higher Q-factor devices and shorter optical lifetimes we can hope to improve this metric.

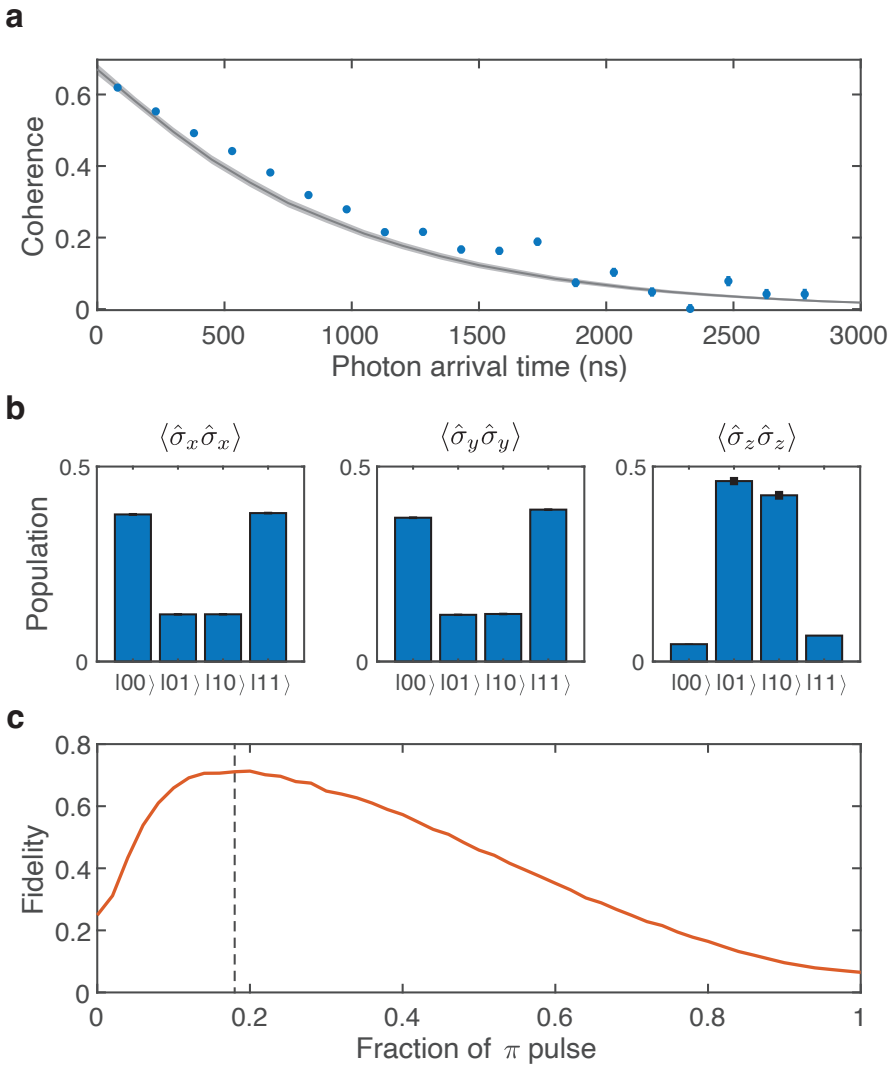


Figure 10.10: Simulation results. a) Entangled state coherence vs detection time, blue marks are experimental data, grey region corresponds to our model (67% confidence interval). The discrepancy between data and simulation is likely due to systematic error from a gradual drift of experiment parameters on timescales shorter than our data acquisition. b) Modelled histograms associated with $xx$, $yy$ and $zz$ population measurements. c) Modelled dependence of entangled state fidelity on $\pi$ pulse area used to prepare weak superposition states at start of the sequence. The dashed line corresponds to the value used in experiments.

## 10.7 Entangling Two Ions in The Same Cavity

In this section we extend the previously described protocol to enable the preparation of entangled states between ions in the same cavity. Generation of local entanglement has applications in Heisenberg-limited quantum sensing [10], and coherence protection of quantum states [277, 278]. Furthermore, these protocols can be adapted to perform two-qubit Bell state measurements on Yb ions in the same cavity [279, 280], which serve as a critical component of advanced quantum networking protocols [281].

There are a few differences in using the previously described protocol to herald an entangled state between two ions in the same device. First, the requirement for phase stability is considerably relaxed. This is because photons emitted by each of the two ions travel in the same optical mode, so any change in optical path length will be cancelled in a common-mode fashion. Hence we do not perform any active phase stabilization.

Consequently, this requires the two optical tones used to drive the ions to be passively phase-stable too. This is ensured by using a single AOM to generate them. Specifically, an AOM is driven at half the optical frequency difference (in this case $468/2$ MHz), we accept both the $0^{\text{th}}$ and $1^{\text{st}}$ diffraction orders. After double-passing the required two tones are generated. More detail on this is presented in Section 9.2.

The final difference relates to the differential z-rotation used to correct the stochastic nature of the Bell State phase (discussed in Section 10.3). For ions in the same device we only have global microwave control, this is because the spin inhomogeneity is much smaller than the typical Rabi frequencies used in our experiments (5 MHz). To solve this issue we utilize the AC Stark shift, which will be discussed in the next section.

For these experiments we use two ions in Device 1: Ion 1 which was previously used for the two device entanglement experiments, and Ion 3 which is 468 MHz lower in frequency. Throughout this section we will use an $|\text{Ion 3, Ion 1}\rangle$ labelling convention for states.

**AC Stark Shift**

In order to apply a differential z-rotation to the two ions we leverage the optical inhomogeneity to implement a differential AC-stark shift [282]. We use a similar protocol as detailed in [157] and follow their derivation of this phase shift.

To illustrate this effect, let us consider the $|1_g\rangle$ and $|0_e\rangle$ levels of a single ion, in isolation. If driven with a detuned optical tone, the resulting Hamiltonian in the laser's rotating frame will be $\mathcal{H} = \Omega/2(|0_e\rangle\langle 1_g| + |1_g\rangle\langle 0_e|) - \Delta|0_e\rangle\langle 0_e|$. Where $\Delta$ is the ion-laser detuning and $\Omega$ is the optical Rabi frequency. If we now consider the case of optical spontaneous emission we can write an additional anti-hermitian contribution to this Hamiltonian corresponding to the situation where no quantum jumps occur (this is a valid approximation for sufficiently large detuning) $\tilde{\mathcal{H}} = \Omega/2(|0_e\rangle\langle 1_g| + |1_g\rangle\langle 0_e|) - (\Delta + i\Gamma/2)|0_e\rangle\langle 0_e|$, where $\Gamma$ is the optical decay rate.

By diagonalizing this Hamiltonian we find that the ground state has shifted in frequency/energy by an amount:

$$\Delta\omega_{\mathrm{AC}} = \frac{\Omega^2}{4}\frac{\Delta}{\Delta^2 + \Gamma^2/4}. \tag{10.11}$$

Now introducing the second ground state energy level ($|0_g\rangle$) and assuming that the optical frequency is sufficiently detuned from the $E$ transition to have minimal effect we see that the effective ground state spin Hamiltonian becomes:

$$\mathcal{H} = -\omega_{01}|0_g\rangle\langle 0_g| + \frac{\Omega^2}{4}\frac{\Delta}{\Delta^2 + \Gamma^2/4}|1_g\rangle\langle 1_g| \tag{10.12}$$

where $\omega_{01}$ is the bare spin transition frequency.

Now we note several key things. First, the energy shift of the $|1_g\rangle$ state is proportional to $\Omega^2$, i.e., the laser intensity. This enables us to precisely control the amount of frequency shift.

Second, it also depends on the detuning $\Delta$, i.e., positive/negative detuning will lead to an increases/decreases in the ground state transition frequency (respectively). Since the optical inhomogeneity is relatively large (the two ions we consider here are detuned by 468 MHz), we can achieve dramatically different AC stark shifts for the two ions. We label the AC-Stark induced spin detuning as $\Delta\omega_{AC}^{(1)}$ and $\Delta\omega_{AC}^{(3)}$ for Ions 1 and 3, respectively.

Experimentally, we are going to use this differential frequency shift to accumulate a differential phase on our two qubits. This requires a sequence which simultaneously

cancels any detuning caused by magnetic field noise whilst accumulating AC Stark phase. We use an XY-8 dynamical decoupling sequence with detuned AC-stark pulses applied during the inter-pulse wait times (see Figure 10.11a). Note, however, that if we applied the light pulses during every wait period, the phase accumulation from consecutive free evolution times would cancel. We therefore apply the light pulses in alternate periods, thereby ensuring accumulation of the AC Stark phase. More precisely, after 4 complete XY-8 periods the accumulated differential phase is given by:

$$\Delta\phi_{\mathrm{AC}} = 16\tau_s(\Delta\omega_{AC}^{(1)} - \Delta\omega_{AC}^{(3)}) \tag{10.13}$$

where $\tau_s$ is the wait time between consecutive $\pi$ pulses. For these experiments we apply an AC Stark tone which is detuned by $\Delta = -47.5$ MHz from Ion 1 and $\Delta = +420.5$ MHz from Ion 3.

First, we measure the AC Stark shift applied to each ion independently by preparing a superposition state $|{+}X\rangle$, applying the AC Stark sequence with a variable optical pulse intensity, and then reading out the $X$ and $Y$ spin quadratures. This lets us extract a phase rotation angle $\phi_{\mathrm{AC}} = \tan^{-1}(\langle\sigma_y\rangle/\langle\sigma_x\rangle)$ for each ion. The solid line in Figure 10.11c shows the difference between these phases (i.e., $\Delta\phi_{\mathrm{AC}} = \phi_{\mathrm{AC}}^{(1)} - \phi_{\mathrm{AC}}^{(3)}$) for different optical pulse intensities. For the largest intensity in this plot the AC Stark frequency shift is -9.5 kHz for Ion 1 and 1.1 kHz for Ion 3.

Next, we demonstrate the effect of this pulse sequence on the entangled Bell states. We herald a Bell state using the dynamic rephasing protocol, then we apply an AC stark sequence thereby causing a differential $z$ rotation on the two ions, the resulting Bell State is:

$$|\psi\rangle = |0_g 1_g\rangle + |1_g 0_g\rangle\, e^{i(\Delta\omega_0 t_0 + \Delta\phi_{\mathrm{AC}})}. \tag{10.14}$$

Finally, we read out the entangled Bell State coherence. Figure 10.11b shows the resulting entangled state coherence plotted against photon arrival time for four AC stark intensities. We can clearly see an increasing phase shift in the Bell state parity oscillation as the AC Stark intensity increases. We correlate this phase shift with the single ion results in Figure 10.11c where the markers correspond to the Bell state phase measurements. We see that there is a close correspondence between the single ion and Bell state results.

We use this differential $z$ rotation to correct the stochastic phase associated with the random photon detection time. Specifically, in each experimental repetition we choose an AC stark intensity such that the condition $\Delta\phi_{\mathrm{AC}} = -\Delta\omega_0 t_0$ is satisfied.

This leads to the preparation of a deterministic Bell state. The tomography results presented in the subsequent section have been performed on Bell states prepared in this manner.

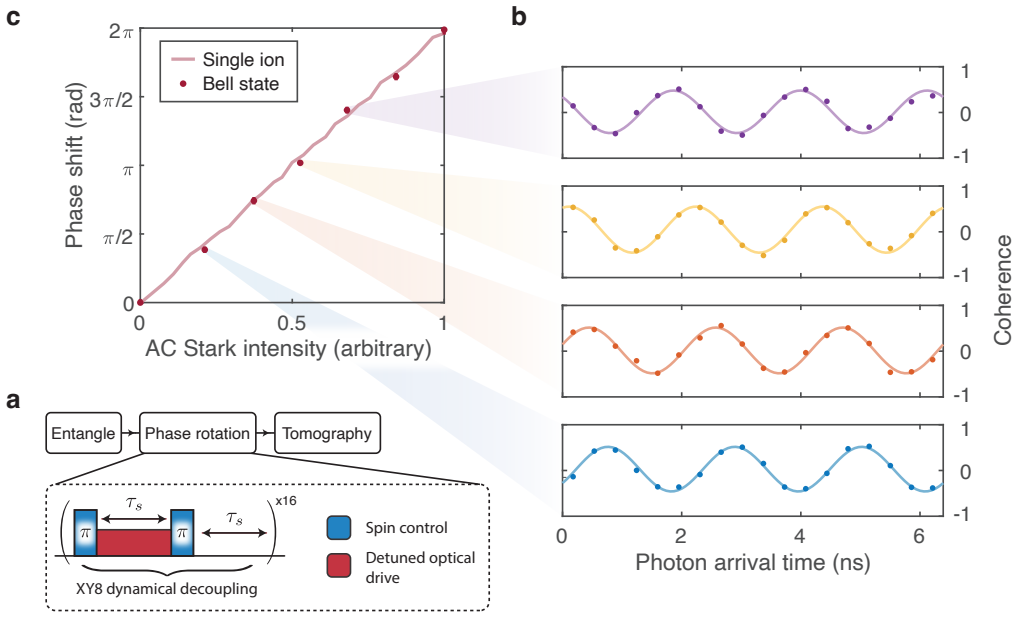


Figure 10.11: AC Stark shift for differential Z rotations of two ions in the same device. a) A dynamical decoupling sequence with embedded AC-Stark pulses is applied between entangled state preparation and measurement. This applies a phase shift to the prepared Bell state which is proportional to the intensity of the AC Stark pulse. b) The phase shift for a specific AC Stark intensity is extracted by correlating the entangled state phase with photon detection time. The AC Stark intensity increases in ascending order of figures in this column. c) The phase shift extracted from the Bell State measurements is plotted against AC Stark pulse intensity (markers). The solid line corresponds to the expected AC Stark phase obtained from single ion measurements.

**Entangled State Tomography**

In order to extract a density matrix for the two ion entangled state we perform the same set of experiments/analysis presented in Section 10.4.

The main difference is that we do not have independent local control of the two qubits, hence measuring in certain two-qubit Pauli bases is non-trivial (for instance $\hat{\sigma}_z \otimes \hat{\sigma}_y$).

These basis rotations can be generated via global control combined with a differential z-rotation. For instance, applying the following sequence of pulses:

$$\left(\frac{\pi}{4}\right)_Y U^{(1)}_{-\pi/2,Z} U^{(3)}_{\pi/2,Z} \left(\frac{\pi}{4}\right)_X \tag{10.15}$$

followed by population basis readout will lead to a measurement in the $z$ basis for ion 1 and $x$ basis for ion 3. Here, $\left(\frac{\pi}{4}\right)_\alpha$ corresponds to a global $\pi/4$ pulse applied about the $\alpha$ axis. $U^{(i)}_{\alpha,Z}$ is a rotation about the $z$ axis by angle $\alpha$ for qubit $i$.

Since the spin frequency difference between the two ions studied is relatively large (1 MHz) we implemented the differential Z rotation gate here via a 250 ns wait. Note that the fidelity of this approach is limited by the spin Ramsey coherence time, this is why we did not use it in the previous section, where a complete $2\pi$ differential $z$ rotation is required. 500 ns of wait time would have lead to a significant reduction in entangled state fidelity.

The results of this tomography are presented in Figure 10.12. The extracted Fidelity is $0.682 \pm 0.006$.

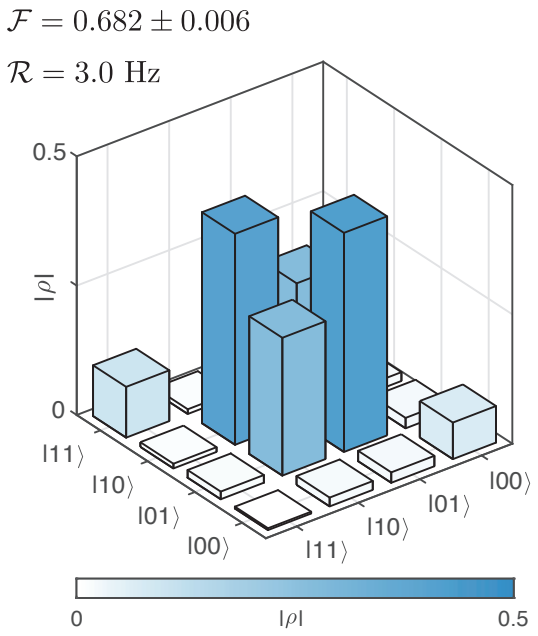


Figure 10.12: Density matrix of the two ion entangled state in a single device. The photon acceptance window corresponds to the first 400 ns of emission and leads to a fidelity of 0.682 ± 0.006 and 3.0 Hz rate.

*Chapter 11*

# OUTLOOK

In this section I provide an outlook on the next stages of this experiment. I will compare our results to other quantum networking platforms and highlight improvements which can be used to achieve state of the art entanglement rates and fidelities. I will also propose some future directions (both related and unrelated to quantum networking). We are already actively pursuing some of these ideas.

## 11.1 Quantum Networking

### Comparison to Other Platforms

Table 11.1 provides a comparison of experimentally demonstrated entanglement rates, fidelities and spin coherence times for several different platforms[1].

| Platform | Fidelity | Rate | Spin Coherence |
|---|---|---|---|
| Rare-earths[2] [155, 158] | 0.72 | 3.1 Hz | 21 ms (760 $\mu$s nuclear) |
| NV Centers [30, 71, 73] | 0.8 | 10 Hz | 1 s (120 s nuclear) |
| SiV Centers [83, 193, 260] | 0.71 | 0.9 Hz | 10 ms/2 s (7 ms nuclear) |
| Quantum Dots [69, 70] | 0.62 | 7.3 kHz | 3 $\mu$s |
| Trapped Ions [62] | 0.94 | 200 Hz | 2 ms |
| Trapped Atoms [23, 281] | 0.79 | 6 Hz | 20 ms |

Table 11.1: Comparison of experimentally demonstrated rates and fidelities for different quantum network nodes.

Note that the silicon vacancy results mentioned here correspond to entangling two centers in the same device, whereas all other platforms have demonstrated remote entanglement generation. Furthermore, the two coherence times quoted (10 ms and 2 s) correspond to the electronic spin and $^{29}$Si nuclear spin, respectively; these are strongly coupled spins and cannot be used as independent quantum memories.

It is also worth noting two areas of development in trapped atom and ion-based quantum networking. First, dual-species quantum nodes, which can leverage optimal properties of one atomic species for storage and computation, and another species for

[1] In obtaining this table I have tried to be as comprehensive as possible; however, it is often hard to provide an apples-to-apples comparison. The pedantic reader should follow the references and check my interpretation of the corresponding experimental results

[2] This work.

quantum communication [63, 283]. Second, the potential for leveraging Rydberg interactions for high fidelity quantum processing in neutral atom-based network nodes [284].

While rare-earth ions and silicon vacancy centers currently have slightly lower rates and fidelities compared to other platforms, the development and optimization of these systems is still at a relatively early stage and there is considerable room for improvement. As discussed in Section 1.6, NV centers have been hindered by a dramatic reduction in coherence properties when incorporated into nanostructures. Quantum dots have been limited by low spin coherence times due to a noisy nuclear spin bath. It is difficult to envisage large improvements in the performance of these two platforms.

**Improving the Rare-Earth Ion Platform**

The average time per entanglement attempt is currently limited by three factors: 24 $\mu$s is spent on $|\text{aux}\rangle$ initialization, 33 $\mu$s on qubit initialization and 10 $\mu$s on phase stabilization. The single photon detection efficiency ($\eta$) is currently limited by: $\kappa_{\text{in}}/\kappa \sim 0.1$, 25% device to fiber coupling efficiency, 65% optical setup efficiency and 85% SNSPD detection efficiency. I believe that a factor of 10 increase in entanglement rate should be achievable for this platform with the following improvements:

- Operating with two ions that have the same lifetime to enable heralding with a larger fraction of the optical emission.
- Fabricating devices with larger $\kappa_{\text{in}}/\kappa$.
- Reducing the optical lifetime to reduce the initialization time.
- Redesigning the fiber-to waveguide coupling scheme (for instance using a tapered fiber approach [285]).

Limitations to the entanglement fidelity were discussed in Section 10.6. To summarize, there are three technical improvements which, if combined, would increase the entangled state fidelity to 0.86. First, reducing the dark count rate from weakly excited ions, this could be achieved by moving to purer samples. Second, improving the optical control fidelity by using larger Rabi frequencies. Finally, if the cavity line-width could be reduced to 4 GHz then dynamic rephasing could be performed on a non-purcell-enhanced transition (the $E$ transition), thus removing the limitation imposed by $T_1$ decay, this would also increase the entanglement rate.

**Multipartite Entangled State Generation**

The single photon protocol presented in this thesis can be naturally extended to prepare multi-qubit W states. Consider the case of three ions. After preparing a weak superposition of all three ions the quantum state would be[3]:

$$|\psi\rangle = (1-\alpha)^{3/2}|000\rangle + (1-\alpha)\sqrt{\alpha}\,(|100\rangle + |010\rangle + |001\rangle) + \alpha\sqrt{1-\alpha}\,(|011\rangle + |101\rangle + |110\rangle) + \alpha^{3/2}|111\rangle\,. \tag{11.1}$$

After subsequent excitation, detection of a single photon and dynamic rephasing the state would be:

$$|\psi\rangle = \frac{1}{\sqrt{3}}\left(|100\rangle + |010\rangle\, e^{-i\Delta\omega_0^{(12)}t_0} + |001\rangle\, e^{-i\Delta\omega_0^{(13)}t_0}\right) \tag{11.2}$$

where $\Delta\omega_0^{(ij)}$ is the static frequency difference between ions $i$ and $j$ and $t_0$ is the photon detection time (note that we are ignoring contributions from $|110\rangle$-type and $|111\rangle$ states as they are suppressed by a probability factor of at least $\alpha$).

Finally, we would need to compensate for two independent stochastic phases: $\Delta\omega_0^{(12)}t_0$ and $\Delta\omega_0^{(13)}t_0$ ; this could be implemented by some combination of AC Stark shifting and phase shifts to the microwave drive depending on which ions are in the same/different nodes. Finally, we would prepare the following W state:

$$|\psi\rangle = \frac{1}{\sqrt{3}}\,(|100\rangle + |010\rangle + |001\rangle)\,. \tag{11.3}$$

The entanglement heralding rate using this protocol would be $\mathcal{R} = 3\eta\alpha$ and the entangled state fidelity would be $\mathcal{F} = (1-\alpha)^2$.

While the W state presented here has somewhat limited use in a quantum network setting, we are also developing protocols to prepare 3-qubit GHZ states using a two-photon detection protocol. Such a state would be useful for quantum secret sharing [31].

[3]Using an |Ion 1, Ion 2, Ion 3⟩ convention.

**Teleportation of Quantum States**

While deterministic quantum teleportation would require improving and incorporating the nuclear spin memory into entanglement experiments (see the next section for more discussion), probabilistic quantum teleportation can already be achieved using the resources demonstrated in this thesis. The protocol we have in mind would be executed as follows.

We would start by preparing Ion 1 in $|\psi\rangle = a\,|0_g\rangle + b\,|1_g\rangle$, where $a$ and $b$ encode the state we wish to teleport onto Ion 2. Ion 2 is prepared in $|\psi\rangle = 1/\sqrt{2}(|0_g\rangle + |1_g\rangle)$ such that the combined quantum state is[4]:

$$|\psi\rangle = \frac{1}{\sqrt{2}}\left(a\,|0_g 0_g\rangle + a\,|0_g 1_g\rangle + b\,|1_g 0_g\rangle + b\,|1_g 1_g\rangle\right). \tag{11.4}$$

After optical excitation and heralding based on a single photon detection at time $t_0$ we prepare the state:

$$\rho = \frac{1}{1+2b^2}\,|\psi(t_0)\rangle\,\langle\psi(t_0)| + \frac{2b^2}{1+2b^2}\,|1_g 1_g\rangle\,\langle 1_g 1_g| \tag{11.5}$$

where

$$|\psi(t_0)\rangle = a\,|0_g 1_g\rangle + b\,|1_g 0_g\rangle\,e^{i\Delta\omega t_0}. \tag{11.6}$$

We then apply a ground state $\pi$ pulse, optically excite for a second time and herald based on a second photon detection, which is measured at time $t_1$. This removes the $|1_g 1_g\rangle$ component leaving us with the following pure state:

$$|\psi\rangle = a\,|1_g 0_g\rangle + b\,|0_g 1_g\rangle\,e^{i\Delta\omega(t_0 - t_1)}. \tag{11.7}$$

Now we perform the dynamic rephasing protocol, with a rephasing time of $t_0 - t_1$. We also correct the stochastic phase by performing a differential z-rotation by an angle $-\Delta\omega_0(t_0 - t_1)$. The result is a pure state:

$$|\psi\rangle = a\,|1_g 0_g\rangle + b\,|0_g 1_g\rangle. \tag{11.8}$$

Note that if we chose $a = b = 1/\sqrt{2}$ then we would be implementing a variant of the Barrett-Kok protocol. Next, we apply a $\pi/2$ pulse to Ion 1's ground state leading to the following state:

$$|\psi\rangle = |0_g\rangle\,(b\,|1_g\rangle + a\,|0_g\rangle) + |1_g\rangle\,(b\,|1_g\rangle - a\,|0_g\rangle). \tag{11.9}$$

We perform single shot readout of the Ion 1 state, if measured in $|1_g\rangle$ we perform a $z$ rotation on Ion 2 by $\pi$ (implemented by a phase shift of the microwave drive). This yields the following state for Ion 2:

$$|\psi\rangle = a\,|0_g\rangle + b\,|1_g\rangle \tag{11.10}$$

[4]Using an |Ion 1, Ion 2⟩ convention.

hence we successfully teleported from Ion 1 to Ion 2. The main issue with this protocol is that it relies on two photon detections, hence it is quite inefficient and also non-deterministic (we would need to prepare multiple copies of the same initial state). A nice benefit is that phase-stabilization of the optical paths would no longer be required.

**Additional Quantum Node Functionality**

There are two aspects of this platform that I believe could be leveraged to implement some novel quantum networking protocols. First, despite the Ramsey-limited cooperativity being relatively low ($C \approx 0.06$), the cooperativity calculated using the pure dephasing rate (i.e., ignoring quasi-static frequency variation) is $\tilde{C} \approx 3$. It is due to $\tilde{C} > 1$ that we were able to demonstrate lifetime-limited entanglement heralding.

It is worth considering if any other quantum networking protocols which would usually require $C > 1$ can be adapted to leverage the $C < 1$, $\tilde{C} > 1$ regime demonstrated here. For instance, one could envisage performing photon-mediated quantum gates involving photon reflections from the cavity, such as those implemented in [23], but where the ion frequency is tracked in real time and used to dynamically adjust the photon frequency.

The second opportunity is to leverage the presence of several spectrally resolvable emitters in each node. In the most basic setting, one could envisage performing multiplexed entanglement generation between pairs of ions in separate nodes. This would lead to an entanglement rate improvement which scales linearly with the number of ion pairs. If deterministic local gates could also be performed between pairs of ions in the same cavity, this could become a useful resource for entanglement distillation [25]. Such interactions could either be implemented via direct magnetic dipole-dipole interactions of the spins (might be a bit tricky due to the dilute nature of our sample with an average interaction strength of 50 Hz), or via cavity mediated interactions [55] (which are also challenging to implement due to their fidelity scaling as $(1 - \mathcal{F}) \sim 1/\sqrt{C}$).

An interesting protocol which could potentially combine both of these research directions involves using additional spectator qubits in each node to achieve a cavity-mediated interaction strength that scales as $(1 - \mathcal{F}) \sim 1/C$ [286]. I would be very interested to see if this protocol could be adapted to leverage the $\tilde{C} > 1$ regime present in our platform.

## 11.2 Nuclear Spins

The Vanadium nuclear spin ensemble surrounding our Yb qubits is a deterministic many-body resource. It is a unique feature of our platform compared to other solid state systems and provides many opportunities for novel scientific exploration.

### Improving the Register

In order to utilize this register in quantum networking protocols we need to improve the fidelity of the swap gate (which is currently only 68% in the population basis). We also need to increase the nuclear spin storage time and, ideally, increase the number of qubits.

Improving the fidelity is difficult as our simulations do not reproduce the experimentally observed results (without the phenomenological decay constant discussed in Section 6.4). As a first step, we need to expand our model to try and identify the dominant infidelity. Some additional aspects that could be considered include: mixing of the $|\text{aux}\rangle$ state with the qubit states, pumping of the nuclear spin ensemble into incoherent classically correlated states, or some additional uncharacterized interactions (such as exchange interactions between Yb and V).

One limitation which we do predict is the imperfect register initialization: currently the single-spin preparation fidelity is 84%, leading to only 50% initialization fidelity into $|\downarrow\downarrow\downarrow\downarrow\rangle$. In the next section we will see how sensing of the nuclear spin ensemble combined with post-selection can be used to improve this fidelity.

Increasing the coherence time can be achieved through improved dynamical decoupling of the register. Specifically, by reducing the duration and increasing the number of Vanadium $\pi$ pulses. There are two technical challenges associated with this. First, the low-frequency RF tones used for vanadium driving tend to heat up our device (when applied through the coplanar waveguide), this could be resolved by using a superconducting waveguide or an off-chip RF coil. The second challenge is more fundamental: due to the relatively small detuning between the register and bath (37 kHz), if we drive the register too strongly, we will also drive the bath spins. This will cause a fluctuation in the Overhauser field, thereby rendering the dynamical decoupling sequence ineffective. One approach to resolve this issue would involve operating with a Rabi frequency where a $\pi$ pulse on the register would lead to a $2\pi$ rotation of the bath, thereby leaving the Overhauser field unperturbed.

Finally there are two different methods we could use to expand the number of qubits stored in the bath: First, assuming the two vanadium spins closest to the Yb

(Shell 1) are detuned from the more distant bath nuclei, they could be used as an additional isolated qubit system. The main challenge is the Ising-type interaction with Yb ($\hat{S}_z\hat{I}_z$), though there are protocols like the DDRF sequence [72] which could be used. The second opportunity would involve encoding multiple qubits in the (relatively large) Hilbert space of the four register spins. This could either involve the *a* or *b* transitions or higher spin excitations within the *c* manifold. For instance, one could consider adapting protocols proposed for multimode superconducting qubit quantum memories [128].

**Preparing GHZ States**

Joint $^{171}$Yb-V GHZ states have the form:

$$|\text{GHZ}\rangle = \frac{1}{\sqrt{2}}\left(|0_g\rangle\,|\uparrow\uparrow\uparrow\uparrow\rangle + |1_g\rangle\,|\downarrow\downarrow\downarrow\downarrow\rangle\right) \tag{11.11}$$

and are an important class of highly entangled quantum states with applications in quantum metrology, storage, and benchmarking. Under free evolution, a defining characteristic of this state is a parity oscillation frequency that is enhanced by the number of participating spins (in this case phase accumulates at $4\omega_c$, in the Yb rotating frame).

In our system, GHZ states can be prepared in a fairly straightforward manner by first polarizing the register and then applying the gate sequence shown in Figure 11.1a.

This sequence requires a controlled rotation of the Vanadium spins conditioned on the Yb state. It turns out that vanadium driving sequence introduced in Section 6.5 already fulfills this requirement: the phase of the driving field (and hence Rabi vector orientation) will depending on the Yb state.

We have performed a preliminary experimental demonstration of this state preparation by measuring a $4\omega_c$ parity oscillation as shown in Figure 11.1b. Fourier transforming this oscillation reveals the presence of four distinct frequency harmonics at $\omega_c$, $2\omega_c$, $3\omega_c$ and $4\omega_c$ (Figure 11.1c). This is due to imperfect preparation of the initial register state and closely correlates to our anticipated 84% single spin initialization fidelity.

We have been exploring methods of using the parity oscillation frequency as a method to sense the number of spins in the *c* manifold and subsequently purify the initialization of our register ensemble.

**Decoherence Protected Subspaces**

We also note the existence of a class of GHZ states that are intrinsically protected from common-mode noise. These states rely on spins with opposite Zeeman

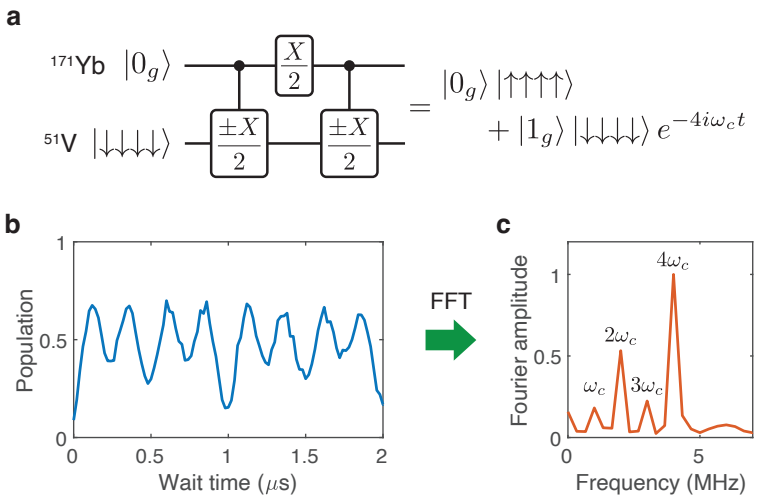


Figure 11.1: Preparation and measurement of GHZ states in Vanadium register ensemble. a) Gate sequence for preparing GHZ states utilizes controlled rotations of the V spins by $\pi/2$ about the $\pm X$ axes, conditioned on the Yb state. Under subsequent free evolution a parity oscillation is expected at $4\omega_c$. b) The GHZ state is prepared, after waiting for a variable time, $t$, the parity is read out by using a similar sequence. c) Fourier transform reveals harmonics at $\omega_c$, $2\omega_c$, $3\omega_c$ and $4\omega_c$ the multiple harmonics are due to imperfect polarization of the register.

sensitivity having equal and opposite detuning under an applied magnetic field. Specifically, remembering that the nuclear quadrupole levels are twofold degenerate (i.e., $|\downarrow\rangle$ contains both $|+7/2\rangle$ and $|-7/2\rangle$ states) we can see that the GHZ state:

$$|\mathrm{GHZ}\rangle = \frac{1}{\sqrt{2}}\left(\left|+\frac{7}{2},+\frac{7}{2},-\frac{7}{2},-\frac{7}{2}\right\rangle + \left|+\frac{5}{2},+\frac{5}{2},-\frac{5}{2},-\frac{5}{2}\right\rangle\right) \tag{11.12}$$

will not accumulate phase generated by correlated noise.

While this will not lead to an improvement in register coherence time (since the Overhauser field is highly uncorrelated), it does provide a novel and highly useful approach to cancel the Knight field: due to the symmetry of our system the Knight field at each Vanadium location is identical (common-mode). Hence, the Yb qubit can be operated[5] without affecting the coherence of the GHZ state, which is critical functionality for an auxiliary quantum node memory.

We are currently working on protocols to prepare such GHZ states and use them for quantum information storage.

[5] I.e., initialized, entangled, and read out.

# BIBLIOGRAPHY


[1] I. H. Deutsch. "Harnessing the power of the second quantum revolution." In: *Physical Review X Quantum* 1.2 (2020), p. 20101.

[2] J. Preskill. *Quantum computing and the entanglement frontier.* 2012. arXiv: 1203.5813 [quant-ph].

[3] P. W. Shor. "Algorithms for quantum computation: Discrete logarithms and factoring." In: *Proceedings 35th Annual Symposium on Foundations of Computer Science*. 1994, pp. 124–134.

[4] D. P. DiVincenzo. "The physical implementation of quantum computation." In: *Fortschritte der Physik* 48.9-11 (2000), pp. 771–783.

[5] P. W. Shor. "Fault-tolerant quantum computation." In: *Proceedings of 37th Conference on Foundations of Computer Science*. 1996, pp. 56–65.

[6] R. Acharya et al. "Suppressing quantum errors by scaling a surface code logical qubit." In: *Nature* 614.7949 (2023), pp. 676–681.

[7] C. H. Bennett and G. Brassard. "Quantum cryptography: Public key distribution and coin tossing." In: *Proceedings of IEEE International Conference on Computers, Systems, and Signal Processing*. India, 1984, p. 175.

[8] A. K. Ekert. "Quantum cryptography based on Bell's theorem." In: *Physical Review Letters* 67.6 (1991), pp. 661–663.

[9] A. Ekert and R. Renner. "The ultimate physical limits of privacy." In: *Nature* 507.7493 (2014), pp. 443–447.

[10] L. Pezzè et al. "Quantum metrology with nonclassical states of atomic ensembles." In: *Reviews of Modern Physics* 90.3 (2018), p. 35005.

[11] J. Abadie et al. "A gravitational wave observatory operating beyond the quantum shot-noise limit." In: *Nature Physics* 7.12 (2011), pp. 962–965.

[12] D. Leibfried et al. "Toward Heisenberg-limited spectroscopy with multiparticle entangled states." In: *Science* 304.5676 (2004), pp. 1476–1478.

[13] E. Pedrozo-Peñafiel et al. "Entanglement on an optical atomic-clock transition." In: *Nature* 588.7838 (2020), pp. 414–418.

[14] J. A. Jones et al. "Magnetic field sensing beyond the standard quantum limit using 10-spin NOON states." In: *Science* 324.5931 (2009), pp. 1166–1168.

[15] H. J. Kimble. "The quantum internet." In: *Nature* 453.7198 (2008), pp. 1023–1030.

[16] S. Wehner, D. Elkouss, and R. Hanson. "Quantum internet: A vision for the road ahead." In: *Science* 362.6412 (2018), eaam9288.

[17] D. Mayers and A. Yao. “Quantum cryptography with imperfect apparatus.” In: *Proceedings 39th Annual Symposium on Foundations of Computer Science*. 1998, pp. 503–509.

[18] D. Gottesman, T. Jennewein, and S. Croke. “Longer-baseline telescopes using quantum repeaters.” In: *Physical Review Letters* 109.7 (2012), p. 70503.

[19] P. Kómár et al. “A quantum network of clocks.” In: *Nature Physics* 10.8 (2014), pp. 582–587.

[20] L. Jiang et al. “Distributed quantum computation based on small quantum registers.” In: *Physical Review A* 76.6 (2007), p. 62323.

[21] C. Monroe and J. Kim. “Scaling the ion trap quantum processor.” In: *Science* 339.6124 (2013), pp. 1164–1169.

[22] Y. Wan et al. “Quantum gate teleportation between separated qubits in a trapped-ion processor.” In: *Science* 364.6443 (2019), pp. 875–878.

[23] S. Daiss et al. “A quantum-logic gate between distant quantum-network modules.” In: *Science* 371.6529 (2021), pp. 614–617.

[24] R. Reichle et al. “Experimental purification of two-atom entanglement.” In: *Nature* 443.7113 (2006), pp. 838–841.

[25] N. Kalb et al. “Entanglement distillation between solid-state quantum network nodes.” In: *Science* 356.6341 (2017).

[26] M. Riebe et al. “Deterministic quantum teleportation with atoms.” In: *Nature* 429.6993 (2004), pp. 734–737.

[27] M. D. Barrett et al. “Deterministic quantum teleportation of atomic qubits.” In: *Nature* 429.6993 (2004), pp. 737–739.

[28] S. Pirandola et al. “Advances in quantum teleportation.” In: *Nature Photonics* 9.10 (2015), pp. 641–652.

[29] P. Drmota et al. *Verifiable blind quantum computing with trapped ions and single photons.* 2023. arXiv: 2305.02936 [quant-ph].

[30] M. Pompili et al. “Realization of a multi-node quantum network of remote solid-state qubits.” In: *Science* 372.6539 (2021).

[31] M. Hillery, Vladimir Buifmmode Buzek, and André Berthiaume. “Quantum secret sharing.” In: *Physical Review A* 59.3 (1999), pp. 1829–1834.

[32] W. J. Munro et al. “Inside quantum repeaters.” In: *IEEE Journal of Selected Topics in Quantum Electronics* 21.3 (2015), pp. 78–90.

[33] H. J. Briegel et al. “Quantum repeaters: The role of imperfect local operations in quantum communication.” In: *Physical Review Letters* 81.26 (1998), pp. 5932–5935.

[34] J. Borregaard et al. “One-way quantum repeater based on near-deterministic photon-emitter interfaces.” In: *Physical Review X* 10.2 (2020), p. 21071.

[35] L.-M. Duan et al. “Long-distance quantum communication with atomic ensembles and linear optics.” In: *Nature* 414.6862 (2001), pp. 413–418.

[36] N. Sangouard et al. “Quantum repeaters based on atomic ensembles and linear optics.” In: *Reviews of Modern Physics* 83.1 (2011), pp. 33–80.

[37] M. Mirhosseini et al. “Superconducting qubit to optical photon transduction.” In: *Nature* 588.7839 (2020), pp. 599–603.

[38] J. Ang et al. *Architectures for multinode superconducting quantum computers.* 2022. arXiv: 2212.06167 [quant-ph].

[39] J. Rochman et al. “Microwave-to-optical transduction with erbium ions coupled to planar photonic and superconducting resonators.” In: *Nature Communications* 14.1 (2023), p. 1153.

[40] T. Aoki et al. “Observation of strong coupling between one atom and a monolithic microresonator.” In: *Nature* 443.7112 (2006), pp. 671–674.

[41] H. Takahashi et al. “Strong coupling of a single ion to an optical cavity.” In: *Physical Review Letters* 124.1 (2020), p. 13602.

[42] S. Haroche. “Nobel Lecture: Controlling photons in a box and exploring the quantum to classical boundary.” In: *Reviews of Modern Physics* 85.3 (2013), pp. 1083–1102.

[43] T. Yoshie et al. “Vacuum Rabi splitting with a single quantum dot in a photonic crystal nanocavity.” In: *Nature* 432.7014 (2004), pp. 200–203.

[44] K. Srinivasan and O. Painter. “Linear and nonlinear optical spectroscopy of a strongly coupled microdisk–quantum dot system.” In: *Nature* 450.7171 (2007), pp. 862–865.

[45] E. M. Purcell. “Spontaneous emission probabilities at radio frequencies.” In: *Physical Review* 69 (1946), p. 681.

[46] A. M. Dibos et al. “Atomic source of single photons in the telecom band.” In: *Physical Review Letters* 120.24 (2018), p. 243601.

[47] A. E. Rugar et al. “Quantum photonic interface for tin-vacancy centers in diamond.” In: *Physical Review X* 11.3 (2021), p. 31021.

[48] D. M. Lukin et al. “4H-silicon-carbide-on-insulator for integrated quantum and nonlinear photonics.” In: *Nature Photonics* 14.5 (2020), pp. 330–334.

[49] S. Noda, M. Fujita, and T. Asano. “Spontaneous-emission control by photonic crystals and nanocavities.” In: *Nature Photonics* 1.8 (2007), pp. 449–458.

[50] W. Redjem et al. “All-silicon quantum light source by embedding an atomic emissive center in a nanophotonic cavity.” In: *Nature Communications* 14.1 (2023), p. 3321.

[51] A. Faraon et al. “Resonant enhancement of the zero-phonon emission from a colour centre in a diamond cavity.” In: *Nature Photonics* 5.5 (2011), pp. 301–305.

[52] A. Sipahigil et al. “An integrated diamond nanophotonics platform for quantum-optical networks.” In: *Science* 354.6314 (2016), pp. 847–850.

[53] A. Gritsch, A. Ulanowski, and A. Reiserer. “Purcell enhancement of single-photon emitters in silicon.” In: *Optica* 10.6 (2023), pp. 783–789.

[54] M. Zhong, R. L. Ahlefeldt, and M. J. Sellars. “Quantum information processing using frozen core Y3+ spins in Eu3+:Y2SiO5.” In: *New Journal of Physics* 21.3 (2019).

[55] R. E. Evans et al. “Photon-mediated interactions between quantum emitters in a diamond nanocavity.” In: *Science* 362.6415 (2018), pp. 662–665.

[56] J. I. Cirac et al. “Quantum state transfer and entanglement distribution among distant nodes in a quantum network.” In: *Physical Review Letters* 78.16 (1997), pp. 3221–3224.

[57] A. Reiserer and G. Rempe. “Cavity-based quantum networks with single atoms and optical photons.” In: *Reviews of Modern Physics* 87.4 (2015), pp. 1379–1418.

[58] M. K. Bhaskar et al. “Experimental demonstration of memory-enhanced quantum communication.” In: *Nature* 580.7801 (2020), pp. 60–64.

[59] L.-M. Duan and H. J. Kimble. “Scalable photonic quantum computation through cavity-assisted interactions.” In: *Physical Review Letters* 92.12 (2004), p. 127902.

[60] E. Janitz, M. K. Bhaskar, and L. Childress. “Cavity quantum electrodynamics with color centers in diamond.” In: *Optica* 7.10 (2020), pp. 1232–1252.

[61] D. L. Moehring et al. “Entanglement of single-atom quantum bits at a distance.” In: *Nature* 449.7158 (2007), pp. 68–71.

[62] L. J. Stephenson et al. “High-rate, high-fidelity entanglement of qubits across an elementary quantum network.” In: *Physical Review Letters* 124.11 (2020), p. 110501.

[63] P. Drmota et al. “Robust quantum memory in a trapped-ion quantum network node.” In: *Physical Review Letters* 130.9 (2023), p. 90803.

[64] S. Ritter et al. “An elementary quantum network of single atoms in optical cavities.” In: *Nature* 484.7393 (2012), pp. 195–200.

[65] T. Đorđević et al. “Entanglement transport and a nanophotonic interface for atoms in optical tweezers.” In: *Science* 373.6562 (2021), pp. 1511–1514.

[66] J. P. Covey, H. Weinfurter, and H. Bernien. *Quantum networks with neutral atom processing nodes.* 2023. arXiv: 2304.02088 [quant-ph].

[67] H. Bernien et al. “Heralded entanglement between solid-state qubits separated by three metres.” In: *Nature* 497.7447 (2013), pp. 86–90.

[68] A. Delteil et al. “Generation of heralded entanglement between distant hole spins.” In: *Nature Physics* 12.3 (2016), pp. 218–223.

[69] R. Stockill et al. “Phase-tuned entangled state generation between distant spin qubits.” In: *Physical Review Letters* 119.1 (2017), pp. 1–6.

[70] R. Stockill et al. “Quantum dot spin coherence governed by a strained nuclear environment.” In: *Nature Communications* 7.1 (2016), p. 12745.

[71] N. Bar-Gill et al. “Solid-state electronic spin coherence time approaching one second.” In: *Nature Communications* 4.1 (2013), p. 1743.

[72] C. E. Bradley et al. “A 10-qubit solid-state spin register with quantum memory up to one minute.” In: *Physical Review X* 9 (2019), p. 031045.

[73] H. P. Bartling et al. “Entanglement of spin-pair qubits with intrinsic dephasing times exceeding a minute.” In: *Physical Review X* 12.1 (2022), p. 11048.

[74] S. Sangtawesin et al. “Origins of diamond surface noise probed by correlating single-spin measurements with surface spectroscopy.” In: *Physical Review X* 9.3 (2019), p. 31052.

[75] S. L. N. Hermans et al. “Qubit teleportation between non-neighbouring nodes in a quantum network.” In: *Nature* 605.7911 (2022), pp. 663–668.

[76] A. Sipahigil et al. “An integrated diamond nanophotonics platform for quantum-optical networks.” In: *Science* 354.6314 (2016), pp. 847–850.

[77] B. C. Rose et al. “Observation of an environmentally insensitive solid-state spin defect in diamond.” In: *Science* 361.6397 (2018), pp. 60–63.

[78] E. I. Rosenthal et al. “Microwave spin control of a tin-vacancy qubit in diamond.” In: *Physical Review X* 13.3 (2023), p. 31022.

[79] X. Guo et al. *Microwave-based quantum control and coherence protection of tin-vacancy spin qubits in a strain-tuned diamond membrane heterostructure.* 2023. arXiv: 2307.11916 [cond-mat.mes-hall].

[80] M. K. Bhaskar et al. “Quantum nonlinear optics with a germanium-vacancy color center in a nanoscale diamond waveguide.” In: *Physical Review Letters* 118.22 (2017), p. 223603.

[81] M. E. Trusheim et al. “Lead-related quantum emitters in diamond.” In: *Physical Review B* 99.7 (2019), p. 75430.

[82] K. D. Jahnke et al. “Electron-phonon processes of the silicon-vacancy centre in diamond.” In: *New Journal of Physics* 17 (2015).

[83] P.-J. Stas et al. “Robust multi-qubit quantum network node with integrated error detection.” In: *Science* 378.6619 (2022), pp. 557–560.

[84] C. P. Anderson et al. “Electrical and optical control of single spins integrated in scalable semiconductor devices.” In: *Science* 366.6470 (2019), pp. 1225–1230.

[85] D. M. Lukin, M. A. Guidry, and J. Vuckovic. “Integrated quantum photonics with silicon carbide: challenges and prospects.” In: *Physical Review X Quantum* 1.2 (2020), p. 20102.

[86] D. J. Christle et al. “Isolated electron spins in silicon carbide with millisecond coherence times.” In: *Nature Materials* 14.2 (2015), pp. 160–163.

[87] R. Nagy et al. “High-fidelity spin and optical control of single silicon-vacancy centres in silicon carbide.” In: *Nature Communications* 10.1 (2019), p. 1954.

[88] S. A. Zargaleh et al. “Evidence for near-infrared photoluminescence of nitrogen vacancy centers in 4H-SiC.” In: *Physical Review B* 94.6 (2016), p. 60102.

[89] B. Diler et al. “Coherent control and high-fidelity readout of chromium ions in commercial silicon carbide.” In: *npj Quantum Information* 6.1 (2020), p. 11.

[90] G. Wolfowicz et al. “Vanadium spin qubits as telecom quantum emitters in silicon carbide.” In: *Science Advances* 6.18 (2023), eaaz1192.

[91] L. Komza et al. *Indistinguishable photons from an artificial atom in silicon photonics.* 2022. arXiv: 2211.09305 [quant-ph].

[92] D. B. Higginbottom et al. “Optical observation of single spins in silicon.” In: *Nature* 607.7918 (2022), pp. 266–270.

[93] Y. Xiong et al. *High-throughput identification of spin-photon interfaces in silicon.* 2023. arXiv: 2303.01594 [quant-ph].

[94] M. R. Wasielewski et al. “Exploiting chemistry and molecular systems for quantum information science.” In: *Nature Reviews Chemistry* 4.9 (2020), pp. 490–504.

[95] S. L. Bayliss et al. “Enhancing spin coherence in optically addressable molecular qubits through host-matrix control.” In: *Physical Review X* 12.3 (2022), p. 31028.

[96] W. E. Moerner and L. Kador. “Optical detection and spectroscopy of single molecules in a solid.” In: *Physical Review Letters* 62.21 (1989), pp. 2535–2538.

[97] D. Wang et al. “Coherent coupling of a single molecule to a scanning Fabry-Perot microcavity.” In: *Physical Review X* 7.2 (2017), p. 21014.

[98] S. L. Bayliss et al. “Optically addressable molecular spins for quantum information processing.” In: *Science* 370.6522 (2020), pp. 1309–1312.

[99] D. Serrano et al. “Ultra-narrow optical linewidths in rare-earth molecular crystals.” In: *Nature* 603.7900 (2022), pp. 241–246.

[100] X. Liu and M. C. Hersam. “2D materials for quantum information science.” In: *Nature Reviews Materials* 4.10 (2019), pp. 669–684.

[101] A. B. D. Shaik and P. Penchalaiah. “Optical quantum technologies with hexagonal boron nitride single photon sources.” In: *Scientific Reports* 11.1 (2021), p. 12285.

[102] H. Akbari et al. “Lifetime-limited and tunable quantum light emission in h-BN via electric field modulation.” In: *Nano Letters* 22.19 (2022), pp. 7798–7803.

[103] R. J. Gelly et al. *An inverse-designed nanophotonic interface for excitons in atomically thin materials.* 2023. arXiv: `2308.13705 [physics.optics]`.

[104] R. Rizzato et al. “Extending the coherence of spin defects in hBN enables advanced qubit control and quantum sensing.” In: *Nature Communications* 14.1 (2023), p. 5089.

[105] A. J. Ramsay et al. “Coherence protection of spin qubits in hexagonal boron nitride.” In: *Nature Communications* 14.1 (2023), p. 461.

[106] C. Fournier et al. “Position-controlled quantum emitters with reproducible emission wavelength in hexagonal boron nitride.” In: *Nature Communications* 12.1 (2021), p. 3779.

[107] A. Chatterjee et al. “Semiconductor qubits in practice.” In: *Nature Reviews Physics* 3.3 (2021), pp. 157–177.

[108] D. D. Awschalom et al. “Quantum technologies with optically interfaced solid-state spins.” In: *Nature Photonics* 12.9 (2018), pp. 516–527.

[109] G. Wolfowicz et al. “Quantum guidelines for solid-state spin defects.” In: *Nature Reviews Materials* 6.10 (2021), pp. 906–925.

[110] A. Abragam and B. Bleaney. *Electron paramagnetic resonance of transition ions.* Oxford: Oxford University Press, 2012.

[111] R. Hull et al. *Spectroscopic properties of rare earths in optical materials.* Berlin: Springer-Verlag, 2005.

[112] A. Kinos et al. *Roadmap for rare-earth quantum computing.* 2021. arXiv: `2103.15743 [quant-ph]`.

[113] T. Zhong and P. Goldner. “Emerging rare-earth doped material platforms for quantum nanophotonics.” In: Nanophotonics 8.11 (2019), pp. 2003–2015.

[114] E. Z. Cruzeiro et al. “Spectral hole lifetimes and spin population relaxation dynamics in neodymium-doped yttrium orthosilicate.” In: *Physical Review B* 95.20 (2017), p. 205119.

[115] S. Welinski et al. “Coherence time extension by large-scale optical spin polarization in a rare-earth doped crystal.” In: *Physical Review X* 10.3 (2020), p. 31060.

[116] P. Stevenson et al. “Erbium-implanted materials for quantum communication applications.” In: *Physical Review B* 105.22 (2022), p. 224106.

[117] M. Rančić et al. “Coherence time of over a second in a telecom-compatible quantum memory storage material.” In: *Nature Physics* 14.1 (2018), pp. 50–54.

[118] M. Zhong et al. “Optically addressable nuclear spins in a solid with a six-hour coherence time.” In: *Nature* 517.7533 (2015), pp. 177–180.

[119] S. P. Horvath et al. *Strong Purcell enhancement of an optical magnetic dipole transition.* 2023. arXiv: 2307.03022 [physics.optics].

[120] R. M. Macfarlane, R. S. Meltzer, and B. Z. Malkin. “Optical measurement of the isotope shifts and hyperfine and superhyperfine interactions of Nd in the solid state.” In: *Physical Review B* 58.9 (1998), pp. 5692–5700.

[121] A. I. Lvovsky, B. C. Sanders, and W. Tittel. “Optical quantum memory.” In: *Nature Photonics* 3.12 (2009), pp. 706–714.

[122] C. Laplane et al. “Multimode and long-lived quantum correlations between photons and spins in a crystal.” In: *Physical Review Letters* 118.21 (2017), p. 210501.

[123] M. P. Hedges et al. “Efficient quantum memory for light.” In: *Nature* 465.7301 (2010), pp. 1052–1056.

[124] A. Ortu et al. “Storage of photonic time-bin qubits for up to 20 ms in a rare-earth doped crystal.” In: *npj Quantum Information* 8.1 (2022), p. 29.

[125] N. Timoney et al. “Single-photon-level optical storage in a solid-state spin-wave memory.” In: *Physical Review A* 88.2 (2013), p. 22324.

[126] D. Lago-Rivera et al. “Telecom-heralded entanglement between multimode solid-state quantum memories.” In: *Nature* 594.7861 (2021), pp. 37–40.

[127] X. Liu et al. “Heralded entanglement distribution between two absorptive quantum memories.” In: *Nature* 594.7861 (2021), pp. 41–45.

[128] S. Probst et al. “Microwave multimode memory with an erbium spin ensemble.” In: *Physical Review B* 92.1 (2015), p. 14421.

[129] L. A. Williamson, Y.-H. Chen, and J. J. Longdell. “Magneto-optic modulator with unit quantum efficiency.” In: *Physical Review Letters* 113.20 (2014), p. 203601.

[130] X. Fernandez-Gonzalvo et al. “Coherent frequency up-conversion of microwaves to the optical telecommunications band in an Er:YSO crystal.” In: *Physical Review A* 92.6 (2015), p. 62313.

[131] X. Fernandez-Gonzalvo et al. “Cavity-enhanced Raman heterodyne spectroscopy in Er3+:Y2SiO5 for microwave to optical signal conversion.” In: *Physical Review A* 100.3 (2019), p. 33807.

[132] J. G. Bartholomew et al. “On-chip coherent microwave-to-optical transduction mediated by ytterbium in YVO4.” In: *Nature Communications* 11.1 (2020), p. 3266.

[133] J. R. Everts et al. “Microwave to optical photon conversion via fully concentrated rare-earth-ion crystals.” In: *Physical Review A* 99.6 (2019), p. 63830.

[134] J. R. Everts et al. “Ultrastrong coupling between a microwave resonator and antiferromagnetic resonances of rare-earth ion spins.” In: *Physical Review B* 101.21 (2020), p. 214414.

[135] R. Kolesov et al. “Optical detection of a single rare-earth ion in a crystal.” In: *Nature Communications* 3.1 (2012), p. 1029.

[136] K. Xia et al. “Spectroscopy properties of a single praseodymium ion in a crystal.” In: *New Journal of Physics* 22.7 (2020), p. 73002.

[137] K. Groot-Berning et al. “Deterministic single-ion implantation of rare-earth ions for nanometer-resolution color-center generation.” In: *Physical Review Letters* 123.10 (2019), p. 106802.

[138] I. Nakamura et al. “Spectroscopy of single Pr3+ ion in LaF3 crystal at 1.5 K.” In: *Scientific Reports* 4.1 (2014), p. 7364.

[139] R. Kolesov et al. “Mapping spin coherence of a single rare-earth ion in a crystal onto a single photon polarization state.” In: *Physical Review Letters* 111.12 (2013), p. 120502.

[140] P. Siyushev et al. “Coherent properties of single rare-earth spin qubits.” In: *Nature Communications* 5.1 (2014), p. 3895.

[141] K. Xia et al. “All-optical preparation of coherent dark states of a single rare earth ion spin in a crystal.” In: *Physical Review Letters* 115.9 (2015), p. 93602.

[142] R. Kolesov et al. “Superresolution microscopy of single rare-earth emitters in YAG and H3 centers in diamond.” In: *Physical Review Letters* 120.3 (2018), p. 33903.

[143] T. Kornher et al. “Sensing individual nuclear spins with a single rare-earth electron spin.” In: *Physical Review Letters* 124.17 (2020), p. 170402.

[144] C. Yin et al. “Optical addressing of an individual erbium ion in silicon.” In: *Nature* 497.7447 (2013), pp. 91–94.

[145] G. G. de Boo et al. “High-resolution spectroscopy of individual erbium ions in strong magnetic fields.” In: *Physical Review B* 102.15 (2020), p. 155309.

[146] J. Yang et al. “Zeeman and hyperfine interactions of a single 167Er3+ ion in Si.” In: *Physical Review B* 105.23 (2022), p. 235306.

[147] G. Hu et al. “Time-resolved photoionization detection of a single Er3+ ion in silicon.” In: *Nano Letters* 22.1 (2022), pp. 396–401.

[148] J. Yang et al. “Spectral broadening of a single Er3+ ion in a Si nanotransistor.” In: *Physical Review Applied* 18.3 (2022), p. 34018.

[149] Y. Zhang et al. “Photoionisation detection of a single Er3+ ion with sub-100-ns time resolution.” In: *National Science Review* (2023).

[150] G. Hu et al. “Single site optical spectroscopy of coupled Er3+ ion pairs in silicon.” In: *Quantum Science and Technology* 7.2 (2022), p. 25019.

[151] Q. I. Zhang et al. “Single rare-earth ions as atomic-scale probes in ultrascaled transistors.” In: *Nano Letters* 19.8 (2019), pp. 5025–5030.

[152] T. Utikal et al. “Spectroscopic detection and state preparation of a single praseodymium ion in a crystal.” In: *Nature Communications* 5.1 (2014), p. 3627.

[153] E. Eichhammer et al. “Spectroscopic detection of single Pr3+ ions on the 3H4-1D2 transition.” In: *New Journal of Physics* 17.8 (2015), p. 83018.

[154] T. Zhong et al. “Optically addressing single rare-earth ions in a nanophotonic cavity.” In: *Physical Review Letters* 121.18 (2018), p. 183603.

[155] J. M. Kindem et al. “Control and single-shot readout of an ion embedded in a nanophotonic cavity.” In: *Nature* 580.7802 (2020), pp. 201–204.

[156] M. Raha et al. “Optical quantum nondemolition measurement of a single rare earth ion qubit.” In: *Nature Communications* 11.1 (2020), p. 1605.

[157] S. Chen et al. “Parallel single-shot measurement and coherent control of solid-state spins below the diffraction limit.” In: *Science* 370.6516 (2020), pp. 592–595.

[158] A. Ruskuc et al. “Nuclear spin-wave quantum register for a solid-state qubit.” In: *Nature* 602.7897 (2022), pp. 408–413.

[159] M. T. Uysal et al. “Coherent control of a nuclear spin via interactions with a rare-earth ion in the solid state.” In: *Physical Review X Quantum* 4.1 (2023), p. 10323.

[160] J.-Y. Huang et al. “Stark tuning of telecom single-photon emitters based on a single Er3+.” In: *Chinese Physics Letters* 40.7 (2023), p. 70301.

[161] A. Ulanowski, B. Merkel, and A. Reiserer. “Spectral multiplexing of telecom emitters with stable transition frequency.” In: *Science Advances* 8.43 (2023).

[162] L. Yang et al. “Controlling single rare earth ion emission in an electro-optical nanocavity.” In: *Nature Communications* 14.1 (2023), p. 1718.

[163] Y. Yu et al. *Frequency tunable, cavity-enhanced single erbium quantum emitter in the telecom band.* 2023. arXiv: 2304.14685 [quant-ph].

[164] K. Xia et al. “Tunable microcavities coupled to rare-earth quantum emitters.” In: *Optica* 9.4 (2022), pp. 445–450.

[165] S. Ourari et al. “Indistinguishable telecom band photons from a single Er ion in the solid state.” In: *Nature* 620.7976 (2023), pp. 977–981.

[166] T. Zhong et al. “High quality factor nanophotonic resonators in bulk rare-earth doped crystals.” In: *Optics Express* 24.1 (2016), p. 536.

[167] S. Chen et al. “Hybrid microwave-optical scanning probe for addressing solid-state spins in nanophotonic cavities.” In: *Optics Express* 29.4 (2021), pp. 4902–4911.

[168] C.-J. Wu et al. “Near-infrared hybrid quantum photonic interface for 171Yb3+ solid-state qubits.” In: *Physical Review Applied* 20.4 (2023), p. 44018.

[169] C. Deshmukh et al. *Detection of single ions in a nanoparticle coupled to a fiber cavity.* 2023. arXiv: 2303.00017 [quant-ph].

[170] M. Pallmann et al. “A highly stable and fully tunable open microcavity platform at cryogenic temperatures.” In: *APL Photonics* 8.4 (2023), p. 46107.

[171] Z. Wang et al. “Single-electron spin resonance detection by microwave photon counting.” In: *Nature* 619.7969 (2023), pp. 276–281.

[172] G. Wolfowicz et al. “Vanadium spin qubits as telecom quantum emitters in silicon carbide.” In: *Science Advances* 6.18 (2020).

[173] A. Ortu et al. “Simultaneous coherence enhancement of optical and microwave transitions in solid-state electronic spins.” In: *Nature Materials* 17.8 (2018), pp. 671–675.

[174] F. Chiossi et al. “Photon echo, spectral hole burning, and optically detected magnetic resonance in 171Yb3+:LiNbO3 bulk crystal and waveguides.” In: *Physical Review B* 105.18 (2022), p. 184115.

[175] J. M. Kindem et al. “Characterization of Yb 3+ 171:YVO4 for photonic quantum technologies.” In: *Physical Review B* 98.2 (2018), pp. 1–10.

[176] T. Böttger et al. “Optical spectroscopy and decoherence studies of Yb3+:YAG at 968 nm.” In: *Physical Review B* 94.4 (2016), p. 45134.

[177] M. Businger et al. “Optical spin-wave storage in a solid-state hybridized electron-nuclear spin ensemble.” In: *Physical Review Letters* 124.5 (2020), p. 53606.

[178] J. H. Weber et al. “Two-photon interference in the telecom C-band after frequency conversion of photons from remote quantum emitters.” In: *Nature Nanotechnology* 14.1 (2019), pp. 23–26.

[179] R. Ikuta et al. “Polarization insensitive frequency conversion for an atom-photon entanglement distribution via a telecom network.” In: *Nature Communications* 9.1 (2018), p. 1997.

[180] M. Bock et al. “High-fidelity entanglement between a trapped ion and a telecom photon via quantum frequency conversion.” In: *Nature Communications* 9.1 (2018), p. 1998.

[181] A. Dréau et al. “Quantum frequency conversion of single photons from a nitrogen-vacancy center in diamond to telecommunication wavelengths.” In: *Physical Review Applied* 9.6 (2018), p. 64031.

[182] A. J. Stolk et al. “Telecom-band quantum interference of frequency-converted photons from remote detuned NV centers.” In: *Physical Review X Quantum* 3.2 (2022), p. 20359.

[183] E. Bersin et al. *Telecom networking with a diamond quantum memory.* 2023. arXiv: 2307.08619 [quant-ph].

[184] E.V. Pestryakov et al. “Availability of new Yb:YVO4 and Yb:GdxY1-xVO4 laser crystals for femtosecond laser systems at low temperature.” In: *Proceedings SPIE*. Vol. 6054. 2006, p. 60540I.

[185] U. Ranon. “Paramagnetic resonance of Nd3+, Dy3+, Er3+ and Yb3+ in YVO4.” In: *Physics Letters A* 28.3 (1968), pp. 228–229.

[186] L. Childress et al. “Coherent dynamics of coupled electron and nuclear spin qubits in diamond.” In: *Science* 314.5797 (2006), pp. 281–285.

[187] M. V. Gurudev Dutt et al. “Quantum register based on individual electronic and nuclear spin qubits in diamond.” In: *Science* 316.June (2007), pp. 1312–1317.

[188] S. Kolkowitz et al. “Sensing distant nuclear spins with a single electron spin.” In: *Physical Review Letters* 109.13 (2012), pp. 1–5.

[189] T. H. Taminiau et al. “Detection and control of individual nuclear spins using a weakly coupled electron spin.” In: *Physical Review Letters* 109.13 (2012), p. 137602.

[190] N. Zhao et al. “Sensing single remote nuclear spins.” In: *Nature Nanotechnology* 7.10 (2012), pp. 657–662.

[191] T. H. Taminiau et al. “Universal control and error correction in multi-qubit spin registers in diamond.” In: *Nature Nanotechnology* 9.3 (2014), pp. 171–176.

[192] C. E. Bradley et al. “A ten-qubit solid-state spin register with quantum memory up to one minute.” In: *Physical Review X* 9.3 (2019), p. 31045.

[193] M. H. Metsch et al. “Initialization and readout of nuclear spins via negatively charged silicon-vacancy center in diamond.” In: *Physical Review Letters* 122 (2019), p. 190503.

[194] A. Bourassa et al. “Entanglement and control of single nuclear spins in isotopically engineered silicon carbide.” In: *Nature Materials* 19.12 (2020), pp. 1319–1325.

[195] G. Wolfowicz et al. “29Si nuclear spins as a resource for donor spin qubits in silicon.” In: *New Journal of Physics* 18.2 (2016).

[196] B. Hensen et al. “A silicon quantum-dot-coupled nuclear spin qubit.” In: *Nature Nanotechnology* 15.1 (2020), pp. 13–17.

[197] D. A. Gangloff et al. “Quantum interface of an electron and a nuclear ensemble.” In: *Science* 364.6435 (2019), pp. 62–66.

[198] D. A. Gangloff et al. “Witnessing quantum correlations in a nuclear ensemble via an electron spin qubit.” In: *Nature Physics* 17.11 (2021), pp. 1247–1253.

[199] D. M. Jackson et al. “Quantum sensing of a coherent single spin excitation in a nuclear ensemble.” In: *Nature Physics* (2021).

[200] D. M. Jackson et al. “Optimal purification of a spin ensemble by quantum-algorithmic feedback.” In: *Physical Review X* 12.3 (2022), p. 31014.

[201] E. A. Chekhovich, S. F. C. da Silva, and A. Rastelli. “Nuclear spin quantum register in an optically active semiconductor quantum dot.” In: *Nature Nanotechnology* 15.12 (2020), pp. 999–1004.

[202] B. Car et al. “Selective optical addressing of nuclear spins through superhyperfine interaction in rare-earth doped solids.” In: *Physical Review Letters* 120.19 (2018), pp. 1–6.

[203] B. Bleaney et al. “Nuclear magnetic resonance of 51V (I=7/2) in lanthanide vanadates: II. The nuclear electric quadrupole interaction.” In: *Journal of Physics C: Solid State Physics* 15.25 (1982), pp. 5293–5303.

[204] B. Bleaney et al. “Nuclear magnetic resonance of 51V (I=7/2) in lanthanide vanadates: I. The paramagnetic shifts.” In: *Journal of Physics C: Solid State Physics* 15.25 (1982), pp. 5293–5303.

[205] H. J. Carmichael. *Statistical methods in quantum optics: Vol. 1: Master equations and Fokker-Planck equations.* Berlin: Springer, 1999.

[206] D. A. Steck. *Quantum and atom optics.* Lecture notes, 2023.

[207] K. Fischer et al. “Dynamical modeling of pulsed two-photon interference.” In: *New Journal of Physics* 18 (2016).

[208] E. Knill et al. “Randomized benchmarking of quantum gates.” In: *Physical Review A* 77.1 (2008), pp. 1–7.

[209] H. Y. Carr and E. M. Purcell. “Effects of diffusion on free precession in nuclear magnetic resonance experiments.” In: *Physical Review* 94.3 (1954), pp. 630–638.

[210] S. Meiboom and D. Gill. “Modified spin-echo method for measuring nuclear relaxation times.” In: *Review of Scientific Instruments* 29.8 (1958), pp. 688–691.

[211] G. de Lange et al. “Universal dynamical decoupling of a single solid-state spin from a spin bath.” In: *Science* 330.6000 (2010), pp. 60–63.

[212] T. Gullion, D. B. Baker, and M. S. Conradi. “New, compensated Carr-Purcell sequences.” In: *Journal of Magnetic Resonance (1969)* 89.3 (1990), pp. 479–484.

[213] C. P. Slichter. *Principles of magnetic resonance*. New York: Springer-Verlag, 1992.

[214] N. Y. Garces et al. “Electron paramagnetic resonance and optical absorption study of V4+ centres in YVO4 crystals.” In: *Journal of Physics: Condensed Matter* 16.39 (2004), p. 7095.

[215] M. Onizhuk and G. Galli. “PyCCE: a python package for cluster correlation expansion simulations of spin qubit dynamics.” In: *Advanced Theory and Simulations* 4.11 (2021), p. 2100254.

[216] D. D. Awschalom et al. “Quantum technologies with optically interfaced solid-state spins.” In: *Nature Photonics* 12.9 (2018), pp. 516–527.

[217] A. Chatterjee et al. “Semiconductor qubits in practice.” In: *Nature Reviews Physics* 3.3 (2021), pp. 157–177.

[218] B. Hensen et al. “Loophole-free Bell inequality violation using electron spins separated by 1.3 kilometres.” In: *Nature* 526.7575 (2015), pp. 682–686.

[219] M. K. Bhaskar et al. “Experimental demonstration of memory-enhanced quantum communication.” In: *Nature* 580.7801 (2020), pp. 60–64.

[220] C. E. Bradley et al. “Robust quantum-network memory based on spin qubits in isotopically engineered diamond.” In: *npj Quantum Information* 8.1 (2022), p. 122.

[221] G. Waldherr et al. “Quantum error correction in a solid-state hybrid spin register.” In: *Nature* 506.7487 (2014), pp. 204–207.

[222] M. H. Abobeih et al. “Fault-tolerant operation of a logical qubit in a diamond quantum processor.” In: *Nature* 606.7916 (2022), pp. 884–889.

[223] J. Randall et al. “Many-body–localized discrete time crystal with a programmable spin-based quantum simulator.” In: *Science* 374.6574 (2021), pp. 1474–1478.

[224] B. Urbaszek et al. “Nuclear spin physics in quantum dots: An optical investigation.” In: *Reviews of Modern Physics* 85.1 (2013), pp. 79–133.

[225] C. Cohen-Tannoudji, J. Dupont-Roc, and G. Grynberg. *Atom-photon interactions.* Weinheim: Wiley-VCH, 2004.

[226] A. Bermudez et al. “Electron-mediated nuclear-spin interactions between distant nitrogen-vacancy centers.” In: *Physical Review Letters* 107.15 (2011), pp. 3–7.

[227] C. L. Degen, F. Reinhard, and P. Cappellaro. “Quantum sensing.” In: *Reviews of Modern Physics* 89.3 (2017), pp. 1–39.

[228] S. R. Hartmann and E. L. Hahn. “Nuclear double resonance in the rotating frame.” In: *Physical Review* 128.5 (1962), pp. 2042–2053.

[229] J. M. Taylor, C. M. Marcus, and M. D. Lukin. “Long-lived memory for mesoscopic quantum bits.” In: *Physical Review Letters* 90.20 (2003), p. 4.

[230] P. Siyushev et al. “Coherent properties of single rare-earth spin qubits.” In: *Nature Communications* 5 (2014), pp. 1–6.

[231] H. Weimer, N. Y. Yao, and M. D. Lukin. “Collectively enhanced interactions in solid-state spin qubits.” In: *Physical Review Letters* 110.6 (2013), pp. 1–5.

[232] J. Choi et al. “Robust dynamic Hamiltonian engineering of many-body spin systems.” In: *Physical Review X* 10.3 (2019), p. 31002.

[233] I. Schwartz et al. “Robust optical polarization of nuclear spin baths using Hamiltonian engineering of nitrogen-vacancy center quantum dynamics.” In: *Science Advances* 4.8 (2018), pp. 1–8.

[234] J. Scheuer et al. “Robust techniques for polarization and detection of nuclear spin ensembles.” In: *Physical Review B* 96.17 (2017), pp. 1–10.

[235] E. Bauch et al. “Ultralong dephasing times in solid-state spin ensembles via quantum control.” In: *Physical Review X* 8.3 (2018), p. 31025.

[236] H. Levine et al. “High-fidelity control and entanglement of Rydberg-atom qubits.” In: *Physical Review Letters* 121.12 (2018), pp. 1–6.

[237] B. B. Blinov et al. “Observation of entanglement between a single trapped atom and a single photon.” In: *Nature* 428.6979 (2004), pp. 153–157.

[238] M. Zukowski et al. “Event-ready-detectors Bell experiment via entanglement swapping.” In: *Physical Review Letters* 71.26 (1993), pp. 4287–4290.

[239] M. O. Scully and K. Drühl. “Quantum eraser: A proposed photon correlation experiment concerning observation and “delayed choice” in quantum mechanics.” In: *Physical Review A* 25.4 (1982), pp. 2208–2213.

[240] C. K. Hong, Z. Y. Ou, and L. Mandel. “Measurement of subpicosecond time intervals between two photons by interference.” In: *Physical Review Letters* 59.18 (1987), pp. 2044–2046.

[241] J. Beugnon et al. “Quantum interference between two single photons emitted by independently trapped atoms.” In: *Nature* 440.7085 (2006), pp. 779–782.

[242] P. Maunz et al. “Quantum interference of photon pairs from two remote trapped atomic ions.” In: *Nature Physics* 3.8 (2007), pp. 538–541.

[243] C. Santori et al. “Indistinguishable photons from a single-photon device.” In: *Nature* 419.6907 (2002), pp. 594–597.

[244] E. B. Flagg et al. “Interference of single photons from two separate semiconductor quantum dots.” In: *Physical Review Letters* 104.13 (2010), p. 137401.

[245] R. B. Patel et al. “Two-photon interference of the emission from electrically tunable remote quantum dots.” In: *Nature Photonics* 4.9 (2010), pp. 632–635.

[246] R. Lettow et al. “Quantum interference of tunably indistinguishable photons from remote organic molecules.” In: *Physical Review Letters* 104.12 (2010), p. 123605.

[247] D. M. Lukin et al. “Two-emitter multimode cavity quantum electrodynamics in thin-film silicon carbide photonics.” In: *Physical Review X* 13.1 (2023), p. 11005.

[248] H. Bernien et al. “Two-photon quantum interference from separate nitrogen vacancy centers in diamond.” In: *Physical Review Letters* 108.4 (2012), p. 43604.

[249] A. Sipahigil et al. “Indistinguishable photons from separated silicon-vacancy centers in diamond.” In: *Physical Review Letters* 113.11 (2014), p. 113602.

[250] A. Sipahigil et al. “Quantum interference of single photons from remote nitrogen-vacancy centers in diamond.” In: *Physical Review Letters* 108.14 (2012), pp. 1–5.

[251] C. Santori, D. Fattal, and Y. Yamamoto. *Single-photon devices and applications.* Weinheim: Wiley-VCH, 2010.

[252] T. Legero et al. “Time-resolved two-photon quantum interference.” In: *Applied Physics B* 77.8 (2003), pp. 797–802.

[253] T. Legero et al. “Quantum beat of two single photons.” In: *Physical Review Letters* 93.7 (2004), p. 70503.

[254] M. O. Scully and M. S. Zubairy. *Quantum optics.* Cambridge: Cambridge University Press, 1997.

[255] K. J. Blow et al. “Continuum fields in quantum optics.” In: *Physical Review A* 42.7 (1990), pp. 4102–4114.

[256] B. Kambs and C. Becher. “Limitations on the indistinguishability of photons from remote solid state sources.” In: *New Journal of Physics* 20.11 (2018).

[257] M. G. Raymer and I. A. Walmsley. "Temporal modes in quantum optics: then and now." In: *Physica Scripta* 95.6 (2020), p. 64002.

[258] J. Hofmann et al. "Heralded entanglement between widely separated atoms." In: *Science* 337.6090 (2012), pp. 72–75.

[259] P. C. Humphreys et al. "Deterministic delivery of remote entanglement on a quantum network." In: *Nature* 558 (2018), pp. 268–273.

[260] D. S. Levonian et al. "Optical entanglement of distinguishable quantum emitters." In: *Physical Review Letters* 128.21 (2022), p. 213602.

[261] S. D. Barrett and P. Kok. "Efficient high-fidelity quantum computation using matter qubits and linear optics." In: *Physical Review A* 71.6 (2005), p. 60310.

[262] S. Bose et al. "Proposal for Teleportation of an Atomic State via Cavity Decay." In: *Physical Review Letters* 83.24 (1999), pp. 5158–5161.

[263] C. Cabrillo et al. "Creation of entangled states of distant atoms by interference." In: *Physical Review A* 59.2 (1999), pp. 1025–1033.

[264] S. L. N. Hermans et al. "Entangling remote qubits using the single-photon protocol: an in-depth theoretical and experimental study." In: *New Journal of Physics* 25.1 (2023), p. 13011.

[265] L. Slodicka et al. "Atom-atom entanglement by single-photon detection." In: *Physical Review Letters* 110.8 (2013), p. 83603.

[266] L. C. Bassett et al. "Electrical tuning of single nitrogen-vacancy center optical transitions enhanced by photoinduced fields." In: *Physical Review Letters* 107.26 (2011), p. 266403.

[267] N. Maring et al. "Photonic quantum state transfer between a cold atomic gas and a crystal." In: *Nature* 551.7681 (2017), pp. 485–488.

[268] Y. Yu et al. "Entanglement of two quantum memories via fibres over dozens of kilometres." In: *Nature* 578.7794 (2020), pp. 240–245.

[269] G. Vittorini et al. "Entanglement of distinguishable quantum memories." In: *Physical Review A* 90.4 (2014), p. 40302.

[270] T.-M. Zhao et al. "Entangling different-color photons via time-resolved measurement and active feed forward." In: *Physical Review Letters* 112.10 (2014), p. 103602.

[271] A. Angerer et al. "Superradiant emission from colour centres in diamond." In: *Nature Physics* 14.12 (2018), pp. 1168–1172.

[272] G. J. Milburn and H. M. Wiseman, eds. *Open quantum systems.* Cambridge: Cambridge University Press, 2009.

[273] R. W. P. Drever et al. "Laser phase and frequency stabilization using an optical resonator." In: *Applied Physics B* 31 (1983), pp. 97–105.

[274] D. F. V. James et al. “Measurement of qubits.” In: *Physical Review A* 64.5 (2001), p. 52312.

[275] Z. Hradil. “Quantum-state estimation.” In: *Physical Review A* 55.3 (1997), R1561–R1564.

[276] M. Grant and S. Boyd. *Graph implementations for nonsmooth convex programs.* Berlin: Springer-Verlag, 2008.

[277] D. A. Lidar, I. L. Chuang, and K. B. Whaley. “Decoherence-free subspaces for quantum computation.” In: *Physical Review Letters* 81.12 (1998), pp. 2594–2597.

[278] D. Kielpinski et al. “A decoherence-free quantum memory using trapped ions.” In: *Science* 291.5506 (2001), pp. 1013–1015.

[279] S. L. Braunstein and A. Mann. “Measurement of the Bell operator and quantum teleportation.” In: *Physical Review A* 51.3 (1995), R1727–R1730.

[280] R. Valivarthi et al. “Efficient Bell state analyzer for time-bin qubits with fast-recovery WSi superconducting single photon detectors.” In: *Optics Express* 22.20 (2014), pp. 24497–24506.

[281] S. Langenfeld et al. “Quantum repeater node demonstrating unconditionally secure key distribution.” In: *Physical Review Letters* 126.23 (2021), p. 230506.

[282] B. B. Buckley et al. “Spin-light coherence for single-spin measurement and control in diamond.” In: *Science* 330.6008 (2010), pp. 1212–1215.

[283] K. Singh et al. “Mid-circuit correction of correlated phase errors using an array of spectator qubits.” In: *Science* 380.6651 (2023), pp. 1265–1269.

[284] P. L. Ocola et al. *Control and entanglement of individual rydberg atoms near a nanoscale device.* 2022. arXiv: 2210.12879 [physics.atom-ph].

[285] B. Zeng et al. *Cryogenic packaging of nanophotonic devices with a low coupling loss < 1 dB.* 2023. arXiv: 2306.09894 [physics.optics].

[286] J. Borregaard et al. “Heralded quantum gates with integrated error detection in optical cavities.” In: *Physical Review Letters* 114.11 (2015), p. 110502.

[287] C. T. Nguyen et al. “An integrated nanophotonic quantum register based on silicon-vacancy spins in diamond.” In: *Physical Review B* 100.16 (2019), pp. 1–19.

*Appendix A*

# IMPURITIES IN $YVO_4$ CRYSTALS

The nominally undoped $YVO_4$ crystal boules used in these projects were grown by Gamdan Optics using the Czochralski method. Impurities were characterized using glow discharge mass spectrometry (GDMS), EAG Laboratories. The results are presented in Figure A.1. The Yb concentration corresponds to 140ppb of all isotopes, assuming natural abundance of different isotopes this corresponds to 20ppb $^{171}Yb^{3+}$.

| Element | Concentration [ ppm wt ] | Element | Concentration [ ppm wt ] |
|---|---|---|---|
| Li | 0.41 | Ag | < 0.5 |
| Be | < 0.01 | Cd | < 1 |
| B | < 0.05 | In | Binder |
| O | Matrix | Sn | < 1 |
| F | < 1 | Sb | < 1 |
| Na | 0.19 | Te | < 0.5 |
| Mg | 0.10 | I | < 1 |
| Al | 2.0 | Cs | < 5 |
| Si | 13 | Ba | < 0.05 |
| P | 0.38 | La | 2.0 |
| S | 4.3 | Ce | 0.24 |
| Cl | 0.24 | Pr | < 0.05 |
| K | < 0.5 | Nd | < 0.05 |
| Ca | 0.53 | Sm | < 0.05 |
| Sc | < 0.05 | Eu | < 0.5 |
| Ti | 0.03 | Gd | 0.41 |
| V | Matrix | Tb | < 0.05 |
| Cr | < 0.1 | Dy | < 0.05 |
| Mn | < 0.05 | Ho | 0.42 |
| Fe | 1.5 | Er | 0.40 |
| Co | < 0.01 | Tm | < 0.05 |
| Ni | 0.26 | Yb | 0.14 |
| Cu | < 0.5 | Lu | < 0.05 |
| Zn | < 0.5 | Hf | < 0.05 |
| Ga | < 0.1 | Ta | < 50 |
| Ge | < 0.5 | W | 0.14 |
| As | < 0.1 | Re | < 0.05 |
| Se | < 0.5 | Os | < 0.05 |
| Br | < 1 | Ir | < 0.1 |
| Rb | < 0.1 | Pt | < 0.5 |
| Sr | < 0.5 | Au | < 0.5 |
| Y | Matrix | Hg | < 0.5 |
| Zr | 0.91 | Tl | < 0.05 |
| Nb | < 0.05 | Pb | < 0.1 |
| Mo | 0.37 | Bi | < 0.1 |
| Ru | < 0.1 | Th | < 0.01 |
| Rh | < 0.5 | U | 0.10 |
| Pd | < 0.5 | | |

Figure A.1: Concentration of impurities present in $YVO_4$ used in this work.

*Appendix B*

# V REGISTER READOUT CORRECTION

Since $^{171}$Yb readout fidelity is > 95% [155], the dominant error introduced during the population basis measurements arises from the swap gate. We measure its fidelity in the population basis by preparing either the $|0_g 0_v\rangle$ state (zero spin excitations) or the $|1_g 0_v\rangle$ state (single spin excitation) and applying two consecutive swap gates such that the system is returned to the initial state. By comparing the $^{171}$Yb population before ($p_{\text{pre}}$) and after ($p_{\text{post}}$) the two gates are applied, we can extract fidelity estimates independently from the $^{51}$V state initialization. Assuming the swap and swap-back processes are symmetric, we obtain a gate fidelity $\mathcal{F}_{\text{sw}} = \sqrt{(1-2p_{\text{post}})/(1-2p_{\text{pre}})}$. This quantity is measured for zero spin excitations leading to $\mathcal{F}_{\text{sw},0} = 0.83$ and with a single spin excitation leading to $\mathcal{F}_{\text{sw},1} = 0.52$.

When measuring the joint $^{171}$Yb–$^{51}$V populations $\{p_{00}, p_{01}, p_{10}, p_{11}\}$ we can use these fidelities to extract a set of corrected populations $\{c_{00}, c_{01}, c_{10}, c_{11}\}$ according to the method described in [67, 287] using

$$\begin{pmatrix} c_{11} \\ c_{10} \\ c_{01} \\ c_{00} \end{pmatrix} = E^{-1} \begin{pmatrix} p_{11} \\ p_{10} \\ p_{01} \\ p_{00} \end{pmatrix}, \tag{B.1}$$

where

$$E = \frac{1}{2} \begin{pmatrix} 1+\mathcal{F}_{\text{sw},1} & 1-\mathcal{F}_{\text{sw},0} & 0 & 0 \\ 1-\mathcal{F}_{\text{sw},1} & 1+\mathcal{F}_{\text{sw},0} & 0 & 0 \\ 0 & 0 & 1+\mathcal{F}_{\text{sw},1} & 1-\mathcal{F}_{\text{sw},0} \\ 0 & 0 & 1-\mathcal{F}_{\text{sw},1} & 1+\mathcal{F}_{\text{sw},0} \end{pmatrix}.$$

We use a similar approach to correct the $\sqrt{\text{swap}}$ gate used to read out the Bell state coherence.

*Appendix C*

# V REGISTER BELL STATE FIDELITY ESTIMATION

Here we derive an expression for the $^{171}$Yb–$^{51}$V Bell-state coherence $\rho_{01} = \langle 1_g 0_v | \, \rho \, | 0_g W_v \rangle$ in terms of the parity oscillation contrast with a correction factor. In particular, when reading out this coherence, we apply a $\sqrt{\text{swap}}$ gate which maps $|\Psi^+\rangle = \frac{1}{\sqrt{2}}(|1_g 0_v\rangle - i\,|0_g W_v\rangle)$ to $|0_g W_v\rangle$ and $|\Psi^-\rangle = \frac{1}{\sqrt{2}}(|1_g 0_v\rangle + i\,|0_g W_v\rangle)$ to $|1_g 0_v\rangle$. Note that reading out the $^{171}$Yb state is sufficient to distinguish the $|\Psi^+\rangle$ and $|\Psi^-\rangle$ states in this measurement. We can account for the readout fidelity of the $|\Psi^\pm\rangle$ states by using a $\sqrt{\mathcal{F}_{\text{sw},1}}$ factor (Appendix B), i.e., if the state $|\Psi^+\rangle$ ($|\Psi^-\rangle$) is perfectly prepared, $^{171}$Yb will be measured in state $|0_g\rangle$ ($|1_g\rangle$) with probability $\frac{1}{2}(1+\sqrt{\mathcal{F}_{\text{sw},1}})$. To span the $^{171}$Yb–$^{51}$V Hilbert space, we also need to consider the effect of the readout $\sqrt{\text{swap}}$ gate when the system is initialized into the other two states: $|1_g W_v\rangle$ or $|0_g 0_v\rangle$. To this end, we assign imperfect readout probabilities of $q_{11}$ and $q_{00}$ for $|1_g W_v\rangle$ and $|0_g 0_v\rangle$, respectively. Specifically, we can represent the dependence of the parity readout on the input state using the following matrix relation:

$$\begin{pmatrix} p_{1,\text{Yb}} \\ p_{0,\text{Yb}} \end{pmatrix} = \mathcal{M}_{\text{swap}} \mathcal{M}_{\text{wait}} \begin{pmatrix} p_{11} \\ p_{\Psi^+} \\ p_{\Psi^-} \\ p_{00} \end{pmatrix} \tag{C.1}$$

with

$$\mathcal{M}_{\text{swap}} = \begin{pmatrix} q_{11} & \frac{1}{2}(1-\sqrt{\mathcal{F}_{\text{sw},1}}) & \frac{1}{2}(1+\sqrt{\mathcal{F}_{\text{sw},1}}) & 1-q_{00} \\ 1-q_{11} & \frac{1}{2}(1+\sqrt{\mathcal{F}_{\text{sw},1}}) & \frac{1}{2}(1-\sqrt{\mathcal{F}_{\text{sw},1}}) & q_{00} \end{pmatrix},$$

$$\mathcal{M}_{\text{wait}} = \begin{pmatrix} 1 & 0 & 0 & 0 \\ 0 & \cos^2(\omega_c t/2) & \sin^2(\omega_c t/2) & 0 \\ 0 & \sin^2(\omega_c t/2) & \cos^2(\omega_c t/2) & 0 \\ 0 & 0 & 0 & 1 \end{pmatrix}.$$

Here $p_{1,\text{Yb}}$ and $p_{0,\text{Yb}}$ are the probabilities of measuring the $^{171}$Yb qubit in $|1_g\rangle$ and $|0_g\rangle$, respectively, and $p_{\Psi^\pm} = \langle \Psi^\pm | \, \rho \, | \Psi^\pm \rangle$ are the probabilities of being in the $|\Psi^\pm\rangle$ Bell states. The contrast $C_{\text{parity}}$ of the parity oscillation between $|\Psi^+\rangle$ and $|\Psi^-\rangle$ is extracted by measuring the difference in the $^{171}$Yb $|1_g\rangle$ populations measured at $t = 0$ and $t = \pi/\omega_c$, allowing us to estimate the Bell state coherence

as $|\rho_{01}| = C_{\text{parity}}/2\sqrt{\mathcal{F}_{\text{sw,1}}}$. This implies that uncorrected and corrected Bell state coherence values differ by a factor of $\sqrt{\mathcal{F}_{\text{sw,1}}} = 0.72$. Using the results presented in Figure 6.12b we obtain corrected and uncorrected estimates for $|\rho_{01}|$ of $0.352 \pm 0.004$ and $0.254 \pm 0.003$, respectively.

We also measure the Bell state populations using the method described in Section 6.7. The corresponding uncorrected (corrected) populations for the four basis states, denoted $p_{ij}$ ($c_{ij}$) are:

$$\begin{aligned}
p_{00} \equiv \langle 0_g 0_v | \, \rho \, | 0_g 0_v \rangle &= 0.16 \pm 0.01 \ (c_{00} = 0.07 \pm 0.02), \\
p_{01} \equiv \langle 0_g W_v | \, \rho \, | 0_g W_v \rangle &= 0.32 \pm 0.01 \ (c_{01} = 0.41 \pm 0.02), \\
p_{10} \equiv \langle 1_g 0_v | \, \rho \, | 1_g 0_v \rangle &= 0.40 \pm 0.02 \ (c_{10} = 0.41 \pm 0.02), \\
p_{11} \equiv \langle 1_g W_v | \, \rho \, | 1_g W_v \rangle &= 0.12 \pm 0.01 \ (c_{11} = 0.11 \pm 0.01).
\end{aligned}$$

To extract the Bell state fidelity and uncertainty, we perform a maximum likelihood analysis of the population and parity oscillation measurements, adopting a similar approach as in [67]. The population measurement involves a series of $n$ experiments with outcomes distributed between the four population states: $\{n_{00}, n_{01}, n_{10}, n_{11}\}$ where $n = n_{00} + n_{01} + n_{10} + n_{11}$. The likelihood function for the uncorrected populations, $\{p_{00}, p_{01}, p_{10}, p_{11}\}$ has multinomial form:

$$\mathcal{L}\left(\{p_{ij}\}|\{n_{ij}\}\right) = \frac{n!}{n_{00}!n_{01}!n_{10}!n_{11}!} p_{00}^{n_{00}} p_{01}^{n_{01}} p_{10}^{n_{10}} p_{11}^{n_{11}} \tag{C.2}$$

where we have assumed a prior uniform over the physical values of $\{p_{ij}\}$, i.e., $0 \leq p_{ij} \leq 1$ and $\sum p_{ij} = 1$. The likelihood function for the corrected populations, $\{c_{00}, c_{01}, c_{10}, c_{11}\}$, is obtained by substituting equation (B.1) into equation (C.2) and assuming a prior uniform over the physical values of $\{c_{ij}\}$, i.e., $0 \leq c_{ij} \leq 1$ and $\sum c_{ij} = 1$. Corrected populations are obtained by maximizing this likelihood function. The error for a specific population (say $c_{00}$) is obtained by marginalizing $\mathcal{L}\left(\{c_{ij}\}|\{n_{ij}\}\right)$ over the other three $(c_{01}, c_{10}, c_{11})$ and taking a 68% symmetric confidence interval.

We extract a likelihood function for the coherence by considering the following model:

$$y_i = 0.5 + \sqrt{\mathcal{F}_{\text{sw,1}}}\rho_{01} \cos(\omega_c t_i) + \epsilon_i \tag{C.3}$$

where $\{t_i, y_i\}$ are the parity oscillation data at the $i^{\text{th}}$ point, $\rho_{01}$ is the corrected coherence, $\mathcal{F}_{\text{sw,1}}$ is the parity oscillation correction factor associated with the swap

gate infidelity, and $\epsilon_i$ is the experimental error assumed to be normally distributed with $\mu = 0$ and unknown $\sigma$. The likelihood function is given by

$$\mathcal{L}\left(\rho_{01}, \sigma | \{t_i, y_i\}\right) = \prod_i \frac{1}{\sqrt{2\pi}\sigma} \exp\left[ -\frac{\left(y_i - 0.5 - \sqrt{\mathcal{F}_{\mathrm{sw},1}}\rho_{01}\cos(\omega_c t_i)\right)^2}{2\sigma^2} \right]. \tag{C.4}$$

We obtain a likelihood for the corrected coherence, $\mathcal{L}\left(\rho_{01}|\{t_i, y_i\}\right)$ by marginalizing over $\sigma$.

The likelihood function for the fidelity is obtained by taking a product of the likelihood function for the populations with the likelihood function for the coherence and evaluating a contour integral at constant $\mathcal{F}$, given by

$$\mathcal{L}\left(\mathcal{F}\right) = \int_{\mathcal{F}} \mathcal{L}\left(\{c_{ij}\}|\{n_{ij}\}\right) \mathcal{L}\left(\rho_{01}|\{t_i, y_i\}\right) d\rho_{01} \prod_{ij} dc_{ij}. \tag{C.5}$$

The Bell state fidelity is extracted by maximizing this likelihood and the error is evaluated as a symmetric 68% confidence interval.